Magnetoelectric Composites for On-Chip Near-Resonance Applications

Yuan Zhou

Dissertation submitted to the faculty of the
Virginia Polytechnic Institute and State University
in partial fulfillment of the requirements for the degree of

Doctor of Philosophy
In
Materials Science and Engineering

Shashank Priya, Chair
Carlos T. Suchicital
Mitsuhiro Murayama
Jean J. Heremans

August 14th, 2014
Blacksburg, Virginia

Keywords: Magnetoelectric, Piezoelectric, Magnetostrictive, Nanostructures, Self-bias, Transformer, Sensor, Energy harvester,

Magnetoelectric Composites for On-Chip Near-Resonance Applications

Yuan Zhou

Abstract

Magnetoelectric (ME) effect is defined as the change in dielectric polarization (*P*) of a material under an applied magnetic field (*H*) or an induced magnetization (*M*) under an external electric field (*E*). ME materials have attracted number of investigators due to their potential for improving applications such as magnetic field sensors, filters, transformers, memory devices and energy harvesters. It has been shown both experimentally and theoretically that the composite structures consisting of piezoelectric and magnetostrictive phases possess stronger ME coupling in comparison to that of single phase materials. Giant magnetoelectric effect has been reported in variety of composites consisting of bulk-sized ME composites and thin film ME nanostructures. In this dissertation, novel ME composite systems are proposed, synthesized and characterized in both bulk and thin films to address the existing challenges in meeting the needs of practical applications. Two applications were the focused upon in this study, tunable transformer and dual phase energy harvester, where requirements can be summarized as: high ME coefficient under both on-resonance and off-resonance conditions, broad bandwidth, and low applied DC bias.

In the first chapter, three challenges related to the conventional ME behavior in bulk ME composites have been addressed (1) The optimized ME coefficient can be achieved without external DC magnetic field by using a self-biased ME composite with a homogenous

magnetostrictive material. The mechanism of such effect and its tunability are studied; (2) A near-flat ME response regardless of external magnetic field is obtained in a self-biased ME composite with geometry gradient structure; (3) By optimizing interfacial coupling with co-firing techniques, the ME coefficient can be dramatically enhanced. Theses co-fired ME laminates not only exhibit high coupling coefficient due to direct bonding, but also illustrate a self-biased effect due to the built-in stress during co-sintering process. These results present significant advancement toward the development of multifunctional ME devices since it eliminates the need for DC bias, expands the working bandwidth and enhances the ME voltage coefficient.

Next, magnetoelectric nanocomposites were developed for understanding the nature of the growth of anisotropic thin film structures. In this chapter following aspects were addressed: (1) Controlled growth of nanostructures with well-defined morphology was obtained. Microstructure and surface morphology evolution of the piezoelectric $BaTiO_3$ films was systematically analyzed. A growth model was proposed by considering the anisotropy of surface energy and the formation of twin lamellae structure within the frame work of Structure Zone Model (SZM) and Dynamic Scaling Theory (DST). In parallel to $BaTiO_3$ films, well-ordered nanocomposite arrays [$Pb_{1.1}(Zr_{0.6}Ti_{0.4})O_3/CoFe_2O_4$] with controlled grain orientation were developed and investigated by a novel hybrid deposition method. The influence of the pre-deposited template film orientation on the growth of ME composite array was studied. (2) PZT/CFO/PZT thick composite film and BTO/CFO thin film were synthesized using sol-gel deposition (SGD) and pulsed laser deposition (PLD) techniques, respectively. The HRTEM analysis revealed local microstructure at the interface of

consecutive constituents. The interfacial property variation of these films was found to affect the coupling coefficient of corresponding ME nanocomposites. Subsequently, a novel complex three-dimensional ME composite with highly anisotropic structure was developed using a hybrid synthesis method. The influence of growth condition on the microstructure and property of the grown complex composites was studied. The film with highly anisotropic structure was found to possess tailored ferroelectric response indicating the promise of this synthesis method and microstructure.

Based on the laminated ME composites, three types of ME tunable transformer designs were designed and fabricated. The goal was to develop a novel ME transformer with tunable performance (voltage gain and/or working resonance frequency) under applied DC magnetic field. Conventional ME transformers need either winding coil or large external magnetic field to achieve the tunable feature. Considering the high ME coupling of ME laminate, two ME transformers were developed by epoxy bonding Metglas with transversely/longitudinally poled piezoelectric ceramic transformer. The influence of different operation modes toward magnetoelectric tunability was analyzed. In addressing the concern of the epoxy bonding interface, a co-fired ME transformer with unique piezoelectric transformer/magnetostrictive layer/piezoelectric transformer trilayer structure was designed. The design and development strategy of thin film ME transformer was discussed to illustrate the potential for ME transformer miniaturization and on-chip integration.

Lastly, motivated by the increasing demand of energy harvesting (EH) systems to support self-powered sensor nodes in structural health monitoring system, a magnetoelectric composite based energy harvester was developed. The development and design concept of the

magnetoelectric energy harvester was systematically discussed. In particular, the first dual-phase self-biased ME energy harvester was designed which can simultaneously harness both vibration and stray magnetic field (H_{ac}) in the absence of DC magnetic field. Strain distribution of the EH was simulated using the finite element model (FEM) at the first three resonance frequencies. Additionally, the potential of transferring this simple EH structure into MEMS scalable components was mentioned. These results provide significant advancement toward high energy density multimode energy harvesting system.

Acknowledgements

First of all, I would like to express my great gratitude to my supervisor Prof. Shashank Priya, for his constant support, patient guidance, invaluable discussion, and great suggestions in carrying out all the project works as well as in writing this thesis. I learned a lot from him on design of experiment, plan of research, carry out multiple projects, write of proposal/manuscript, and present of scientific results. His passion, enthusiasm, hard work and endless quest to perform high quality research have made a deep impression on me during the entire course of my doctoral student career.

I would also like to thank all my committee members for their valuable time in evaluating my research work and provide useful suggestions and comments. I am very appreciating Prof. Carlos Suchuicital for his help in experiment set-up, laboratory issues and useful discussion and suggestions on my research work. His patient in reviewing my prelim document line by line impressed me a lot and all those detailed comments provide great support toward refining my dissertation. I am very thankful to Prof. Mitsuhiro Murayama for his helpful discussion and great support on TEM characterization and analysis. I would also like to express my sincere thanks to Prof. Jean Heremans for his effort in serving as my committee and assessing my dissertation.

I have been really very fortunate to join the group of Bio-inspired Materials and Devices laboratory (BMDL) and Center for Energy Harvesting Materials and Systems (CEHMS). I enjoy the time with so many wonderful lab mates and friends and would like to express my appreciation for their generous help in course work, research projects and even daily life. In

particularly, I would like to thank Dr. Chee-sung Park for his kind help on experiential training and great suggestions on my research projects. I would like to express my gratitude to Dr. Yongke Yan and Dr. Deepam Maurya for their useful discussions and suggestions related to design of experiments and scientific paper writing. We had a great time in multiple cooperating projects. I am very thankful to Su-Chul Yang and Dr. Kyung-Hoon Cho for their support and encouragement on my research. I would like to thank Daniel and Dragan for their help and discussions on FEM modeling. I am also feel great honor to have wonderful colleagues and friends like Bo Chen, Yu Zhao, Ron, Shashaank, Nathan, Alex, Tony, Keyur, Natthapong, Hyun-Cheol and all the other members in Professor Shashank Priya's group.

I would like to express my profound thanks to all the collaborators for their contribution and efforts in these excellent works. I would like to express my gratitude to Dr. Ashok Kumar, National Physical Laboratory, New Deihi, India for his help with Raman spectroscopy measurement and analysis. I am very thankful to Dr. Chun-Hsien Wu for fruitful discussions and kind help with TEM measurement and characterization. I would like to thank Dr. S. S. N. Bharadwaja at Penn State University for helpful suggestions and discussions on thin film growth and characterization. I am very thankful to Dr. Seyit at Penn State University for his helpful discussions on piezoelectric transformer measurement. I would like to thank Dr. Jungho Ryu, Korea Institute of Materials Science, South Korea and Dr. Mirza Bichurin at Novgorod State University, Russia for their useful and insightful discussion on magnetoelectric composites and applications.

I am very thankful to John McIntosh, Stephen McCartney and Navin J. Manjooran for their help with SEM/TEM/AFM training and sample preparation at Nanoscale

Characterization and Fabrication Laboratory (NCFL) of Virginia Tech. I would like to give my thanks to Dr. Dwight Viehland and Dr. Jiefang Li for equipment support on ME measurement, PFM and VSM. Assistance from Dr. Jianjun Yao and Dr. Zhiguang Wang from Dr. Viehland's group is greatly acknowledged. I also appreciate the generous help from my colleagues: Dr. Wenle Li, Menghui Li, Dr. Yuchang Wu, Zhipeng Tian, Dr. Junqi Gao, Dr. Ying Shen, David Berry, Dr. Wenwei Ge, Dr. Yaojin Wang. I appreciate all the staffs and professors in MSE Department for their help.

I gratefully acknowledge the financial support from AFOSR through Young Investigator Program, the Office of Naval Research for supporting the research through Center for Energy Harvesting Materials and Systems, National Science Foundation, and the Office of Basic Energy Science, Department of Energy.

Last, but most importantly, I wish to express my deepest appreciation to my family. I would like to thank my dear parents Mr. Jianxin Zhou and Mrs. Yaling Cui for their love, endless support and encouragement. I would like thank all the other family members for their continuous support. In particularly, I would like to express my gratitude to my wife Li Gui for her patience, encouragement and unconditional support both in my PhD study and life.

Table of contents

List of Figures

List of Tables

1. Introduction

1.1 Multiferroic & Magnetoelectric materials

Multiferroic (MF) magnetoelectric (ME) materials have attracted great interest due to their technological importance in various applications such as magnetic field sensors, filter, transformer, information storage devices and energy harvesters.[1] In general, ferroic materials, including ferroelectric, ferromagnetic, and ferroelastic materials etc., exhibit hysteretic behavior between physical parameters (magnetization M, polarization P, strain ε) and their conjugate external stimuli (magnetic field H, electric field E, external stress σ).[2] The term "multiferroic" is used for the materials having more than one ferroic orders in a single phase.[3] The multiferroic coupling allows tuning of two or more physical parameters under external stimuli, as shown in Figure 1.1(a).[2] Out of various interesting phenomenon, one of the most appealing property of the multiferroic is the magnetoelectric coupling, which results in magnetoelectricity, as shown in Figure 1.1(b).[4] It is a product property of piezoelectricity and magnetoelasticity, where a large variation in spontaneous polarization can be obtained under external magnetic field or a change in magnetization can be obtained by applying electric field. The magnitude of ME coupling in naturally occurring single phase compounds ($BiFeO_3$, Cr_2O_3, $YMnO_3$) is extremely small at room temperature.[5,6,7] Therefore, to obtain larger ME coupling at room temperature, ME composites consisting of magnetostrictive and piezoelectric materials have been developed. In ME composites, the magnetic-field-induced strain (magnetostriction) in magnetostrictive phase is transferred to piezoelectric component through elastic coupling, and consequently generating electrical charges and vice versa.

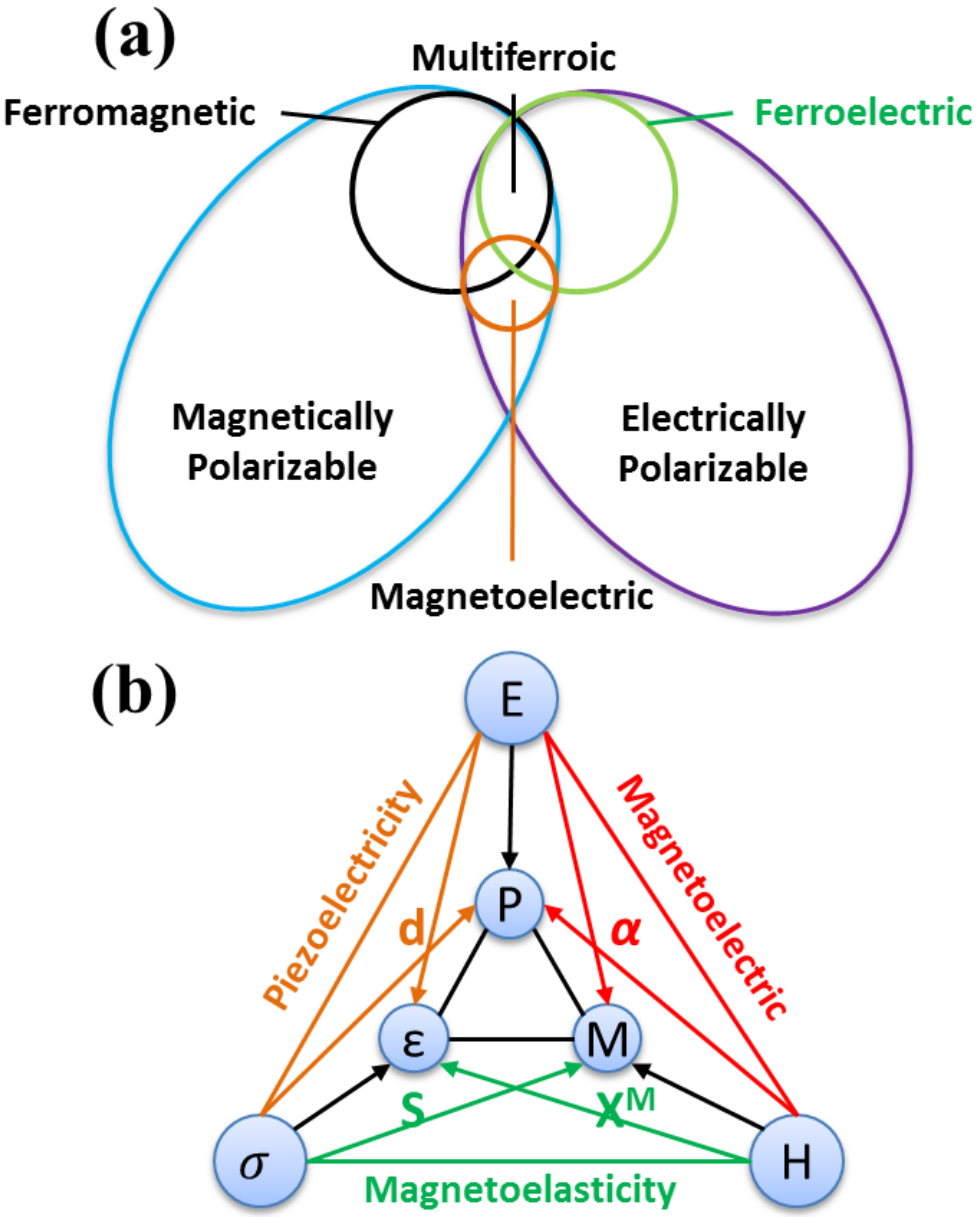

Figure 1.1 (a) The relationship between multiferroic and magnetoelectric materials. Notice that only small group of materials are both multiferroic and magnetoelectric. (b) Schematic diagram illustrating different physical relationships present in ferroic materials. (Adapted from [4])

Based upon the external stimuli, this magnetoelectric interaction can be described as:[1]

$$\text{Direct magnetoelectric (DME) effect} = \frac{\text{Magnetic}}{\text{Mechanical}} \times \frac{\text{Mechanical}}{\text{Electric}} \quad (1\text{-}1)$$

$$\text{Converse Magnetoelectric (CME) effect} = \frac{\text{Electric}}{\text{Mechanical}} \times \frac{\text{Mechanical}}{\text{Magnetic}} \quad (1\text{-}2)$$

In DME effect, the ME coupling coefficient is characterized by the ratio of applied AC magnetic field (H_{ac}) and induced AC electric field (E_{ac}) $\alpha_{\text{DME}} = \frac{\delta E_{ac}}{\delta H_{ac}}$. In CME effect, it is described as field conversion ratio between applied AC electric field and induced AC magnetic field, $\alpha_{\text{CME}} = \frac{\delta B_{ac}}{\delta E_{ac}}$. This coupling is tightly related to the intrinsic properties of each constituents and the effectiveness of elastic coupling between the two. Efforts have been addressed to enhance the ME voltage coefficient through various materials combination and configurations.

1.2 Magnetoelectric composite

Magnetoelectric composite can be realized through the interactions between the magnetostrictive and piezoelectric materials.[8] The transfer of magnetic field induced strain (magnetostriction) from the magnetostrictive phase to the piezoelectric phase occurs through the elastic coupling. Prior research on ME materials shows that composites exhibit much higher magnitude of ME coefficient than single-phase materials.[1,8,9,] In addition, the design and synthesis of ME composites offer more flexibility in cost-effectiveness and freedom in meeting the shape and size constraints. In the past decade, ME composites with diverse set of material, connectivity and microstructure have been developed through a variety of processing techniques.[1,10,11,12]

1.2.1 Classification

In general, ME composites can be categorized into different groups based upon phase connectivity, materials selection, operation mode and synthesis method, as listed in Table 1.1.

Connectivity is a critical parameter in composites and was described first for piezoelectric composite structure proposed by Newnham *et al.*[13] The connectivity in general can be given by $\frac{(n+3)!}{3!n!}$, where n is number of phases. For a two phase system, there are ten types of connectivity, as shown in Figure 1.2.

Table 1-1 Classification of magnetoelectric composites

Characterization	Classes		
Applied input	DME	CME	
Connectivity	0-3	2-2	1-3
Operation mode	L-T/ T-L	T-T	L-L
Material	All ceramics	Ceramic-Metal	Polymer-Metal
Synthesis	Bonding	Co-fired	Thin/Thick film

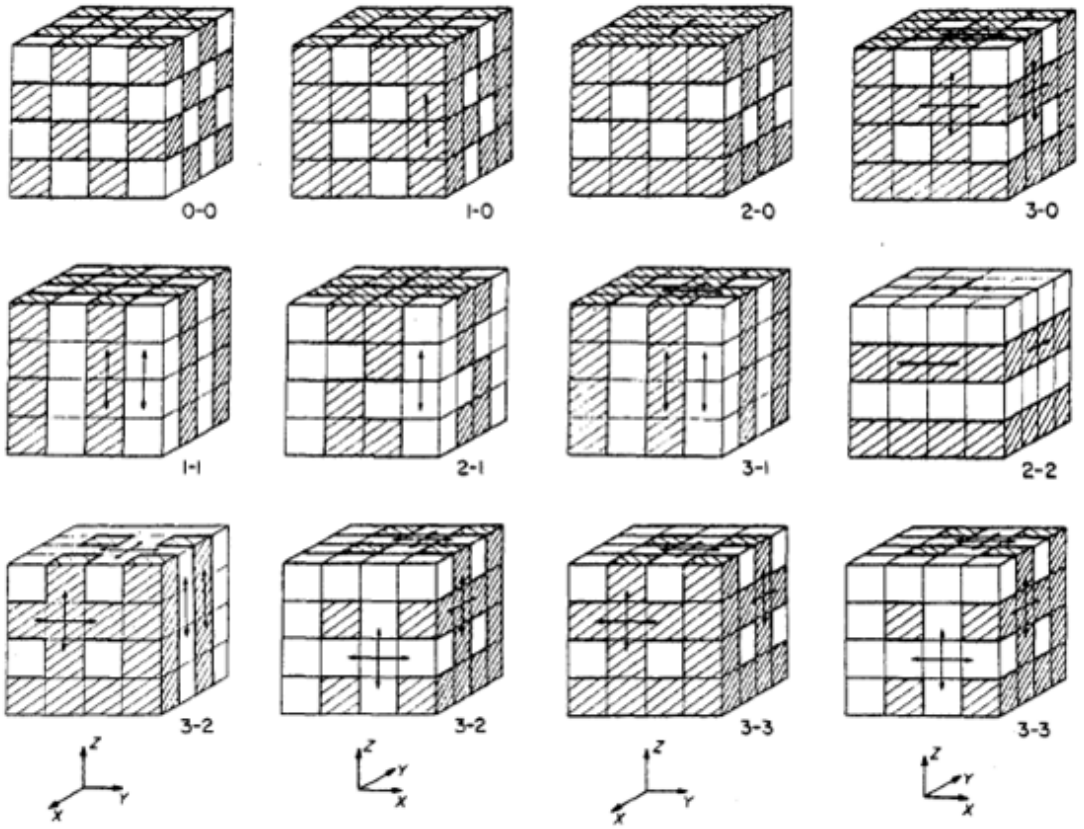

Figure 1.2 Different types of connectivity of the two phase composite system. Reprinted with permission from [13], Copyright 1978, Elsevier.

Considering the phase connectivity, two-phase ME composite system is typically classified into three common groups[1], as shown in Figure 1.3: (i) 0-3 type particulate composite, where the first number denotes the magnetic phase (0 dimension particles) embedded in the matrix of piezoelectric phase (3 dimension), (ii) 2-2 type laminate, where the layer-by-layer architecture consists of alternate magnetic and piezoelectric phase, and (iii) 1-3 type cylinder-matrix composite, where nano/micro-rods of magnetic phase are embedded in the piezoelectric matrix.[9] The 2-2 type ME laminate structures preserve the physical characteristics of individual phases, minimize the interfacial damping, and exhibit negligible leakage, thereby resulting in higher ME coupling. A sandwich type configuration with two distinct phases is a commonly utilized structure in this category.[8] The 1-3 type composites were mainly explored at the micro and nanoscale where they can be easily synthesized through the self-assembly process.[14] The 2-2 type laminates have been widely investigated due to the ease of fabrication and design flexibility.[8,9] The most common configurations for the 2-2 type laminates are magnetostrictive/piezoelectric (MP) bilayer structure and magnetostrictive/ piezoelectric/magnetostrictive (MPM) trilayer structure.

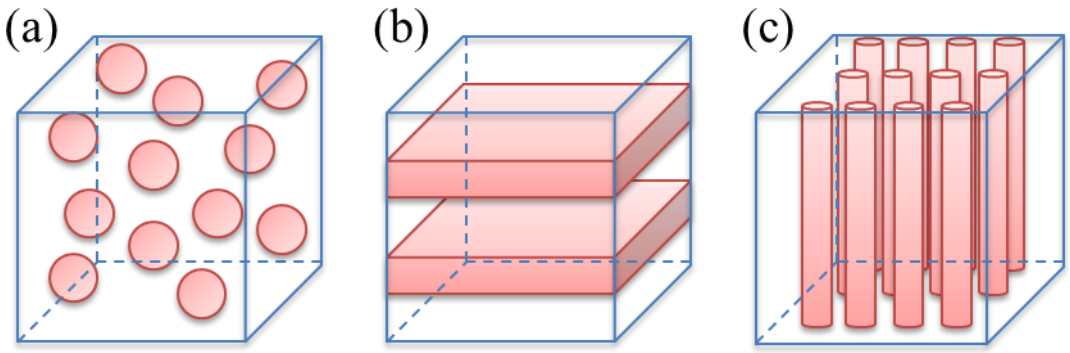

Figure 1.3 Schematic diagram of ME composites with three different connectivity: (a) 0-3 type particulate composite, (b) 2-2 type laminate composite, and (c) 1-3 type cylinder-matrix composite.

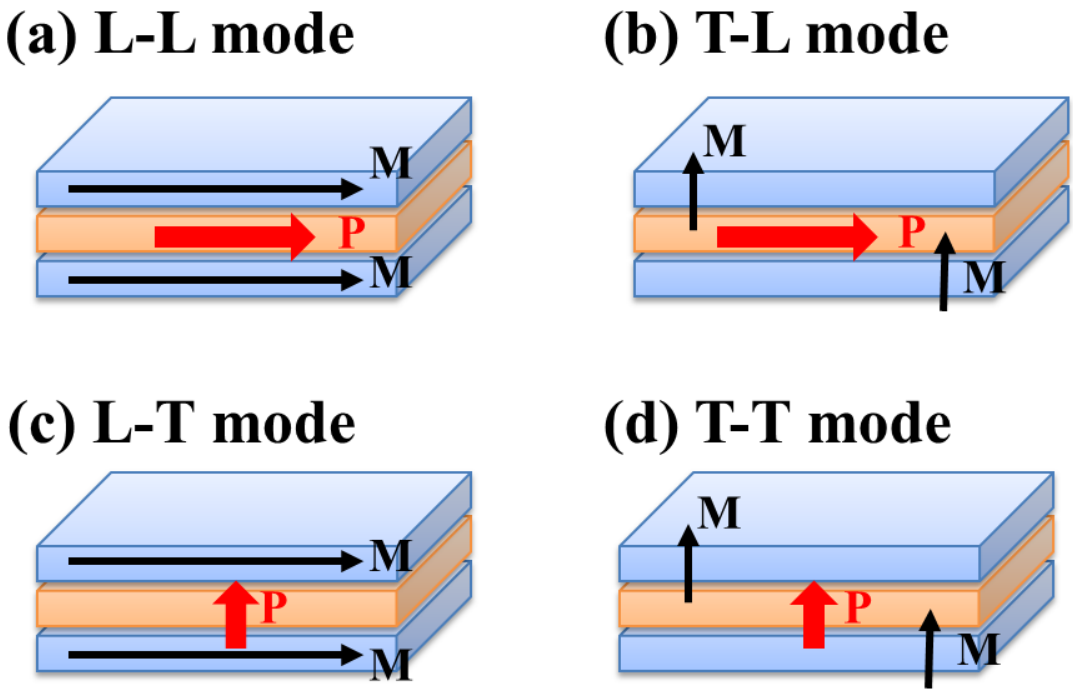

Figure 1.4 Schematic illustration of ME composite with four basic operation modes: (a) L-L; (b) T-L; (c) L-T; (d) T-T. M represent magnetization direction, P represent polarization direction.

Basing on different combination of poling and magnetization direction, we can identify four basic operation modes as L-T/T-L, T-T, L-L, where the first letter represents magnetization orientation, the second letter denotes polarization direction, "L" stands for longitudinal, and "T" for transverse, as shown in Figure 1.4. All these modes can be easily realized by fabricating structures through epoxy bonding of layers with different magnetization/poling conditions. Both theoretical calculation and experiments demonstrated that the magnitude of ME voltage coefficient for laminates follows the order (L-L)>(L-T/T-L)>(T-T).[8] Generally, the ME voltage coefficient of L-L mode structure is nearly an order of magnitude higher than those of L-T type laminates.[15] This is due to the efficient stress transfer ($d_{33}>2d_{31}$ since Poisson's ratio is smaller than 0.5) when the piezoelectric layer is longitudinally poled. The small value of (T-T) mode is a result of the demagnetization effect of the magnetostricitive phase. It is also important to mention here that other more complex modes such as composites in form of bimorph, unimorph, ring, and cylindrical structures have also been developed as alternative choices towards designing suitable energy harvesters.[16,17,18]

1.2.2 Materials selection

A suitable selection of piezoelectric and magnetostrictive materials is an essential step towards high performance ME composite. Srinivasan *et al.* have proposed the variation of ME coefficient with piezoelectric coefficient, piezomagnetic coefficient and elastic compliance of piezoelectric and magnetostrictive materials. For 2-2 type laminate composites, the ME coefficient are given as:[19]

$$\frac{\delta E_3}{\delta H_1} = \frac{-2d_{31}^p q_{11}^m v^m}{(s_{11}^m + s_{12}^m)\varepsilon_{33}^P v^p + (s_{11}^p + s_{12}^p)\varepsilon_{33}^P v^m - 2(d_{31}^p)^2 v^m} \quad (1\text{-}3)$$

$$\frac{\delta E_3}{\delta H_3} = \frac{-2d_{31}^p q_{13}^m v^m}{(s_{11}^m + s_{12}^m)\varepsilon_{33}^P v^p + (s_{11}^p + s_{12}^p)\varepsilon_{33}^P v^m - 2(d_{31}^p)^2 v^m} \quad (1\text{-}4)$$

where E_k and H_k are vector components of the electric and magnetic field; v denotes the volume; S_{ij} is an compliance coefficient; d_{ki} is a piezoelectric coefficient; q_{ki} is a piezomagnetic coefficient; ε_{kn} is an permittivity. The superscripts "m" and "p" represent the magnetostrictive and piezoelectric phase respectively. Clearly, the piezoelectric phase ($d_{31}^p, s_{11}^p, s_{12}^p, \varepsilon_{33}^P$) and magnetostrictive phase ($q_{11}^m, q_{13}^m, s_{11}^m, s_{12}^m$) play an important role toward large magnetoelectric response.

1.2.2.1 Piezoelectric materials

Generally, for piezoelectric materials, high piezoelectric voltage constant ($g=d/\varepsilon$), low dielectric and piezoelectric losses are desired. As shown in Table 1.2, there are multiple groups of piezoelectric materials such as random ceramics, textured ceramics, single crystals and polymers, where d_{33} is the longitudinal piezoelectric constant, d_{31} is the transverse piezoelectric constant, ε_r is the relative dielectric constant, k_{33} is the longitudinal electromechanical coupling coefficient, and T_c is the Curie temperature. Selection depends on composite processing techniques such as mixed oxide ceramic processing, hot-pressing, lamination, co-firing, injection molding and extrusion.

Table 1-2 List of typical piezoelectric materials. [9,8,20,21]

	Materials	d_{33}(pC/N)	d_{31}(pC/N)	ε_r(1kHz)	k_{33}	T_c(^{o}C)
Random ceramics	$BaTiO_3$	190	-78	1700	0.49	120
	PZT-5	400	-175	1750	0.72	360
	APC 855 (soft PZT)	630	-276	3300	0.76	250
	APC 840 (hardPZT)	290	-125	1250	0.72	325
Textured ceramics	NBT-BT	322			0.57	90
	PMN-PZT	1100		2310	0.84(k_p)	204
Single crystal	PMN-PZT	1530		4850	0.93	211
Polymer	PVDF		-28	6	0.2(k_t)	170

One of the first ME composite was developed by using $BaTiO_3$ (BTO) as the piezoelectric phase.[22] To further enhance the ME coupling, $Pb(Zr,Ti)O_3$ (PZT) based compositions have replaced BTO as the piezoelectric phase for its larger electromechanical coefficients. With the development of relaxor-based single crystals such as $Pb(Zn_{1/3}Nb_{2/3})O_3$–$PbTiO_3$ (PZN-PT) and $Pb(Mg_{1/3}Nb_{2/3})O_3$–$PbTiO_3$ (PMN-PT), the performance of ME composite can be dramatically enhanced based on their ultra-high electromechanical properties (d_{33}>2000 pC/N and k_{33}>92%).[9] However, the low Curie temperature and high cost hinder their application for ME composites. In addressing this challenge, alternative strategy of texturing ceramics was proposed. Yan et al. have demonstrated template grain growth (TGG) technique that yields microsctructure with <001> preferred grain orientation resulting in high d and g value comparable to that of single crystal [21]. By utilizing this textured ceramics as the piezoelectric layer in the ME composites, a 3.4 times improvement of α_{ME} was realized as compared to that of random ceramics.[21] Lead-free random and textured ceramics was also considered for fabricating ME composites.[20] Other than these ceramic materials, polymeric piezoelectric compositions such as polyvinylidene difluoride (PVDF) have been utilized for developing highly flexible ME devices.[12,23]

1.2.2.2 Magnetostrictive materials

Magnetostrictive materials are defined as materials that undergo a change in shape due to the variation of the magnetization states under external magnetic field. Similar to ferroelectric, the mechanism of magnetostriction can be related to the motion of magnetic domains. The magnetic domains are randomly oriented initially, leading to a

zero-net-magnetization. However, upon application of the magnetic field, these domains can be reoriented along the direction of the applied external magnetic field, giving rise to a dimension change, as illustrated in Figure 1.5. The material deformation can be quantified through magnetostriction (λ) coefficient with saturation value (λs). Table 1.3 provides a list of commonly used magnetostrictive materials for ME composites.

Among the magnetostrictive materials listed in Table 1.3, ferrites have larger electrical resistance in comparison to the metal/alloy magnetic materials but smaller magnetostriction. Ferrites are widely used in co-processing with piezoelectric ceramics due to their stability under high temperature. Magnetic alloy Terfenol-D exhibits large magnetostriction (1400ppm) with small permeability ($\approx$10). Terfenol-D is suitable for high performance ME laminate but requires large DC magnetic bias to reach the saturation magnetostriction. Metglas has extremely high relative permeability of >10000 and high piezomagnetic coefficient (q) but requires low processing temperatures. Metglas-based ME laminates require extremely small H_{bias}[15,24]. Both of these materials are quite attractive magnetostrictive phase for the fabrication of ME laminate composites.

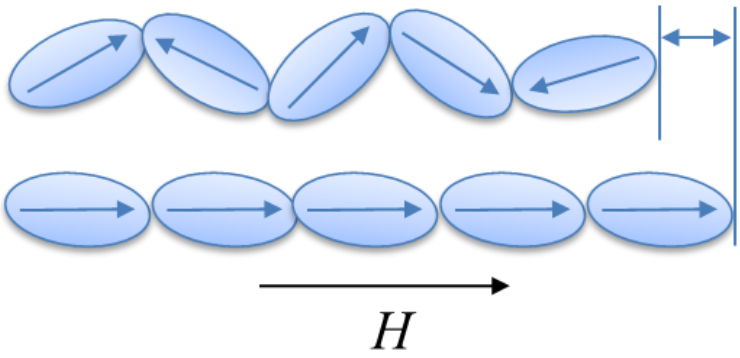

Figure 1.5 Schematic of magnetic domain rotation.

Table 1-3 List of typical magnetostrictive materials.[9,8]

	Materials	λs (ppm)
Ceramic	Fe_3O_4	40
	$NiFe_2O_4$	-26
	$CoFe_2O_4$	-110
Metal	Fe	-9
	Co	-62
	Ni	-33
Alloy	Terfenol-D ($Tb_{1-x}Dy_xFe_2$)	1400
	Galfenol (Fe-Ga)	200
	Metglas ($Fe_{81}Si_{3.5}B_{13.5}C_2$)	40

1.2.3 Synthesis of ME composite

A variety of synthesis techniques have been used for fabricating ME composites, including epoxy bonding, co-firing, thick film printing and thin film deposition.

1.2.3.1 Epoxy bonding

Epoxy bonding is widely used for synthesizing ME laminates because of its easy fabrication process and low cost.[8] Since this process does not require high temperature, most of the material combinations are suitable. Epoxy bonding reduces the misfit strain at the interface arising by the thermal expansion mismatch between the different layers. It also eliminates the atomic inter-diffusion and/or chemical reaction between the layers. Thus, it offers great design flexibility than conventional ceramic processing techniques. However, the epoxy layer with low mechanical strength dampens the generated strain, induces noise floor and therefore limits the ME response.[25] Further, manual fabrication process presents another challenge in implementation of industrial manufacturing.[26,27]

1.2.3.2 Co-firing

To optimize the ME interface coupling, direct bonding that completely excludes the epoxy in the composite is necessary. Co-firing technique not only enhances the elastic coupling between phases, but also dramatically decreases the cost due to its compatibility with industrial production process that commonly used for multilayer capacitors. Considering the materials characterization, co-firing of piezoelectric ceramics and ferromagnetic ceramics process is developed.[28,29,9] However, it is extremely challenging as a result of the large

difference in shrinkage rates and thermal expansion mismatch among different phases.

1.2.3.3 Thin film deposition

It has been widely accepted that strong interfacial bonding between two phases are required for a large ME response. However, either the low mechanical strength from the epoxy bonding or the possibility of inter-diffusion during the high temperature co-firing process may limit the bonding between the two phases. More importantly, these two methods result in another issue that the large sample size may limit its implementation for MEMS-scale functional ME devices. In addressing these issues, thin film deposition method has been widely employed in the development of ME composites.[4,6,14,4,30] Nanostructure thin film composites including 0-3 type particular films, 2-2 type layered heterostuctures, and 1-3 type vertical heterostructures have been investigated using either physical vapor deposition (PVD) methods (pulsed laser deposition, sputtering, molecular beam epitaxial) or chemical vapor deposition (CVD) methods (sol-gel spin coating, metal-organic chemical vapor deposition). By optimizing the deposition parameters and materials selection, ME composite thin films with coherent interfaces exhibiting various nanostructures were developed by precise control of the lattice mismatch and thickness between the two phases.[4,31]

1.2.3.3 Thick film printing

For practical applications, such as sensors or energy harvesting systems, the size effect limits the signal of ME voltage output, even though large ME coupling can be achieved in the thin film composites. For a film at 100 nm scale, the real ME voltage detected from the films might be negligibly small on the order of μV level.[11] Therefore, to enhance the voltage output

of the ME films, thick films at micron scale are highly demanded. Ryu et al. demonstrated an efficient method for fabricating thick films using aerosol deposition (AD).[11,32,] Piezoelectric and magnetostrictive nano-powders were sprayed on substrate through high pressure gas flow at room temperature. A high print rate with the magnitude of several microns/min can therefore be obtained. Composite films with various material phases, thickness and configuration can also be easily printed on metal/ceramic substrates with high density and good interfacial bonding strength.[32,33,34]

1.2.4 Conventional ME composites: Bulk and thin film

1.2.4.1 Particulate ME composite

0-3 type particulate composites, as illustrated in Figure 1.3(a), can be fabricated by the combination of particulate magnetostrictive phase homogeneously dispersed in the piezoelectric matrix. In order to achieve significant ME performance, the synthesis requirements can be summarized as: (i) thermal and chemical equilibrium of individual phases at the synthesis temperature, (ii) small elastic mismatch between the grains of individual phases, (iii) high dielectric insulation and resistivity of the overall composite, and (iv) large magnetostriction and piezoelectric effects of the composite. The effect of composition, geometry, sintering process, and grain size was studied and it was shown that magnetoelectric coupling can be improved from 26 mV/cm.Oe to more than 400 mV/cm.Oe by optimizing these parameters. This magnitude is much higher than that of single phase ME materials[35]. However, the magnitude of ME coupling was still lower than theoretical prediction for these type of the elastically coupled systems. This is believed to be related to

the high leakage current through ferromagnetic particles[35]. Therefore controlling leakage current in 0-3 particulate composites helps in achieving superior ME coupling through sintering.

1.2.4.2 Laminate ME Composite

2-2 type ME laminates structures can overcome the leakage problem, preserve the physical characteristics of individual phases, minimize the interfacial damping and thus provide larger ME coupling. A sandwich type configuration with two distinct phases is commonly used structure in this category. Piezoelectric and magnetostrictive phases can be bonded together by using epoxy resin or could be co-fired to form the multilayer laminates. By selecting proper composition, piezoelectric vibration modes, magnetic field orientation and optimized dimensions, one can obtain high ME coefficient (100~1000 mV/cm.Oe). To exemplify, push-pull mode ME laminates consisting of PMN-PT fibers and Metglas were found to exhibit giant ME coefficient of 52 V/cm.Oe at 1kHz under optimal DC magnetic bias 8 Oe, which enabled detection of extremely low magnetic field on the order of 1pT.[26]

1.2.4.3 Cylinder-Matrix ME composite

1-3 composites have been mainly explored at the micro and nano-scale where they can be easily synthesized through the self-assembly processes. At bulk scale, 1-3 composites can be fabricated through the dice-and-fill procedure but have limitation with respect to the aspect ratio of the rods.[36] To overcome this limitation, another process has been proposed where PZT rod is embedded in a Terfenol-D/epoxy mixture (TDE).[37] The experiments have demonstrated that the coupling between the PZT rod and TDE medium can generate much

larger ME response (18.2 V/cm.Oe at 84 kHz at 1.5 kOe) than the other three-phase composite reported in literature at the time of publishing this result.

1.2.4.4 Nanostructured composite thin films

In comparison to bulk ME composite with various connectivity as discussed above, the nanostructured thin film composites provide potential for enhanced ME coupling due to the possibility of higher interlayer interaction.[1,38] Motivated by the on-chip integration of magnetoelectric components, nanostructured composites of ferroelectric and magnetic oxides have been synthesized on lattice matching substrates with varying orientation and connectivity. The commonly experimented geometries are bilayers, heterostructures, self-assembled structures and nanowires. One early example of nanostructured composite is the 1-3 vertical heterostructure reported by Zheng *et al.* where arrays of magnetic CFO nano-pillars were embedded in a ferroelectric BTO matrix.[39] In that work, it was demonstrated that the self-assembled composites can possess large ferroelectric and ferromagnetic response, however ME coupling in such structures is debatable. Nanocomposite thin films have been explored via variety of synthesis techniques including physical deposition techniques (e.g. pulsed laser deposition, sputtering), chemical solution processing (sol-gel spin-coating) and chemical vapor deposition. However, the ME response of the nanostructure still remains a challenge. In 1-3 type structure, high leakage current due to continuous path of low resistance ferrite pillars limits the ME response. In 2-2 type layered geometry, the ME coupling was dramatically affected by clamping effect from the substrate. Owing to these challenges, it has been difficult to detect a significant ME charge from these

nanostructures. Indirect measurement method has been proposed by measuring the change of magnetization at Curie temperature, as shown in Figure 1.6.[39] This finding opens the possibility that ME coefficient might be measured in ultra-thin multiferroic composite thin films.

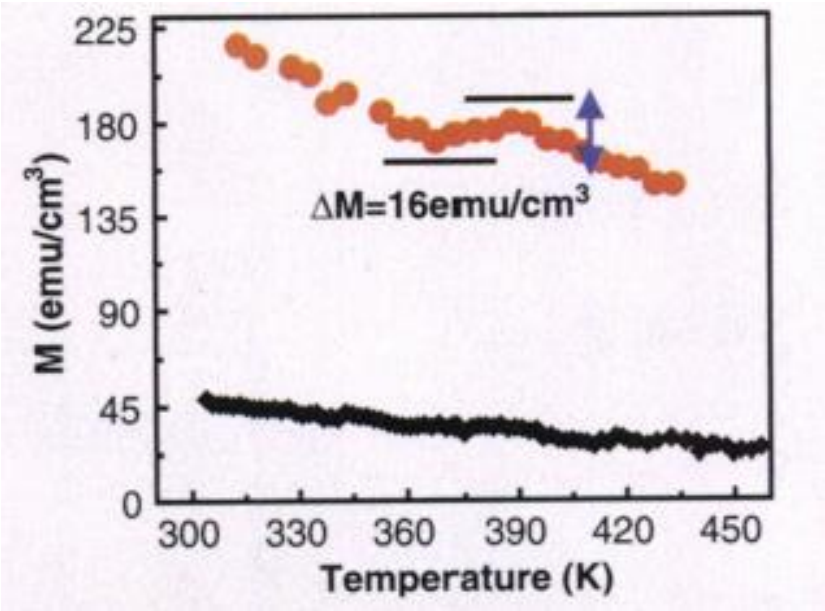

Figure 1.6 Magnetization versus temperature curve measured at H=100 Oe, which shows a distinct drop in magnetization at the ferroelectric Curie temperature for the vertically self-assembled nanostructure (red curve); the multilayered nanostructure (black curve) shows negligible change in magnetization. Reprinted with permission from [39], Copyright 2004, AAAS.

1.3 Characterization of magnetoelectric coupling

It can be seen from the above discussion that the possibilities are numerous for designing magnetoelectric composites (materials, connectivity, operation mode, synthesis method and so on). To better understand these composites, investigation of their working behavior would be important in illustrating the effect of specific variables associated with the performance. In the following section, the characteristic behavior of some representative conventional magnetoelectric composites is described.

1.3.1 DC magnetic field dependent response (ME vs H_{dc})

In magnetoelectric composites, the measured direct magnetoelectric coupling coefficient is the field conversion ratio between applied H_{ac} and induced E_{ac} under H_{dc}, $\alpha_{ME}=\delta E_{ac}/\delta H_{ac}$. In general, under a constant AC magnetic field, the ME coupling coefficient first increases with increasing H_{dc}, reaching a maximum at an optimized DC bias (H_{bias}), and then decreases with further increasing H_{dc}. This peak behavior in response to varying H_{dc} can be further explained by using the relationship as given below:[40]

$$\alpha_{ME} = \left|\frac{\partial T}{\partial S} \times \frac{\partial D}{\partial T} \times \frac{\partial E}{\partial D}\right| \times \frac{\partial S}{\partial H} \ , \tag{1-5}$$

where S is the mechanical strain, T is the mechanical stress, D is the electric displacement, E is the electric field, and H is the magnetic field. Since the first part of the above expression is a non-magnetic factor, one can re-write Eq. (1-5) as:

$$\alpha_{ME} \propto \frac{\partial S}{\partial H} = \frac{d\lambda}{dH} = q, \tag{1-6}$$

which indicates that the ME coefficient is directly related to the nature of ferromagnetic phase (λ: magnetostriction, q: piezomagnetic coefficient) and the effectiveness of elastic

coupling between the two phases. The dependence of α_{ME} on q indicates the requirement for additional H_{dc}. In summary, typical behavior of the α_{ME}, λ, q and their relationship as a function of H_{dc} can be illustrated as shown in Figure 1.7.

From the above discussion, one can clearly notice that the ME coupling coefficient essentially tracks the variation of q, which is proportional to the rate of change in λ. Depending on the optimum magnetic DC bias, ME composites can exhibit maximum ME coefficient. Therefore, based upon the composition and shape of ferromagnetic phase, one can tune the magnitude of optimum DC bias ranging from 5 Oe to 6.8 kOe.[1,10,41] Each of these ME composites has different ME behavior due to the difference in coercive field, permeability and magnetization. The volume fraction of magnetostrictive phase also affect the ME character including H_{bias}.

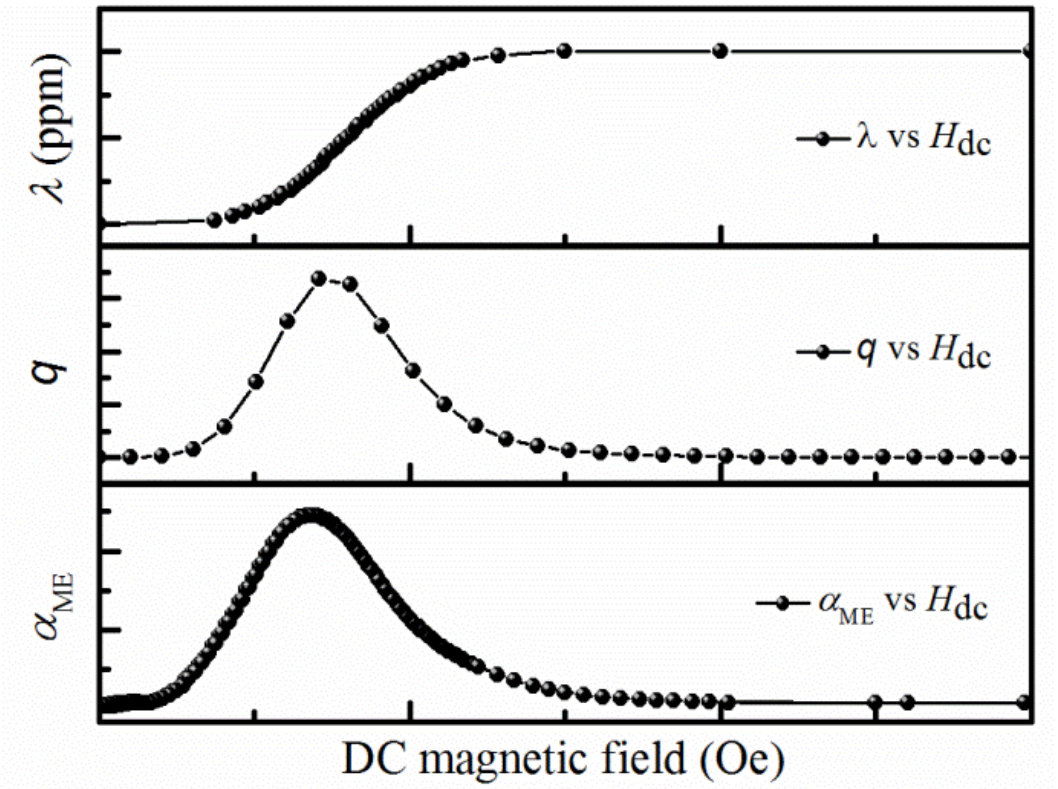

Figure 1.7 Typical magnetoelectric behavior as a function of DC magnetic field.

1.3.2 AC frequency dependent response (ME vs f_{ac})

Another important phenomenon of the ME composite is the ME coupling as a function of applied AC magnetic field (ME vs f_{ac}). When an AC magnetic field is applied at frequency corresponding to electromechanical resonance (EMR) for the piezoelectric phase or ferromagnetic resonance (FMR) for the magnetic phase in the ME composite, the ME voltage coefficient shows a peak behavior with the magnitude increased by a factor of up to 100X.[8,10] Bichurin et al. proposed a theoretical model for bilayer NFO-PZT laminates, which showed 40 times increase in $a_{ME,33}$ at electromechanical resonance compared to that of off-resonance.[42] Similar theories have been developed for the ME effect at ferromagnetic and magnetoacoustic resonance in the composites.[43],[44] Cho et al. analyzed the direct and converse magnetoelectric effect in laminate composites and found that DME is maximized at f_a while the CME is maximized at f_r, as shown in Figure 1.8.[40] This phenomenon can be further explained by using piezoelectric constitutive equations and combining it with frequency dependent capacitance of piezoelectric layer.

Generally, for application of ME composite in EMR range, the fundamental resonance frequency can be tuned by the length of the laminates (l) where the first longitudinal resonance is given as $f_L=1/(2l\sqrt{\rho s_{11}})$ (ρ is the laminate density, s_{11} is the elastic compliance of the laminate).[8] However, for practical use of the composites at low frequency, the corresponding composite dimension would be prohibitively large. Therefore, a model was developed for bilayer ME composite working at bending mode, which shows enhanced coupling at low frequency in a unimorph configuration.[45] Alternative approaches which utilize unique laminate configurations have been proposed to achieve low resonance

frequency within limited size of the components. Using these approaches, resonance enhancement of the ME coefficient has been achieved in the frequency range of 100Hz, using cm-long laminates.

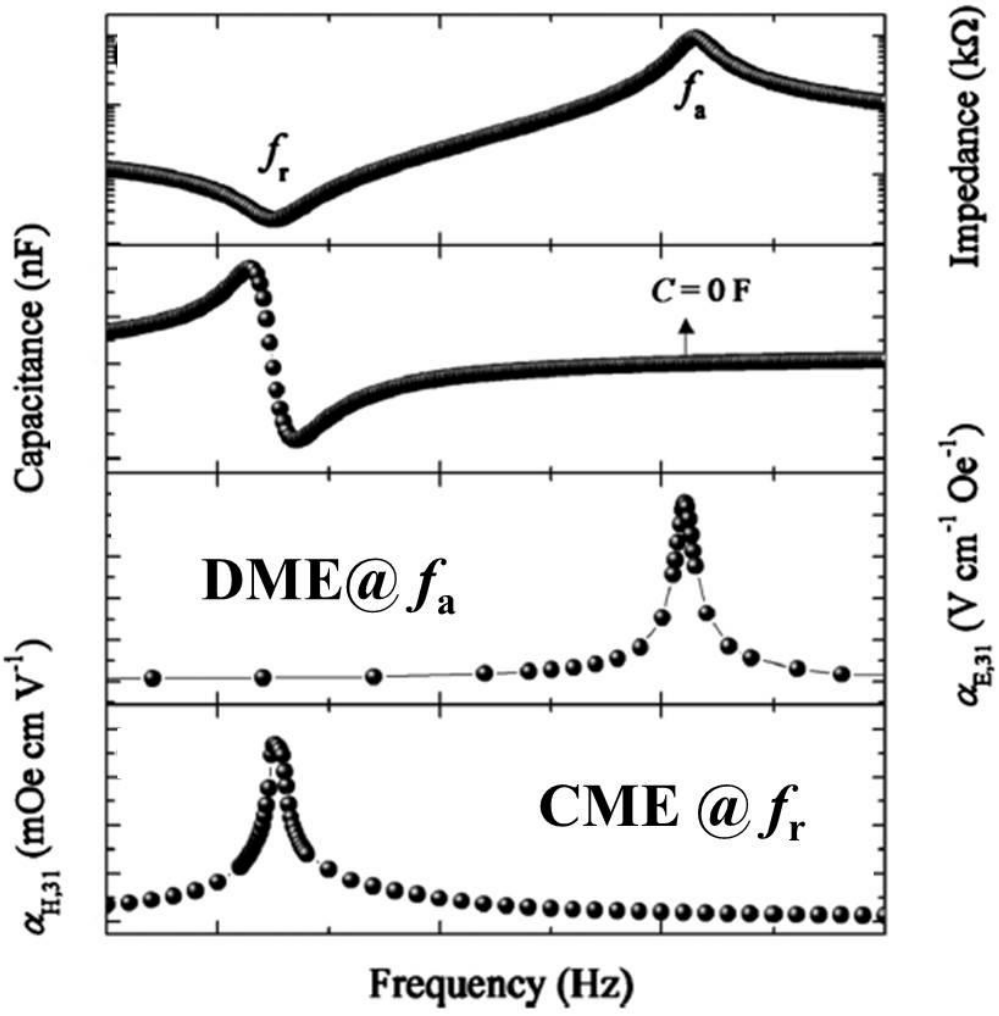

Figure 1.8 Impedance, capacitance and ME voltage coefficient as a function AC frequency. Reprinted with permission from [40], Copyright 2011, AIP Publishing LLC.

1.3.3 Configuration effect (ME vs Configuration)

It is known that ME response as a function of DC magnetic field is tightly related with the nature of magnetostrictive materials. Thus, there are lots of studies on shapes (disk, cylinder, plate, toroid, sphere, and so on) and sizes (numbers of layers, layer thickness, length and width) of the magnetostrictive material.[1] It is widely accepted that ME composite with rectangular shape having large length/width aspect ratio, small thickness and optimized volume ratio will generate higher ME voltage coefficient.[8] To better understand this ME vs. configuration relationship, the size-induced demagnetization effect was taken into consideration. For ferromagnetic materials, the demagnetization field is directly proportional to demagnetization factor (N_d), $H_d=MN_d$ (M is the magnetization), where N_d is dependent on the dimension and geometry. Thus, the internal effective magnetic field (H_{eff}) in the magnetic phase can be written as $H_{eff}=H_{bias}-H_d$, where H_{bias} is the induced external magnetic field. Therefore, in order to achieve same magnitude of H_{eff}, one needs to apply larger H_{bias} when H_d is larger and vice-versa.[46] Furthermore, this can also be co-related with the magnetic flux concentration (B_{eff}) in magnetic phase:

$$B_{eff} = \mu_0(H_{eff}+M) = \mu_0(H_{bias}+M)-\mu_0 MN_d, \quad (1\text{-}7)$$

where a smaller N_d results in a stronger B_{eff}. It is also noticed that high magnetic flux concentration in magnetic phase has positive effect on the magnetoelectric response of ME laminates.[47,48] Thus some researchers use the enlarged magnetic layer to boost the effective magnetic flux density along the piezo/magnetic interface for larger ME coefficient.

1.3.4 Self-biased ME effect

Considering the composition gradient and geometry, one can tune the optimum DC bias to as low as several Oe. However, it is still necessary to use permanent magnet or electromagnet to provide DC magnetic bias, which in turn hinders their implementation on thick or thin film platform. Thus, a novel design is desired if one needs to develop a ME composite with large tunable α_{ME} in the absence of DC magnetic field. This will pave the way for on-chip devices utilizing magnetoelectric phenomenon such as energy harvesters, AC magnetic field sensors and high frequency circuit components.

In order to address the requirement for DC magnetic sources, efforts to reduce H_{bias} have been emphasized. Researchers were able to tune the magnitude of optimum DC bias ranging from 6.8 kOe to 5 Oe by optimizing the composition and geometry of magnetostrictive phase.[1,10,15] However, the requirement for the DC bias still hinders their implementation in miniaturized devices. The self-biased effect could be an effective answer to this issue. As a result, magnetoelectric composites with large non-zero a_{ME} in the absence of DC magnetic field, namely "Self-biased ME effect", have been developed in various configurations using different strategy. Figure 1.9 illustrates the schematic of self-biased ME composites in comparison to that of conventional ME composites.

The highlights in the development of self-biased ME composites can be summarized in Figure 1.10. Observation of self-biased ME effect was first reported by Srinivasan et al. in 2002 as they found hysteresis and remanence of a_{ME} as a function of H_{bias} in co-fired LSMO-PZT laminates.[29] Similar behavior was also found in other laminates.[49] However, this phenomenon did not attract much attention in the following decade and most of the efforts

were focused on optimizing materials, structures and working mode to enhance the ME voltage coefficient and sensitivity.[1,8]

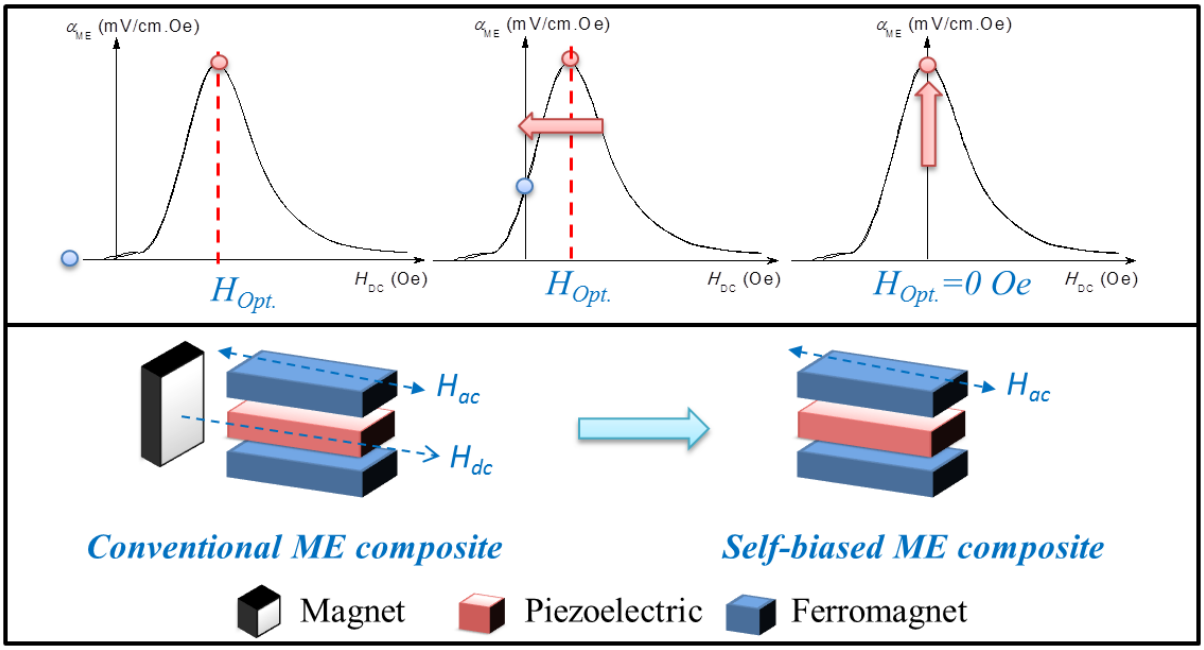

Figure 1.9 Schematic of conventional ME effect behavior and self-biased ME behavior.

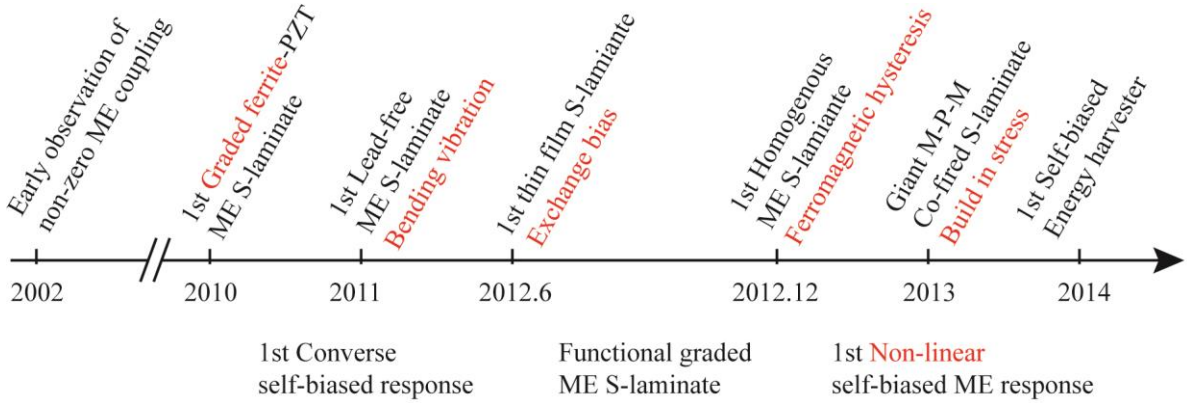

Figure 1.10 Milestones for the development of self-biased magnetoelectric composites.

In 2010, Mandal et al. demonstrated a compositionally graded ferrite/PZT laminate structure which produced non-zero ME voltage at zero DC magnetic bias.[50] They first correlated this non-zero ME behavior with the presence of flexural deformation and grading induced out-of-plane internal magnetic field in the ferrite. Subsequently, Yang et al. presented a methodology that regular ME laminate composites can possess self-biased ME response by changing vibration mode through electrical connections.[51] Soon after that, Srinivasan et al. systematically investigated the hysteresis and remanence in magnetoelectric coefficient in functionally graded magnetostrictive-piezoelectric layered composites and proposed a theoretical model for the self-biased graded composites.[52,53,54] In their work, Yang et al. first analytically studied the lead-free based self-biased laminates and proposed an electrically controlled core-free magnetic flux control devices by using the self-biased converse magnetoelectric effect.[51,55,56] Meanwhile, alternative approaches have been suggested for the case of thin films that rely on the angular dependence of exchange bias field from a multicomponent magnetic system to provide a non-zero piezomagnetic coefficient at zero bias.[57,58]

This discovery is technically important for applications such as magnetic field sensors, core-free magnetic flux control devices and electrically controlled magnetic memory devices.[56,59,60] However, practical implementation of these structure into MEMS scale devices is difficult due to the complex synthesis process of heterogeneous graded structure. Further, the self-biased effect due to the magnetization grading induced build-in field lacks the feasibility for tunability. Thus, even though these structures are intriguing their implementation for realization of on-chip components and tunable devices will be limited.

1.4 Applications

Several promising applications have been studied in literature including magnetic field sensors, transformers, tunable devices, filters, oscillators, memory devices, energy harvesters, etc. Among these, three applications were focus of this study and are briefly described below.

1.4.1 Magnetic sensors

As the variation of magnetoelectric voltage coefficient is dependent on the magnetic field input, thus by monitoring the change of ME voltage output, one can detect the change of either AC magnetic field or DC magnetic bias. The working mechanism can be explained as follows: on application of a magnetic field on the composite a strain will be induced and transferred to piezoelectric phase resulting in a proportional charge. The input magnetic field on ME composite consists of an AC magnetic field with a DC magnetic bias. Either of these two can be detected by providing the other component. Thus, one can use the ME composite as AC/DC magnetic field sensor.[26,61] By selecting high performance piezoelectric and magnetostrictive materials and combining them with a suitable structure, it is possible to detect small magnetic fields as low as about 1 pT at a frequency of only several Hz.[26]

1.4.2 Transformers and tunable devices

ME transformers have important application as voltage gain devices. High voltage gain has been reported in ME laminates consisting of Terfenol-D and PZT.[62,63] The working mechanism can be described as following: an AC magnetic field is induced in the ME laminate through a solenoid with n turns wrapped around the laminate. When this AC field is

at the resonance frequency of the laminates, a giant magnetoelectric voltage output can be obtained through ME coupling effect, offering potential for high voltage miniature transformer application. ME transformer has the advantage of high voltage gain and wider working bandwidth than the conventional piezoelectric transformer and does not require secondary coils with a high-turn ratio than the conventional electromagnetic transformer.

ME composites have the potential as dual electric and magnetic field tunable devices. For example - in the case of ME transformer, induced strain in the magnetic layer is tightly related to the applied magnetic field. Since the magnetic field is coupled to the piezoelectric layer, change of magnetic field can lead to a large shift in the working resonance and voltage output, providing the basis for a magnetic-field-tunable device[64]. On the other hand, mechanical stress in the piezoelectric layer induced by the applied electric field is coupled to the ferrite layer which in return provides shift in the magnitude of generated magnetic field, thereby working as an electric-field-tunable device[65].

1.4.3 Energy harvesting system

Magnetoelectrics can be used to generate power from stray magnetic field in an industrial environment. An oscillating magnetic field present in the surrounding of industrial facilities like large induction motor will induce an AC stress on the piezoelectric layer through magnetostriction. This stress can be further converted into electric charge through direct piezoelectric effect, acting as a magnetic field energy harvester. Magnetoelectrics can also be used to convert vibration energy into electricity though piezoelectric layer, acting as a dual-phase energy harvester which can simultaneously capture energy from mechanical

vibration and stray magnetic field.[66] This dual-phase harvester is expected to enhance energy collection and conversion efficiency.

1.5 Chapter summary

Although ME composites have been investigated for several decades, there are still several fundamental challenges in realization of high performance ME composites and functional devices. The performance of ME functional devices is tightly related to the materials selection, structure, processing method, operating mode, size effect and other dynamic parameters. Table 1-4 summarized a list of factors to be considered in the development of ME composites and devices, including an overview of the features, challenges as well as the suggested fabrication methods. Comprehensive understanding of these factors provides guidance towards the design of high performance magnetoelectric composites and devices.

Table 1-4 List of factors to be considered in the design of magnetoelectric energy harvester

Design factors	Features	Challenges	Realization
Materials	Piezoelectric Magnetostrictive	α_{ME}	Appropriate combination
Synthesis	Epoxy bonding Thin film deposition	Low coupling Low power	Co-firing Thick film printing
Characterizations	ME vs H_{dc}	H_{bias} Narrow bandwidth	Self-biased ME Wideband
	ME vs f_{ac}	f_r Narrow bandwidth	Low frequency Broadband
	ME vs Configuration	Volume ratio Size effect	Demagnetization Thin film device

2. Motivation, Objective and Plan of research

Magnetoelectric materials possess the capability of inducing electrical polarization by applied magnetic field, and/or magnetization variation by applied electric field, which provides great potential for development of multifunctional devices. In order to fulfill this potential, the focus in this thesis was on understanding the science of magnetoelectric behavior and apply this understanding to develop novel functional devices. The objective of this research is to design, synthesize and characterize magnetoelectric composites with enhanced functional performance, understand their structure-property relationship, and develop functional devices based on the ME composites. Specifically, the following topics are covered in the chapters of this thesis.

(1) Bulk magnetoelectric composites

For ME bulk structures, great potential still exists if one can further increase the ME coupling by (a) overcoming the requirement of magnetic DC bias, (b) expanding the working bandwidth in terms of magnetic field response, and (c) modifying the interfacial contacts of the composites.

(a) Eliminating the need for DC bias: Previous investigations have found that ME composites consisting of magnetostrictive and piezoelectric phases have maximum ME voltage coefficient under applied AC magnetic field with optimum DC magnetic biases. However, the requirement of DC magnetic source (permanent magnet or coil) hinders their way towards device miniaturization and on-chip application. Thus, it would be extremely beneficial if a large ME voltage coefficient can be achieved in the absence of DC bias with a simple ME

laminate structure. In this thesis, bilayer Ni/PZT laminate was investigated that exhibits self-biased phenomenon. An in-depth understanding of the self-biased effect of Ni based laminate was developed by conducting systematic experiments and numerical modeling. This novel phenomenon opens great possibility in developing next generation energy harvesting systems, portable magnetic field sensors and ME composite based on-chip devices.

(b) Increasing the working bandwidth: Both experimental and theoretical calculation demonstrated peak ME coupling coefficient in response to varying DC magnetic field under a constant AC magnetic field. Thus, upon slight variations of the applied H_{dc}, the magnitude of α_{ME} may decrease dramatically, leading to an unstable ME response. In addressing this issue, a stable ME response with respect to varying DC magnetic bias was demonstrated in geometry gradient self-biased ME composites. The ME response of the gradient composites was found to be almost independent of H_{dc} in the range of 0~260 Oe, which is almost 6.5~38 times larger than that of conventional ME composites. This is significant advancement in the field of ME composites opening the pathways for high stability ME applications.

(c) Improving ME coupling: It is well-known that large ME coupling in bulk ME composite is desired for practical device applications. Most of the prior studies have utilized epoxy bonding to achieve laminate structure, which has the drawback of reduced strain transfer. Co-fired structures provide the opportunity of interfacial engineering to obtain the optimum strain transfer from two phases. However, phases with dissimilar crystal structure/ thermal expansion coefficient and inter-diffusion during high temperature sintering hinders the development of co-fired ME composites. In this study, a suitable process was developed that is able to overcome these challenges and provide fundamental understanding of self-biased

phenomenon in co-fired laminates with single phase magnetic material.

(2) Magnetoelectric nanostructures

ME nanostructures are interesting but it is difficult to control the growth of desired ME nanostructure morphology with good coupling. In this thesis, two aspects were addressed: (a) controlled growth of nanostructure, and (b) manipulating the nanocomposite interface to modulate the piezoelectric and ME characteristics.

(a) Controlled growth of nanostructure: To better understand the growth of heterostructured ME thin film composite, it is necessary to study the microstructural changes (nucleation & growth, effect of crystal orientation) for piezoelectric and magnetostrictive phases. Specifically, piezoelectric materials are important since they generate charges in the ME composite. It is well-known that piezoelectric properties depend on the polarization distribution of individual domains, which is affected by the nanostructure, grain size and orientation. Synthesis of nanoscale structures such as nano-pillar, nano-belt and star-like morphology has the potential towards achieving better compatibility or improved performance. $BaTiO_3$ was chosen as an archetype model piezoelectric system. In parallel to pulsed laser deposition (PLD), a hybrid deposition method was developed to control the film growth orientation via a pre-deposited well-ordered buffer layer. Thin film nanocomposites (CFO/PZT) of highly textured crystallization and well-ordered multi-orientation arrays were used for further scanning probe microscopy studies.

(b) Manipulation of the nanocomposite interface: The 2-2 type sandwich ME composites with selected high performance piezoelectric/magnetostrictive compositions are known to exhibit high magnetoelectric response. Effective elastic coupling through coherent interfaces

has been considered to be an important factor resulting in enhanced magnetoelectric response. Accordingly, in this thesis, investigation of the nanocomposite interface was conducted through comparative analyses of HRTEM and electrical data that explains the origin of high ME response in 2-2 type ME nanocomposites. The deposited film endures large in-plane constraint from the substrate, hindering further improvement in the magnitude of the ME coupling. In order to reduce the limitation of clamping effect, a complex three-dimensional ME composite was developed to understand the potential of the highly anisotropic structure synthesized by a hybrid deposition process.

(3) Magnetoelectric tunable transformers

Most of the published work on ME applications has focused on sensors with enhanced coupling effect. However, there has been limited work in the area of fully functional ME devices. Considering the magnetic/electric field controlled polarization in ME materials, it is interesting to study the tunability feature. Therefore, different types of ME transformers were developed in this thesis that exhibited good frequency tunability under external DC magnetic field and they were arranged from three different aspects: (a) Epoxy bonded ME transformer; (b) Co-fired ME transformer; (c) Thin film ME transformer.

(a) Epoxy bonded ME transformer: Considering the working mode of ME composites, two ME transformer structures were synthesized by epoxy bonding magnetostrictive materials with the unipoled/long-type piezoelectric transformer in a laminate configuration. The ME transformer consists of transversely poled piezoelectric transformer working under longitudinal DC magnetic field (H_{dc}) was first investigated, namely L-T mode ME transformer. A tunable feature was observed in the magnitude of the voltage gain and working

resonance frequency with applied external magnetic field. However, the requirement of large H_{dc} with low tunability presents another concern. Alternatively, an attempt was made at bonding the Metglas with a longitudinally poled piezoelectric transformer. In this structure, the strain transfer is more efficient under longitudinal H_{dc}, leading to a dramatic enhancement in the frequency tunability at low magnetic bias.

(b) Co-fired ME transformer: Although the epoxy bonded ME transformer exhibited good ME coupling and magnetic field induced tunablity, the bonding operation and low mechanical strength of the epoxy layer is still a concern. In order to eliminate the need of using epoxy, a novel structure consisting of two unipoled piezoelectric transformers and a magnetostrictive layer was synthesized using low temperature co-firing ceramic technique (LTCC) in a laminate configuration. This cost-effective composite with excellent magnetic tunablity feature opens the possibility of developing on-chip miniaturized ME transformers.

(c) Thin film ME transformer: To meet the requirement of device miniaturization, the development of thin film ME transformer was explored. A simple ME transformer consisting of a layer of magnetostrictive material deposited in the center of a ring-dot type unipoled piezoelectric thin film transformer was designed. Alternatively, a new magnetostrictive substrate based ME thin film transformer was proposed and is briefly discussed.

(4) Magnetoelectric energy harvester

Advances in integrated circuits, sensors, and actuators have led to decreased power consumption to a point where energy harvesting (EH) systems can be used to supply sufficient power to these circuits and wireless devices. Specifically, in a structural health monitoring system, there is an increasing interest in developing self-powered sensor nodes

with smart architecture that utilize all the environmental resources available to meet the dynamic power requirement. Unused power can be tapped from environment in the form of structural vibrations (including strain and acceleration) and magnetic field available from industrial machines, transportation vehicles, human activity, and buildings. Energy harvesting systems can be broadly classified based on the voltage generation mechanism such as piezoelectric, electromagnetic, magnetoelectric, dielectric elastomers and electrets.

Among them, magnetoelectric energy harvesting is a relatively new concept with limited number of investigations on quantifying the variety of harvester architectures. The voltage can be induced in a magnetoelectric composite through external magnetic and vibrations. Various devices and structures around us generate stray magnetic fields as a result of the components inherent to their operation. In addition, magnetoelectric energy harvester can be made to work as a vibration energy harvester to create an additive voltage effect. In this thesis, a detailed study was conducted on the magnetoelectric energy harvesters. A novel self-biased ME energy harvester that generates voltage in the absence of DC bias is proposed and discussed in detail. Principles behind the design to harvest energy from mechanical vibrations and magnetic fields individually or simultaneously are illustrated. This dual-phase ME energy harvester design not only dramatically enhanced the power density of the current ME EH systems, but also provides great potential toward implementing MEMS-scalable energy harvesters.

3. Bulk Magnetoelectric composites

ME materials provide opportunity towards developing new applications such as tunable transformers, filters, resonators, and dual-phase energy harvesters.[1,67] Prior research on ME materials has shown that bulk piezoelectric/magnetostrictive composites exhibit much stronger response than single-phase materials. In the past decade, bulk ME composites with various connectivity and structures have been developed in order to improve the ME coefficient and sensitivity.[9,8] These experimental investigations have been complimented by the theoretical modeling which has led to the understanding of the role of various material and structural parameters.[1,10]

However, there are still several challenges of conventional ME composites which have not been addressed, including (1) need of optimized DC bias for high ME coupling; (2) narrow working bandwidth around the optimal magnetic DC bias; and (3) limited ME voltage coefficient using epoxy bonding techniques.

In this chapter, in addressing these challenges, I will discuss the working principle of the tunable self-biased magnetoelectric composites, illustrate their application toward near-flat ME response in terms of DC bias and demonstrate a co-firing method to enhance the interfacial coupling between consecutive phases.

3.1 Tunable self-biased ME composite in homogenous laminates*

In direct ME effect, the measured coupling coefficient is the field conversion ratio between the applied AC magnetic field (H_{ac}) and the induced AC electric field (E_{ac}), $\alpha_{ME}=\delta E_{ac}/\delta H_{ac}$, which is directly related to effectiveness of elastic coupling between two phases and piezomagnetic coefficient ($q=d\lambda/dH$, λ: magnetostriction) of magnetostrictive phase. The dependence of α_{ME} on q indicates the requirement for additional DC magnetic bias (H_{bias}).[41] Depending upon the composition and shape of magnetostrictive phase, one can tune the magnitude of optimum DC bias ranging from 5 Oe to 6.8 kOe. [1,10,41] However, these composites then require permanent magnet or coil as DC magnetic bias source, which hinders their implementation on thick or thin film platform. In this section, a homogenous two-phase magnetostrictive (ferromagnetic)-piezoelectric composite structure with a large tunable α_{ME} in the absence of DC magnetic field was presented. This structure opens the possibility for designing MEMS-scalable energy harvesting components.

3.1.1 Experimental

$0.8[Pb(Zr_{0.52}Ti_{0.48})O_3]$-$0.2[Pb(Zn_{1/3}Nb_{2/3})O_3]$ + 2 mol%MnO_2 (PMT) were synthesized by conventional mixed oxide method and shaped into plates of dimension 10×5×0.3 mm^3. After poling, 0.15-mm-thick Metglas sheet (4 layers, 2605SA1, Metglas Inc., USA) or "*n*" layers of 0.15-mm-thick Ni foil (McMaster -Carr, USA) with different lateral dimension were laminated on the PMT plate by using epoxy resin (West System, USA) to form the bilayer laminates. The ME effect was measured in L-T mode (longitudinally magnetized and

*Reprinted with permission from [46], Copyright 2012, AIP Publishing LLC.

transversely poled) configuration with sample located in the center of the Helmholtz coil (H_{ac}) which itself was located in the center of large electromagnet (H_{dc}). The induced voltage was monitored using a lock-in amplifier. The magnetization of the ferromagnetic layer was measured by using vibrating sample magnetometer (VSM 7340, Lake Shore Cryotronics). The magnetic domain structure was observed by magnetic force microscopy (Dimension Icon AFM, Bruker) in the tapping-lift mode. Magnetostriction was measured by using the strain gauge and Wheatstone bridge. Impedance spectrum of the laminate was measured by an LCR meter (HP4194A, USA).

3.1.2 Working Mechanism of Self-biased ME behavior

The magnetoelectric properties of the Ni-PMT and Metglas-PMT bilayer laminates was first characterized as a function of DC magnetic field H_{dc} at 1 kHz with H_{ac}=1Oe, as shown in Figure 3.1. The α_{ME} of Metglas-PMT bilayer structure shows non-hysteretic cyclic response as a function of H_{dc}, with maximum occurring at 68 Oe. Most of the ferromagnetic materials exhibit zero piezomagnetic coefficient when H_{dc} = 0 and consequently negligible α_{ME} near zero bias. In comparison, it is noticed that the α_{ME} of Ni-PMT bilayer shows a hysteretic behavior during H_{dc} sweep (anticlockwise direction), with a large response of ~±63.3 mV cm^{-1} Oe^{-1} at zero DC magnetic bias, ~72.5% of its maximum α_{ME} value (87.3 mV cm^{-1} Oe^{-1}). It should be further noted here that this laminate system does not have magnetic gradient structure. Considering the intrinsic relationship for α_{ME} of composites= $|\frac{\partial T}{\partial S} \times \frac{\partial D}{\partial T} \times \frac{\partial E}{\partial D}| \times \frac{\partial S}{\partial H}$, where first part is non-magnetic factor, one can derive $\alpha_{ME} \propto \frac{\partial S}{\partial H} = \frac{d\lambda}{dH} = q$. The effective λ was estimated by integrating α_{ME} with respect to the H_{dc} as shown in the inset of Figure 3.1.

Metglas-PMT shows symmetrical λ-behavior with respect to H_{dc} while the tendency of λ for Ni-PMT was asymmetric. Thus, the hysteretic behavior is related to the nature of magnetostrictive materials.

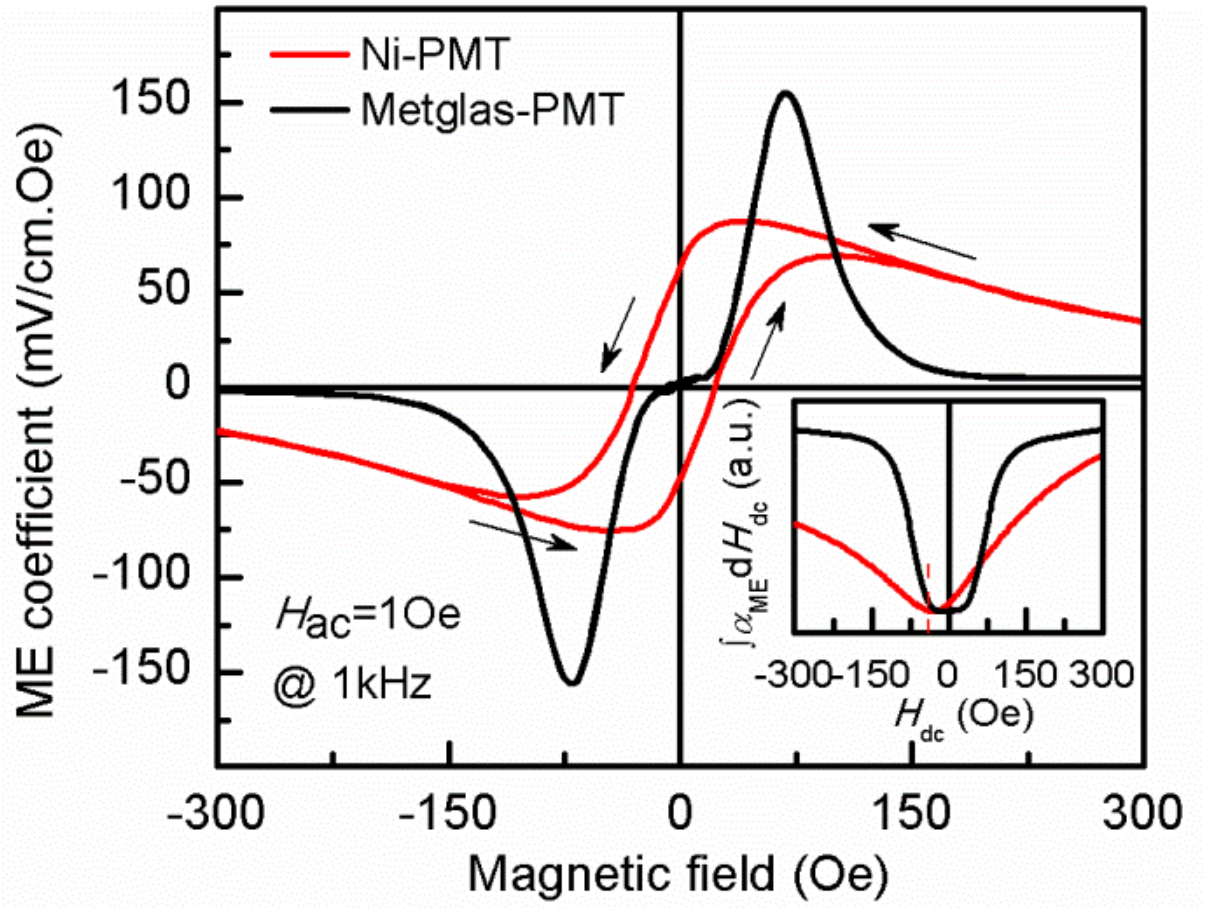

Figure 3.1 ME coefficients (α_{ME}) of Ni-PMT and Metglas-PMT bilayer laminates as function of DC magnetic field (H_{dc}). Inset shows integral values of ME coefficient with respect to magnetic field.

In order to further elucidate the reason for self-biased hysteretic behavior, magnetization (M) of Ni and Metglas were measured as a function of H_{dc} in longitudinal direction (in-plane) as shown in Figure 3.2(a). The hysteretic behavior of magnetization for Ni in the range of ±300 Oe can be immediately noticed in comparison with Metglas. This phenomenon could be attributed to the change in the structure of magnetic domains in both materials. Magnetic force microscopy (MFM) was conducted on Ni and Metglas surface to understand the differences in magnetic domain structure as shown in inset image of Figure 3.2(a). Nanosized striped domains in Metglas can be easily aligned in the direction of applied H-field exhibiting small coercive field and high reversibility. The absence of grain boundary in amorphous metglas contributes towards the lower coercive field. However, nickel foil was found to possess macrosized domains with long range ordering which resulted in larger coercive field than that of Metglas. Once the magnetic domains were reoriented, it required higher field to achieve the random state resulting in larger hysteresis in the magnetization curve. This difference in the hysteretic behavior originating from the differences in the crystallinity and domain structure is reflected in the magnetization response. This magnetization behavior can be also correlated with magnetostriction through the relation given as: [68,69]

$$\varphi \sim \frac{3\lambda\sigma}{(K+2\pi M^2)} \quad \text{or} \quad \lambda \propto M^2, \tag{3-1}$$

where φ is the angle of magnetic moments, K and σ are the anisotropy constant and stress, respectively. As shown in Figure 3.2(b), M^2-H curves indicate that there was no obvious hysteresis in Metglas, while large hysteresis occurs in Ni. Using Equation (3-1), and considering $\alpha_{ME} \propto q = d\lambda/dH$, the relationship of $\alpha_{ME} \propto dM^2/dH$ can be obtained. Hence, the magnitude of dM^2/dH can be used to predict the behavior of ME composites

with respect to applied magnetic field. It was found that the $(\mathrm{d}M^2/\mathrm{d}H)$-$H$ behavior of Metglas and Ni based laminates matched well with experimental data shown in Figure 3.1 Note that Figure 3.2(b) shows only the qualitative nature of effective λ, q behavior of magnetostrictive layer and not quantitative values. Therefore, it is believed that difference in the domain and microstructure of Metglas and Ni as observed by MFM and resultant different behavior of M^2-H and $(\mathrm{d}M^2/\mathrm{d}H)$-$H$ behavior are the origin of the self-biased ME response. Based on this hypothesis, the in-plane magnetostriction (λ_{11}) was measured as a function of applied H_{dc}. It can be clearly seen from Figure 3.2(c) that the behavior of λ_{11} was similar to that of M^2-H curve. Using λ_{11} curves, the q_{11} curves were calculated as shown in Figure 3.2(d). These measurements confirmed that Ni has hysteretic behavior in comparison to Metglas.

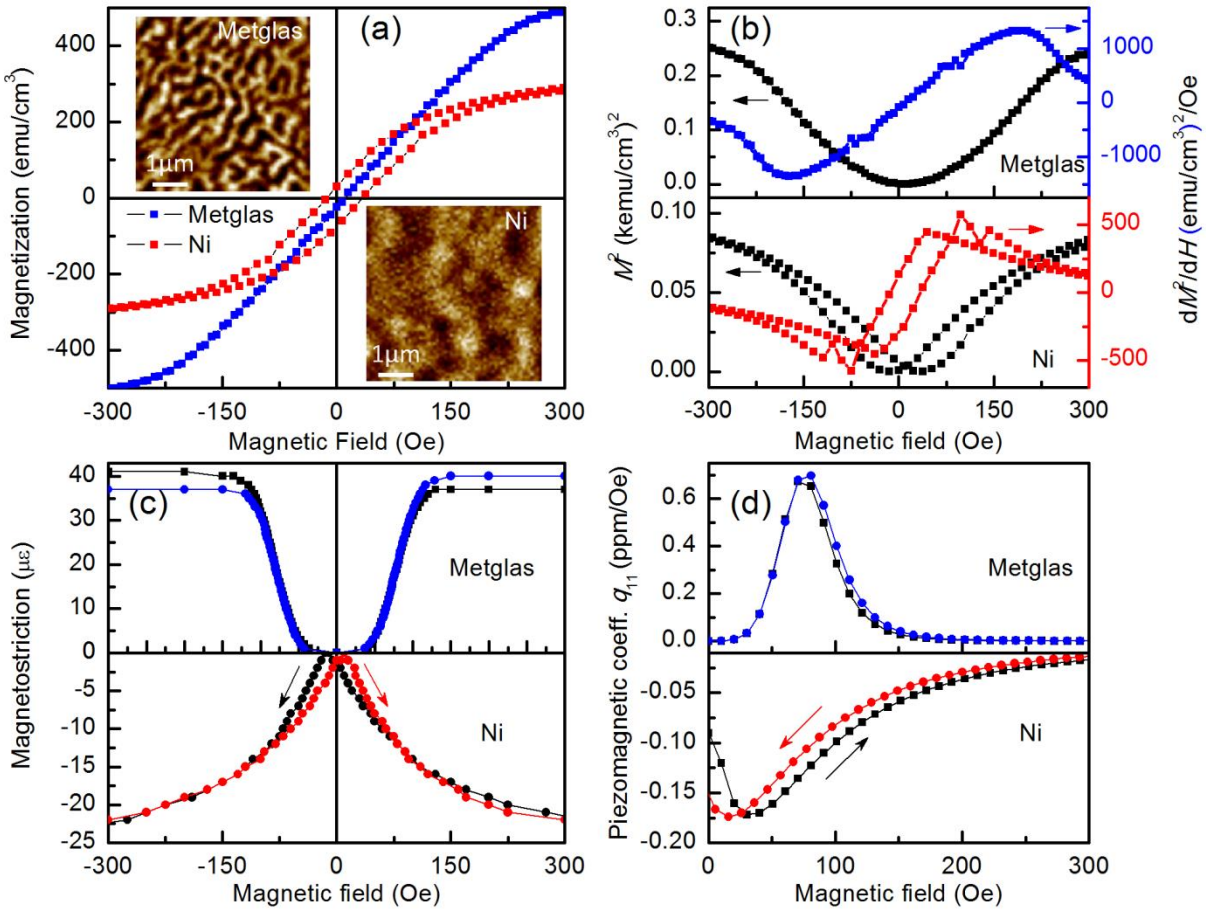

Figure 3.2 (a) Magnetization-magnetic field (M-H) response. Inset shows magnetic domain images on the surface of Metglas and Ni scanned by MFM; (b) square magnetization-magnetic field (M^2-H) and differential of square magnetization-magnetic field [(dM^2/dH)-H]; (c) DC magnetic field (H_{dc}) dependence of the magnetostriction (λ_{11}); (d) DC magnetic field (H_{dc}) dependence of piezomagnetic coefficients (q_{11}) for Ni and Metglas.

3.1.4 Geometry and Demagnetization effect

From the point of view of functional ME devices, it is important to control the magnitude of self-biased ME voltage coefficient. Thus, I investigated the effect of geometry on tunability of self-biased response. Firstly, N layers (1, 2, 4) of Ni sheets with same dimension ($10\times5\times0.15mm^3$) were laminated on to the PMT plates. As shown in Figure 3.3(a), the variation in a_{ME} exhibited similar trend as function of H_{dc} under varying thickness ratio ($t_{m/p}$). In all cases, a_{ME} shows hysteretic loop with anticlockwise direction sweep. The values of increasing-field maximum (a_{H1}) and decreasing-field maximum (a_{H2}) with thicker Ni layer were notably higher than that for thinner ones, while also requiring larger magnetic biases (increasing-field optimum, *H1* and decreasing-field optimum, *H2*). The magnitude of self-biased point (a_{H0}) slightly decreases as thickness ratio increases as shown in Figure 3.3(c). The maximum self-biased ME response was achieved at $t_{m/p}$= 0.5. Next, we fixed the thickness ratio at $t_{m/p}$=0.5 and varied the lateral dimension as shown in Figure 3.3(b). It can be seen in this figure that the magnitude of $a_{H0\sim H2}$ increased dramatically as lateral ratio ($L_{m/p}$) increased from 0.5 to 2. Notably, a giant self-bias coefficient (a_{H0}/a_{H2}) of 97% was achieved at $L_{m/p}$=2, compared to 34.4% and 72.5% at $L_{m/p}$=0.5 and 1, as shown in Figure 3.3(d). The hysteresis loop was tilted toward y-axis as the optimum magnetic bias (*H1* and *H2*) decreased. Based upon these results, one can obtain and tune the self-bias coefficient by selecting suitable magnetic phase with proper geometry and dimension.

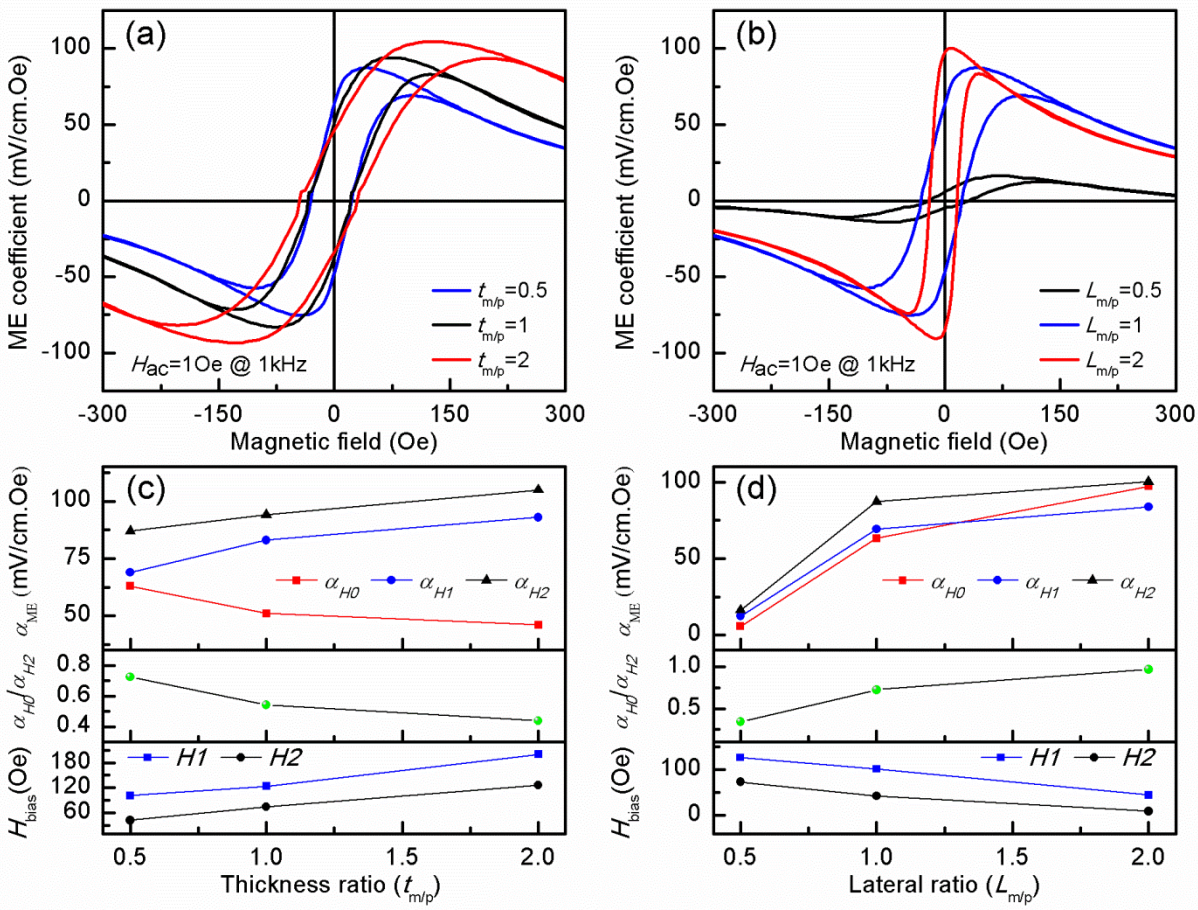

Figure 3.3 (a) ME voltage coefficient (α_{ME}) of Ni-PMT laminates with varied thickness ratio; (b) ME voltage coefficient (α_{ME}) of Ni-PMT laminates with varied lateral dimension; (c) ME voltage coefficient values of self-biased point (a_{H0}), increase-field maximum (a_{H1}, *H1*), decrease-field maximum (a_{H2}, *H2*) and self-bias coefficient (a_{H0}/ a_{H2}) as function of thickness ratio; (d) ME voltage coefficient values of self-biased point(a_{H0}), increase-field maximum (a_{H1}, *H1*), decrease-field maximum (a_{H2}, *H2*) and self-bias coefficient (a_{H0}/ a_{H2}) as function of lateral dimension.

The ME response of Ni-PMT laminate can be explained by taking into account the constitutive piezoelectric and piezomagnetic behavior. Figure of merit for the ME composite in L-T mode is given as: [70]

$$a_{\mathrm{E},31} = \frac{dE_3}{dH_1} = \frac{nq_{11}g_{31}}{nS_{11}^{\mathrm{p}}(1-k_{31}^2)+(1-n)S_{11}^{\mathrm{m}}}, \quad (3\text{-}2)$$

where E_k and H_k are vector components of the electric and magnetic field, n is the volume fraction of magnetic phase $n = {}^{\mathrm{m}}v/({}^{\mathrm{p}}v+{}^{\mathrm{m}}v)$, v denotes the volume, q_{11} is piezomagnetic coefficient, g_{31} is piezoelectric voltage coefficient, S_{ij} is compliance coefficient, and k_{31} is electromechanical coupling coefficient. The superscripts "m" and "p" represent the magnetostrictive and piezoelectric phase respectively. This relationship clearly reflects the important role of material parameters of piezoelectric phase ($g_{31,}$ S_{11}^{p}) and magnetostrictive phase ($q_{11,}$ S_{11}^{m}) towards achieving large magnetoelectric response. At specific bias magnetic field, the magnitude of piezomagnetic coefficient is fixed. For a given piezoelectric phase, the ME voltage coefficient in the laminated composite is mainly determined by the magnetic phase ratio n, $a_{\mathrm{ME}} \propto n$. By fixing the piezoelectric layer dimensions, as we increase the magnetic phase thickness ratio or lateral dimension, the volume ratio n will increase. In this study, for volume ratio of less than ~0.67, the maximum a_{ME} (a_{H1} *and* a_{H2}) increased with increasing n at an optimum bias field, which is consistent with the prediction based upon Equation (3-2). However under zero-bias condition, it is found that the value of a_{ME} (a_{H0}) decreased with increasing thickness ratio, which is contradictory to the prediction by Equation (3-2). Moreover, there are some questions in Figure 3.3 that need to addressed as listed here: (i) For same magnetic phase volume ratio, why a_{ME} under zero-bias condition shows different value and tendency as a function of thickness and lateral dimension? and (ii)

Why H_{bias} shifts back and forth as a function of sample shape and size?

To better explain above questions and the tunable nature of self-biased ME response, the size-induced demagnetization effect was taken into consideration.[71] For ferromagnetic materials, the demagnetization field is directly proportional to demagnetization factor (N_d), $H_d = MN_d$ (M is the magnetization), where N_d is dependent on the dimension and geometry. Thus, the internal effective magnetic field (H_{eff}) in the magnetic phase can be written as:

$$H_{eff} = H_{bias} - H_d, \tag{3-3}$$

where H_{bias} is the induced external magnetic field. For a finite, non-spherical ferromagnet, a good approximation to N_d can be found from the general ellipsoid solution of Osborn[72]:

$$N_d \approx (wt/l^2)(\ln(4l/(w+t)) - 1), \tag{3-4}$$

where l is length, w is width and t is thickness. Figure 3.4(a) shows the variation of N_d as a function of magnetic phase ratio. Clearly, a smaller N_d will result in a lower H_d, and thus a more effective H_{eff}. Therefore, in order to achieve same magnitude of H_{eff}, one need to apply larger H_{bias} when H_d is larger and vice-versa, which is also compatible with experimental data shown in Figure 3.3(c) and 3.3(d). However, it is difficult to determine how the magnetization of a material varies with the external magnetic field due to shape/location induced anisotropy. Therefore using Equation 3-3 and considering the magnetization relationship $B=\mu_0(H+M)$, the effective magnetic induction can be found as:

$$B_{eff} = \mu_0(H_{eff}+M) = \mu_0(H_{bias}+M) - \mu_0 M N_d, \tag{3-5}$$

Again, it can be seen that a smaller N_d will result in a stronger B_{eff}. Further, it has been shown that high magnetic flux concentration in magnetic phase has positive effect on the magnetoelectric response of ME laminates. [48,47] Thus, there should be correlation between the

tunable feature of self-biased ME response and the variation of magnetic flux concentration of magnetic phase with geometry.

To find this correlation, finite element simulation using ANSYS multiphysics (version 14) was conducted for Ni sheets with dimensions similar to those used in the experiments. The magnetostatic modeling assumed the nickel is in air and has relative permeability of 600 and coercive force (in the axial length direction) of 0.7 Oe.[73] A parallel flux boundary condition was applied around the magnet. For each simulation, the magnet was meshed between 10,000 - 100,000 points and the simulations were within 0.01% accuracy. Figure 3.4(b) shows that laminates with thicker magnetic phase sheet possess weaker magnetic induction, which will further result in decrease in ME coupling. The laminates with longer magnetic phase sheets produced a much stronger magnetic induction as shown in Figure 3.4(c), and a resultant large increase in ME coupling. By using the results shown in Figure 3.4(b) and 3.4(c), I can further compute line scans of the magnitude of magnetic flux density along the axial center-line of the Ni sheets with different geometry in Figure 3.4(d), which is also compatible with the results obtained from Figure 3.4(a) and Equation 3-5. These results match well with the experimental data in Figure 3.3 and imply that tunable self-biased ME effect was obtained due to magnetic flux concentration variation occurring due to size-induced demagnetization effect.

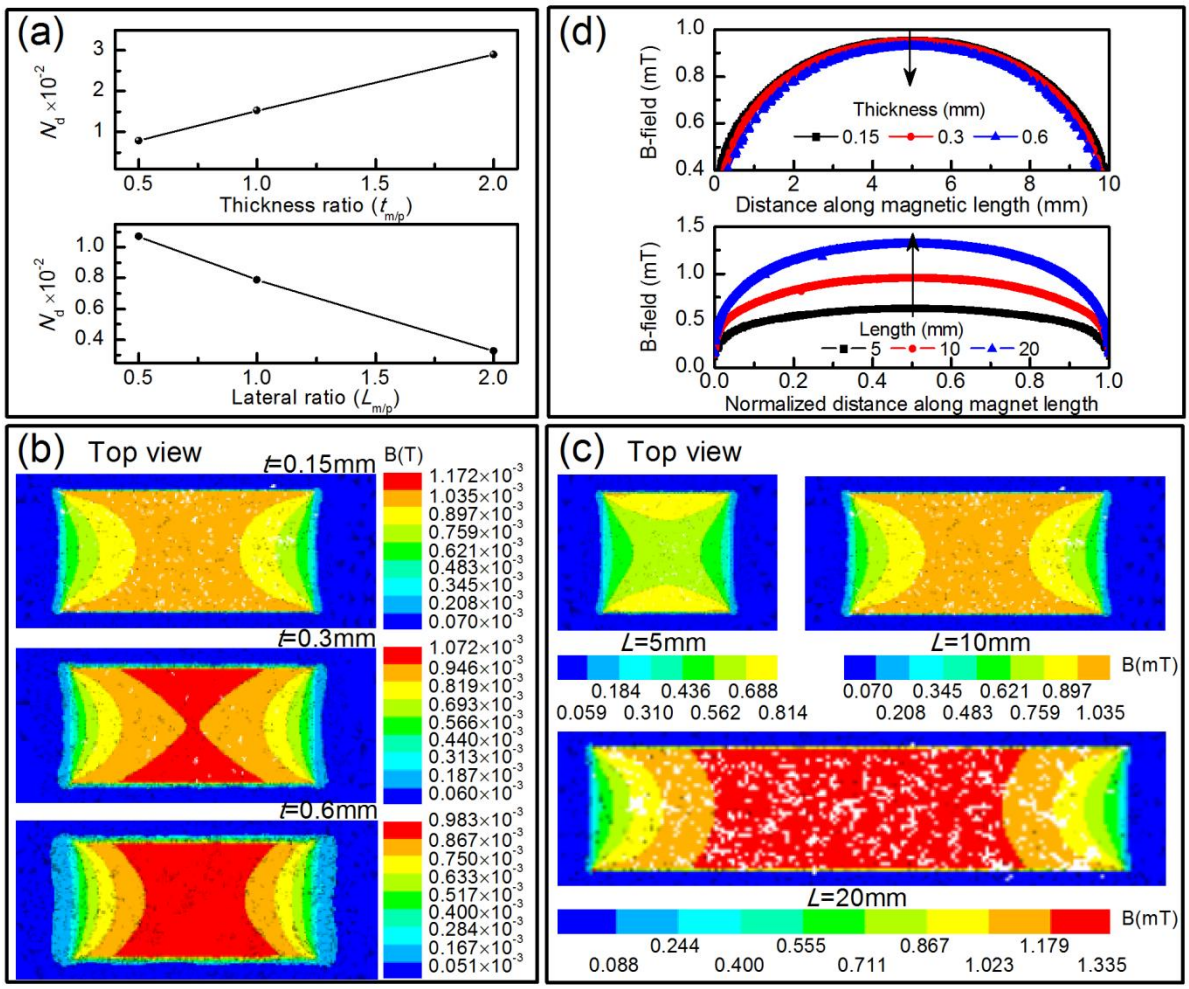

Figure 3.4 (a) Demagnetization factor variation as function of sample thickness/lateral ratio; (b) In-plane magnetic field strength along the center plane of Ni sheets for variation in thickness, with fixed in-plane size, in response to zero DC bias field, as simulated by ANSYS; (c) In-plane magnetic field strength along the center plane of Ni sheets for variation in length, with fixed thickness, in response to zero DC bias field; (d) Line scan traces of magnetic flux density along the axial centerline of Ni for variation in thickness and length.

3.1.6 Resonance Enhanced ME response

To achieve the best ME performance, working at electromechanical resonance of piezoelectric phase is necessary.[42] Therefore, I investigated the frequency dependence of self-biased ME response in optimized Ni-PMT laminate ($L_{m/p}$=2). Figure 3.5(a) shows the impedance spectrum and ME response under varying H_{dc} condition. The frequency dependence of a_{ME} shows resonance peaks corresponding to bending modes. It can be noticed that even though there is no H_{dc}, self-biased ME response follows the same trend and has similar magnitude of voltage coefficient as to that of sample in biased conditions. Figure 3.5(b) shows the effect of magnetic field strength (H_{ac}) under zero bias (H_{dc}=0 Oe) condition at different frequency. Linear increase in ME voltage was observed with increasing AC voltage on Helmholtz coil (H_{ac}). Further increase in the linear slope was achieved by working at resonant mode. The a_{ME} values of 585.7 mV cm^{-1} Oe^{-1} at 15.5 kHz and 91.2 mV cm^{-1} Oe^{-1} at 1 kHz given by the slope matched well with the measured value in Figure 3.5(a). These results illustrate that under zero DC bias condition, high ME response can be sustained in homogenous ME laminates.

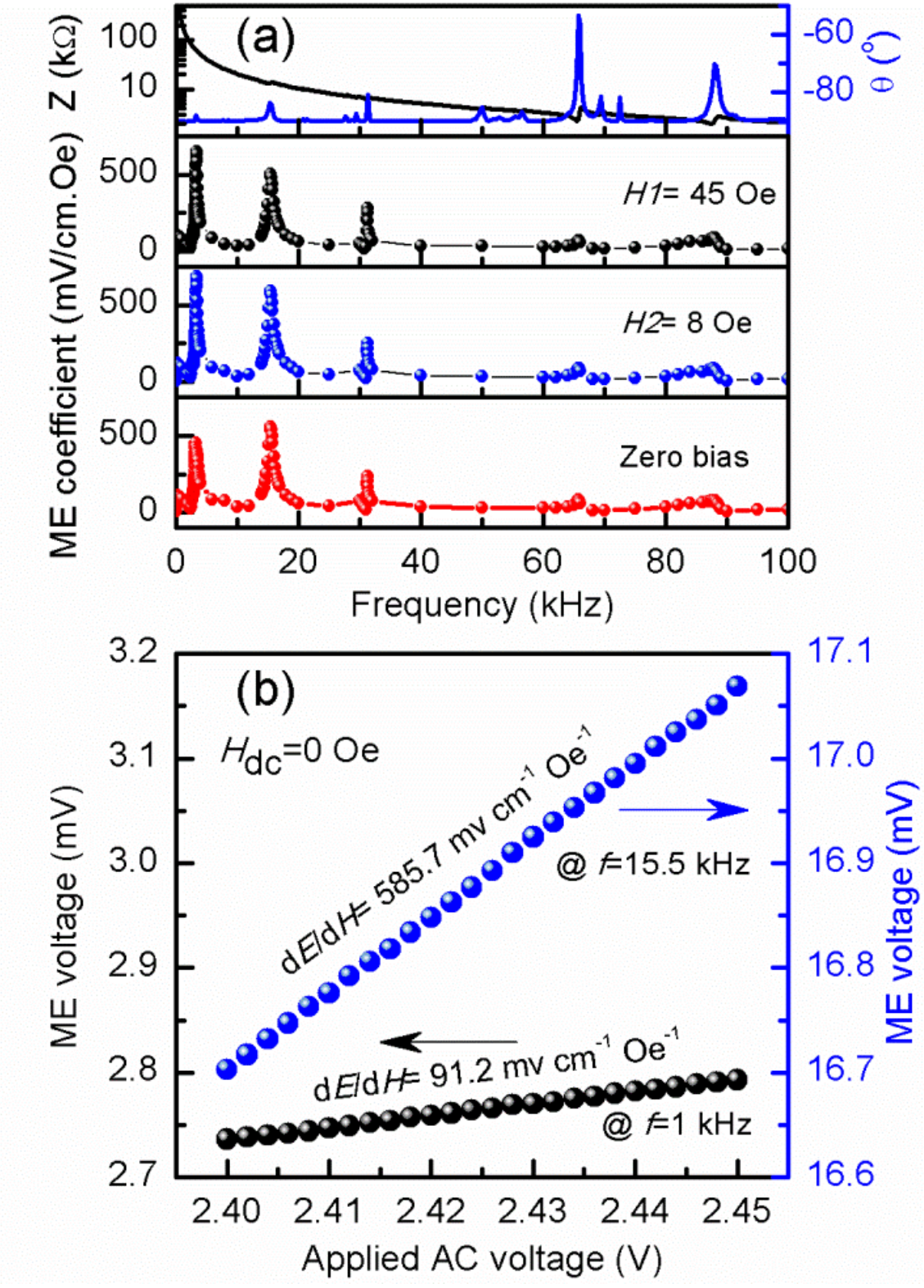

Figure 3.5 (a) Impedance and phase spectrum and its ME voltage coefficient as function of applied AC frequency; (b) Source free (H_{dc}=0 Oe) ME voltage output of Ni-PMT laminate measured at 1kHz and 15.5kHz under various applied AC voltage on Helmholtz coil (H_{ac}).

The magnitude of the ME coefficient can be further increased by developing the flexural resonant structure mounted in cantilever configuration. I fabricated a ME composite operating in L-L mode consisting of a MFC (dimension 40×10 mm^2, Model: M-4010-P1, Smart Material Corp., USA) and 1 layer of 0.15-mm-thick Ni foil with dimension of 80×10 mm^2. The ME effect was measured in L-L mode configuration and the result is shown in Figure 3.6. The α_{ME} of Ni-MFC bilayer shows a hysteretic behavior during H_{dc} sweep (anticlockwise direction) with a large response of ~1254 mV cm^{-1} Oe^{-1} at zero DC magnetic bias, ~90.8% of its maximum α_{ME} value (1381 mV cm^{-1} Oe^{-1}). Please note that these measurements were conducted in off-resonance condition at 1 kHz.

In conclusion of this section, the homogenous two-phase ferromagnetic-piezoelectric laminate Ni/PMT composite was demonstrated to exhibit a large self-biased ME response. A tunable self-biased response was achieved in bilayer composite structure with homogeneous ferromagnetic layer which has great advantage in integration with MEMS-scale devices.

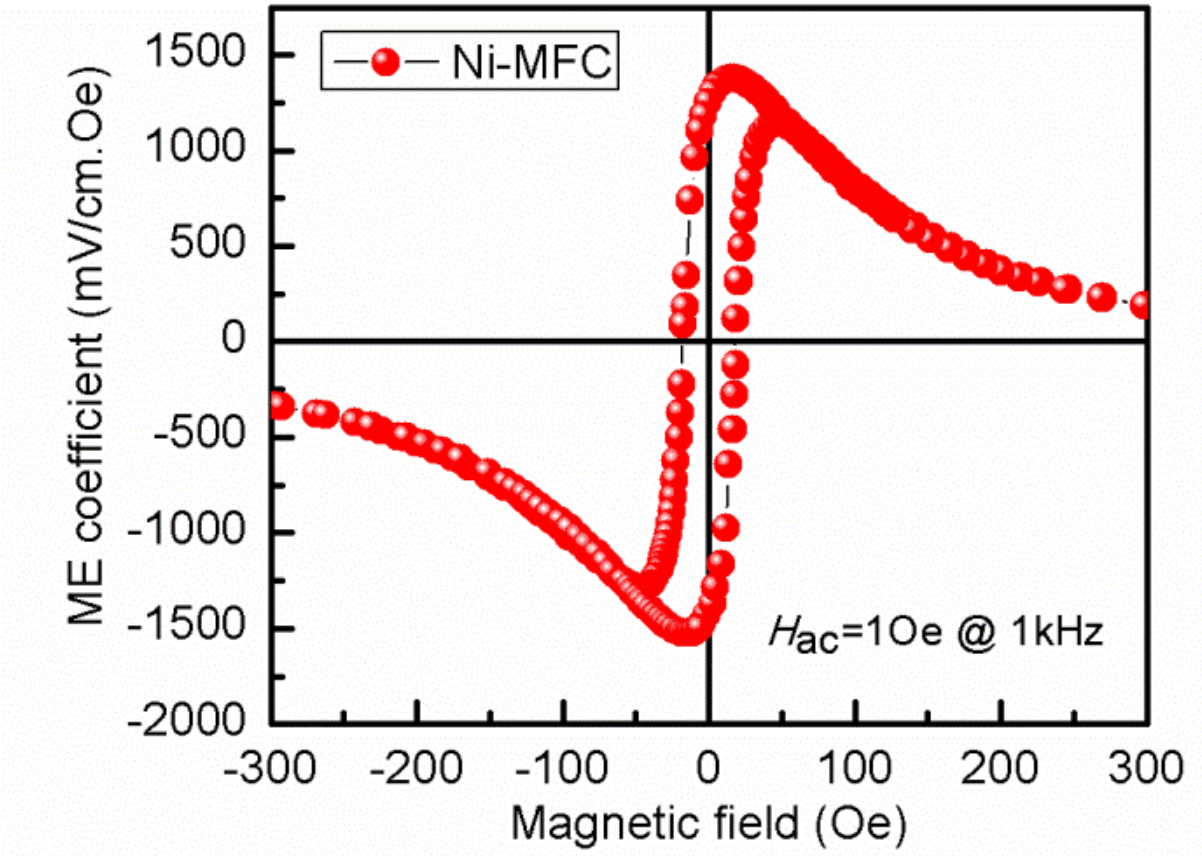

Figure 3.6 ME coefficients of Ni-MFC bilayer laminates as a function of DC magnetic field.

3.2 Near-flat self-biased ME response in geometry gradient composites*

In general, under a constant applied AC magnetic field, the ME coupling coefficient (α_{ME}) shows a peak behavior in response to varying DC bias (H_{bias}). The DC magnetic field dependence is due to the piezomagnetic coefficient variation as a function of H_{dc}. The peak behavior presents a challenge as slight variations in the magnitude of the applied H_{bias} could result in significant modulation in the magnitude of the α_{ME}. Thus, from the practical point of view two issues related to the conventional ME composite behavior should be resolved: (1) The requirement of H_{bias} imposes limitation in the fabrication and miniaturization of the electronic components, and (2) The peak behavior limits the operating range around the optimal magnetic DC bias. These two issues should be addressed in order to open the application space for the ME composites. In this section, a self-biased ME composites that exhibit flat and stable response over a wide range of magnetic DC bias was demonstrated.

3.2.1 Geometry gradient ME composite design

The first question that needs to be answered is: "How to control the magnitude of optimum DC bias and ultimately create the self-biased magnetoelectric response?" In the previous section, my study has revealed that by selecting Ni as the ferromagnetic phase, a self-biased magnetoelectric response can be obtained due to its non-zero piezomagnetic coefficient under the low field condition[46]. Therefore, nickel was selected as the magnetostrictive phase in this study. For adjusting the self-biased ME response, it was found that high magnetic flux concentration in the magnetic phase has positive effect.[46,48] By

*Reprinted with permission from [74], Copyright 2014, AIP Publishing LLC.

considering the influence of demagnetization effect, the effective magnetic flux density can be expressed as: [46]

$$B_{\text{eff}} = \mu_0(H_{\text{eff}} + M) = \mu_0(H_{\text{bias}} + M) - \mu_0 M N_{\text{d}}, \quad (3\text{-}6)$$

where H_{eff} is the internal effective magnetic field and can be written as:

$$H_{\text{eff}} = H_{\text{bias}} - H_{\text{d}} = H_{\text{bias}} - MN_{\text{d}}, \quad (3\text{-}7)$$

M is the magnetization, H_{bias} is the applied external magnetic field, H_{d} is the demagnetization field proportional to the demagnetization factor (N_{d}). The demagnetization factor for a finite non-spherical ferromagnet was found to be dependent on its geometry.[75] Thus, one can tune the magnitude of the self-biased ME response by modifying the *B*-field distribution through the variation in geometry of the ferromagnetic phase. In order to achieve the same magnitude of H_{eff}, one needs to apply larger H_{bias} when $H_{\text{d}}/N_{\text{d}}$ is larger and vice-versa.

The magnetic flux density distribution of Ni was estimated by a magnetostatic simulation using the finite element model (FEM, ANSYS MAXWELL 15.0). Ni plate with different thickness (t=0.2, 0.4, 0.6 mm) but same planar dimension of 20×5 mm^2 and different length (l=5, 10, 20 mm) but same cross-section dimension of 5×0.2 mm^2 were used in this simulation. In this model, all Ni plates were placed in the air and assigned relative permeability of 600 and coercive field force (in the axial length direction) of 0.7 Oe[73] to approximate the real behavior of the Ni. A magnetostatic insulating boundary condition was applied to the Ni. In each case, the nickel was meshed with a maximum element mesh size of 100μm and the simulations were completed within 1% accuracy. Figure 3.7 (a) and (b) show the simulated magnetic flux density distribution along Ni plates as function of thickness and length. One can clearly notice that thicker nickel exhibits weaker magnetic induction. The

increase in length of the Ni resulted in enhancement in the magnitude of magnetic induction. These results led us to the assumption that by designing a composite with separate Ni sections in geometric gradient configuration, one can manipulate the self-biased ME response through combination of the output from separate sections of the composite.

Two different geometry gradient unimorph configurations was first designed and fabricated [Thickness gradient composite (TGC) and Length gradient composite (LGC)] based on these simulations, as shown in Figure 3.7(c) and (d). In Figure 3.7(c), a Ni foil with thickness of 0.2 mm was first machined into a 王 structure with three beams of same lateral dimension (20×5 mm^2). Next, I stacked different number of Ni layers on each section to achieve a gradient thickness of 0.2, 0.4 and 0.6 mm. A different configuration shown in Figure 3.7 (d) referred as LGC, consists of a 0.2 mm thick Ni length gradient architecture with three beams in various lateral dimension (5×5, 10×5, 20×5 mm^2). All of the beams were separated by a bridge of dimension 5×5×0.2 mm^3. The contour plots illustrate the magnitude of magnetic flux density distribution along the gradient structure. Transversely poled piezoelectric plates (PSI-5A4E, Piezo System) with dimension of 10×5×0.2 mm^3 were attached in the center of each beam using epoxy (West System, USA, with curing at room temperature for 24 hours). In both TGC and LGC, the piezoelectric plates were electrically connected in parallel. The ME voltage coefficient was measured by applying the DC magnetic field (H_{dc}) longitudinally with the sample placed in the center of the Helmholtz coil under an AC magnetic field (H_{ac}). ME voltage induced on the laminate was monitored using lock-in amplifier, and the strength of the H_{dc} was monitored using Gauss meter (F. W. BELL, Model 6010).

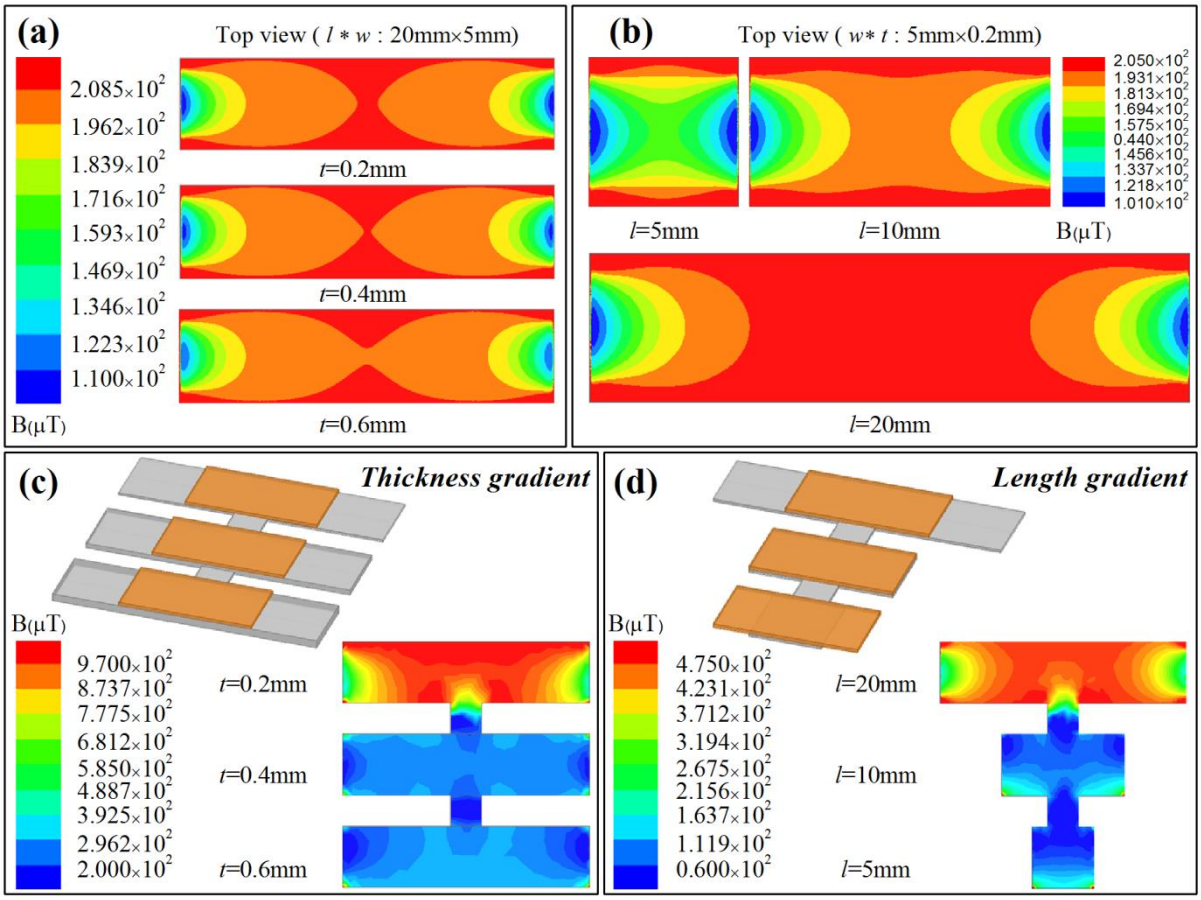

Figure 3.7 FEM simulation data for in-plane magnetic flux density distribution along the Ni plates with (a) variation in thickness, and (b) variation in length. Schematic diagram of the geometry gradient magnetoelectric laminates depicting (c) a thickness gradient composite with three beams of different thickness, and (d) a length gradient composite with three beams of different length. The inset contour plots show the corresponding simulated magnetic field strength distribution using ANSYS MAXWELL.

3.2.2 ME coupling characterization

Figure 3.8(a) and (b) show the ME voltage coefficient of the thickness and length gradient composites as function of H_{dc} with H_{ac}=1Oe at 1 kHz. For comparison, the ME coefficient from each Ni/PZT section was also measured separately. In all cases, the magnitude of α_{ME} shows hysteretic behavior during H_{dc} sweep, in agreement with prior study on Ni-piezoelectric laminates[46]. Large self-biased ME response (α_{H0}) was obtained with the magnitude of ~183 mV cm^{-1} Oe^{-1} (TGC) and ~86 mV cm^{-1} Oe^{-1} (LGC) respectively. The ME bandwidth (ΔH) of the composite is defined as the DC magnetic bias difference between the lower and upper half power points (3 dB) where the ME coefficient has dropped by a factor of $1/\sqrt{2}$ or 0.707. Benefit from the self-biased hysteretic behavior, both for TGC (ΔH=97.5Oe) and LGC (ΔH=137.3Oe), is illustrated in terms of the larger bandwidth than the conventional ME composite (ΔH=6.9Oe)[41]. It should be noted that TGC and LGC exhibited reduced ME coefficient in comparison to the response from the individual sections in the composite due to the charge redistribution occurring from the parallel electrical connection.

Figure 3.8 (c) and (d) summarize the individual ME responses from separate sections of the composite. From these results, several important observations can be made: (1) Thinner or longer Ni plate possesses larger magnetic flux density, (2) Laminates with stronger *B*-field exhibit notably higher self-biased ME coefficient (α_{H0}/α_{Max}) while requiring lower H_{bias}, (3) The magnitude of α_{Max} increases dramatically as the magnetic phase volume ratio increases, (4) Magnitude of individual response from separate sections of the composite plays an important role towards determining the total ME response.

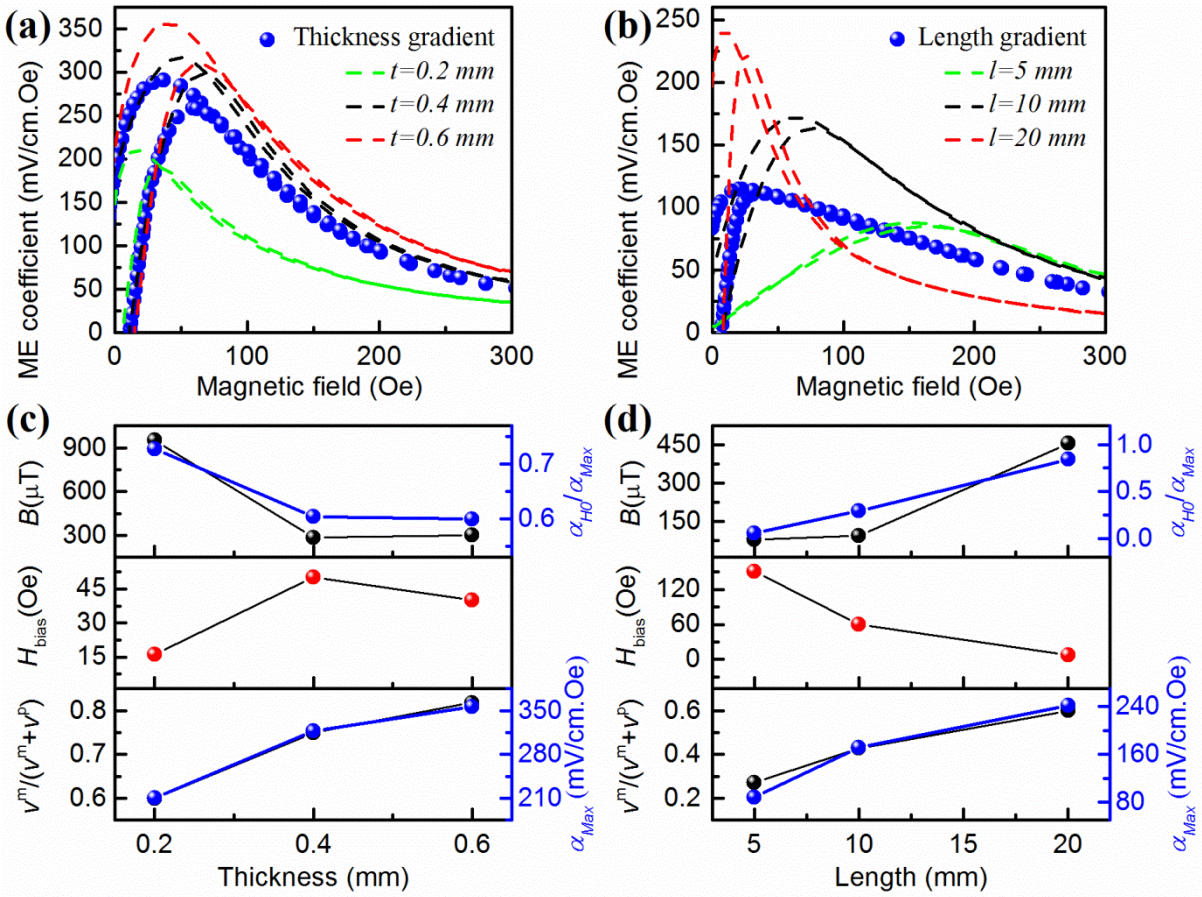

Figure 3.8 ME voltage coefficient of the geometry gradient composites: (a) thickness gradient composite and its corresponding ME behavior with varying thickness, and (b) length gradient composite and its corresponding ME behavior with varying length. Characteristic ME response from each Ni/PZT section of the geometry gradient composites (c) as a function of Ni thickness, and (d) as a function of Ni length. All the measurements were taken under H_{ac}=1Oe at 1 kHz.

3.2.3 Optimization of geometry gradient composite

Guided by these results, I redesigned the dimensional gradient composite having a larger geometry separation to generate a broadband response. In this new design referred to as complex gradient composite (CGC), a one short and thick beam ($10\times5\times0.6$ mm^3) was connected with a long and thin beam ($20\times5\times0.2$ mm^3) as shown in Figure 3.9(a). Large variation of magnetic flux density was realized in each section of the CGC. The ME coefficient of the composite demonstrated a large self-biased effect (a_{H0}/a_{Max}=0.72), as shown in Figure 3.9(b). The ME response of CGC is combined behavior of the two sections. The individual peaks corresponding to each section were brought in vicinity of each other by modulating the geometry resulting in a flat response as function of H_{dc}. This result clearly demonstrates the wideband self-biased magnetoelectric response in CGCs.

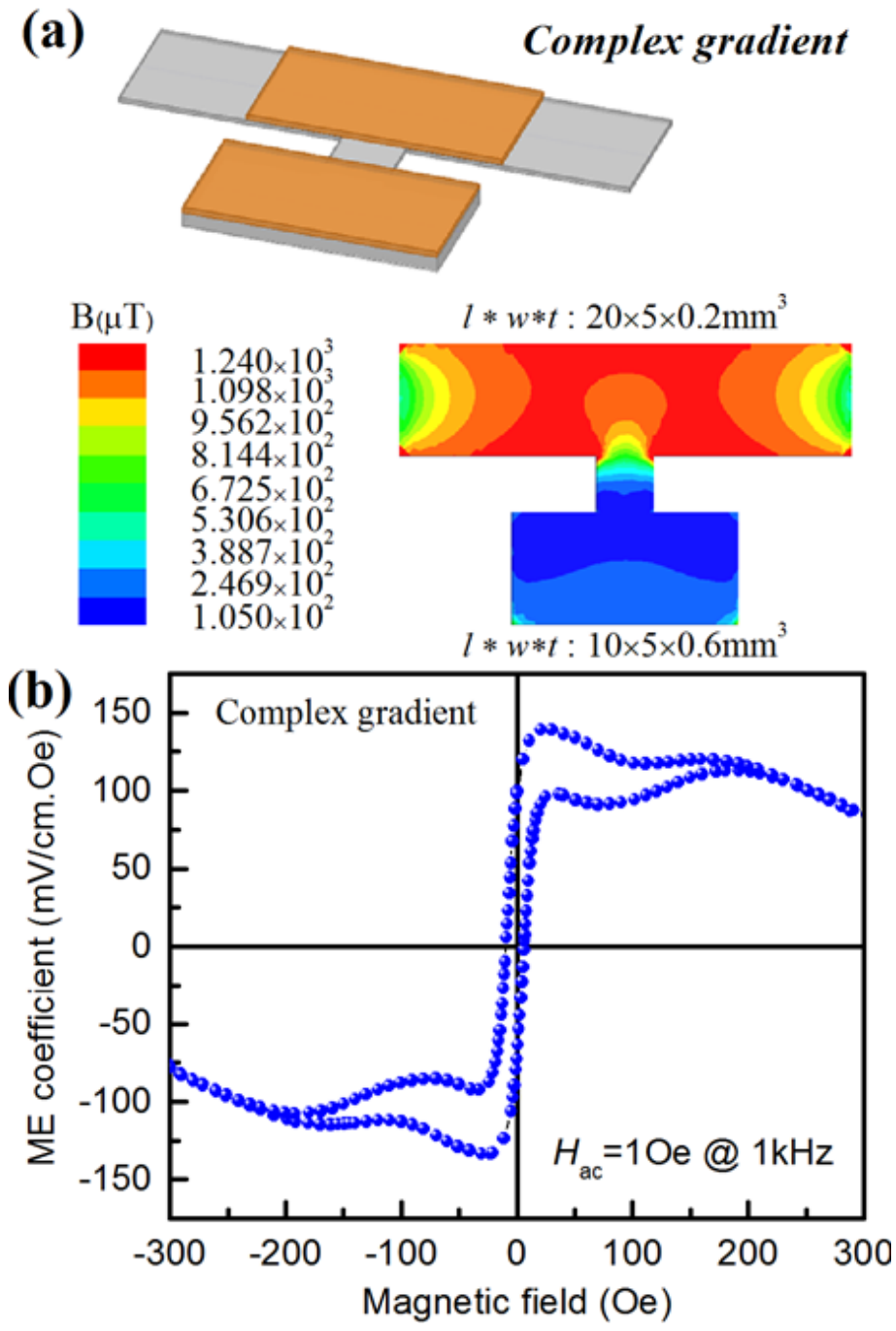

Figure 3.9 **(**a) Schematic diagram and the simulated magnetic flux density distribution of the complex gradient magnetoelectric composite, (b) ME voltage coefficient of the complex gradient composite as a function of DC magnetic field under H_{ac}=1Oe at 1kHz.

Next, I investigated the effect of AC magnetic field frequency and DC magnetic field bias on the ME response. Figure 3.10(a) shows the ME coefficient of each section in the CGC. The first peak (139 mV cm^{-1} Oe^{-1} @ H_{bias}= 30 Oe) and the second peak (120 mV cm^{-1} Oe^{-1} @ H_{bias}= 159 Oe) were associated with the large and small beam component of the CGC respectively. The combined response of the structure exhibited a large bandwidth of ~260Oe which is almost 38 times of the conventional Metglas/PZT composite[41]. Figure 3.10(b) shows the ME coefficient at low frequency (10 Hz), off-resonance frequency (1 kHz) and at the resonance frequency (4.49 kHz) as a function of H_{dc}. The wideband ME behavior was found to occur at all the frequencies with enhanced ME coefficient. The α_{Max} was improved exhibiting the magnitude of 0.24 V cm^{-1} Oe^{-1} and 5.35 V cm^{-1} Oe^{-1} at 10 Hz and 4.49 kHz. To investigate the stability of self-biased ME response, I measured the ME coefficient as a function of frequency under various H_{dc}= 0, 30, 159 Oe, as shown in Figure 3.10 (c). All the ME responses followed the similar trend and had similar range of α_{ME} (~6 V cm^{-1} Oe^{-1}) at ~4.49 kHz, even without external H_{dc}. The excellent stability of the self-biased ME response in this design offers significant advantage towards developing magnetoelectric energy harvester[3,17] that can scavenge the magnetic field energy regardless of the ambient H_{dc}. It should be noted that prior research on the magnetoelectric harvesters has revealed that the requirement of H_{bias} is problematic towards high power density[66,76]. The structure can also be used to detect the external H_{ac} by monitoring the variation of ME voltage based on the conversion ratio between the two parameters, $\alpha_{ME}= \delta E_{ac}/\delta H_{ac}$. In Figure 3.10(d), I measured the ME voltage output as function of applied H_{ac} under wide range of H_{dc} from 0Oe to 260Oe. Linear increase in ME voltage output was observed under various H_{dc} with similar slope as

the applied AC voltage was varied in the Helmholtz coil, indicating a small variation of α_{ME} regardless of the magnitude of external H_{dc}. This result suggests a great potential of implementing this structure into a high stability/sensitivity AC magnetic field sensor.

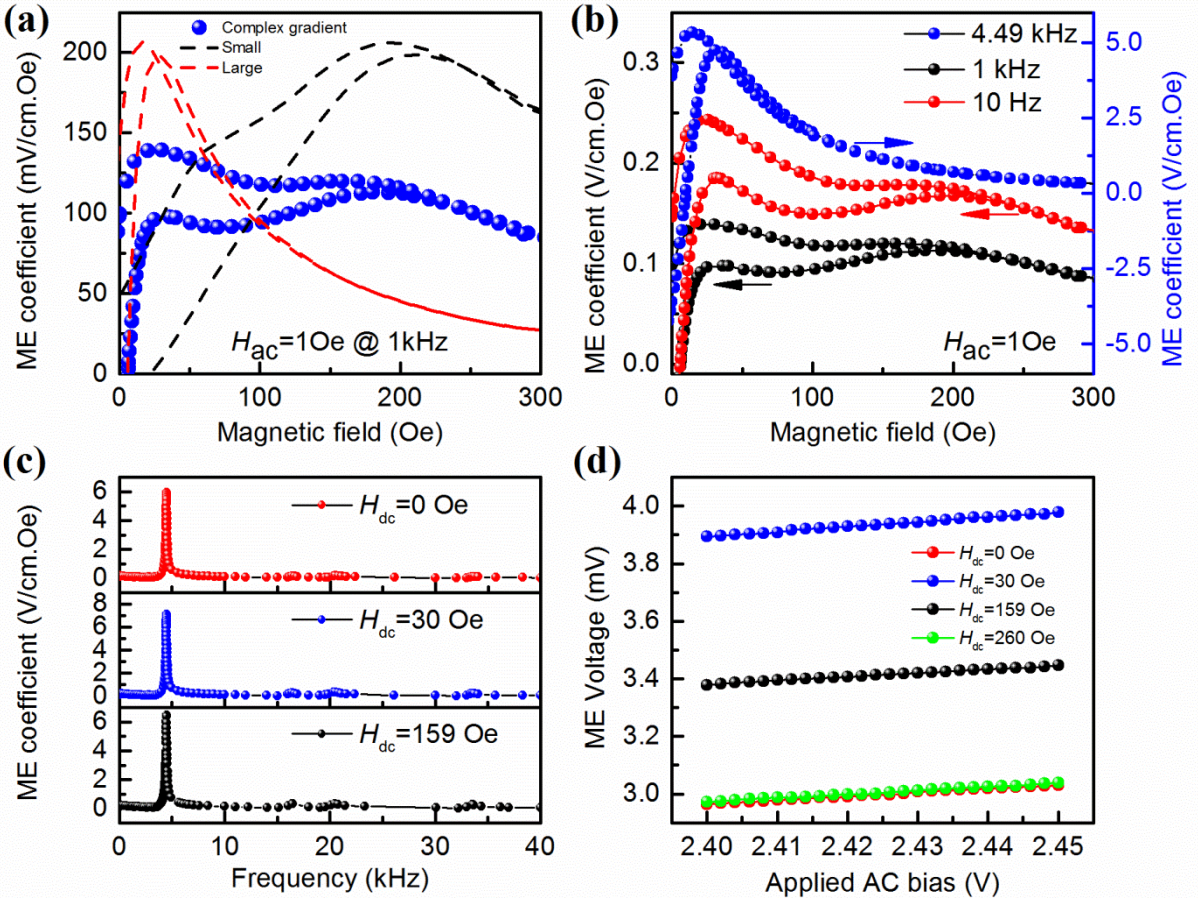

Figure 3.10 ME response of the complex gradient composite: (a) ME voltage coefficient of the CGC and its corresponding individual section ME behavior with varying DC magnetic field under H_{ac}=1Oe at 1kHz, (b) ME voltage coefficient at low frequency (10Hz), off-resonance frequency (1kHz) and resonance frequency (4.49kHz) as a function of DC magnetic field with H_{ac}=1Oe, (c) ME voltage coefficient as a function of applied AC frequency with H_{dc}=0, 30 and 159 Oe respectively, and (d) ME voltage output measured at H_{dc}=0, 30, 159 and 260 Oe under various applied AC voltage on Helmholtz coil (H_{ac}).

Table 3.1 lists the ME properties of various ME composites, including conventional Metglas/PZT laminates (c-ME)[41,46], wideband ME laminate (w-ME)[77], co-fired ME composite (Co-fired)[78], self-biased ME composite (s-ME)[46] and geometry gradient ME composites (TGC, LGC, and CGC). The effective wideband quality factor of the ME laminate can be expressed as $Q = \Delta H/H_{bias}$, where large Q factor with low H_{bias} and high ΔH is desired. Following conclusion can be drawn from this table: (1) Compared to conventional ME composites, giant ΔH with the magnitude of 261.3 Oe was achieved in complex gradient composite, which is ~650%-3800% higher, (2) All the self-biased ME composites exhibited a higher magnitude of Q compared to conventional ME composites, indicating either a much wider bandwidth or a lower H_{bias}, (3) Geometry gradient structure dramatically enhances the bandwidth of ME composite. Thus, the combination of self-biased ME effect and geometry gradient structure not only helps in eliminating the need for DC magnetic bias, but more importantly enhances the ME response stability in a wide range of DC bias.

In conclusion of this section, I designed and fabricated a series of geometry gradient Ni/PZT composites. The design was able to provide a wideband self-biased ME response. By optimizing the structural and geometrical parameters of the ferromagnetic phase, a significantly flat and stable self-biased ME response over a wide DC magnetic bias (ΔH=261.3 Oe) was demonstrated. This wideband behavior provides great advancement towards development of the high stability/sensitivity magnetoelectric energy harvester and AC magnetic field sensor.

Table 3-1 Magnetoelectric properties of various ME composites

Sample	H_{bias} [Oe]	$\triangle H$ [Oe]	$Q=\triangle H/H_{\text{bias}}$	a_{H0} [mV/cm.Oe]	a_{Max} [mV/cm.Oe]	a_{H0}/a_{Max}
c-ME[41]	5	6.9	1.4	~0	22×10^3	~0
c-ME[46]	69.0	39.7	0.6	~0	154.66	~0
w-ME[77]	220	~122	0.6	~0	88	~0
Co-fired[77]	3.0	33.9	11.3	1316.4	1347.1	0.98
s-ME[46]	15.5	89.0	5.7	1254.0	1381.2	0.91
TGC	37.0	97.5	2.6	183.4	290.7	0.63
LGC	22.4	137.3	6.1	86.0	114.6	0.75
CGC	30.1	261.3	8.7	99.4	139.0	0.72

3.3 Giant self-biased ME coupling in co-fired textured layered composites*

Gaint magnetoelectric (GME) effect has been reported in a variety of magnetostrictive-piezoelectric laminate composites consisting of ferrite, Terfenol-D, and Metglas as magnetostrictive phase and $Pb(Zr,Ti)O_3$ (PZT) and $Pb(Mg_{1/3}Nb_{2/3})O_3$-$PbTiO_3$ (PMN-PT) as piezoelectric phase.[26,41,79,8] In these composites, the measured ME coefficient was found to be directly related to the effectiveness of elastic coupling at the interface of two phases. The widely used method for synthesis of laminate composites is bonding of magnetostrictive layer (such as Metglas, Terfenol-D) and piezoelectric layer (such as PZT, PMN-PT) using epoxy resin. This method limits the misfit strain at the interface arising due to thermal expansion mismatch between the layers and atomic interdiffusion and/or chemical reaction between the layers. However, the epoxy layer is much softer than both magnetostrictive alloy and ferroelectric ceramic and thus it will dampen the generated strain resulting in loss of efficiency. Furthermore, high cost of raw materials (large dimension PMN-PT single crystal fibers) and manual fabrication process (polishing on the order of 200 μm followed by lamination) presents challenge in implementation at commercial scale. Therefore, in order to increase the ME effect while keeping the cost down, materials with large magnetostrictive and piezoelectric coefficient is demonstrated in a co-fired configuration.

---

*Reprinted with permission from [78], Copyright 2013, AIP Publishing LLC.

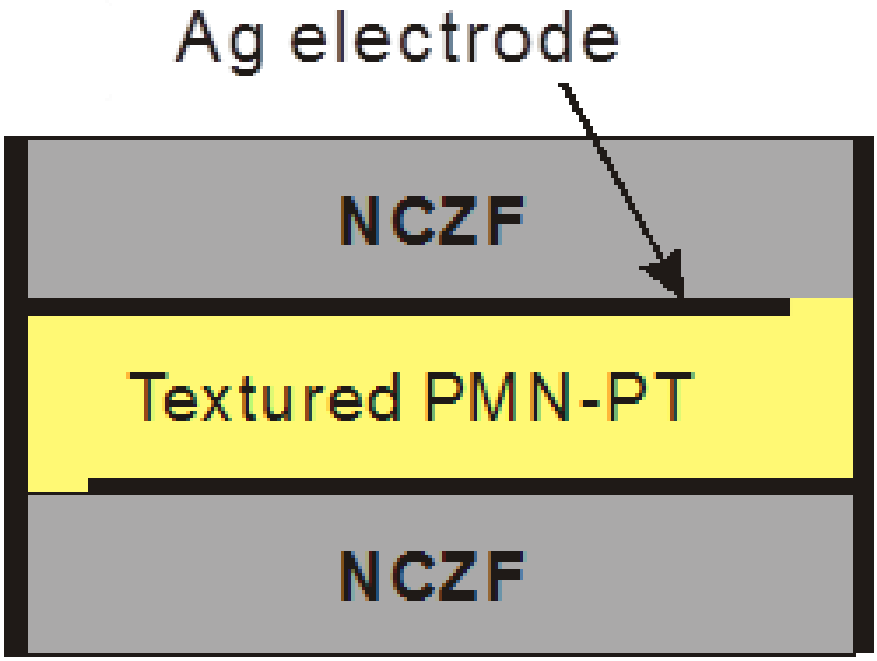

Figure 3.11 Schematic diagrams of different types of layered ME composite structures.

3.3.1 Synthesis Co-fired ME composites

Figure 3.11 presents the schematic configuration of the co-fired magnetostrictive/ piezoelectric/ magnetostrictive (M/P/M) laminate structure with Ag inner electrode. Compositions corresponding to $Pb(Mg_{1/3}Nb_{2/3})O_3$-32.5$PbTiO_3$ [PMN-PT] and $(Ni_{0.6}Cu_{0.2}Zn_{0.2})Fe_2O_3$ [NCZF] were used as piezoelectric and magnetostrictive materials respectively. Low relative permittivity <001> BT micro-crystals (ε_r= 130) were selected as templates. Experimental details was detailed listed below.

PMN-PT powders and NCZF powders were synthesized by the conventional mixed oxide method using reagent-grade raw materials of $2PbCO_3{\cdot}Pb(OH)_2$, $MgNb_2O_5$, Nb_2O_5, TiO_2, NiO, CuO, ZnO, and Fe_2O_3, respectively. After mixing and drying, the mixture was calcined at 750 ^oC for 2 h. Calcined powders were ball milled again for 24 h, dried, and sieved. For tape casting, the slurry was prepared by mixing PMN-PT matrix powder with 55 *wt*% organic binder (Ferro 73225, Vista, CA) in 45% toluene/ethanol solvent and ball milling for 24 hours. Then 1 *vol*% $BaTiO_3$ (BT) templates were dispersed into the slurry and mixed by magnetic stirring for 24 hours. Excess toluene was removed by evaporation until the slurry reached a solid content of 80 %. The slurry was then poured in to the reservoir of tape caster and casted through the doctor blade with gap of 300 μm on silicone-coated Mylar (polyethylene terephthalate) carrier film. The casted slurry was dried at room temperature. NCZF green tapes and random PMN-PT green tapes were fabricated in the same way as textured PMN-PT tape without adding BT template. Six layer of random/textured PMN-PT or NCZF green tapes were stacked and laminated using a uniaxial hot press at 80 ^oC to achieve a single thick piezoelectric or magnetostrictive layer. A commercial silver paste

(9770, DuPont, NC, USA) was screen printed on top of the piezoelectric layer using 325 mesh stainless steel screen resulting in dried electrode layer with thickness of 10~20 μm. The printed patterns were dried at room temperature for 10 minutes and then dried at 150 ^{o}C for another 10 minutes. The printed tape was diced, stacked and laminated at 80 ^{o}C under pressure of 20 MPa for 15 min. The laminated green tapes were heated to 400 ^{o}C with a heating rate of 0.3 ^{o}C min^{-1}, held for 2 hours to burn the organic binder and then sintered at 930 ^{o}C for 4 hours in air. The sintered multilayer textured samples were terminated using low temperature silver ink and then cured at 100 ^{o}C for 30 minutes. The specimens were poled by applying DC field of 40 kV cm^{-1} for 15 min.

The as-fabricated samples were placed in the center of the Helmholtz coil (alternating magnetic field, H_{AC}) which was located at the center of electromagnet (DC biased magnetic field, H_{DC}). ME voltage coefficient of the laminate was measured at 1 kHz H_{AC} (1 Oe) under various H_{DC} using a lock-in amplifier. The induced P under an applied magnetic field was monitored by using a ferroelectric tester (Radiant: Precision Premier II, USA).[80] The measurement system based upon modified Sawyer–Tower technique that allows direct measurement of the P behaviour corresponding to the applied H. The sample was placed in the center of a Helmholtz coil which excited H_{AC} from the DRIVE output of the tester. The output from the sample was connected to the RETURN input of the ferroelectric tester. Magnetostriction for NCZF was measured by using the strain gauge and Wheatstone Bridge. The magnetization of the composite was measured by using vibrating sample magnetometer (VSM).

3.3.2 Microstructure and chemical stability

Figure 3.12(a) shows the optical image of co-fired NCZF/Textured-PMN-PT/NCZF (abbreviated as C-N/T/N) laminate composite synthesized at 930 ^{o}C for 4 h with dimensions 16 × 4 × 0.4 mm^{3}. Co-firing of piezoelectric ceramic layer, Ag metal electrode layer and ferrite ceramic layer is extremely challenging due to the large difference in shrinkage rates and thermal expansion mismatch. By using fine PMN-PT matrix powder and by adjusting the ratio of sintering aid (Cu) content in NZF as described in the experimental section, we sucessfully co-fired the multilayer composite. Figure 3.12(b) shows the cross-sectional scanning electron microscopy (SEM) images of C-N/T/N composite. There was no trace of delamination or micro-crack and the thickness of textured PMN-PT piezoelectric layer and NCZF magnetoelectric layer was similar. The interfacial atomic diffusion and/or chemical reactions occuring during the sintering process at high temperature was found to be negligble. Energy dispersive spectroscopy (EDS) line scanning analysis results are shown in Figure 3.12(b) indicating the high chemical stability of NCZF, Ag, and PMN-PT. In a prior study conducted on NCZF / PZN-PZT system, the diffusion length for Cu was found to be in the range of 30 μm.[81] In our case, Ag electode layer acts as an effective barrier layer for Cu migration and thus provides a sharp interface by limiting the diffusion. EDS analysis of C-N/T/N cross-sectional area [Figure 3.12(c)] shows the dense microstructure and sharp interface across different layers. The thickness of Ag electrode and PMN-PT piezoelectric layer was 10 μm and 140 μm respectively. Figure 3.12(d) shows the fracture surface SEM images and corresponding planar x-ray diffration (XRD) patterns of different layers. For textured PMN-PT layer synthesized by template grain growth (TGG) method, brick wall-like

microstructure with well aligned BT templates (black lines) in the PMN-PT matrix was obtained. Increase of {00l} XRD peak intensity and decrease of other peaks clearly indicates the formation of texture. In TGG process, BT template crystals are aligned in PMN-PT matrix powder by tape-casting process. High temperature treatment (or sintering process) results in the nucleation and growth of PMN-PT matrix on the aligned BT template crystals yielding textured ceramics. Matrix PMN-PT and $BaTiO_3$ (BT) template form an excellent couple due to high chemical stability and good lattice match. It has previously reported that PMN-PT with 1 *vol*% template content sintered at 1150 ^{o}C for 10 h was fully textured (Lotgering factor f = 98%), and piezoelectric coefficient d_{33} increased to 1000 pC N^{-1} compared to its random counterpart (520 pC N^{-1}).[82] This large enhancement in piezoelectric property of <001> textured ceramics was found to be related to the formation of "engineered domain state" which facilitates the rotation of <111> polarization toward the <001> direction.[83,84] In this work, the kinetics of templated grain growth were reduced due to the low co-firing temperature of 930 ^{o}C resulting in lower texture degree (f= 66%).

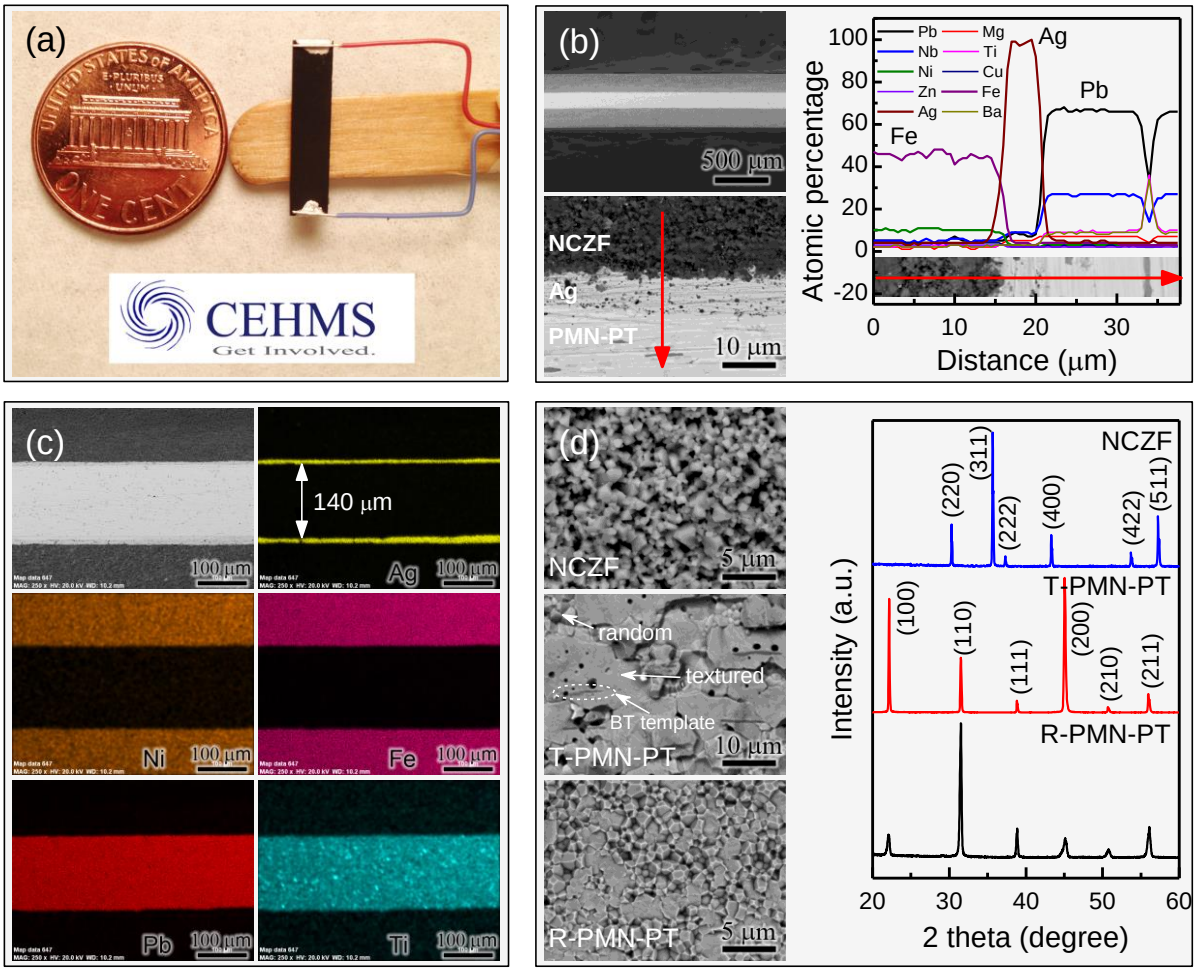

Figure 3.12 (a) Optical image of co-fired NCZF/T-PMN-PT/NCZF laminate; (b) polished cross-sectional SEM images and EDS/SEM element line scanning analysis; (c) element mapping of co-fired NCZF/T-PMN-PT/NCZF laminate; (d) fracture cross-sectional SEM images and planar XRD patterns of different layers.

3.3.3 ME response of co-fired laminate

Figure 3.13(a) shows the change in ME voltage coefficient (α_E) as a function of DC magnetic field at off-resonance frequency of 1 kHz. Although the magnetostriction of Metglas (λ=40 ppm) is twice that of NCZF (λ≈20 ppm), the maximum α_E of co-fired NCZF/random-PMN-PT/NCZF (abbreviated as C-N/R/N) is two times as that of epoxy bonded Metglas/random-PMN-PT/Metglas (abbreviated as B-M/R/M) laminate. Further improvement was achieved for co-fired textured sample (C-N/T/N). The large enhancement in ME voltage coefficient was related to the formation of high performance textured ceramics.[83,84] In Figure 3.13(a), it also can be observed that there is strong hysteretic ME response in co-fired composite. Considering the relation $\alpha \propto q = d\lambda/dH_{\mathrm{DC}}$, we estimated the effective λ behavior by integrating α with respect to the H_{DC} as shown in Figure 3.13(b). Epoxy bonded Metglas/PMN-PT/Metglas shows symmetrical λ-behavior with respect to H_{DC}, while the tendency of λ for co-fired composites was found to be asymmetric. The variation of α_E with frequency of applied H_{AC} is shown in Figure 3.13(c). It can be seen that the maxium α_E displays excellent stability. A giant ME volatage coefficient (>1200 mV cm^{-1} Oe^{-1}) at zero-bias was achieved in C-N/T/N composite. Figure 3.13(d) shows that dynamic change in charge (Q) or polarization (P) of ME composite (Radiant: Precision Premier II, USA) was measured under the condition of H_{AC}=1 Oe at f=1 kHz and H_{DC}=0 Oe. ME charge coefficient $\alpha_{ME,Q}$ can be written as:

$$\alpha_{ME,Q} = \frac{dE}{dH} = \frac{dQ}{dH_{AC}} \times \frac{1}{Ct} = \frac{dP}{dH_{AC}} \times \frac{A}{Ct}, \qquad (3\text{-}8)$$

where C, A, t are the capacitance, area and thickness of the piezoelectric layer, respectively.

Large polarization and charge induced by AC magnetic field under zero DC bias, and calculated ME charge coefficient $\alpha_{ME,Q}$ is shown in Figure 3.13(d) further confirming the presence of strong ME effect under zero bias. The time delay of $\alpha_{ME,Q}$ related to H_{AC} can be observed in Figure 3.13(d), which is attributed to the interface between magnetostrictive and piezoelectric layer. Compared to ME coefficient of 30 mV cm^{-1} Oe^{-1} obtained for NKNLS-NZF/Ni/NKNLS-NZF trilayer laminate (40×) and ~400 mV cm^{-1} Oe^{-1} obtained for functionally graded Ni-NZFO-PZT laminate composites (3×) at zero-bias, this co-fired composite exhibited extremely high response.[51,54] Recently, slightly larger zero-bias magnetoelectric coefficient of 1.65 V cm^{-1} Oe^{-1} in a quasi-one dimensional ME sensor has been reported at 100 Hz compared to our case (1.47 V cm^{-1} Oe^{-1}).[85] However, the co-fired multilayer composite based on LTCC has advantage of integration with other circuit components such as multilayer capacitor, resistor, inductor, and conductor to fabricate fully packaged electronic devices.

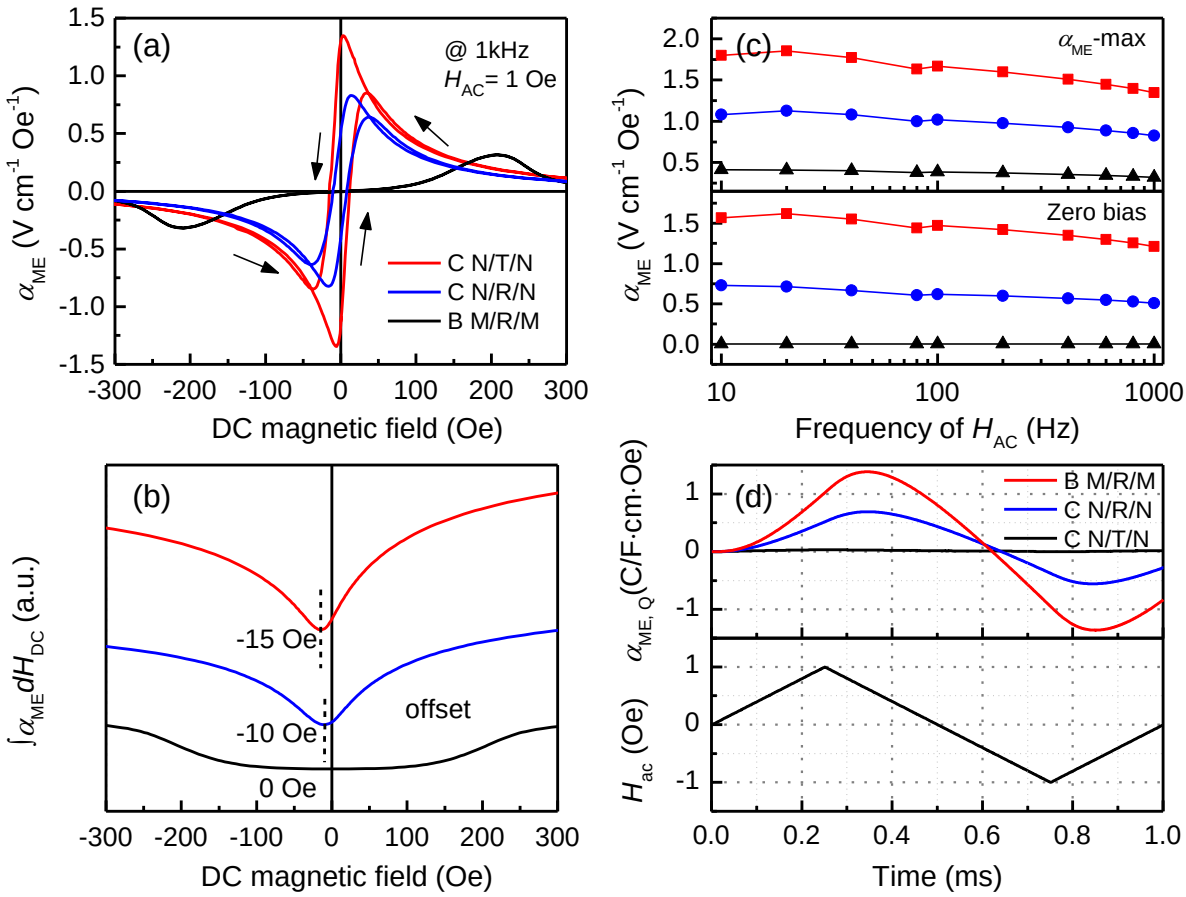

Figure 3.13 (a) ME voltage coefficients (α_{ME}) of co-fired NCZF/T-PMN-PT/NCZF (C-N/T/N), NCZF/R-PMN-PT/NCZF (C-N/R/N), and epoxy bonded Metglas/R-PMN-PT/Metglas (B-M/R/M) laminate; (b) Integral values of α_{ME} with respect to the DC magnetic field; (c) ME voltage coefficients (α_{ME}) as a function of the frequency of applied ac magnetic field (H_{AC}); (d) Dynamic ME charge coefficients (α_{ME}) and applied ac magnetic field spectra as a function of time for C-N/T/N, C-N/R/N composite, and epoxy bonded Metglas/R-PMN-PT/Metglas (B-M/R/M) laminate, under zero-DC magnetic field.

The giant ME response of co-fired composite and self-biased hysteretic behavior can be explained by taking into account the piezoelectric and magnetostrictive characteristics. Figure of merit for the ME composite can be derived as following:

$$\alpha_{ME} = \frac{\partial E}{\partial H} = \underbrace{\left|\frac{\partial E}{\partial D} \times \frac{\partial D}{\partial T} \times \frac{\partial T}{\partial S}\right|}_{P-layer} \times \underbrace{\left|\frac{\partial S}{\partial H}\right|}_{M-layer} = \left|\frac{d}{\varepsilon \times s}\right| \times q\,, \tag{3-9}$$

where E is the output electric field, H is the applied magnetic field, S is the mechanical strain, T is the mechanical stress, D is the electric displacement, d is the piezoelectric constant, ε is the dielectric constant, s is the elastic compliance of piezoelectric layer (P-layer), and q is piezomagnetic coefficient of magnetostriction layer (M-layer). Since the parameters d, ε and s of piezoelectric materials are independent of applied magnetic field (H), we focused our investigation on the magnetization (M) of NCZF as a function of magnetic field in longitudinal direction by using vibrating sample magnetometer (VSM) as shown in Figure 3.14(a). The ME behavior can be correlated with magnetostriction (λ) and magnetization (M) as: [68]

$$\varphi \sim \frac{3\lambda\sigma}{(K + 2\pi M^2)} \qquad \text{or} \qquad \lambda \propto M^2\,, \tag{3-10}$$

where φ is the angle of magnetic moments, K and σ are the anisotropy constant and stress respectively. As shown in Figure 3.14(c), the plot of $\partial M^2 / \partial H$ can predict the hysteretic nature of piezomagnetic coefficient ($q = d\lambda/dH$) with respect to applied magnetic field, which is in accordance with the ME result shown in Figure 3.13(a). To further confirm the variation of q as a function of H_{DC}, in-plane magnetostriction coeffficients (λ_{11}) was measured in parallel to applied H_{DC} by strain gauge method. As shown in Figure 3.14(e), the behavior of in-plane piezomagnetic coefficient ($q_{ij} = d\lambda_{ij}/dH$) was similar to that of

$\partial M^2 / \partial H$ and the ME result shown in Figure 3.13(a). Due to the inherent hysteresis in NCZF, the magnetostriction coeffficient (λ) is asymmetric [Figure 3.13(b)] and displays "butterfly" characteristic [Figure 3.14(b)(d)].

On the other side, there is negligible effect of the interfacial coupling on the self-biased response, the role of internal stress has to be taken into account. Silver electrode layer has much larger thermal expansion coefficient (~18 ppm) than that of piezoelectric phase (~2 ppm) and ferrites (~10 ppm), and thermal conductivity of Ag is much higher than that of piezoelectric phase and ferrite.[86] Differential thermal expansion and thermal conductivity could result in built-in interface strain which is comparable to magnetostrictive strain (20 ppm in free condition). To confirm this hypothesis, co-fired M/P/M composite without the Ag electrode was characterized. As shown in Figure 3.15, the hysteresis of ME response was dramatically reduced. Srinivasan et al. have also shown that the hystersis was noticeable with increase in the number of co-fired layer in the NZF and PZT composite without Ag inner electrode.[28] This result clearly shows the relationship between the hysteretic behavior and internal stress arising due to the thermal expansion mismatch between metallic and ceramic layers.

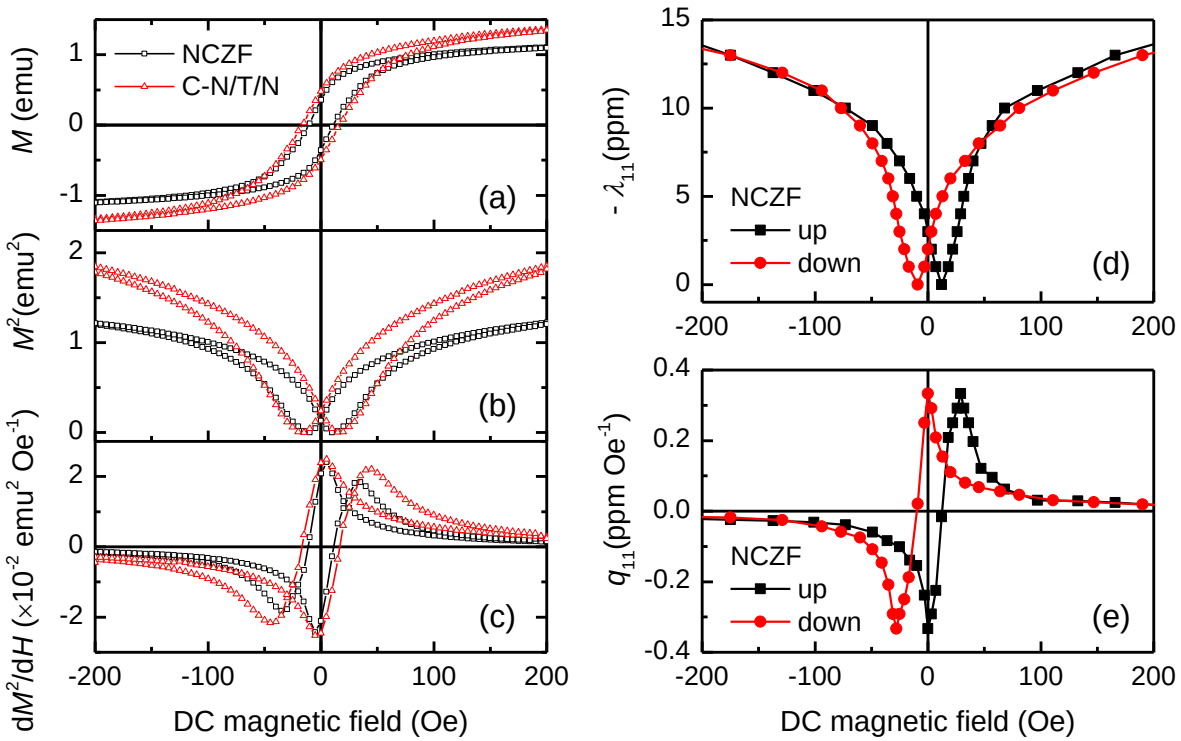

Figure 3.14 (a) Magnetization-magnetic field (*M*-*H*) loops, (b) square of magnetization as a function of magnetic field, and (c) differential of square magnetization-magnetic field [(dM^2/d*H*)-*H*] plot for pure NCZF (not co-fired) and C-N/T/N structure. DC magnetic field (H_{DC}) dependence of (d) the magnetostriction (λ) and (e) piezomagnetic coefficients (q) of NCZF (not co-fired).

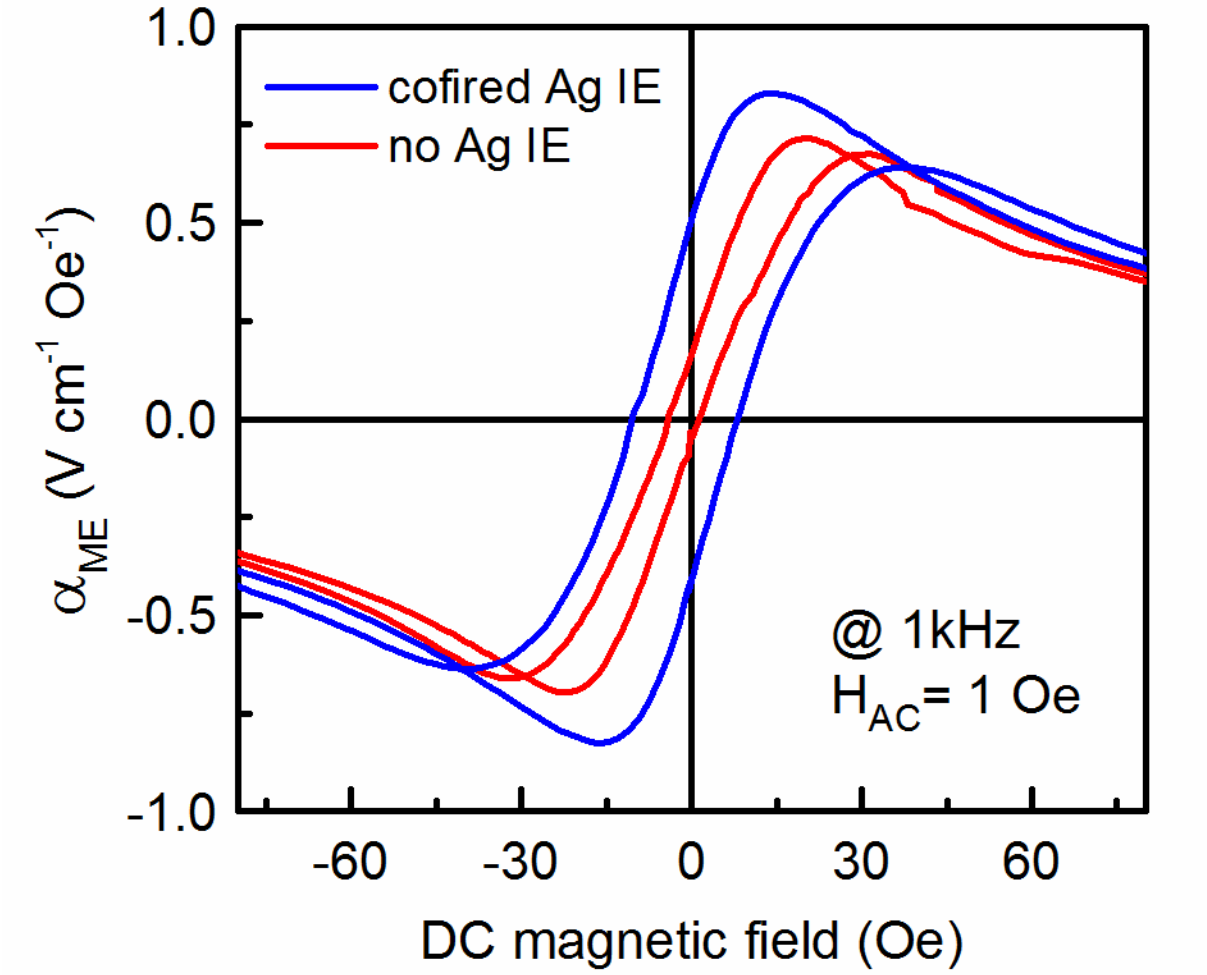

Figure 3.15 ME voltage coefficients (α_{ME}) of co-fired NCZF/R-PMN-PT/NCZF with and without Ag inner electrodes (IE).

To further understand the effect of interface condition (such as effect of epoxy and electrode) on the ME coupling, induced polarization (P) – magnetic field (H) loops were measured. Figure 3.16 shows the normalized induced polarization (P) as a function of the AC magnetic field for epoxy bonded Metglas/random-PMN-PT/Metglas [B-M/R/M (epoxy)], co-fired NCZF/random-PMN-PT/NCZF without Ag inner electrode [C-N/R/N (no)], co-fired NCZF/random-PMN-PT/NCZF with Ag inner electrode [C-N/R/N (Ag)] and co-fired NCZF/textured-PMN-PT/NCZF Ag inner electrode [C-N/T/N (Ag)], at f=1 kHz under optimum DC magnetic field. The normalization was conducted by using the P_{max} value. The hysteresis presents in this figure indicates the nonlinear behavior of magneto-elastic coupling which can be attributed to the losses associated with the transfer of elastic strain and scattering at the interface due to the presence of surface irregularities and defects.[80] Co-fired samples had less interfacial dissipation than epoxy bonded laminates. Further, co-fired samples with Ag electrode showed smaller hysteresis as compared to co-fired sample without Ag electrode because of reduced Cu diffusion. Small difference between the co-fired textured and random sample indicates that the nonlinearity was mainly dependent on the interface microstructure.

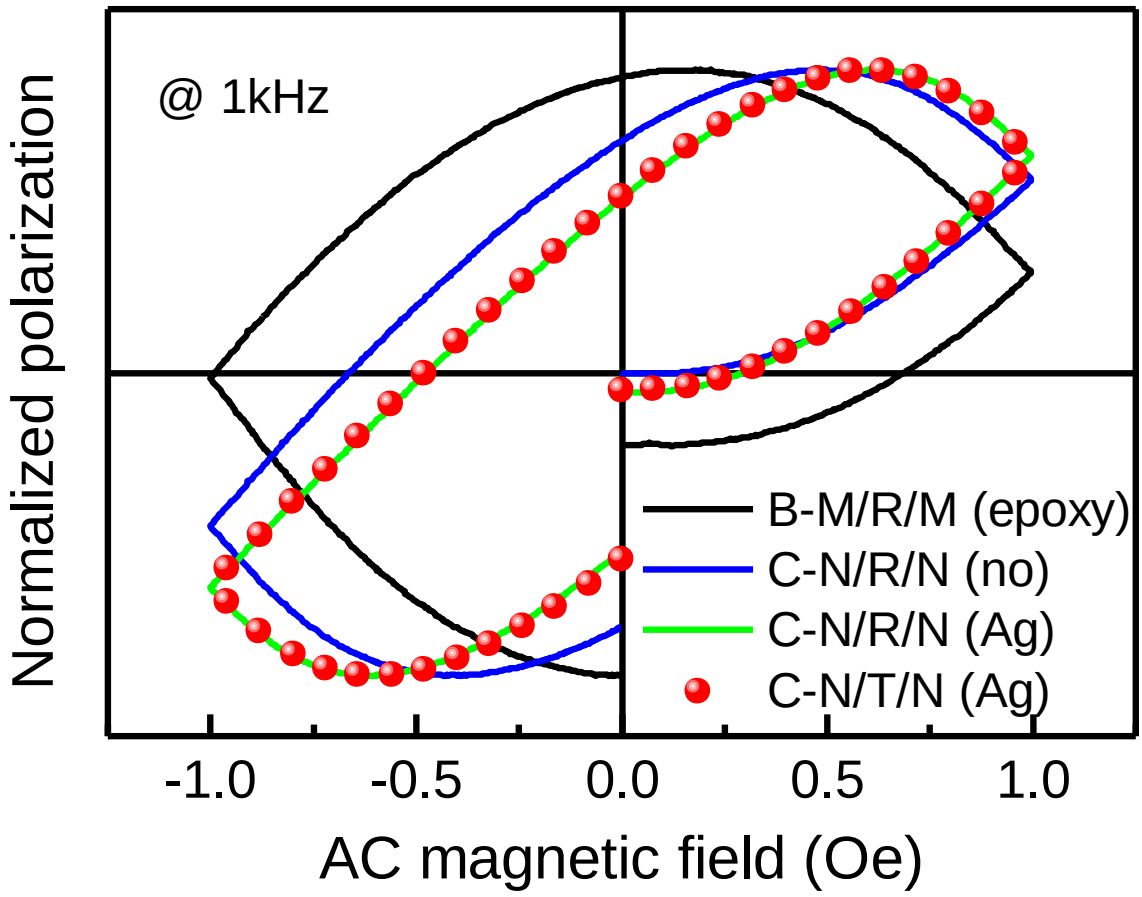

Figure 3.16 Nomalized polarization (P) – AC magnetic field (H) loops for epoxy bonded Metglas/random-PMN-PT/Metglas [B-M/R/M (epoxy)], co-fired NCZF/random-PMN-PT/NCZF without Ag inner electrode [C-N/R/N (no)], co-fired NCZF/random-PMN-PT/NCZF with Ag inner electrode [C-N/R/N (Ag)], co-fired NCZF/textured-PMN-PT/NCZF without Ag inner electrode [C-N/T/N (Ag)].

Table 3.2 lists the dielectric and ME properties of co-fired composites. Following conclusion can be drawn from this data: (1) Compared to epoxy bonded Metglas/PMN-PT/Metglas, the maximum α_E of NCZF/R-PMN-PT/NCZF was 2~3 times higher in magnitude (827 mV cm^{-1} Oe^{-1}); (2) Texturing further increases the magnitude of α_E (1346 mV cm^{-1} Oe^{-1}) by 63%; (3) Textured ceramics show low loss due to "engineered domain configuration"; (4) The dielectric constant of textured sample was suppressed by using low permittivity BT template crystals; and (5) Co-fired composites with Ag electrode show large α_E under zero-bias of the order of 1214 mV cm^{-1} Oe^{-1}. Taking into account Equation (3-9) and the results of Table 3.2, the giant ME response of co-fired textured sample can be easily explained. It should also point out that lower losses of textured sample plays an important role in enhancing the α_E which can be understood by taking into account the modified piezoelectric voltage coefficient (g_{31}) given as:[87]

$$g_{31}^{*} = g_{31}\frac{1}{\left(\tan\delta' + \tan\theta' + \dfrac{C - C_f}{C_f}\right)} \tag{3-11}$$

where C-C_f/C_f is the rate of capacitance change, C is capacitance at a given frequency, C_f is capacitance at 1 kHz, and tanδ' and tanθ' are the intensive dielectric loss and piezoelectric loss respectively.

In conclusion, NCZF/PMN-PT/NCZF layered composite with Ag inner electrodes were successfully co-fired at low temperature (930 ^{o}C). The co-fired NCZF/textured PMN-PT/NCZF layered composites exhibited 5× increase in α_E compared to conventional epoxy bonding Metglas/PMN-PT/Metglas composite. Further, these composites exhibited giant self-bias phenomenon which was associated with hysteresis of NCZF magnetostrictive

materials and built-in stress arising from Ag electrode due to mismatch in thermal expansion coefficient. These cost-effective composites with excellent ME properties open the possibility of mass production of numerous magnetoelectric applications.

Table 3-2 Dielectric and magnetoelectric properties of co-fired layered ME composite (1kHz)

Sample	Electrode	ε_r	tanδ	dE/dH (max) [mV cm^{-1} Oe^{-1}]	dE/dH (zero-bias) [mV cm^{-1} Oe^{-1}]
C-N/R/N	co-fired	1135	0.7%	1346	1214
C-N/T/N	co-fired	1336	1.1%	827	510

3.4 Chapter summary

In summary of this chapter, investigations addressing the challenges of conventional ME coupling have been performed and systematically studied. Achievements can be detailed listed from three aspects as given below:

(1) Eliminating the need for DC bias: Self-biased magnetoelectric effect, characterized as large ME voltage coefficient under zero DC magnetic field, was demonstrated in homogenous two-phase magnetostrictive-piezoelectric (Ni-PZT) laminates. Experimental results illustrate the method for tuning the magnitude of self-bias effect via geometry effect and provide understanding behind the hysteretic changes. This phenomenon was further modeled by considering the magnetization hysteresis with shape-induced demagnetization effect. The self-biased response was found to be directly related to the nature of magnetization and can be tuned by variation in demagnetization state and the resultant differential magnetic flux distribution. These results present significant advancement toward development of AC magnetic field sensor and magnetoelectric composite based on-chip devices by eliminating the need for DC bias.

(2) Increase the working bandwidth: ME composites that exhibit flat and stable response over a wide range of magnetic DC bias were realized in geometry gradient configuration. By adjusting the configuration of the magnetostrictive layer, one was able to control the magnitude of self-biased magnetoelectric coefficient. The ME response was found to be almost independent of the applied DC bias in the range of 0~260Oe. This bandwidth is almost 650%~3800% higher than that of the conventional ME composites. This

significant advancement leads great potential towards the development of high stability/sensitivity magnetic field sensors and energy harvesters.

(3) Enhancing the ME interfacial coupling: Co-fired magnetostrictive / piezoelectric / magnetostrictive laminate structure with silver inner electrode were synthesized and characterized. Integration of textured piezoelectric microstructure with enhanced physical properties was demonstrated to improve the ME coupling. Direct bonding of the consecutive phases with high chemical stability and sharp phase boundary further strengthened their interfacial coupling, leading to a giant ME voltage coefficient. The low-temperature co-fired layered structure not only provides a cost-effective method toward large fabrication of ME composites, but also significantly enhanced the ME coupling through direct bonding.

4. Magnetoelectric Nanostructures

The ME effect in composite thin films is dependent upon microstructure, connectivity and the interfacial coupling properties between piezoelectric and magnetic phases. Motivated by on-chip integration, nanostructured composites of ferroelectric and magnetic oxides have been deposited on various substrates with different connectivity (0-3, 1-3 and 2-2) via diverse synthesis method. Although these ME nanostructures may imply application of microelectronic devices, it remains a challenge that how to precisely control the growth of desired ME nanocomposites with precisely manipulated composition, nanostructure and interface.

In this chapter, I will discuss ME nanocomposites investigations about these challenges from two perspectives:

(1) Control growth of nanostructure: Both microstructure and surface morphology of a continuously piezoelectric film and well-ordered nanocomposite arrays with controlled grain orientation will be discussed.

(2) Manipulate nanocomposite interface: Interfacial effects in 2-2 layered magnetoelectric thin/thick films will be systematically investigated. Subsequently, a novel complex three-dimensional ME composites with highly anisotropy structure will be discussed.

4.1 Microstructure and surface morphology evolution of pulsed Laser deposited piezoelectric BTO films*

Barium titanate [$BaTiO_3$, (BTO)] thin and thick films have been extensively investigated owing to their high dielectric, ferroelectric, and non-linear optical properties. [88,89,90] These films have been deposited on various substrates (e.g. Si, $SrTiO_3$, MgO) using diverse deposition techniques (e.g. sol-gel, sputtering, pulsed laser ablation) targeting applications such as capacitors, ferroelectric memory, optical modulators, magnetoelectrics, and microelectromechanical systems (MEMS).[89,90,91,92,93,94,95] Recently, there have been investigations on the design of nanoscale structures, such as nano-pillar, nano-belt, and star-like nanostructure,[10,11,12] that have contributed towards the understanding of the growth mechanisms in thin films. Depending upon the thickness of the film, deposition technique and deposition conditions, variety of microstructures can be obtained. In order to further improve the process compatibility and piezoelectric property, unveiling the growth mechanism and morphological evolution of thin films is of utmost importance.

4.1.1 Thickness effect: crystallinity, microstructure, and properties

BTO films with various thicknesses were deposited on platinized silicon substrate by using KrF excimer pulsed laser deposition system (λ=248 nm, Neocera, LLC). Stoichiometric BTO ceramic target was synthesized by conventional sintering method using an analytical reagent grade ~99.9% pure oxide powder of $BaTiO_3$ from Johnson Matthey, Ward Hill, MA, USA. The powder was milled in a polypropylene jar with zirconia milling balls and ethanol

*Reprinted with permission from [96], Copyright 2013, The Royal Society of Chemistry.

(99.5%, Sigma-Aldrich, St. Louis, MO) for 24h, dried, pressed into disk-like target (diameter: 1 inch, thickness: 0.25 inch), and cold isostatically pressed at 130 MPa for 5 min. The sample was then heated in air at 5^{o}C/min and sintered at 1350 ^{o}C for 2 h. Before deposition, Pt coated Si substrates were ultrasonic cleaned using acetone, ethanol and DI water, respectively. Then the substrates were transferred to the chamber and vacuum down to the pressure of 5x10^{-6} torr. During all the depositions, the laser energy density, repetition rate and the oxygen pressure was kept at ~2.5 J/cm^{2}, 10 Hz and 100mTorr respectively. The film morphology was controlled by the deposition time and temperature. Deposition time was controlled by the number of laser pulses with fixed deposition rate (10Hz). In order to vary the film thickness, the number of laser pulses was varied from 20000 to 100000. The substrate temperature was kept constant at 800^{o}C during deposition. In order to investigate the effect of temperature, the substrate temperature was changed from 600^{o}C to 1000^{o}C, while keeping number of pulses constant at 60000. X-ray diffraction (XRD, PANalytical X'Pert, Cu*Ka*, Philips) and Raman spectroscopy (Jobin-Yvon T6400 Triple spectrometer) were used to characterize the crystallinity and orientation of the BTO films. The film morphology and microstructure were investigated by using field emission electron scanning electron microscopy (FE-SEM, Zeiss LEO 1550). Bright field imaging and high-resolution transmission electron microscopy (HRTEM) were conducted in a FEI Titan 80-300 scanning/transmission electron microscope (S/TEM). The microscope was operated at 300 kV and a standard setting for HRTEM imaging was a 70 μm C2 aperture with an objective lens defocus of -58 nm. The topography and ferroelectric measurements were performed using a scanning probe (Bruker Dimension Icon, USA) with a piezoelectric force microscope (PFM). Conductive diamond coated silicon

cantilevers (DDESP-FM-10, Bruker) were used for PFM. For local hysteresis loop measurement, the out-of-plane piezoelectric response was measured at selected locations on the ferroelectric film surface as a function of dc bias superimposed on the ac modulation bias. The deflection sensitivity of the tip was 94.9 nm/V and the AC drive amplitude was 3.5V (20 kHz) during the DC bias sweep.

Figure 4.1(a) shows the XRD patterns of the BTO films with varying thicknesses deposited on the (111)Pt/Ti/SiO_2/Si substrate at 800 ℃. These films exhibited (111) preferred orientation without any secondary phase. The degree of (111) preferred orientation was determined by the Lotgering fator method: $f_{(111)}= [P_{(111)}-P_0]/[1-P_0]$, $P_{(111)}= \Sigma I_{(111)}/\Sigma I_{(hkl)}$, $P_0= \Sigma I_{0(111)}/\Sigma I_{0(hkl)}$. where $\Sigma I_{(111)}$ and $\Sigma I_{0(111)}$ are the (111) peak intensity of the BTO film and the random powder, and $\Sigma I_{(hkl)}$ and $\Sigma I_{0(hkl)}$ are the summation of XRD peak intensities of all the hkl peaks in the BTO film and random powder, respectively. The diffraction patterns 2θ scan from 20^o to 80^o were used to calculate the *f* factor. The degree of (111) preferred orientation $f_{(111)}$ was significantly enhanced from 77 to 94% with increasing thickness. This preferred orientation of BTO film was attributed to the lattice match between (111) BTO film and (111) oriented underlying Pt layer. The lattice mismatch (*f*) between a film and substrate can be determined using the expression:

$$f=(a_s-a_f)/a_s \times 100\% \ , \qquad (4\text{-}1)$$

where a_s and a_f refer to the lattice parameters of the substrate and film respectively. The lattice mismatch along both (100) and (111) direction were calculated to be ~-1.8% (a_{BTO}=3.992Å, c_{BTO}=4.036Å, a_{Pt}=3.92Å). This small mismatch leads to the (111)-preferential growth of the film on Pt electrode in order to minimize the interface energy.[97,98,99] The

crystallinity of thin films was found to increase with increase in film thickness and grain growth. Therefore, thin films with higher thickness were found to depict higher intensity of BTO (111) peak and thereby increased degree of texture. This agrees well with the Van der Drift's model[100] for vapor-deposited film, where preferred orientation growth was attributed to the evolutionary selection.

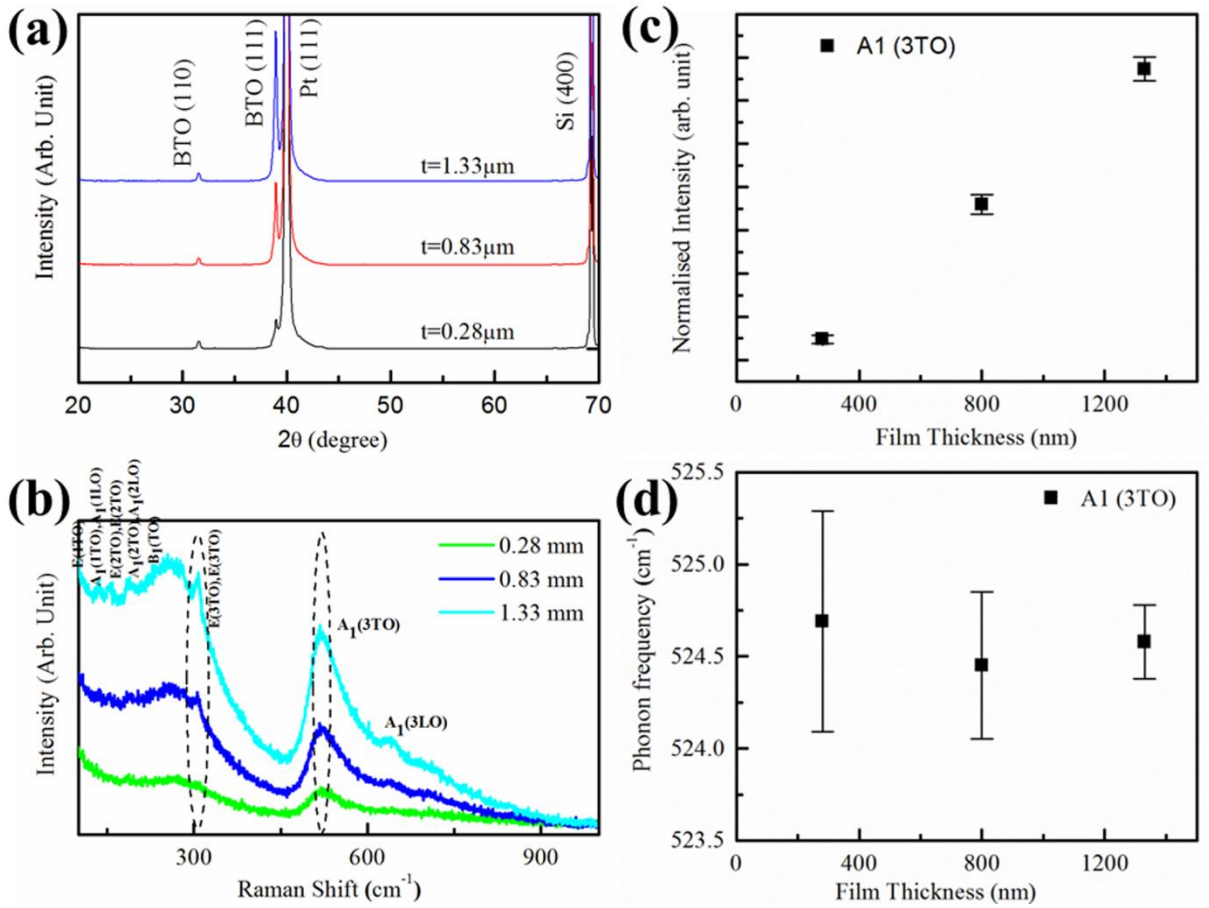

Figure 4.1 (a) X-ray diffraction patterns of BTO films with different thickness, (b) Raman spectra of BTO films with different thickness, (c) Normalized A1(3TO) phonon intensity as function of film thickness, and (d) A1(3TO) phonon peak position as function of film thickness.

Unpolarized Raman spectra were measured to identify the structure of films as a function of thickness as shown in Figure 4.1(b). Tetragonal $BaTiO_3$ has C_{4v} symmetry, which allows $3A_1+1B_1+4E$ Raman active optical modes and $1A_1+E$ acoustic modes.[101,102] There is further splitting in A_1 and E modes to transverse optic (TO) and longitudinal optic (LO) modes due to long range electrostatic force associated with lattice iconicity. Consequently, the Raman active modes in BTO tetragonal phases are: $3A_1(TO)+3A_1(LO)+3E(TO)+3E(LO)+1E(LO+TO)+1B_1$. More optical modes due to the dielectric anisotropy can be seen in the Raman spectra. As for the film with 1.33 μm thickness, almost all of the E(LO), E(TO), A_1(TO), A_1(LO), and B_1 modes can be successfully assigned in the spectra. Some interesting features of the Raman spectra are as follows: (i) the thickest film show that all the Raman active modes matched with single crystal, indicating its excellent crystallinity, (ii) intensity of the spectra drops with thickness, (iii) E(3TO) and E(3LO) modes are absent in the 0.28 μm thin films and (iv) an upward shift of A_1(3TO) mode and diffuse nature of A_1(3TO) mode. It is believed that the smaller grains are responsible for low intensity, diffuse A_1(3TO) mode, and absence of several lowest E and A modes in the 0.28 μm thin films.

To clarify the Raman spectra, the well-defined A1(3TO) mode was simulated as a function of film thickness using the damped harmonic oscillator (DHO) model[103,104].

$$S(\nu) = \sum_i \frac{\chi_{0i}\Gamma_i\nu_{0i}^2\nu}{(\nu^2-\nu_{0i}^2)+\Gamma_i^2\nu^2} F(\nu,T), \tag{4-2}$$

where population factor $F(\nu,T)=[n(\nu)+1]$ for Stokes scattering and $n(\nu)=[\exp(h\nu/kT)-1]^{-1}$. The parameters in Equation (4-2), amplitude χ_0 (in arbitrary units), the mode frequency ν_0, the damping constant Γ, and the temperature T, describe phonon mode as a damped harmonic

oscillator. It would be hard to simulate the low frequency phonons due to weak intensity and unable to distinguish the modes for thin film (0.28 μm). It is shown that the normalized A1(3TO) phonon intensity increases linearly with increase in the film thickness [Figure 4.1(c)] whereas phonon peak position are almost same [Figure 4.1(d)]. This might be one of the reasons that thicker film shows well defined Raman signal matched with the BT single crystal. Raman selection rule for perfect epitaxial films or single crystal BTO suggests that the weak E(3TO) and E(3LO) modes indicate the lower symmetry of the system and less c-axis oriented polar domains[105]. It means thinner film should show poor preferential orientation and functional properties as can be seen from XRD and piezoelectric data respectively. The above observation is also well supported by the XRD data where the intensity ratio of (111) to (110) peaks is quite small for 0.28μm film compared to 1.33μm. However for any quantitative analysis, one should perform polarized Raman studies on epitaxial BTO thin films where the dielectric leakage in the cross polarization will be minimal.

Figure 4.2 shows the planar and cross-section SEM images of the BTO films as a function of film thickness. When the film thickness was ~0.28 μm, the microstructure exhibited a fine columnar structure [Figure 4.2 (a) and (d)] with the in-plane grain size of 56 nm. The interface between the BTO and Pt layers was continuous, while the surface morphology exhibited pyramid-like shapes. As the film thickness was increased to 0.83 μm, the microstructure coarsened and the in-plane grain size increased to 78 nm as shown in Figure 4.2 (b) and (e). At the same time, the surface morphology changed from pyramid to star-like shape. Furthermore, when the film thickness was increased to 1.33 μm, the grain

morphology changed to six-fold hexagram as shown in Figure 4.2 (c) and (f). This morphology stays uniform along the surface with average in-plane grain size of 98 nm. The growth habit plane of BTO has been previously characterized[106] and the films with preferred grain orientation exhibited good electrical properties as compared to random ones[107]. However, no detailed information on the mechanism describing the microstructural evolution has been reported.

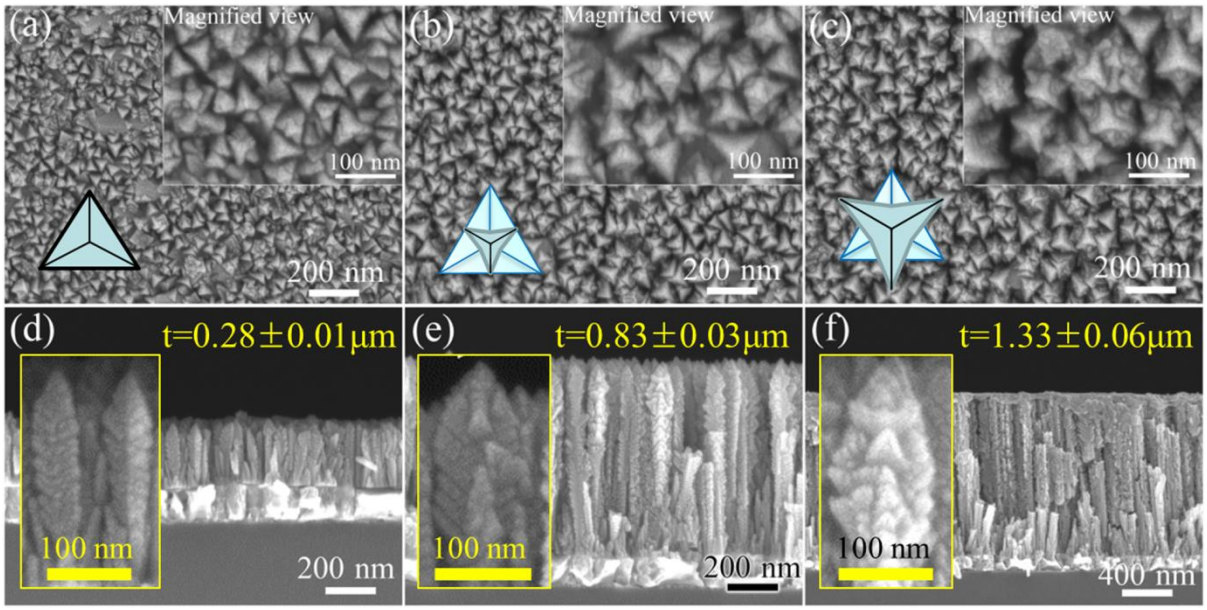

Figure 4.2 Planar and cross-section views of BTO films show the morphology changes as a function of film thickness: (a) and (d) 0.28±0.01 μm, (b) and (e) 0.83±0.03 μm, (c) and (f) 1.33±0.06 μm.

Piezoelectric response of the deposited BTO films was measured by using PFM as shown in Figure 4.3. The d_{33} values increased with film thickness. The measured effective d_{33} ($d_{33,eff}$) values were found to be 18, 20, and 24 pm/V respectively for 0.28, 0.83, and 1.33 μm-thick BTO films. Kim et al. have reported that the random 0.25 μm-thick BTO film on Pt/Si substrate had the $d_{33,eff}$ value of 14.3 pm/V.[108] In comparison with this prior result, it was found that orientation control leads to significant rise in the $d_{33,eff}$ value. The enhancement of $d_{33,eff}$ values with film thickness was attributed to: (i) preferred orientation (ii) increase in grain size, (iii) reduction in substrate clamping, and (iv) increase in crystallinity.

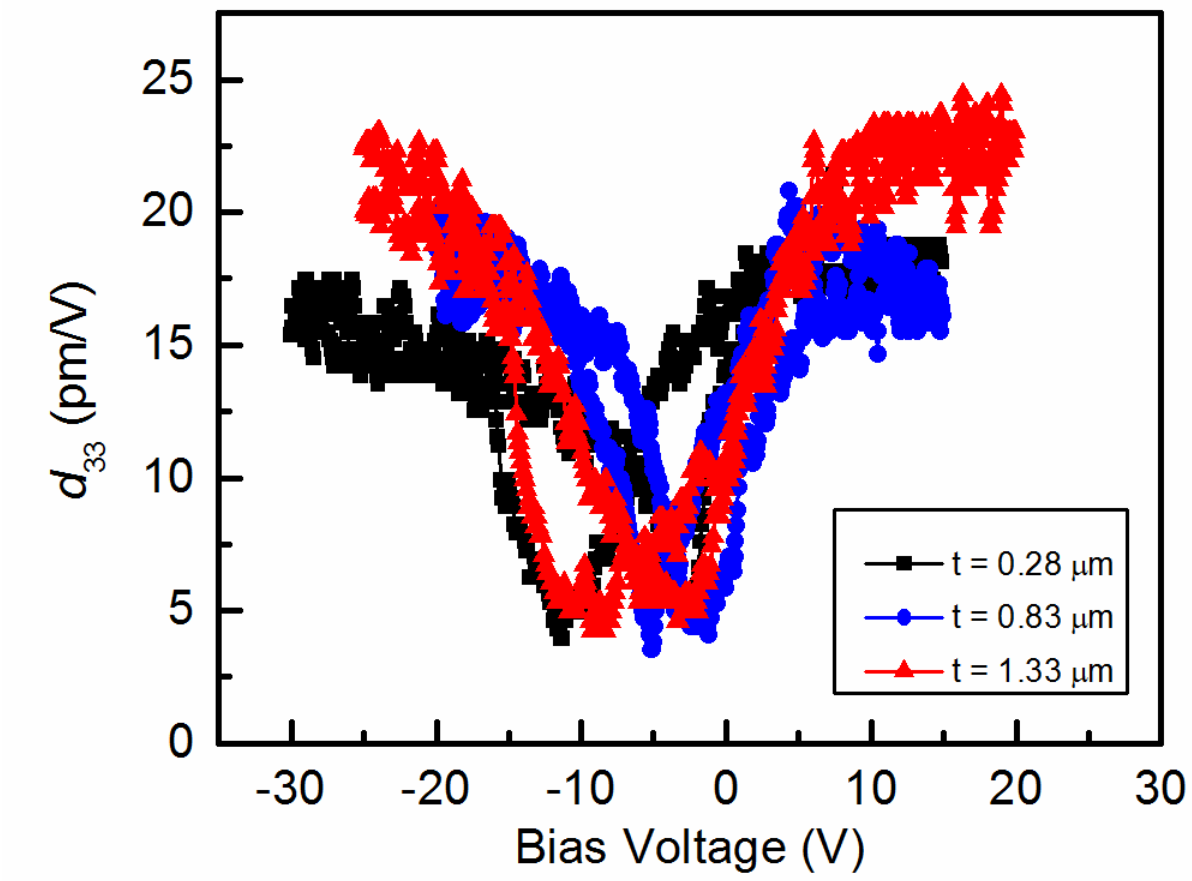

Figure 4.3 Piezoelectric responses of BTO films with varying thickness.

4.1.2 SZM and DST analysis

Morphology evolution models such as Dynamic Scaling Theory (DST)[109] and Structure Zone Model (SZM)[110,111] have provided the important foundation for understanding the growth of films. While theoretical predictions provided by these models describe a general morphology development, they fail to explain the evolution process such as the correlation between the occurrence of defects and the growth mode[109-112]. In thin film growth, the introduction of misfit dislocation is energetically favored at the interface with substrate and the formation of dislocation will relieve strain to form a semicoherent interface[113]. However, the systematic information regarding the relationship between the induced defects and the growth modes is still missing.

Generally, morphological evolution in vapor deposited films can be explained by taking into account the SZM model predictions[110] which suggest that the development of microstructure is a universal function of the ratio between the deposition and melting temperature (T_s/T_m). All the as-grown BTO thick films show a compact columnar growth habit, while the surface morphology varies from pyramid to star-like to hexagram. The columns, which extend through the entire film thickness, exhibited sharp terminating ends and secondary growth in the lateral direction for thicker films resulting in an enlarged diameter, as shown in Figure 4.2 (d), (e) and (f). Inset image shows how the coherent grains are stacked to form the columns. This uniform columnar structure matches well with the description ascribed to zone II in SZM model, where regular arrangement of uniform columns appears in the range of T_s/T_m<0.5-0.55 (T_s=800 ℃, T_m=1625 ℃, T_s/T_m=0.49). Also, zone II can be characterized by evolutionary growth due to adatom diffusion[110]. However, the

observed surface morphology changes in the present case are the function of film thickness and are not expected by the SZM model. Moreover, although in this experiment, the T_s/T_m ratios ($0.4<T_s/T_m<0.5$) corresponds to the upper limit for the appearance of a zone II morphology, hexagram grains with equiaxed characteristic belongs to zone III ($T_s/T_m>0.5$-0.55) morphology.

To better explain these surface morphological changes, the surface structures were investigated by atomic force microscopy [Figure 4.4(a)] and dynamic scaling analysis. The growth evolution can be taken as a process of columnar coarsening, which can be statistically characterized by two parameters: the interface width ω (or root-mean-square roughness, RMS), and a lateral correlation length (related to the lateral size of the surface features such as columnar diameter, d). Both ω and d dependence on the deposition thickness/time (t) were estimated by statistical studies of the AFM and SEM images, as shown in Figure 4.4(b). The RMS roughness and average columnar size, according to the power law relations, is given as[109]:

$$\omega \sim t^{\beta} \ , \ d \sim t^{1/z}, \tag{4-3}$$

where β and $1/z$ are the growth and coarsening exponents respectively. The deduced coarsening exponent for BTO is $1/z=0.35\pm0.03$, which is similar to the theoretical prediction for a growing surface destabilized by a non-local geometric shadowing effect ($1/z\sim0.33$). [114,115,116] The high β value (>0.5) also agrees with this interpretation[117].

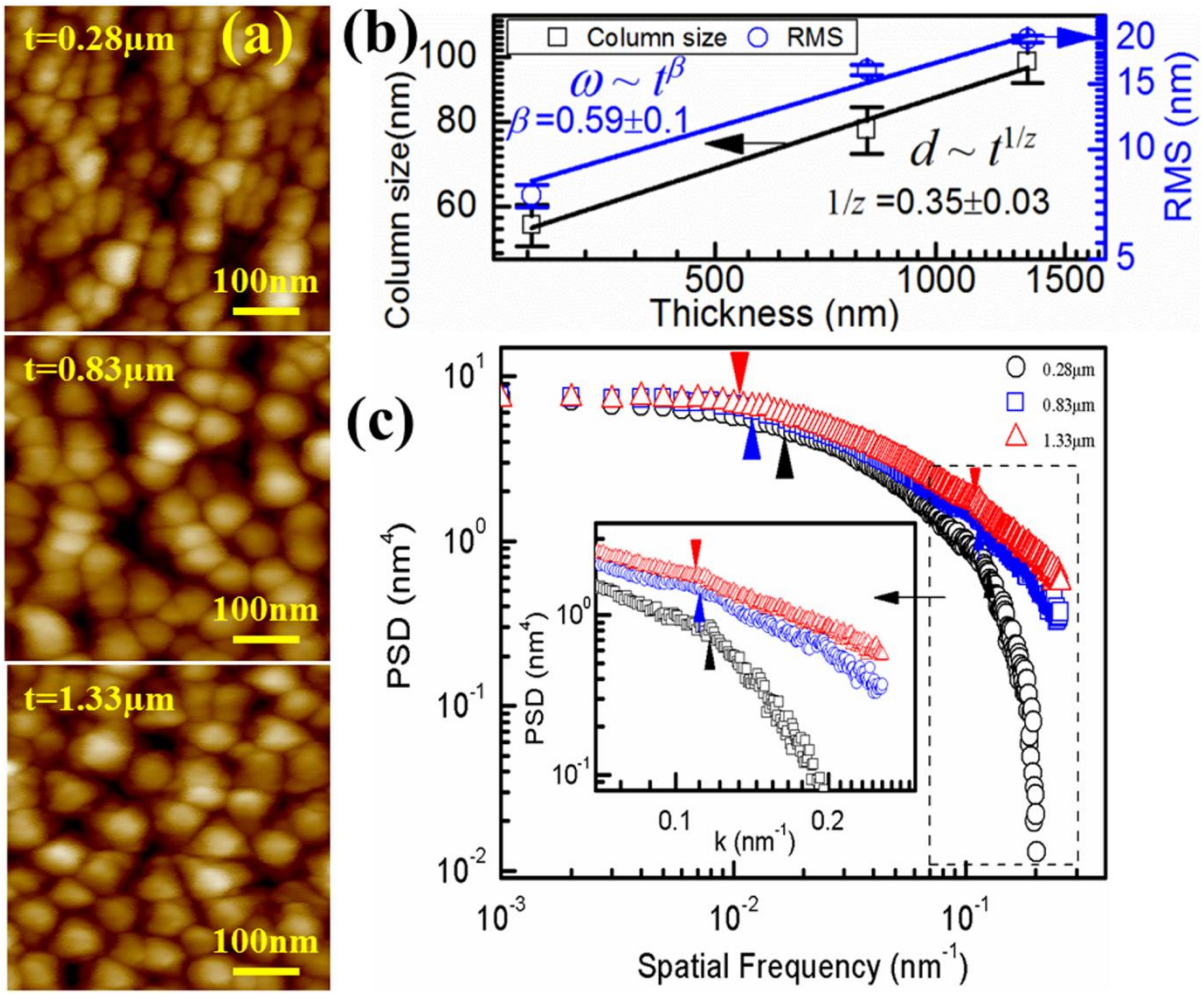

Figure 4.4 (a) AFM images of as grown BTO films with different thickness. (b) Logarithmic plot of the columnar coarsening in BTO films deposited at 800^{o}C in 100mTorr on platinized silicon substrates. (c) PSD curves calculated from AFM images of BTO films of different thickness.

The spatial resolution of the roughness and correlations between roughness and specific surface features are discussed by power spectral density (PSD) analysis [Figure 4.4(c)], as [117,118]:

$$\mathrm{PSD}\,(\mathrm{k},\mathrm{t}) \propto \mathrm{k}^{-(D+2a)} f(k^z t) \tag{4-4}$$

where k is spatial frequency (or inversely, lateral dimension), and t is growth time. For $k^z t >> 1$, $f(k^z t) =$constant, $\mathrm{PSD}\,(\mathrm{k},\mathrm{t}) \propto \mathrm{k}^{-(D+2a)}$. The dimension of the system is D=2, and a is the roughness coefficient. It can be noticed that the PSD curves exhibit several distinct regions, a frequency-independent roughness at low frequency and two frequency-dependent regions at higher frequency, implying combination of two processes controlling the development of the surface morphologies. In agreement with the previous work on PSD curve analysis[115,118], it is suggested that: (1) In the high frequency regime, the lateral surface growth is driven by atomic diffusion mechanism, which may result in the grain coalescence. This interpretation is also in agreement with the SZM model in zone II, where the thick film growth is dominated by adatom surface diffusion[110]. (2) In the intermediate frequency region, the growth mechanism can be described as a balance between roughening (random fluctuations in depositing flux) and smoothing process (diffusion at the growth front with local structure unchanged)[109]. In addition, it can be noticed that the frequency of transition between the various regimes, marked by arrows in Figure 4.4(c), clearly exists and they both shift to lower value of k as thickness increases, implying the presence of a coarsening process[115]. These transition frequencies of each curve represent the average specific surface feature (small grains or branch of hexagram-shaped grains) size (~8-10nm), column diameter (~50-100nm), respectively, and is coherent to the experimental observation.

From these results it can be concluded that the growth dynamic behavior is tightly correlated with surface roughness, spatial length and specific surface features (branch of hexagram-shaped grains) during growth, which in turn can be used to predict corresponding growth mechanism, such as shadowing effect and surface diffusion.

4.1.3 Local nanostructure analysis

In order to further elucidate the grain coalescence behavior, the local nanostructure of the column with hexagonal feature was studied in a thick BTO film grown at 800 ℃ by TEM. Figure 4.5(a) shows a typical TEM bright field cross-section image of the BTO/Pt sample. The film has a well-developed columnar structure with a feather-like morphology growing along the vertical columnar boundary. The column has a central stem (column) with array of lateral protrusions (one of the as-grown hexagonal branches). To investigate the detailed atomic structure of both the column and protrusions, a series of high-resolution transmission electron microscopy (HRTEM) images [Figure 4.5(b)~(d)] was taken from the regions marked in Figure 4.5(a), where region “A” [Figure 4.5(b)] and “B” [Figure 4.5(c)] refer to selected protrusions of the column, region “C” [Figure 4.5(d)] denotes the interface between the substrate and film. Although there are some local defects in the BTO film, the major growth direction of the columnar structure and the protrusions were determined to be <111> and <110> from the FFT patterns, inset in Figure 4.5(b) and (c). Among the HRTEM images, there are planar defects distributed all across the central column and at the vicinity of the protrusions along the [111] axis as shown in Figure 4.5(b) and (c). These planar defects were identified to be twins by comparing the periodic structure of the planar defects in the HRTEM

image to a simulated twinned structure as shown in Figure 4.5(f). The appearance of the streaking spots in FFT patterns is due to the presence of these nano-twins. Figure 4.5(d) illustrates the HRTEM image of region “C” that denotes the interface between the substrate and film. The interface is coherent and highlighted by dashed line. FFT pattern further confirms that majority of the BTO film growth occurs epitaxially from the substrate along the <111> orientation. The results illustrate that both columnar structures and protrusions have preferred orientation and twin lamellae are widely distributed among them. However, there are some questions that need to be addressed here: (i) Why BTO twin lamellae structure was formed? (ii) Instead of preferred growth orientation along <111>, why were the protrusions formed along <110> direction? and (iii) How did the twin lamellae structure affect the film growth mechanism and surface morphology?

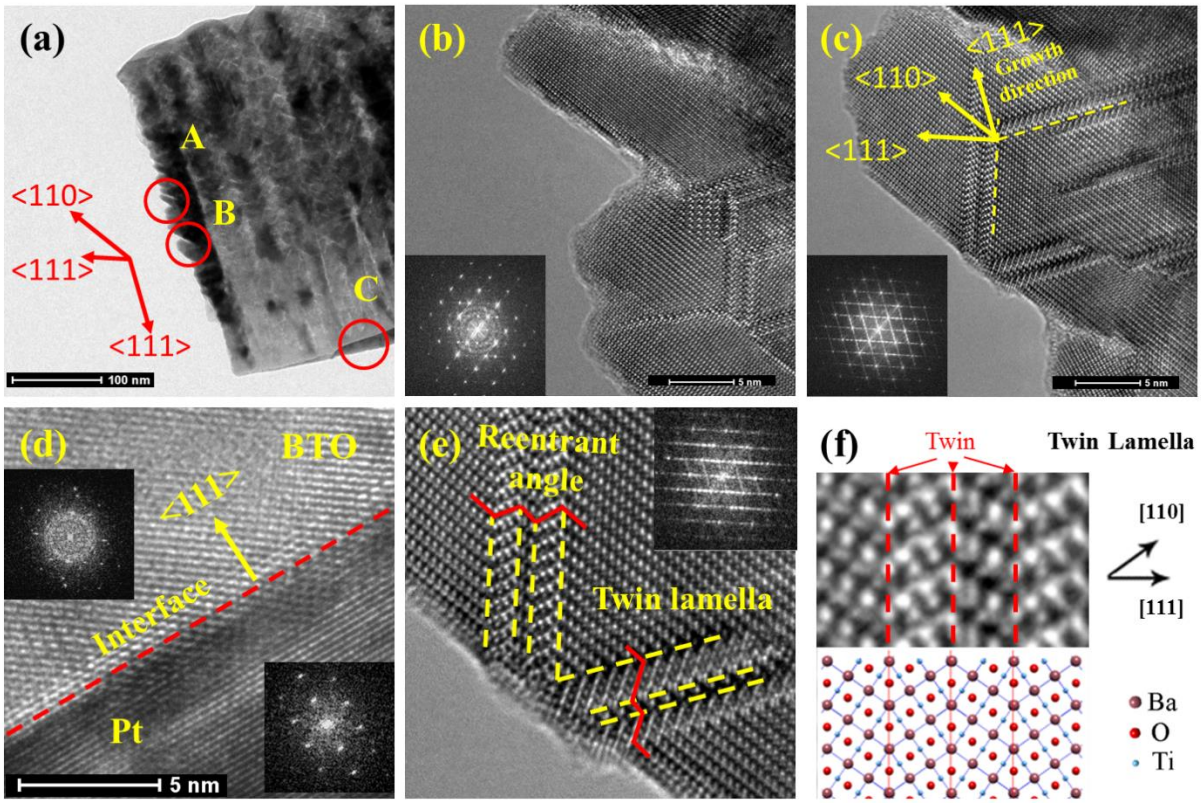

Figure 4.5 TEM characterization of BTO thin film fabricated by pulsed laser deposition (a) Bright field image of BTO thick film synthesized at 800 ℃; (b) HRTEM image of region A; (c) HRTEM image corresponding to the region B; (d) The lattice fringes indicate a part of the BTO and Pt interface, which corresponding to the region C; (e) HRTEM image of the film with lamella twins, inset is FFT pattern generated from the twin lamellae; (f) Comparison of experimental and simulated twin lamellae structure.

Twin lamellae structure has been widely observed in ceramic, single crystal and thin films[119,120,121]. Several growth mechanisms for twins have been reported and some of the relevant ones for the present discussion are summarized here. Jia et al. suggested that twin nucleation could occur from dissociation of a perfect <111> edge dislocation.[122] Jang et al. have explained the formation of twin lamellas as an approach to release the small misfit between two growing islands during coalescence process[123]. With respect to planar defect, the cause of the formation of (111) twin lamellae could be explained by the maintenance of a TiO_6 octahedron and the presence of a hexagonal BTO structure[123]. Based on these prior results, with respect to the generation of defects during the non-equilibrium film growth process, a mechanism for formation of twins to release the stress during growth is proposed. Jang et al.[124] have reported that the grain growth in thicker film is expected to give rise to complex faceted lamella twins. In this study, the faceted twin lamellae were observed along vertical and lateral equivalent <111> direction, as shown in Figure 4.5(e). This can be explained by the enhancement of lateral grain growth in thicker film as a result of less competition between columns. The preferred growth orientation along equiaxed <111> direction can be expected by the Drift's model[100].

It is also noticed that reentrant facet angles were formed along the twin lamellae boundaries, as marked by red lines in Figure 4.5(e). The reentrant facet angle, is a byproduct of twin lamellae structure, and has positive effect towards stabilizing the atoms on-site such that it enhances the growth parallel to the twin boundaries, namely twin-assisted growth[119]. Therefore, protrusion growth along the intermediate <110> direction is a result of the competition between the equalized <111> lateral growth and twin lamellae enhanced growth.

Compared with the surface morphology, the protrusions obtained by slanting lateral growth correspond to the hexagram-shaped topography. Consequently, it is believed that the twin lamellae structure in thicker film, with enhanced slanting lateral growth, is the origin for the hexagram-shaped topography.

4.1.4 Temperature morphological evolution

In order to further elucidate this mechanism, the morphology evolution as a function of temperature was further considered. The film growth is a kinetic process, thus it is tightly related with the atom mobility and driving force, since Growth rate = Mobility × Driving force[125], as:

$$v = M \times (\Omega + Wmc) \quad (4\text{-}5)$$

where v is the velocity of crystal growth front and M is mobility function. The driving force has two components, a weighted mean curvature (Wmc) that expresses the decrease in the integral of the specific surface free energy and a volume phase change component, Ω. In pulsed laser deposition, film growth is a non-equilibrium process. The kinetic energies (mobility) of adatoms are determined by the substrate temperature, while the driving forces are regulated by the minimization of surface and interface energy. Therefore, one can assume that the formation of hexagram-shaped topography is the result of insufficient energy of the adatoms to rearrange in a thermodynamically equilibrium configuration. If the mobility of adatoms were high enough to reach the energetically stable site, twins may not be produced and the morphology will go back to normal pyramid-shape structure.

According to this hypothesis, BTO films were deposited with fixed time/number of

pulses (100mins/60000 pulses), deposition rate (10 Hz) and oxygen pressure (100 mTorr), as a function of substrate temperature from 600^{o}C to 1000^{o}C. From a comparison of plane-view SEM, Figure 4.6 shows a full tendency of surface morphology development. As expected for a twin lamellae induced lateral growth, hexagram-shaped topography was observed at 800^{o}C [Figure 4.6(c)]. With increasing temperature, these surface grains eventually coalesced and formed the energetically stable pyramid-shaped grains [Figure 4.6(d)]. With further increase in temperature, larger equaxied hexagonal grains were formed at 1000^{o}C [Figure 4.6(e)]. These results are consistent with prior expectation, where the surface morphology of the film becomes energetically favorable when the mobility of the atom is increased.

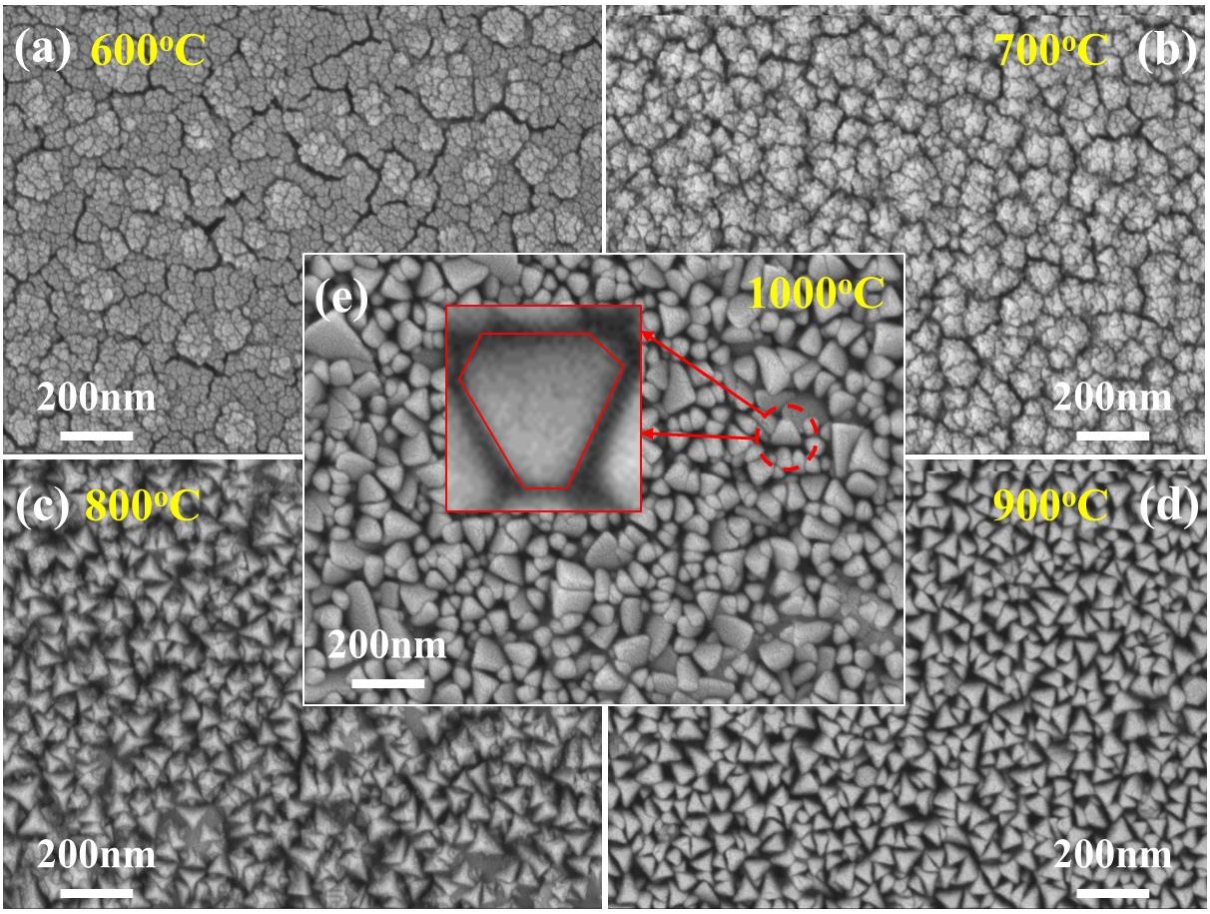

Figure 4.6 Planar views of BTO films show the morphology changes as a function of growth temperature: (a) 600 ℃, (b) 700 ℃, (c) 800 ℃, (d) 900 ℃ and (e) 1000 ℃.

4.1.5 Model of morphology evolution

Accordingly, the above analysis opens the possibility of explaining the morphology evolution as highlighted in Table 4.1. However, it can be also noted that none of these models can be used to fully describe the morphology development process. Therefore, based on integration of these analyses, the whole growth and evolution model can be described as follows: (i) *Nucleation*: at the beginning of the growth, (111)-faceted BTO nuclei were favorably formed on the Pt surface to minimize the surface and interfacial energy[89-93], as illustrated in Figure 4.7(a). The strain caused by the lattice mismatch can be accommodated by elastic deformation as the film is thinner than the critical thickness[126]. (ii) *Growth*: during the initial stages, epitaxial growth occurred where grain was mainly grown along the thickness direction as a result of restriction from neighboring grains and substrate. Subsequently, the film assumed a columnar structure while maintaining the pyramid shape surface morphology given by (111) orientation [Figure 4.7(b)]. (iii) *Coarsening*: with increasing film thickness, the influence of the substrate would decrease and a competitive grain growth between different orientations occurred. Faceted twin lamellae structure was formed as grain growth continued, where the resultant reentrant facet edge further enhanced the parallel growth along twin boundaries. The competition between equiaxed <111> growth [Figure 4.7(c)] and reentrant angle aided growth resulted in an enhanced slanted lateral growth along <110> direction. Topology changes from the pyramid to the hexagram as the lateral growth occurs [Figure 4.7(d)]. (iv) *Surface energy anisotropy*: Once the film thickness increased, the grain structure with high aspect ratio attempts to achieve equiaxed configuration which is more energetically stable. Perovskite has the lowest surface energy on

{100} plane [127]. As the grain growth occurs along (111) direction, the surface consists of {100} planes to minimize the surface energy. Consequently, the surface would be (111)-faceted single crystal rod as shown in Figure 4.7(e).

In summary of section, I studied the microstructure and growth mechanism of BTO thick films deposited on platinized silicon substrate by pulsed laser deposition. It is observed that the hexagram grain morphology evolution existed in a highly textured $BaTiO_3$ thick film. The evolution of surface morphology was discussed within the framework of SZM and DST models. The growth mechanism was further modeled by considering anisotropy of surface energy and the formation of twin lamellae structure. This work provides new insights toward the growth and microstructure evolution of BTO thick films. It is believed that this comprehensive understanding of the growth mechanism of BTO films will improve the process compatibility.

Table 4-1 Characteristics of different type of models for explaining the microstructure and morphology evolution.

Model	SZM	DST	Twin Lamellae
Factor	Ts/Tm	Roughness (Height & lateral)	Local nanostructure
Prediction	Microstructure	Surfacial characteristics	Grain coalescence
Features	Columnar	Hexagram grains	Protrusions
Mechanism	Atomic diffusion	Non-local shadowing effect & atomic diffusion	Reentrant facet angle assisted lateral growth

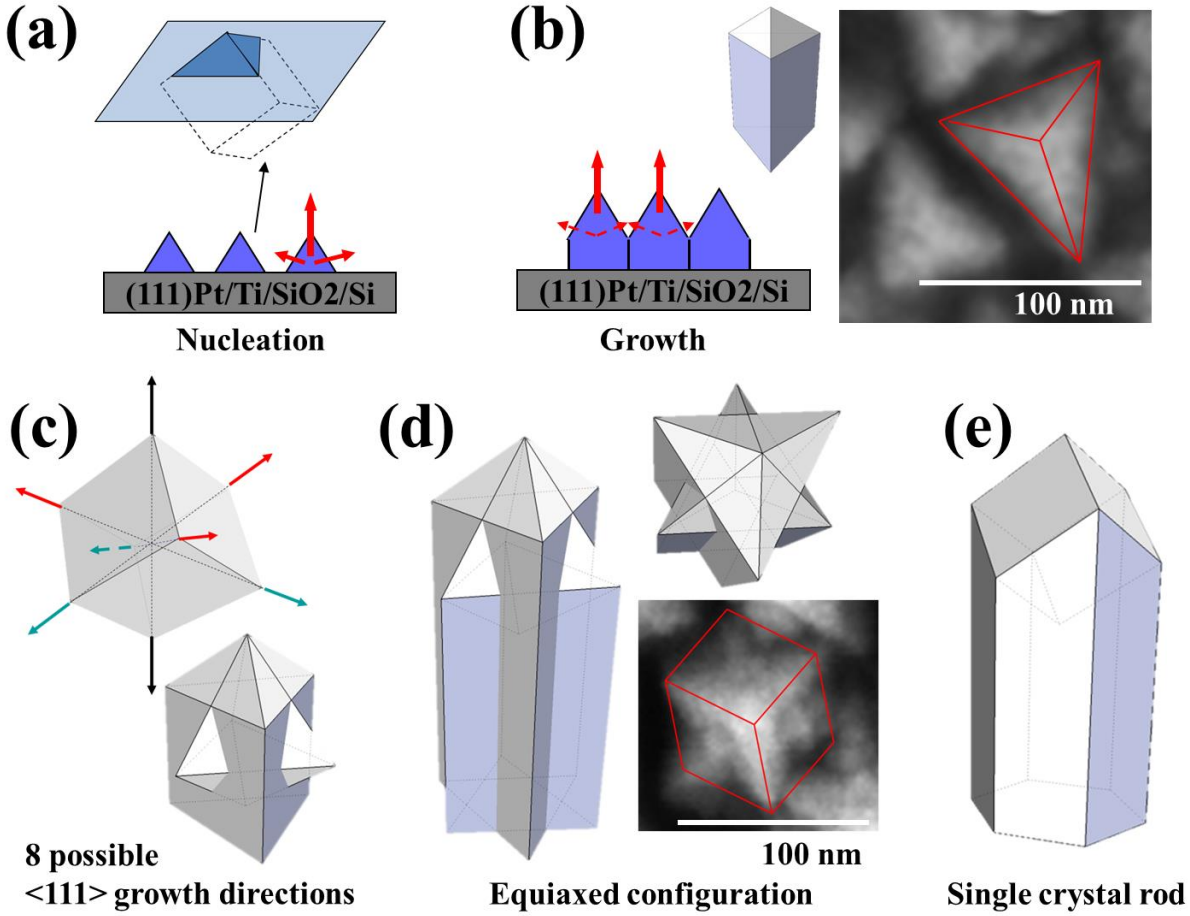

Figure 4.7 Schematic of growth mode for BTO film: (a) Nucleation step, (b) Growth in thin film, (c) Coarsening (Lateral growth), arrows indicate 8 possible <111> growth directions: 2 normal-to-plane (black), 3 above the plane (red) and 3 below the plane (blue) along the diagonal axis. (d) Equiaxed grain growth with coarsening in thick film, (e) Expected grain shape.

4.2 Growth of CFO/PZT ME composite array with multi-orientation

In the two phase composites magnetoelectric thin films, the morphology stability was controlled by the orientation of substrate or annealing condition. Because magnetoelectric coupling performance is strongly related to the nanostructures of the consecutive constituent thin films, it is necessary to check the nanostructure of the composites thin films. Recently developments in thin film technologies offer the opportunity to control the grain size, shape, orientation and distribution precisely through continuous film or well-ordered patterns. In particular, by controlling the film orientation, the anisotropy ferroelectric and/or ferromagnetic properties may change accordingly, which provide a great potential for tunable ME response and on-chip functional devices. In this section, a novel hybrid deposition method was introduced to investigate the grain orientation control in a well-ordered magnetoelectric nanocomposite array.

4.2.1 Well-ordered thin film array via Hybrid deposition

Patterns can be made by various technologies such as focused ion beam, e-beam lithography or photolithography. However, these bottom-up methods involves complex and tedious process and are very expensive. In addressing these problems, a novel hybrid synthesis method was developed.

This method based on the Aerosol Jet® deposition technology, which has been shown to be highly promising for mask-less cost-effective production of thick composite films. The ability of this technology is to directly print solution based inks in desired patterns under atmospheric condition without the need for lithography or vacuum deposition techniques.

Figure 4.8 shows the schematic and picture of the Aerosol Jet® deposition system. During deposition, the ink was first aerosolized in the ultrasonic atomizer and then nitrogen gas carried the aerosols to the deposition nozzle, where the sheath gas (a secondary nitrogen stream) focuses the material into fine lines and draws the specific features defined by the CAD. Structures with specific shape and geometry can be drawn using any commercial CAD software and then converted into a readable tool path.

In this study, the composition of the stock solution was $Pb_{1.1}(Zr_{0.6}Ti_{0.4})O_3$ (PZT) with a concentration of 0.4M to form the ink. A well-ordered PZT pattern was printed onto Pt(111)/Pt/SiO_2/Si substrates (Inostek, Seoul, Korea) at room temperature with velocity of 5mm/s. Pyrolysis of the as-printed samples were taken on a hot plate at 300 ^oC for 3mins. Subsequently, all the samples were post annealed at 725^oC for 30mins in a rapid thermal anneal furnace to control the crystallization and film orientation. Then a layer of PZT and CoF_2O_4 (CFO) film was deposited subsequently on the patterned substrate in vacuum chamber with KrF (λ=248nm) excimer laser at energy density of 2.0~3.0J/cm^2 and 10Hz repetition rate. Substrate temperature was set at room temperature with 1mTorr oxygen pressure during deposition. In-situ post annealing was conducted at 650^oC at 3Torr background pressure after deposition. Crystallinity and preferential orientation of the hybrid films were investigated by X-ray diffraction (X'Pert High Score Plus). The microstructure and thickness of the films were determined by field emission-scanning electron microscopy (FE-SEM; LEO Zeiss 1550). The piezoelectric/magnetic domain structure was observed by piezoelectric force microscopy (PFM) and magnetic force microscopy (MFM) (Dimension Icon AFM, Bruker) in the contact mode and tapping-lift mode, respectively.

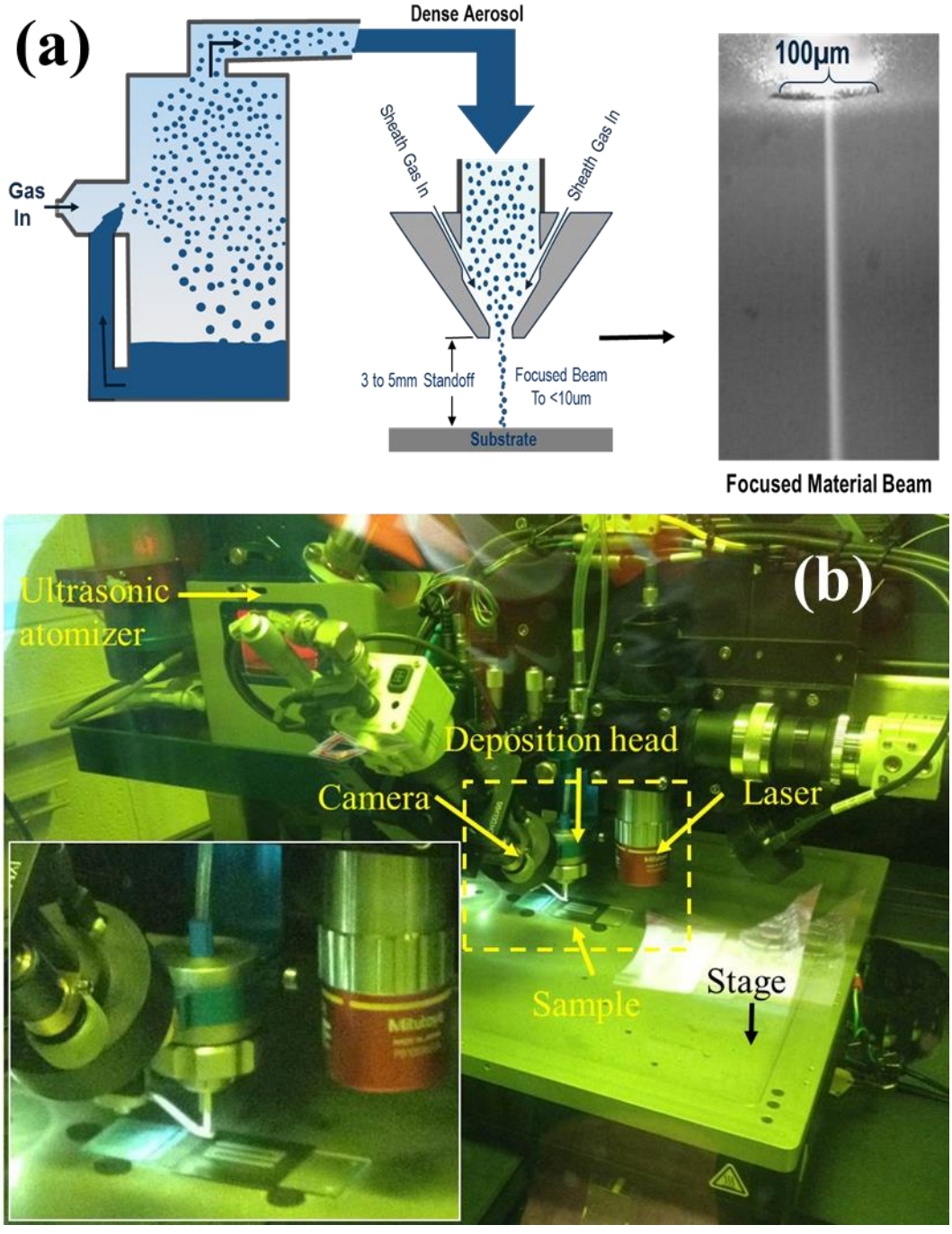

Figure 4.8 (a) Schematic diagram of the working principle of Aerosol-jet deposition process; (b) Picture of the Aerosol Jet® printer with deposition head aligned on a Ni foil plate. Inset shows the magnified image of the deposition head and pre-printed patterns on Ni.

Figure 4.9 illustrates the result of as-printed PZT array pattern on pt-coated silicon. Part (a) shows schematic and optical microscopy images of pre-deposited PZT film with ordered pattern. The well-arranged arrays consist numbers of square patterns with dimension 1μm×1μm. After printed on the substrate, the as-deposited pattern was pyroliyzed at 300^{o}C for 3mins and annealed at 725^{o}C for 30mins. X-ray diffraction pattern shows that highly (100) textured PZT film are formed after thermal treatment.[Figure 4.9(b)] This indicates that the pattern with different shape can be printed as desired, and can be controlled with preferred orientation by post thermal treatment.

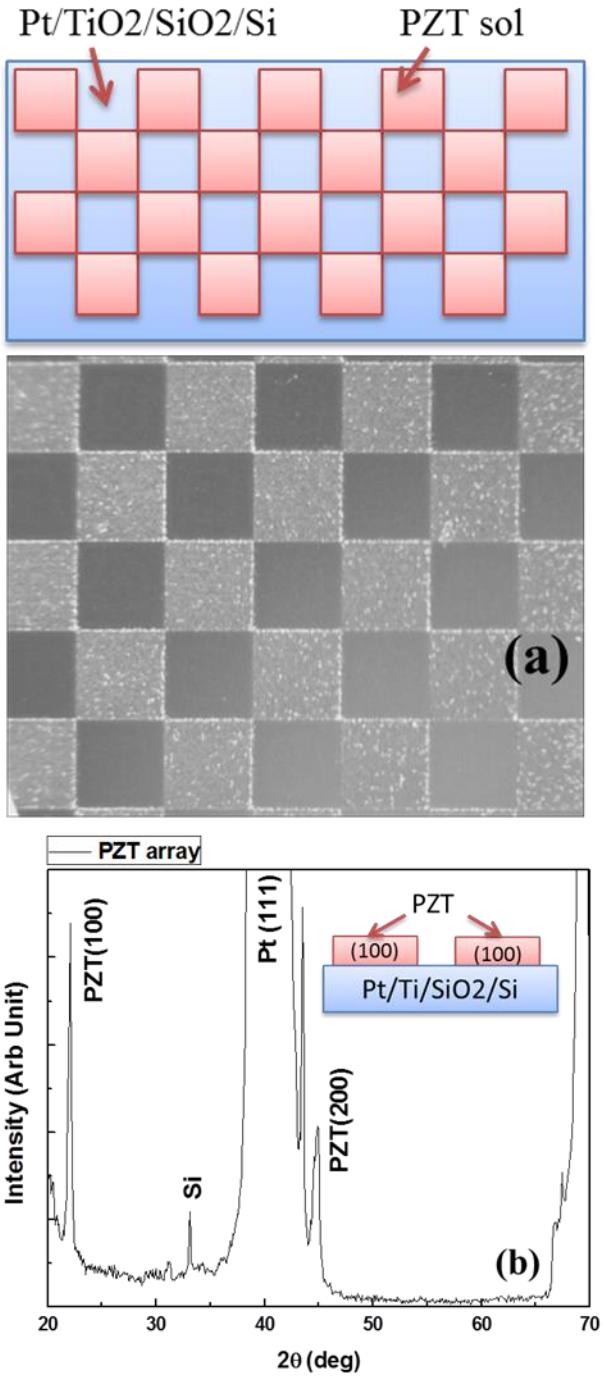

Figure 4.9 (a) Schematic and optical microscope image of printed PZT array; (b) X-ray diffraction pattern of PZT array after thermal annealing.

4.2.2 Orientation control via tempelate growth

It is known that film growth is tightly related with the substrate, grain orientation can be controlled by pre-deposited buffer layer with different orientation. In order to understand the substrate effect on film growth, PZT film was deposited on Pt-coated silicon substrates with and without pre-deposited (100) orientated PZT template. As shown in Figure 4.10(a) and (b), notable differences between these two samples can be found: (1) Film grown on the seed layer illustrates highly (100) textured orientation, whereas the template-free film shows multiple peaks. (2) It is noticed that the predominant peaks of the multi-oriented film are (100) and (111) orientation. These results demonstrate that, by manipulating the growth orientation of the template layer, one is expected to obtain a well-ordered nanocomposite film with controlled orientation at selected area, as illustrated in Figure 4.10(c). Thus, a subsequent layer of PZT film was deposited on the (100) oriented PZT array using pulsed laser deposition. Figure 4.10(d) shows the XRD pattern of the hybrid deposited PZT film. The film possesses two dominant peaks of (100) and (111), which is compatible with the hypothesis on orientation control as described in Figure 4.10(c).

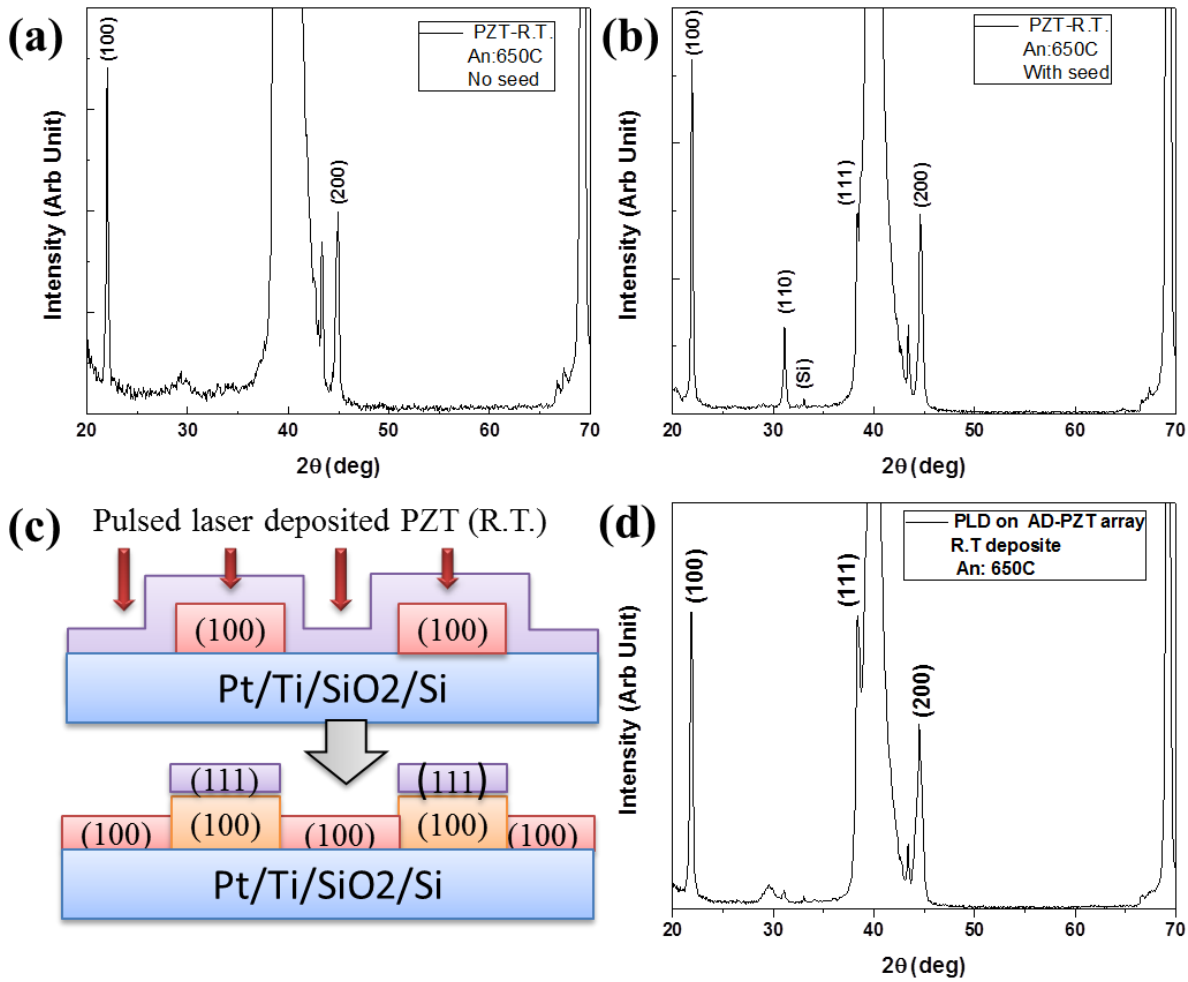

Figure 4.10 X-ray diffraction pattern of PZT film (a) growth without template; (b) with template; (c) Schematic of film orientation variation on PZT array template; (d) XRD of the hybrid deposited PZT film.

4.2.3 ME nanocomposite array

Next, a ME nanocomposite array was obtained with a layer of CFO film deposited on the hybrid PZT template. Figure 4.11 shows the schematic diagram and SEM images of the as-deposited CFO/PZT nanocomposite array. From the figure, one can clearly identify the grain shape difference between template area (Positive region) and exposure area (Negative region). Figure 4.11(b) and (c) show the microstructure of the as-grown CFO grains on positive area. Two different grain geometries (triangular and square) were identified, indicating the film grown on positive area has predominant orientation of (111) and (100). Figure 4.11(d) and (e) illustrate that CFO film with square and rectangular shaped grains [(100) preferred orientation] are dominant across the negative region. These results match well with the orientation of the PZT template layer as shown in Figure 4.10, representing a good following of the crystallization with respect to the buffer layer.

It is noticed that the grain size is also sensitive to template layer. Films on positive region possess larger grain size that that of negative area. Both surface and interfacial energy plays an important role toward grain growth. PZT buffer layer with multi-orientation not only serves as nucleation sites for the formation of CFO grains, but also induces lattice mismatch. As evident from Figure 4.11, without the template layer, the CFO interfacial region is notably stressed and illustrates smaller grain size. The compressive stress presumably comes from PZT buffer layer with different orientation. To minimize interfacial energy between grains and the buffer layer, grains grown into a columnar morphology with increasing thickness, as shown in Figure 4.11(f) and (g). These observation clearly demonstrate that: (1) the regularity of the PZT grain orientation controlled by pre-deposited buffer layer formed after PLD

deposition and post-annealing; (2) this growth regularity was passed onto the CFO columns which subsequently grown on the PZT array.

Note that, in addition to work as a patterned template, PZT array plays several important roles: (1) Printed PZT template can possess various preferred orientations via thermal treatment, which is an advantage for the post-deposit film orientation control. Films with controlled orientation further provide the way of tailoring the physical properties across the composite. (2) PZT is a well-known piezoelectric material with good electrical performance, which can serve as an active layer to generate charge or domain motion with induced strain across the ME composite.

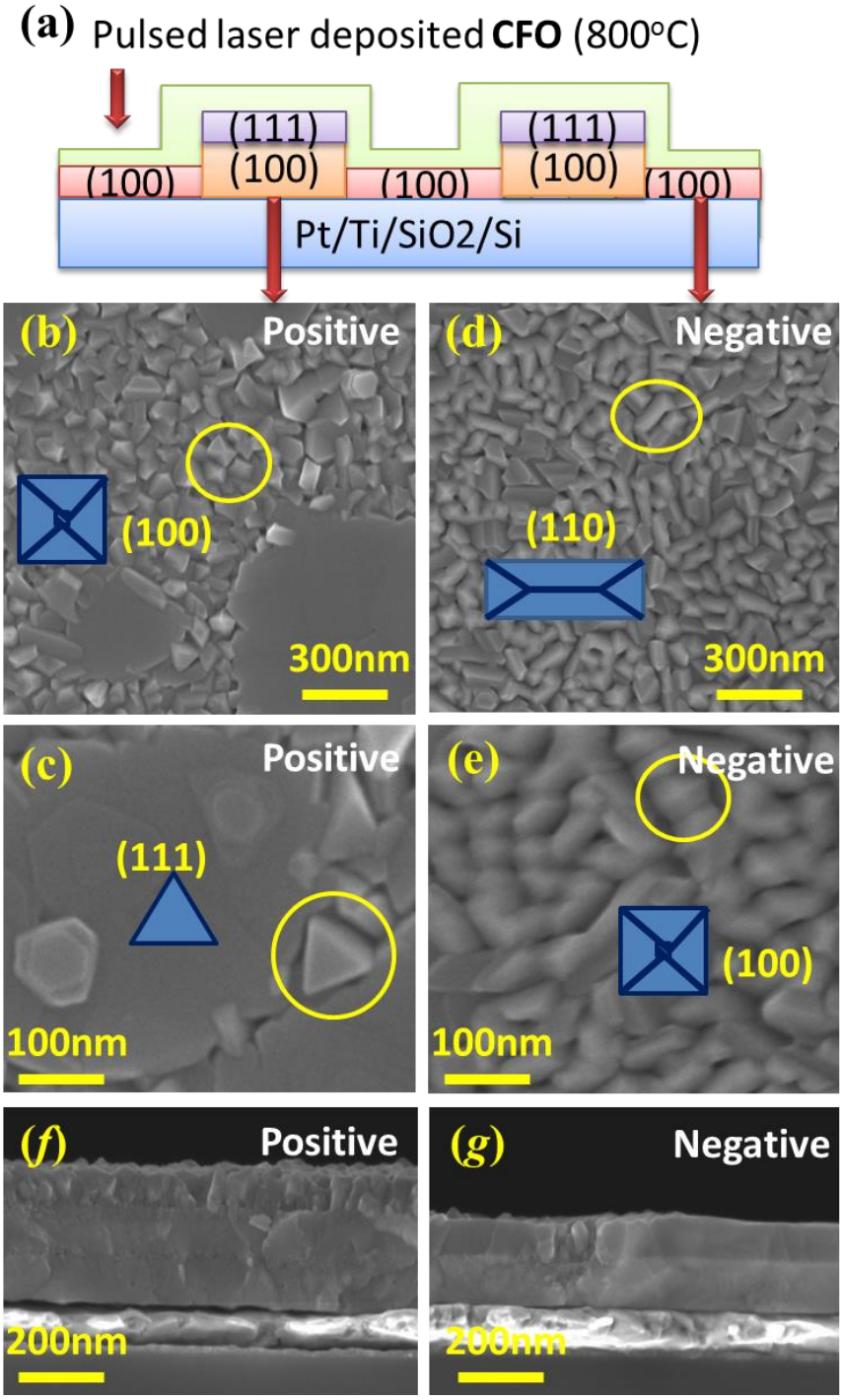

Figure 4.11 (a) Schematic of hybrid deposited PZT/CFO ME composite array; (b) and (c) SEM images of CFO grain growth on positive area of the PZT array; (d) and (e) SEM images of CFO grain growth on negative area of the PZT array; (f) and (g) Cross-section view of CFO film grow on positive and negative area of the PZT array.

MFM and PFM were then used to investigate the magnetic and ferromagnetic domain structure in the CFO/PZT ME composite array, which can be also used to understand the structure-property relationship. For this purpose, the sample was bonded on a conductive metal disc with silver epoxy, which serves as the bottom electrode for the PFM measurement. The topographic AFM images are shown in Figure 4.12(a) and (b) and the corresponding magnetic domain phase images are listed in Figure 4.12(c) and (d). From the AFM images, the negative area was smoother than that of positive area, showing a lower degree of roughness. From the MFM images, it is noticed that the magnetic domains in positive region [Figure 4.12(c)] are in similar size with respect to corresponding grains, whereas magnetic domains in negative region [Figure 4.12(d)] show a cluster-like configuration with larger size. This magnetic domain variation can be devoted to the grain orientation difference and the resultant magnetization anisotropy.

These results demonstrate that one can manipulate the physical performance of the nanocomposite film through control of nanostructure.

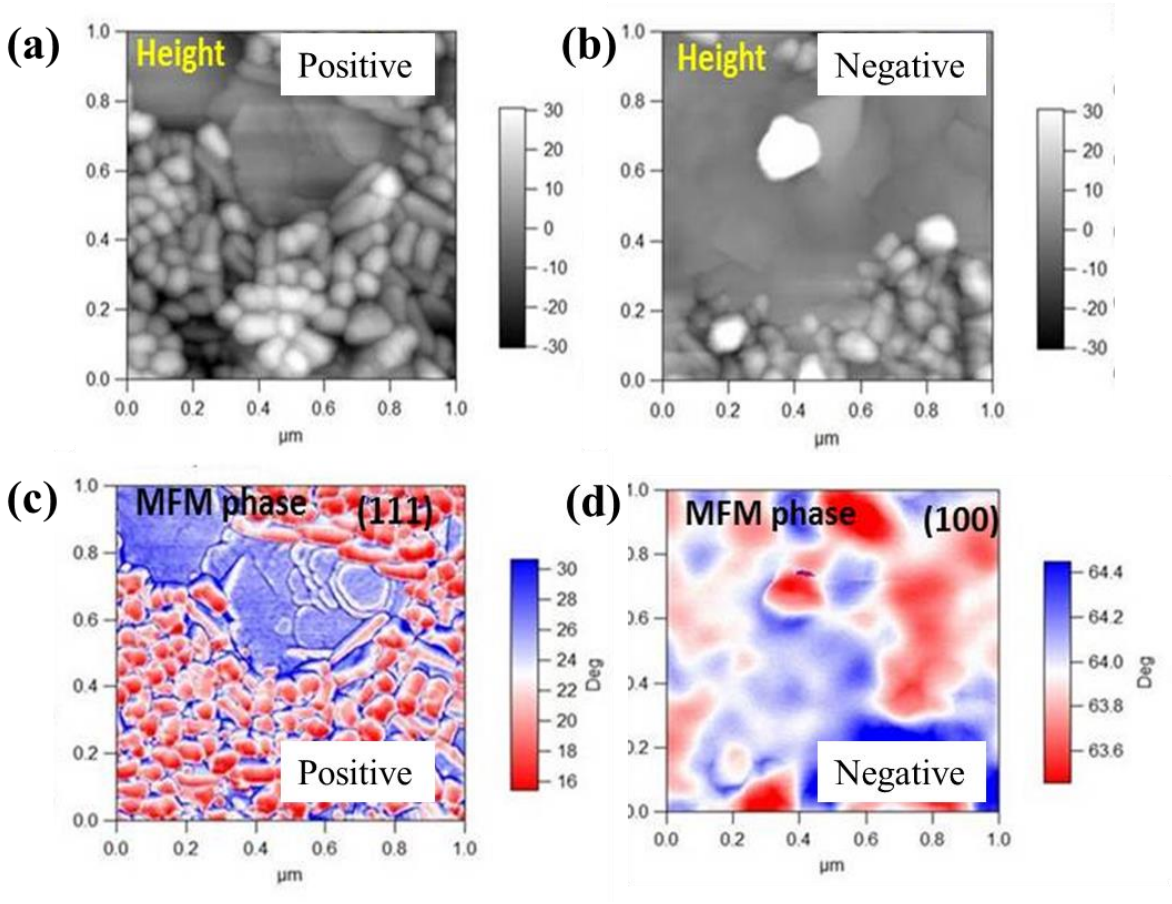

Figure 4.12 Topography and magnetic domain images on the CFO/PZT ME composite array surface of (a) and (c) positive area; (b) and (d) negative area.

Figure 4.13 shows the piezoelectric response (PR) data of the negative region through PFM mapping. A Bruker Dimension Icon with a conductive diamond coated silicon cantilever tip (DDESP-FM-10, Bruker) was used to conduct piezoresponse force microscopy (PFM). High speed PFM was used in resonance enhanced mode at an operating frequency of ~520 kHz. The deflection sensitivity of the tip was 97.47 nm/V. Interestingly, the PR signal (both phase, amplitude and data as shown in Figure 4.13(b)~(d)) obtained from the film surface illustrate significant contrast, indicating the film is strongly piezoelectric. However, the surface of the film is CFO, non-piezoelectric phase, which should have no piezoelectric response under applied electric field. Specifically, the PR amplitude data with highlighted region in small grains indicate stronger response, whereas region with larger grains does not have significant contrast. It is noticed that, grain size on the other side reflect different orientation, and the piezoelectric response must originate from the bottom PZT layer. Thus, these PFM images demonstrate that the domain distribution of the composite film is tightly related to the grain orientation. Moreover, PR amplitude image indicate that magnetic grain with smaller size has better elastic coupling in layered ME composite than larger ones.

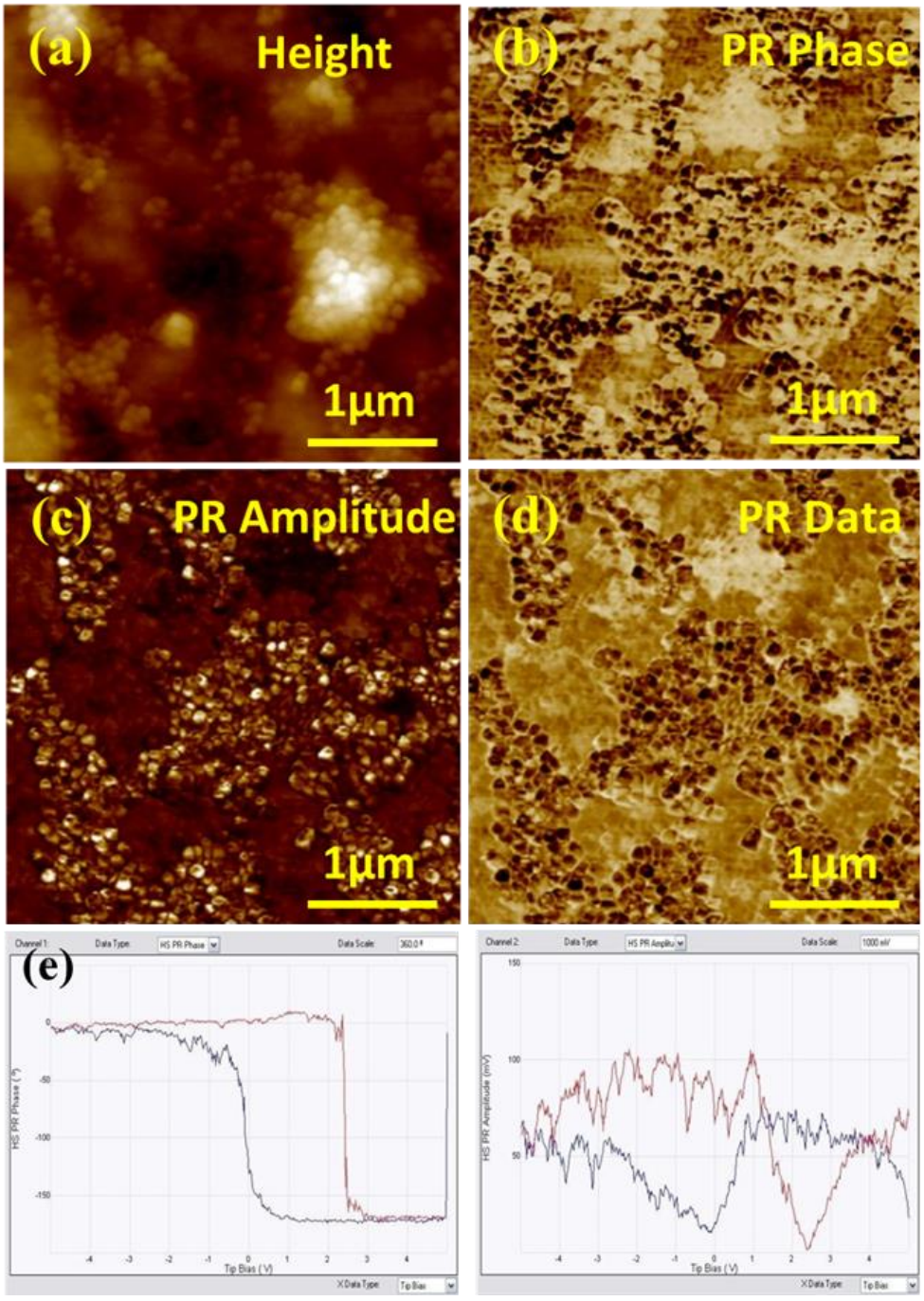

Figure 4.13 AFM and PFM study of negative area: (a) AFM topography image of an area of 4µm×4µm; (b),(c) and (d) the corresponding piezoresponse phase, amplitude and data image; (e) the local piezoelectric hysteresis loops measured in negative area: left part shows the phase angle variation under tip bias sweep, right part shows the amplitude variation under tip bias sweep.

In order to get a better insight on the local piezoelectric properties of the small grain regions, piezoelectric hysteresis loop was performed at selected point on the film surface as a DC tip bias is swept with a constant AC bias of 4V. Figure 4.13(e) shows the PR phase and amplitude variation under applied DC tip bias. The average amplitude of the small grain could reach up to 70 mV. Meanwhile, the PR phase shows a clearly variation of 180 ^{o}C during electric field switching, suggesting that the film is highly polarizable and the ferroelectric domains are easily switched. It is also noted that there is a horizontal shift of the hysteresis loop toward positive bias, which can be attributed to the formation of space charges at the film/electrode interface.

In conclusion, pre-deposited PZT template has been shown to be capable of controlling grain orientation and size of post-deposited CFO films. Both piezoelectric and magnetic domains were found to illustrate different structure and response according to grain orientation. These results confirm controlling of piezoelectric or magnetic properties via domain engineering. Also, large piezoresponse can be detected from the surface of non-piezoelectric phase across the CFO/PZT composite. These observations provide a new method to identify the coupling between the magnetic phase and piezoelectric phase in composite ME thin films.

4.3 Interfacial effects in magnetoelectric thin/thick composite films

ME effect is a product property governed by the elastic coupling occurring at the interface of piezoelectric and magnetostrictive phases. ME coupling in layered composites can be significantly affected by the strain transfer efficiency along the contact interface in the composites. A comprehensive understanding of the interfacial properties of ME thin/thick composite films will require systematic experimental investigations with varying structure and microstructure to develop a database that can be used to develop detailed computational models. Accordingly, in this section, two different ME composite thin/thick films were synthesized and analyzed. Using sol-gel deposition (SGD) and pulsed laser deposition (PLD) techniques, PZT/CFO/PZT thick composite film and BTO/CFO thin film heterostructure were synthesized to understand the nature of elastic coupling. The schematic diagram and microstructure of these as-grown structures are illustrated in Figure 4.14.

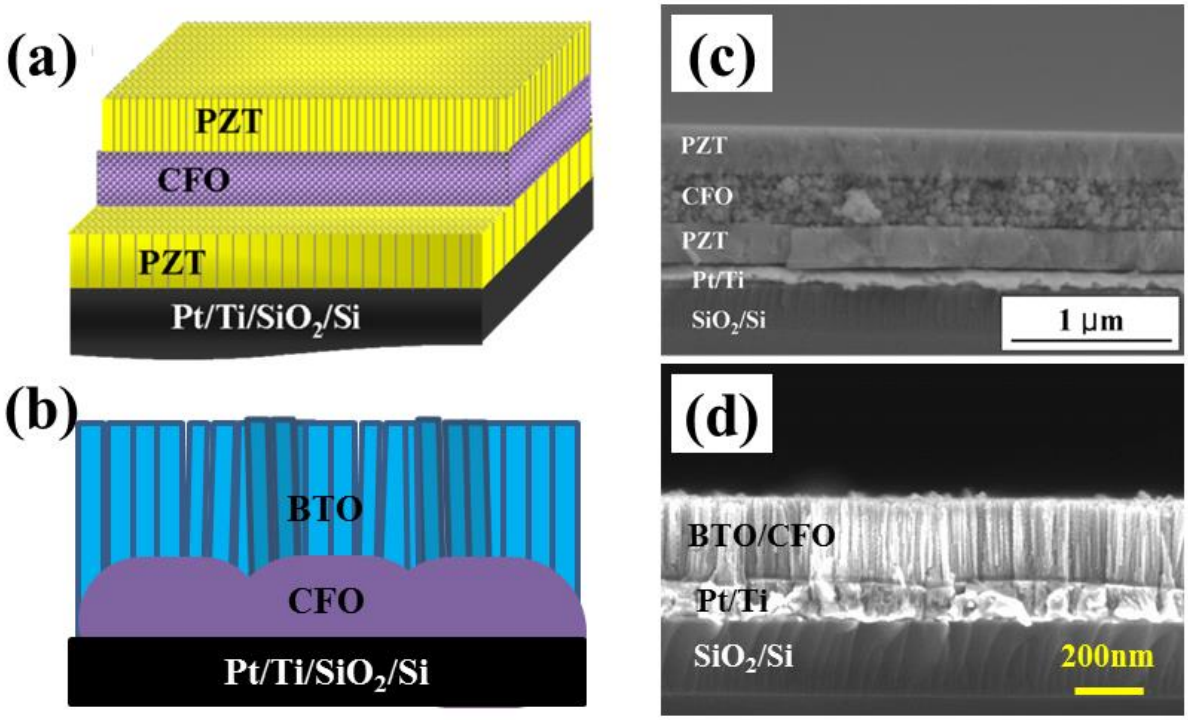

Figure 4.14 Schematic diagram and cross-section SEM image of (a)(c) PZT/CFO/PZT composite thick film; (b)(d) BTO/CFO composite thin film on $Pt/Ti/SiO_2/Si$ substrate.

4.3.1 Trilayer PZT/CFO/PZT composite thick film

PZT and CFO solution were synthesized by sol-gel process. For the PZT solution (0.4M), lead(II) acetate trihydrate [$Pb(CH_3CO_2)_2\ 3H_2O$] was dissolved in 2-Methoxyethanol [$CH_3OCH_2CH_2OH$]. Zr-propoxide [$Zr(OCH_2CH_2CH_3)_4$] and Ti-isopropoxide {$Ti[OCH(CH_3)_2]_4$} were diluted in n-propanol (n-C_3H_7OH.) and chelated by acetyl acetone ($CH_3COCH_2COCH_3$). The lead-methoxyethanol solution was added to the Zr-Ti solution and stirred. A 1:1 H_2O/n-propanol solution was added to the stock solution to partially hydrolyze it. The composition of the stock solution was $Pb_{1.1}(Zr_{0.6}Ti_{0.4})O_3$ with a concentration of 0.4M. For the CFO solution, Co-nitrate hexahydrate [$Co(NO_3)_2\ 6H_2O$] and Fe-nitrate nonahydrate [$Fe(NO_3)_2\ 9H_2O$] were dissolved in ethylene glycol [$HOCH_2CH_2OH$]. Citric acid [$C_3H_4OH(COOH)_3$] was added as a stabilizer. The composition of the 0.2M stock solution was $CoFe_2O_4$. Both of the stock solutions were aged for 24 hrs. Each layer was synthesized by spin-coating at 3000 rpm for 60 sec, followed by pyrolysis at 300^oC for the 5 min in air and post-annealing at 650^oC for 15 min. Thick composite film was synthesized by coating multiple layers on platinized silicon substrate. The final thickness of the composite was ~1μm as indicated in Figure 4.14(c).

Figure 4.15 shows the cross-sectional TEM images of the PZT/CFO/PZT (PMP) composite film deposited on Pt/Ti/SiO_2/Si substrate. The film possesses dense microstructure for each phase and good adhesion along the interface. Diffraction patterns illustrate that both PZT and CFO were well crystallized without any trace of amorphous phase, as shown in the inset of Figure 4.15(a). Interestingly, it is found that PZT layers exhibited columnar structure while the CFO layer had granular structure. Columnar PZT films have been typically

observed on other substrates but it is quite unusual that a dense columnar film was found to grow on top of the granular CFO layer. It is well-known that heterogeneous nucleation and growth of PZT film on platinized Si substrates lead to columnar structure.[11] The nucleation and growth of the CFO layer was homogenous which resulted in a granular microstructure. PZT film grown on the granular CFO film will have lattice mismatch which is expected to drive the film to form similar columnar structure as that for PZT on Pt surface.

In order to further elucidate the growth mechanism along the pervoskite and spinel interface, the local nanostructure of the interfacial region was investigated. High resolution TEM (HRTEM) image [Figure 4.15(b)] was taken from the interface marked by dashed line in Figure 4.15(a). The interface was coherent and no distinct structural defect was observed. Based on the diffraction patterns, the lattice parameters for CFO and PZT were estimated to be 8.37Å and 4.08Å, respectively. There was only ~2.5% lattice mismatch between the two layers [PZT (100) and CFO (200)], which led to continuous structure. The absence of structural defect, as identified by the HRTEM image, confirms the lattice accommodation between PZT (100) and CFO (200). This indicates that the PZT was locally nucleated and grown on the CFO layer with columnar structure.

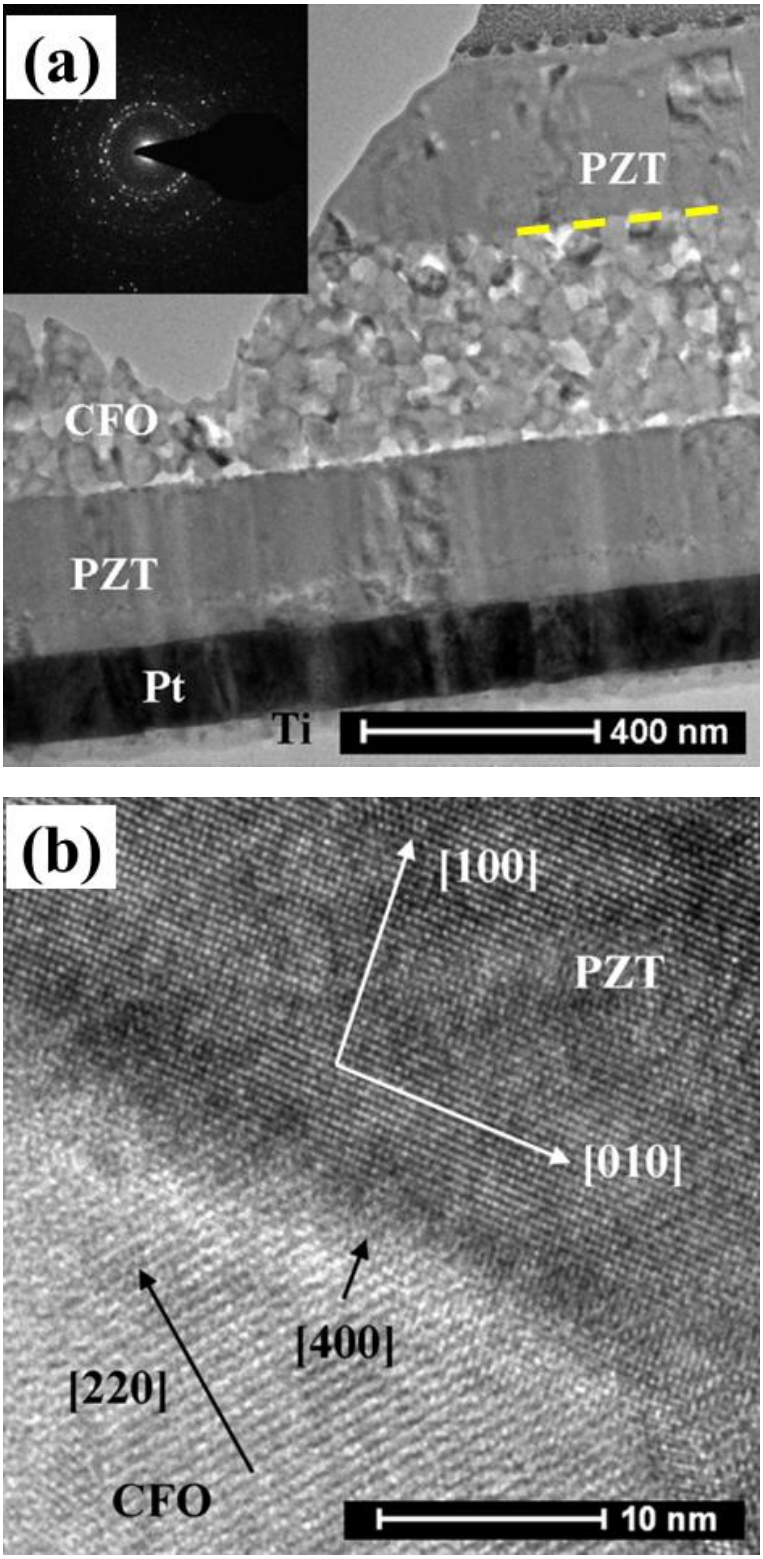

Figure 4.15 (a) Cross-sectional TEM image and (b) High resolution TEM image of PZT/CFO/PZT composite thick film on Pt/Ti/SiO_2/Si substrate.

Electrical properties and ME voltage coefficient were characterized on this thick film composite to quantify the effect of interface on coupling coefficient. Figure 4.16(a) shows the polarization–electric field (*P*-*E*) curves for composite film at the frequency of 1 kHz. Remnant polarization (P_r) and coercive field (E_c) increased with increasing electrical drive. At an applied electric field of 200 kV/cm, the magnitude of P_r and E_c were measured to be 0.28 μC/cm^2 and 74.4 kV/cm, respectively. The poor ferroelectric hysteresis loops were mainly due to (i) inactive CFO layer during electrical driving, and (ii) lossy interfaces derived from elemental diffusion. Both are explained in Figure 4.16(b), which shows the variation of dielectric constant and loss as a function of frequency. The inactive CFO layer under electrical driving led to the low dielectric constant value. Loss factor possess higher value at low frequency and drops with increasing frequency. This phenomenon mainly results from the space charge effect at the lossy interfaces, as discussed in pervious study.[12]

Next, the ferromagnetic property of the composite was measured by vibrating sample magnetometer (VSM) at room temperature, as shown in Figure 4.16(c). The in-plane M-H hysteresis loop was found to be similar to that previously reported composites films, with remnant magnetization of 73 emu/cm^3 and coercive magnetic field of 1.7 kOe. Finally, after poling the PMP composite film under the DC electric field of 200 kV/cm, the ME voltage coefficient as function of H_{DC} was monitored by lock-in amplifier, as shown in Figure 4.16(d). The maximum ME output voltage coefficient was measured to be 26 mV.cm^{-1}.Oe^{-1} at H_{DC}= ~ 1.7 kOe. This demonstrates reasonable ME coupling for the PMP structure. The PMP laminate without internal electrodes could be considered a leaky composite due to the leakage channels formed by interface diffusions. However, these leakage channels are short length

and disconnected from the top and bottom electrodes. The poling direction and leakage channel direction are perpendicular to each other so it is not a major factor in the poling process. But, the presence of semi-conducting M layer shields the field applied onto the bottom P layer and thus affects the poling degree. Another factor that influences the ME coefficient of the P-M-P structure is related to the elastic deformation. Intuitively, the applied magnetic field will result in radial deformation of the M-layer, but this deformation is constrained by the presence of top P-layer.

The advantage of the PMP structure is the simplicity in its fabrication. Further improvement in the properties can be obtained by enhancing the conductivity of the M-layer without having detrimental effect on the piezo-magnetic coefficient. Also, the thickness ratio of the P-layer with respect to M-layer can be optimized. In summary: (1) the poor effective ferroelectric value of the PMP structure was related to the lossy interface; (2) ME behavior strongly depends on the mechanical and electrical impedance matching between the ferroelectric and ferromagnetic phases; (3) PMP structure with improved ME coefficient can be obtained by reducing the clamping effect.

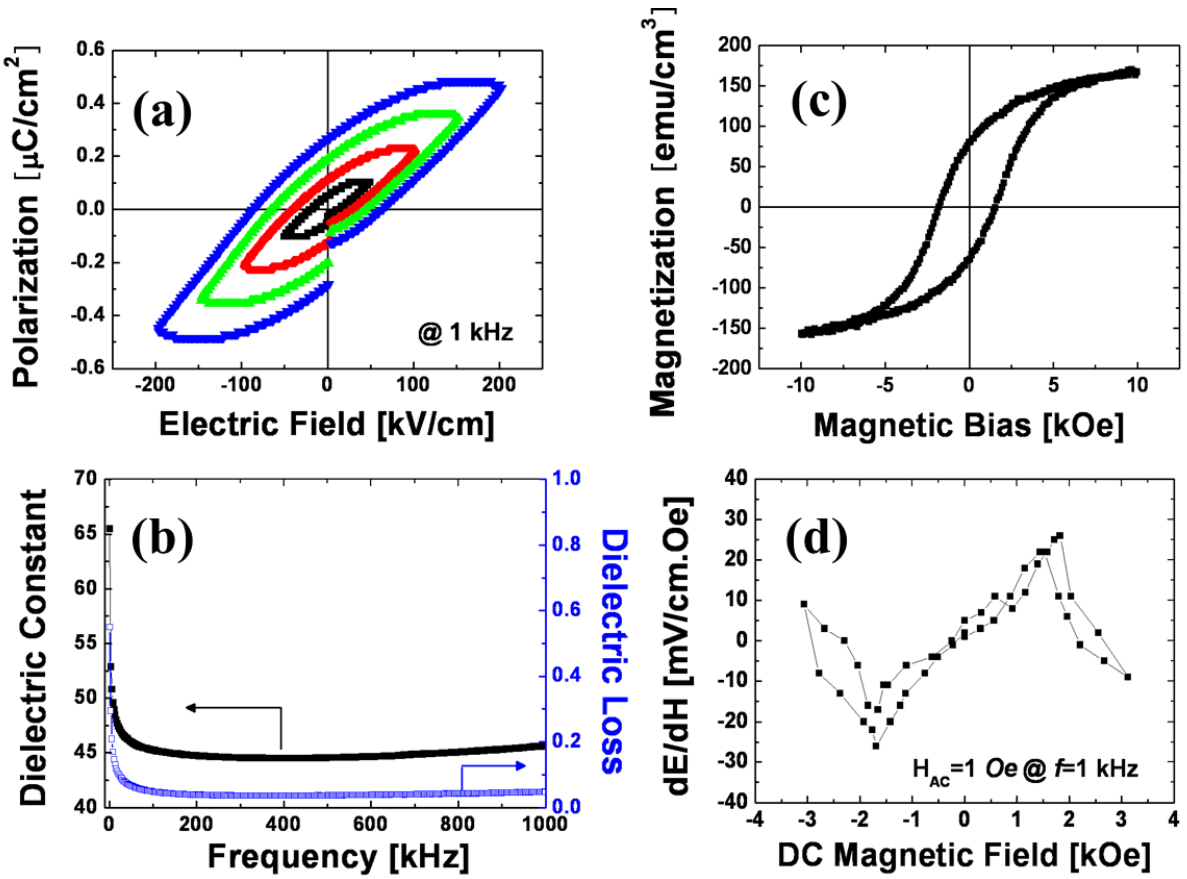

Figure 4.16 Ferroelectric, ferromagnetic and magnetoelectric properties of the composite film: (a) P-E curve, (b) dielectric constant and loss, (c) M-H curve, (d) ME responses as a function of DC magnetic field under constant AC magnetic field.

4.3.2 Bilayer BTO/CFO thin film heterostructure

Bilayer BTO/CFO heterostructure was developed by using pulsed laser deposition. A KrF excimer laser beam (λ=248nm) was directed onto a rotating BTO/CFO target in order to produce a plume consisting of ions and clusters as the precursors for film growth. The platinized Si substrate was mounted on the holder placed at a distance of 15 cm from the target, after it was ultrasonically cleaned with acetone and ethanol. The laser frequency was maintained at 2.5~3 J/cm^2 with a 10Hz repetition rate. The substrate temperature and oxygen pressure were kept at 800^{o}C and 100 mTorr, respectively. As-grown CFO films were treated with ion bombardment for various times before BTO growth, namely ion-bombardment-assisted deposition (IBAD). All films were annealed in-situ at deposition temperature for 15 mins and cooled to room temperature afterward. The final thickness of the heterostructure was ~200nm as shown in Figure 4.14(d).

Ion-bombardment-assisted deposition (IBAD) has been previously used to improve the adhesion, releasing the build-in strain during PLD, and tailoring the surface morphology of the as-grown films. Utilizing IBAD for the layered ME heterostructure offers a unique means for controlling the film interface and subsequently electrical and magnetic properties. In this study, we utilized IBAD on as-grown CFO film surface with different time intervals to alter the interfacial properties of the BTO/CFO thin film heterostructure.

Figure 4.17 shows the TEM images of the IBAD treated BTO/CFO heterostructure for 10mins deposited on Pt/Ti/SiO_2/Si substrate. From the cross-section in Figure 4.17(a), one can distinguish the bottom electrode Pt, a thin layer of CFO (~10nm), and the top BTO layer (~200nm) with columnar structure, from bottom to top respectively. The interface between

the BTO and CFO was continuous, while the columns extended through the entire BTO film. The columns terminated with sharp tops and were found to exhibit lateral structures with respect to each other. This columnar structure matches well with description to zone II in SZM model, where regular arrangement of uniform columns appears at the range of T_s (substrate temperature)/T_m (melting temperature of as grown materials)<0.5-0.55[13].

To further reveal the interfacial properties, the local nanostructure of the interfacial region was investigated by HRTEM as shown in Figure 4.17(b). The interface was coherent along both BTO/CFO and CFO/Pt, which is highlighted by the dashed line. FFT pattern further confirms that majority of the CFO film was grown epitaxially from the substrate along <111> orientation, inset in Figure 4.17(b). Although some defects were observed in BTO film, the general growth direction of the column were determined to be <111> from the FFT pattern. However, instead of smooth surface, faceted CFO grain was formed with a plane parallel to the substrate surface. The inclined facet was measured to have an angle of ~50^o along the normal line of the substrate, which is similar to the angle between ion bombardment direction and the normal line of the substrate. Thus, this faceted structure may have arisen from the ion-bombardment-assisted deposition.

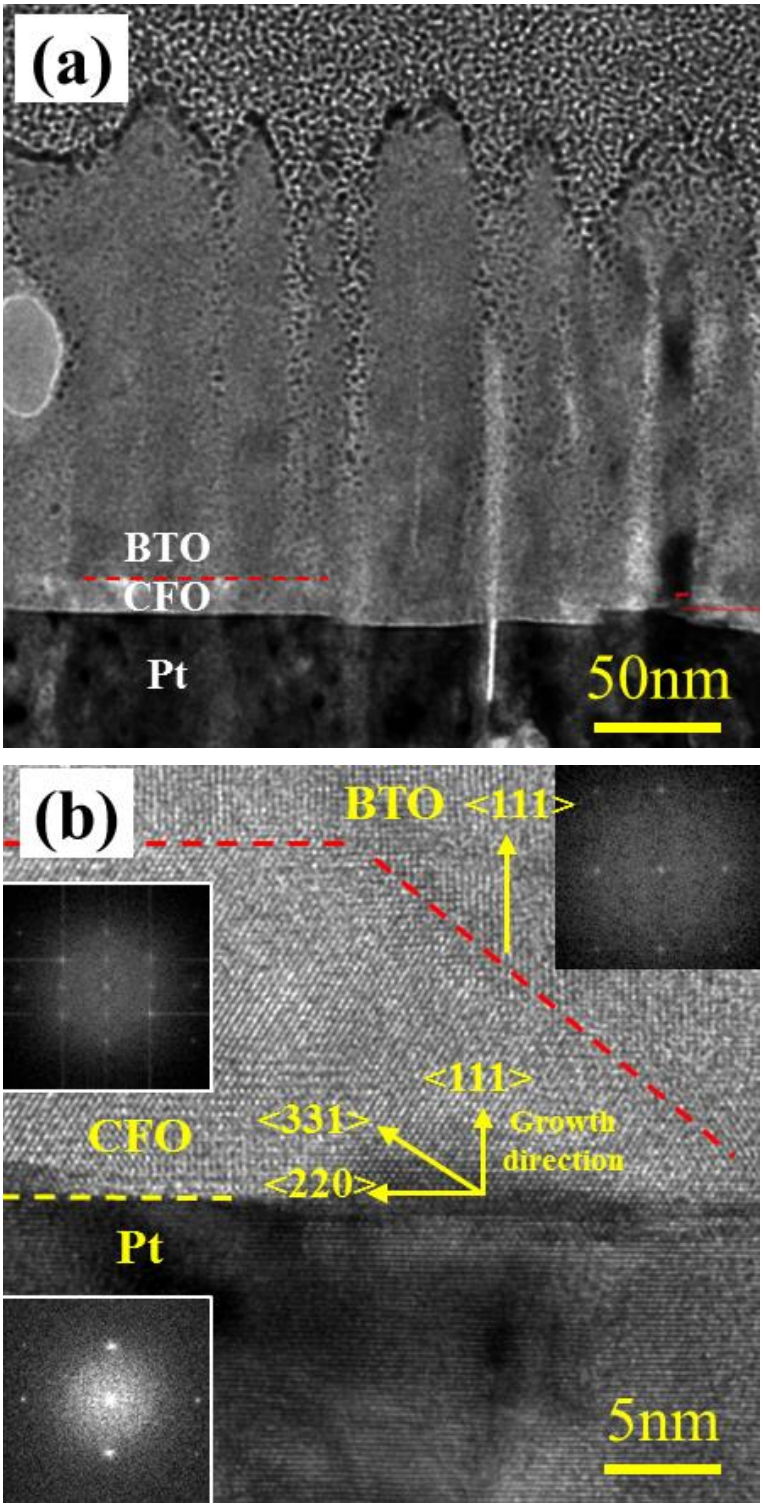

Figure 4.17(a) Cross-sectional TEM image and (b) High resolution TEM image of BTO/CFO think film heterostructure on Pt/Ti/SiO_2/Si substrate.

Next, the P-E loops for BTO/CFO heterostructures with varied IBAD treatment time was measured, as shown in Figure 4.18(a). A well-developed hysteresis loop was observed in comparison with the P-M-P composite thick film. This is mainly due to the fact that inactive CFO film, as an intermediate layer between BTO and Pt, has less effect on BTO during electrical driving. Further, it is noticed that both the remanent polarization and coercive field declined with longer IBAD time. It is worth mentioning that the growth conditions for BTO layer were fixed among all the heterostructures. The evolution of ferroelectric hysteresis loops may be attributed to: (i) defects were induced with increasing IBAD time, which in turn increased the lossy effect of the bottom CFO layer, and (ii) induced faceted CFO grains resulted in lowering of texture fraction of post-deposited BTO film.

Based on the above analysis, magnetoelectric coupling among the deposited heterostructures with modified interface was explored. *P-E* curve of each sample was measured as a function of external DC magnetic field. In Figure 4.18(b), variation of remanant polarization (ΔPr) with applied DC magnetic field is plotted. ΔPr was found to be proportional to $H_{DC,}$ increasing with the applied field magnitude. Interestingly, the slope of ΔPr variation reduced down first and then increased with increasing IB exposure time. The negative effect of IB on polarization magnitude can be assigned to roughness induced between the BTO and CFO interface which reduced the elastic strain coupling. This result clearly shows that smooth epitaxial-quality interface is required for higher ME coupling. The gain in the ME coupling with long IBAD time may be attributed to two reasons: (1) larger interfacial area between two phases as a result of increasing in surface roughness via IBAD; (2) enhancement of interfacial bonding between pervoskite and spinel via the

ion-bombardment modification process.

IBAD offers a unique approach for controlling the ME film interface and tuning the magnitude of elastic coupling. Further investigations on the origin of the changes in ME coupling due to IBAD are needed. However, it is believed that the IBAD will be a promising method to develop giant magnetoelectric thin film heterostructure with optimum composition and interfacial properties.

Two laminate ME composite films (bilayer BTO/CFO thin film and trilayer PZT/CFO/PZT thick film) were deposited, characterized and analyzed to understand the mechanism of ME coupling. PMP structure with good ME coupling was found to provide strong interfacial bonding between ferroelectric and ferromagnetic phases. ME coupling of PMP structure can be further enhanced by reducing the clamping effect. IBAD assisted BTO/CFO heterostructure resulted in significant changes in ME coupling. This new method of tuning interfacial properties provides a great potential toward developing giant magnetoelectric thin film ME composite. The results of this section show that interfacial properties (microstructure, growth mechanism, preferred orientation, elastic coupling) play an important role in magnetoelectric composite thin/thick films. Comprehensive understanding of the interface can be used to further enhance ME coupling.

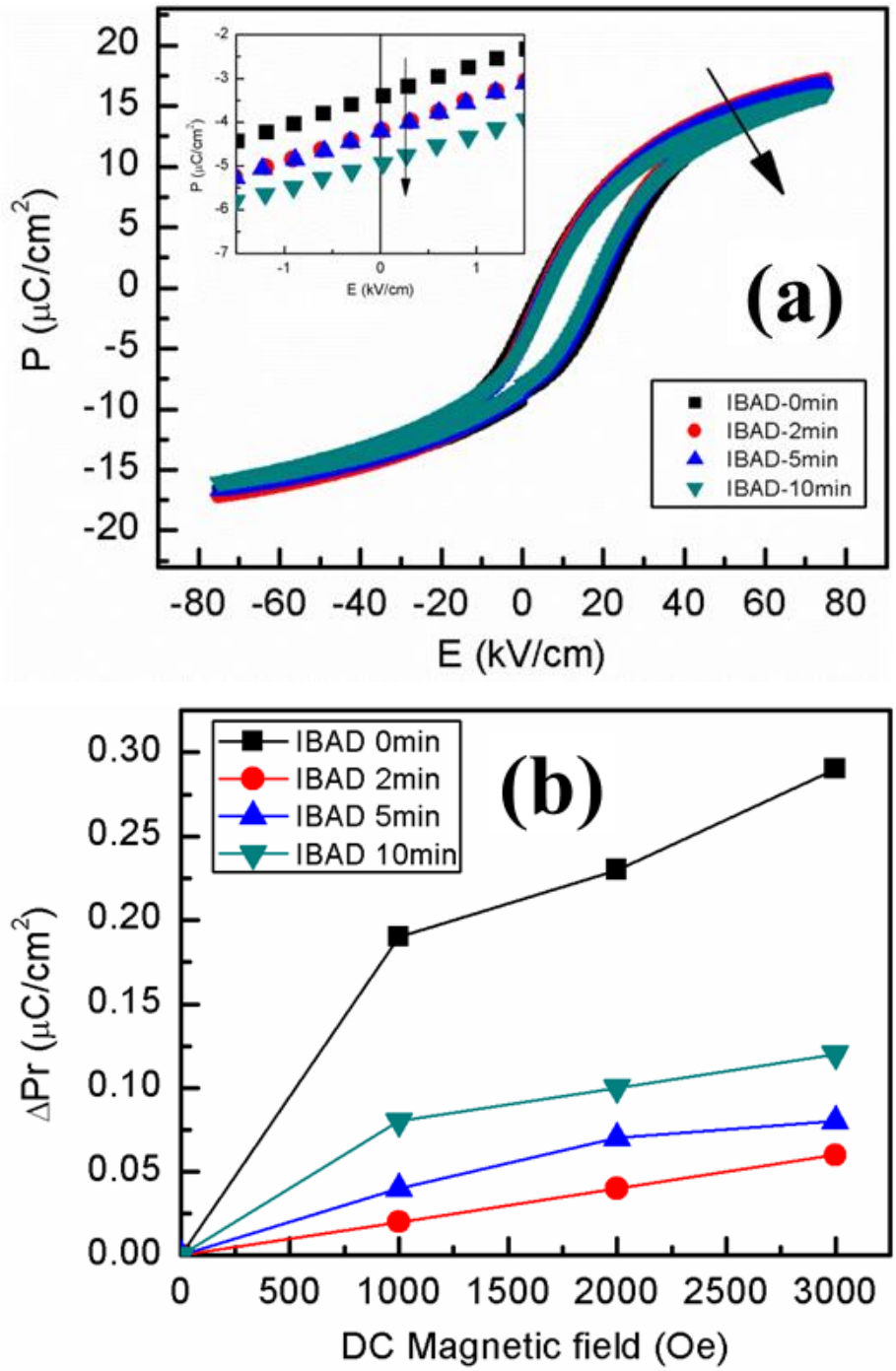

Figure 4.18 Ferroelectric property and magnetoelectric coupling performance of the thin film heterostructure: (a) P-E curve as a function of ion bombardment time, (b) Remnant polarization variation as a function of external DC magnetic field.

4.4 Complex 3D magnetoelectric composite on Aerosol patterned substrate

Nanostructured ME thin film composites have been deposited on various substrates with different connectivity (0-3, 1-3 and 2-2). For 1-3 type connectivity, although one can observe ME coupling through atomic force microscopy based techniques[128], the inherent leakage problem still limits the magnitude of ME effect as magnetic pillars with low resistance penetrate the whole film thickness and connect with bottom electrode. On the other hand, 2-2 type heterostructure reduces the leakage problem, which could lead to visible ME effect.[129] However, this structure exhibits weak ME effect due to the large in-plane constraint from substrates.[19] In this section, a novel complex three-dimensional ME nanostructure was fabricated by using hybrid synthesis method to overcome the problems with prior structures.

4.4.1 Mask-less Mesoscale hybrid deposition process

A novel synthesis method was developed that not only provides a well-ordered arrangement of nanoscale magnetoelectric structures but also simplifies the classical top-down patterning. The hybrid deposition process starts with a $BaTiO_3$ (BTO) geometrical pattern printed by Aerosol Jet® deposition on a platinized silicon substrate and then uses pulsed laser deposition (PLD) to grow multilayers of BTO and $CoFe_2O_4$ (CFO). After in-situ annealing at high temperatures, the deposited films self-assemble into complex structure. Lastly, $Pb_{1.1}(Zr_{0.6}Ti_{0.4})O_3$ (PZT) sol-gel was coated to achieve homogeneous top surface. The main criterion for selection of PZT was to show that this process can integrate multiple materials on the same structure providing alternate arrangement of BTO, CFO, PZT. A combination of these three deposition techniques can be used to fabricate large-area arrays of

magnetoelectric structures. Crystallinity and preferential orientation of the hybrid films were investigated by X-ray diffraction (X'Pert High Score Plus). The microstructure and thickness of the films were determined by field emission-scanning electron microscopy (FE-SEM; LEO Zeiss 1550). Energy Dispersive Spectrometer (EDS) analysis was performed on selected films using Bruker EDX system. For electrical characterization of films, a circular top Pt electrode with a diameter of 0.5mm was deposited by sputtering and ferroelectric properties were measured by Sawyer-Tower circuit. Details of the deposition process are described below:

(a) Aerosol-jet printing: BTO powder with an average particle size of ~1.05 μm and specific surface area of ~6.3 m^2/g were added to carrier solution composed of ethanol, ethylene glycol, glycerin, poly(acrylic acid-co-maleic acid) (PAA) and DI water to form the ink. The ink was first aerosolized in the atomizer. After that, nitrogen gas carries the aerosol through the connecting lines to deposition nozzle where sheath gas focuses the streamline of material into fine features, as illustrate in Figure 4.8(a). The BTO films were patterned onto the Pt(111)/Pt/SiO_2/Si substrate (Inostek, Seoul, Korea) at temperature of 100 ℃ with 1mm/s printing speed.

(b) Pulsed Laser Deposition: Stoichiometric targets of BTO and CFO were synthesized by using the conventional solid reaction sintering method. Films were deposited in vacuum chamber with KrF (λ=248nm) excimer laser at energy density of 2.0~3.0J/cm^2 and 10 Hz repetition rate. Substrate temperature was varied from 400 ^oC to 800 ^oC with 100~150 mTorr oxygen pressure during deposition. In-situ post annealing was conducted at 400 mTorr background pressure after deposition. BTO films of 280 nm were deposited on

aerosol-patterned substrates followed by CFO layer with thickness of 80nm. The optimal growth condition for CFO thin film on top of BTO-AD template was found to be 800^{o}C.

(c) Sol-gel spin-coating: The detailed procedure for the sol-gel synthesis of PZT films is described elsewhere.[130] Lead (II) acetate trihydrate, zirconium propoxide, and titanium isopropoxide were dissolved in 2-methoxyethanol. The composition of the stock solution was $Pb_{1.1}(Zr_{0.6}Ti_{0.4})O_3$ with a concentration of 0.4M. Each layer was synthesized by spin coating at 3000 rpm for 45 sec followed by pyrolysis at 250^{o}C for 1.5 min in air and post-annealing at 800^{o}C for 45 min. Thick PZT films were synthesized by coating multiple layers. The final thickness of the top PZT layer was ~600nm.

4.4.2 Temperature stability and growth evolution

Figure 4.19 shows the representative surface SEM images of pulsed laser deposited BTO film grown on aerosol-jet printed patterns that were initially synthesized on Pt(111)/Ti/SiO_2/Si substrate. In order to study the effect of geometry of printed patterns on the morphology of PLD films, several patterns was developed as shown in Figure 4.19(a),(e),(i) and (m) within dimension of 200 µm x 200 µm x 1 µm. In Figure 4.19, it is found that PLD deposited BTO layer did not affect the underlying pattern morphology when the growth temperature was lower than 500^{o}C. With higher temperature, as-printed patterns became rough and coarse. These micrographs indicate that the coarseness is closely related to the growth temperature of the PLD film. This change might be related to the constrained sintering of the underlying printed BTO particles at higher deposition temperatures. The densification rate of the printed films is significantly lower than that of the PLD film, which

results in additional tensile stress and reduces the adhesion. In addition to coarsening, the printed polycrystalline films undergo differential densification as evident from the microstructure showing dense regions surrounded by large porous region.

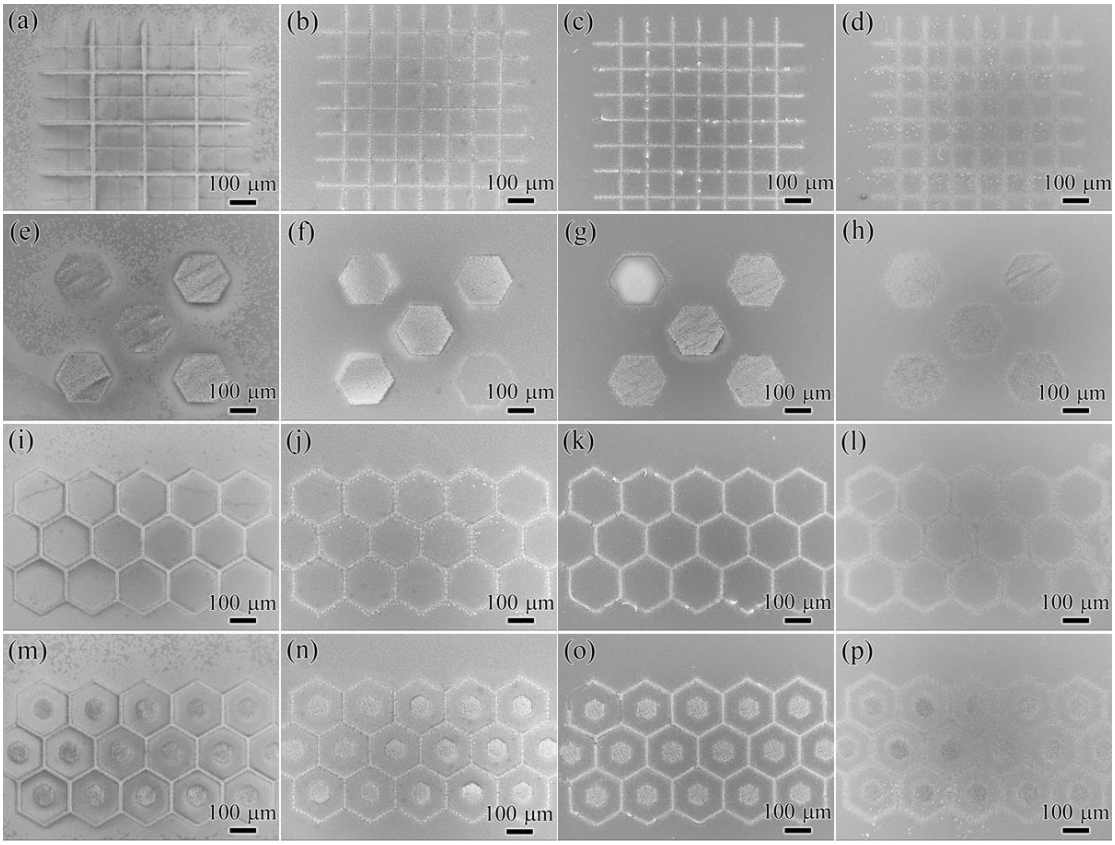

Figure 4.19 SEM images of BTO film deposited on top of the pattern printed by aero-jet deposition process. The images are shown for the films deposited at varying temperatures: (a,e,i,m) 400^{o}C, (b,f,j,n) 500^{o}C, (c,g,k,o) 600^{o}C, and (d,h,l,p) 700^{o}C.

Figure 4.20 shows the XRD patterns of the BTO films deposited on aerosol jet printed substrate at different temperatures. As-deposited aerosol patterns exhibited polycrystalline phase, which is expected because the ink mainly constituted of crystallized BTO powder. However, with pulsed laser deposited BTO film, the post-annealed film exhibited varying predominant orientation. With increasing deposition temperature, as grown films show (111)-preferred orientation with narrow crystallite size distribution. When the deposition temperature was kept at 400^{o}C, only (110) and (111) peaks for BTO can be observed, indicating that the BTO film remains in random polycrystalline structure. When the growth temperature increased to 600^{o}C, a broad (200), (210) and (211) peaks start to appear. With further increase in deposition temperature, (111) peak became sharper and all the other peaks gradually diminished. From these results, it can be concluded that the BTO films starts to sinter at 600^{o}C and achieve a (111) preferred orientation above this temperature. The phase evolution for BTO film can be understood by noticing that deposition was conducted on bottom electrode layer which has preferred (111) orientation. Thus, heterogeneous nucleation and growth on platinized silicon substrate at high temperature drives the sintering process and adoption of the bottom layer texture results in minimization of the surface energy.

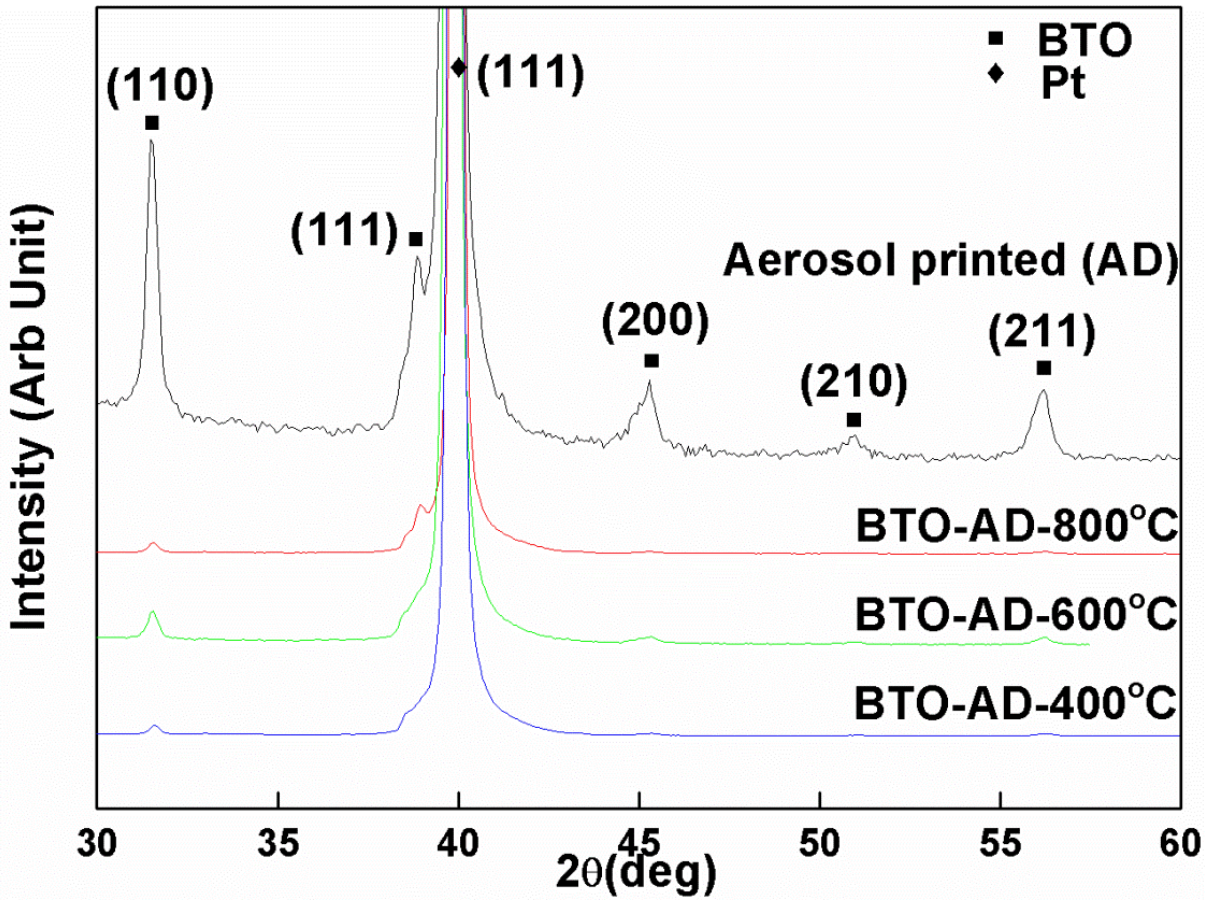

Figure 4.20 $\theta - 2\theta$ scan for pulsed laser deposited BTO film on aerosol printed substrates at different temperatures.

In order to study the film growth process, SEM images were obtained on the positive (film grown on aerosol printed pattern) and negative (film grown on platinized silicon substrate) area. Figure 4.21(a)~(e) show the high magnification image of BTO film grown on positive area, along with low magnification SEM images that indicates pattern features (insets). A notable difference in microstructure can be found in films deposited on positive area in temperature range of 400 ^{o}C to 800 ^{o}C. BTO island size at 400 ^{o}C was in the range of 250 nm~300 nm whereas at high temperature of 800 ^{o}C the size changes to 50~100 nm. As mentioned earlier, this instability is mainly indicative of the surface tension driven thermodynamic requirement for minimization of the surface energy. The grain shape at high temperature was found to be pyramidal that is indicative of (111)-oriented BTO facets. The sintering starts at temperature of 600~700 ^{o}C which was determined by noticing the emergence of (111) preferred triangular grain morphology in Figure 4.21(d). Inset figures in Figure 4.21(a)~(e) with relatively low magnification provide more details on interface between positive and negative areas. With increasing substrate temperature, BTO nanoparticles begin to spread and were randomly arranged thoughout the pattern. Large flower-like islands could be found in Figure 4.21(d) and (e), and when deposition temperature was increased to 800^{o}C, patterned lines were coarse with low density of nanoparticles. Based on the elemental mapping shown in Figure 4.21(f), it can be concluded that there was no significant diffusion between the positive and negative areas. These results further indicate differential constrained sintering.

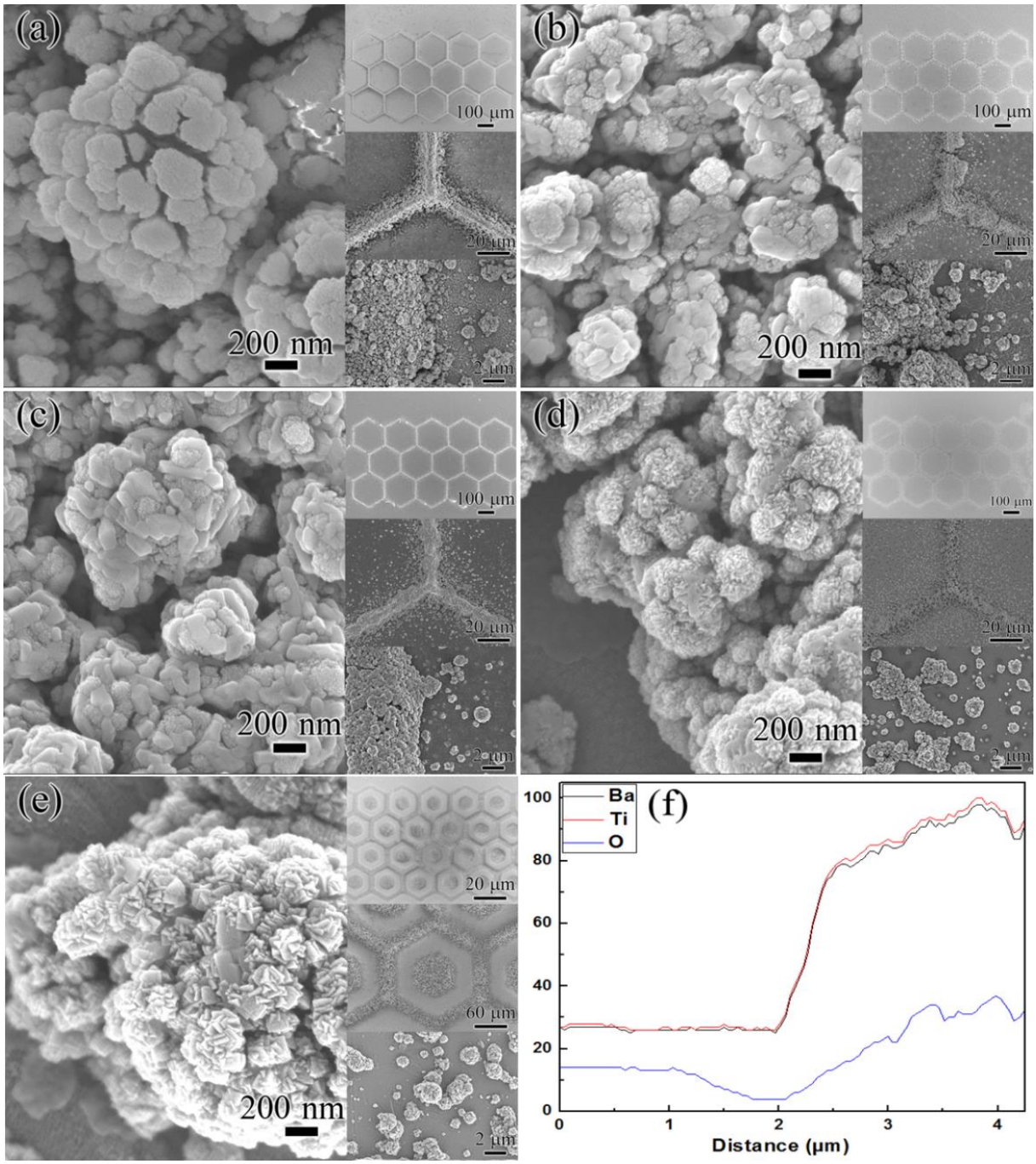

Figure 4.21 SEM image of BTO film grown on aerosol printed hexagnal pattern at (a) 400^{o}C; (b) 500^{o}C; (c) 600^{o}C; (d) 700^{o}C; (e) 800^{o}C; (inset shows three low magnification SEM images) (f) EDS element line mapping across positive and negative boundary.

Figure 4.22 plots the BTO grain size variation in positive area (inset shows SEM micrographs in negative area, which reflects grain size) as a function of deposition temperature. The BTO grain size in positive area was found to increase from 10 to 180nm with deposition temperature from 400 ^{o}C to 600 ^{o}C. At 700 ^{o}C, the grain size significantly reduced to 20 nm and exhibited minor change with higher temperature. This result distinguishes from the conventionally deposited films.[131] This is considered to be result of the two-step growth in positive and negative area. The aerosol patterned film deposited at 400 ^{o}C exhibits an island structure without formation of any distinct grains at the surface. When the deposition temperature went up to 500 ^{o}C, large columnar island structures appear. With even higher deposition temperature, islands became much larger and grew though the whole substrate. At this time, the PLD deposited film is still in the amorphous state and can conform to the shrinkage occurring in the aerosol patterned film. When the deposition temperature was increased to 600~700 ^{o}C, heterogeneous nucleation occurred in the negative area and small nuclei begin to form in PLD deposited film as shown in Figure 4.22(d). The growth of these nuclei depends upon several factors including anisotropic grain boundary energy, interfacial strain energy, and interfacial mobility. For grain sizes approaching PLD film thickness, grain boundaries and junctions lead to the development of large perturbations that eventually intersect the substrate and cause the film to break up into islands with (111) facets. Grains with orientations having low surface energies are favored during growth and escape from the pinning due to the pin holes, mechanical defects and grain boundary junctions formed with the aerosol printed layer. This results in the bimodal distribution of grains in the final microstructure. Therefore, with this hybrid process, the BTO pattern can be sucessfully

printed and subsequently works as a positive template to control the grain distribution for PLD-BTO film growth. On the other hand, it proves that one can control the pattern by varying growth temperature and can obtain dense patterns at relatively low temperature.

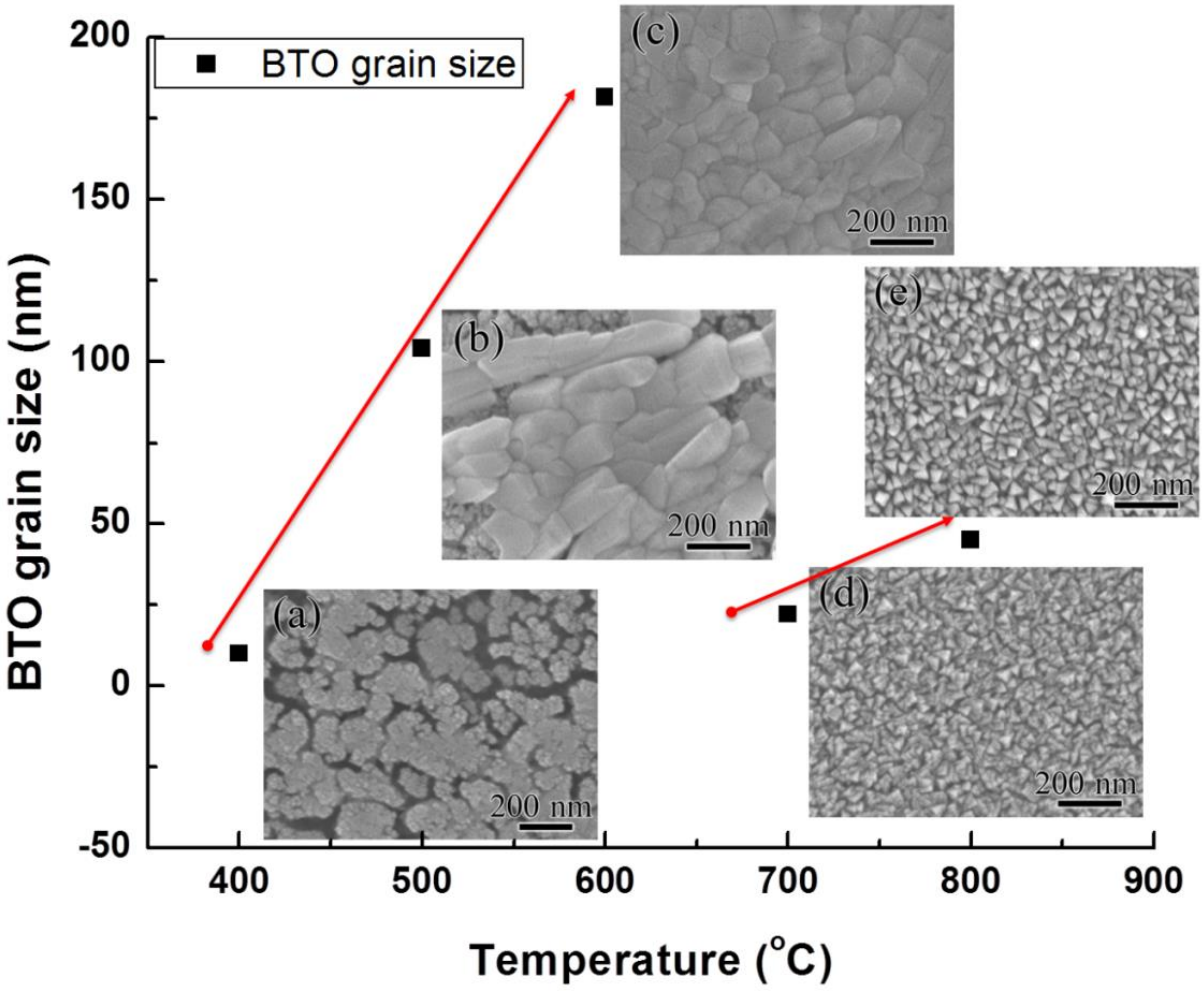

Figure 4.22 BTO grain size in positive area as a function of deposition temperature. The inset SEM images show microstructure evolution in negative area relative to the same temperature.

4.4.3 Assembly of Complex 3D ME nanocomposite

Based on the understanding of microstructure evolution on aerosol deposited pattern, flower-like islands formed at 800^{o}C were selected as template for complex 3D ME composite structure, as shown in Figure 4.23. This condition was utilized because it not only helps in achieving highly oriented film with controllable flower-like structure in three dimensions that can break the symmetry of two dimensional layer by layer films, but also increases the contact area between piezoelectric template and magnetostrictive layer. Hence, another layer of CFO with thickness around 80 nm was deposited on BTO-AD template with flower like islands to form the green matrix for complex 3D ME composites. On top of the CFO layer, sol-gel spinning was used to form a smooth surface with PZT solution.

Figure 4.23 illustrates the microstructure evolution during each step of complex composite synthesis. Figure 4.23(e) and (h) show CFO film possess triangular morphology, following the (111) oriented BTO film with the flower-like islands. PZT film was formed with a smooth surface on flower-like islands as shown in Figure 4.23(f) and (i). Figure 4.23(j) and (l) show the morphology change for the film grown in negative area. It is noticeable that CFO grain size is around 65 nm as compared to 45 nm for BTO grains. Moreover, CFO grains have triangular morphology with sharper edge. When the top layer of PZT was spin coated on the template, it formed smooth, dense and crack-free film as shown in Figure 4.23(l). Also it is noticeable that top PZT layer had a fibrous columnar structure which is attributed to grain growth suppression from CFO seed layer[130], as shown in Figure 4.23(o). In other words, the migration of grain boundaries in the PZT layer was inhibited by the pinning effect of the grain boundary of the seed layer.

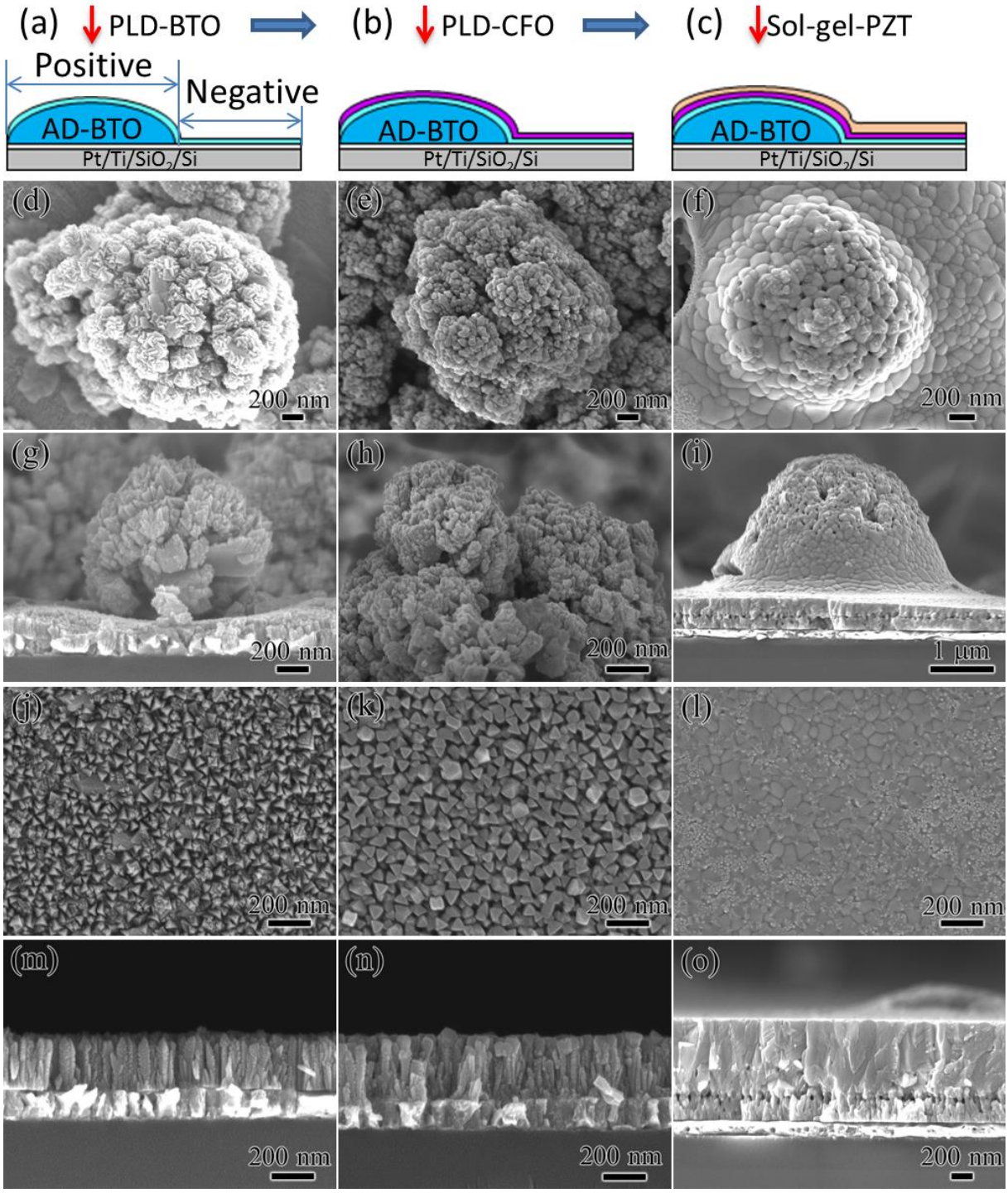

Figure 4.23 Schematic and SEM micrographs of Complex 3D ME composite structure at each step of fabrication, (a, d, g, j, m) PLD deposited BTO film on AD pattern; (b, e, h, k, n) CFO film grew on as deposited BTO-AD template; (c, f, i, l, o) PZT sol-gel spin coating film on CFO-BTO-AD matrix.

Figure 4.24(a) shows the XRD patterns of as-grown composite at different stages. It can be noted that the (111) peak of BTO with CFO thin film on top became sharper as compared to BTO-(111) peak in BTO aerosol printed template. The is mainly attributed to further grain growth in the BTO film during CFO deposition period. However, it is hard to resolve CFO film because the thickness is quite small to be reflected in XRD measurement. One can clearly find (111) and (110) peaks of PZT for as-grown complex 3D ME composite, which demonstrate good growth quality of PZT film. It should be also noticed that the PZT top layer has (111) predominant orientation. Figure 4.24(b) illustrate room temperature ferroelectric hysteresis loops for 3D complex ME composites. For positive area, the remnant polarization ($2P_r$) was 51.6 μC/cm^2, similar to the value of BTO single crystal and highly textured PZT films[130] The obtained polarization on negative area exhibits lager magnitude $2P_r$=55.36 μC/cm^2. The ferroelectric variation between positive and negative area is probably related to the aerosol printed template clamping effect.

In this section, 3D complex ME composites were successfully designed and fabricated by aerosol printing, PLD and sol-gel deposition techniques onto platinized Si substrate. PLD deposition was carried out on aerosol printed substrate to study the growth-microstructure relationship as a function of temperature. It was found that the BTO films have two-step growth on as-printed template. The crystallized BTO films exhibit a highly predominant (111) orientation. Subsequently grown CFO and PZT followed the same preferred orientation with columnar grain structure. Ferroelectric measurement shows that 3D complex ME composite possess large remnant polarization.

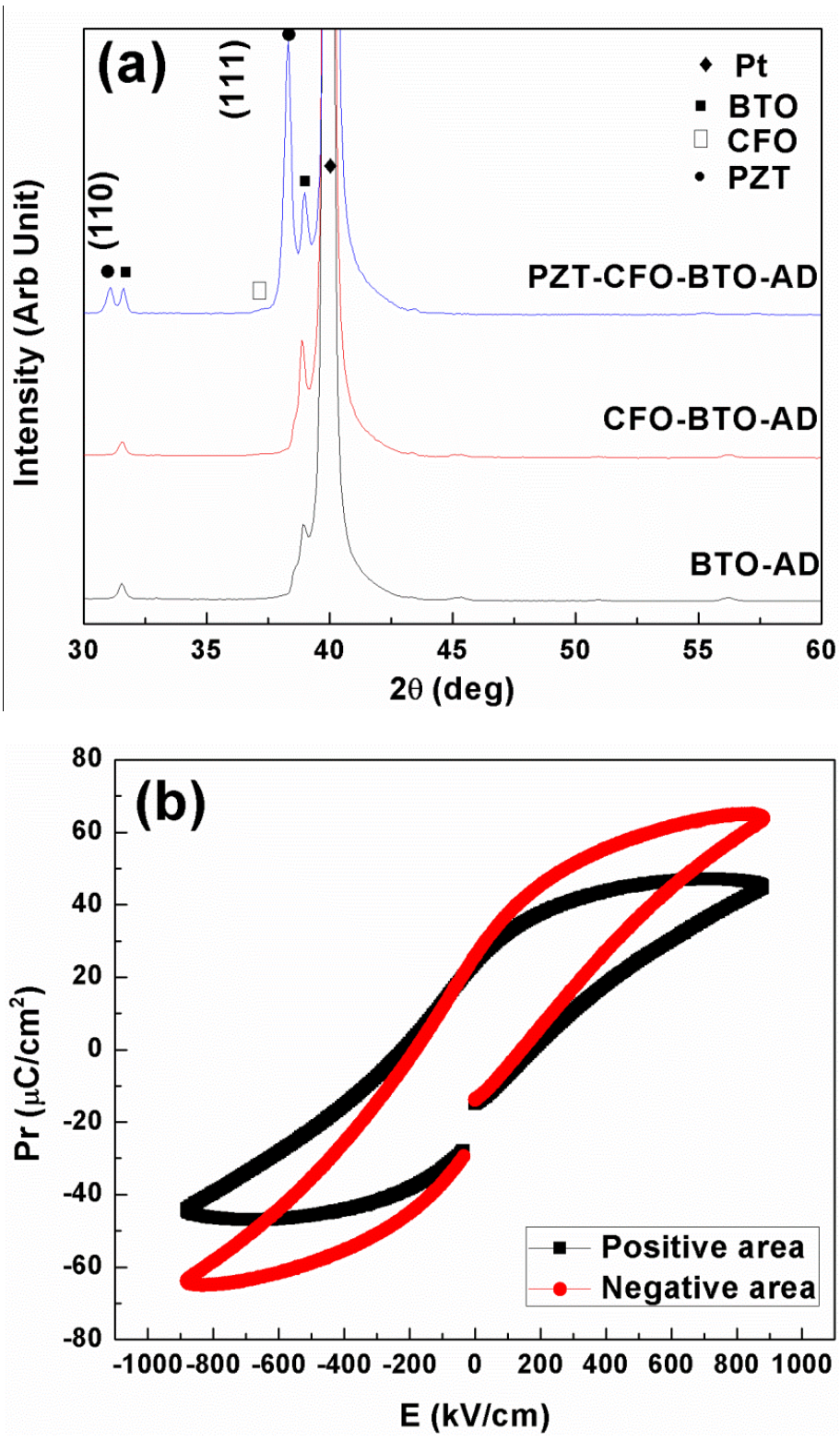

Figure 4.24 (a) XRD pattern of Complex 3D ME composite structure at each step of fabrication, and (b) Polarization-electric field loops for positive area and negative area in 3D complex ME composites.

4.5 Chapter summary

In summary of this chapter, investigations directed at addressing the nanostructure control and interfacial engineering of ME thin/thick film nanocomposites have been performed.

(1) Control growth of nanostructures: (a) On one side, a comprehensive understanding of the pulsed laser deposited $BaTiO_3$ films was provided by conducting a systematic study of the morphology and microstructure evolution as a function of deposition conditions. Structure – property relationships were investigated by conducting the local piezoreponse force microscopy and high resolution transmission electron microscopy measurements. The evolution of microstructure and surface morphology was discussed within the framework of Structure Zone Model (SZM) and Dynamic Scaling Theory (DST). A growth model was finally presented in elucidating the temporal and spatial morphology development process by considering anisotropy of surface energy and the formation of twin lamellae structure. These results will lead to new insights toward the growth and microstructure of thick films and are believed to improve the process compatibility. (b) On the other side, the growth interaction between pre-deposited well-ordered template and post deposited films was studied by controlling the morphology (grain size, shape and distribution) of the template as a function of film orientation. A novel hybrid deposition method was proposed to provide an easy, flexible, and cost-effective technique for development of well-ordered ME nanocomposite arrays. Orientation–microstructure–property relationships were investigated by conducting magnetic force microscopy (MFM) and piezoreponse force microscopy (PFM).

Post-deposited film growth within or without the template performs multi-orientated grains with different physical properties. This hybrid deposition method provide a new way of manipulating well-ordered ME nanocomposite arrays and will help us better understand growth of controllable nanostructure and their intergradation into multi-functional devices.

(2) Manipulate nanocomposite interface: A systematical study of the interfacial properties of ME thin/thick composite films were provided by investigating the interfacial and magnetoelectric properties of two different ME nanocomposite: sol-gel deposited PZT/CFO/PZT thick film and ion-bombardment-assisted pulsed laser deposited BTO/CFO thin film. Interfacial microstructure and the ME performance of these heterostructures were analyzed to understand the nature of elastic coupling. ME behavior strongly depends on the mechanical and electrical impedance matching, substrate clamping effect and interfacial contacting between the ferroelectric and ferromagnetic phases. Comprehensive understanding of the interfacial properties (microstructure, growth mechanism, preferred orientation, elastic coupling) is an essential step toward enhancing ME coupling. Further, in addressing the inherent problems (leakage problem, substrate clamping) of ME nanocomposites with conventional phase connectivity (1-3, 2-2. 0-3), a novel 3D complex ME composite was developed using a hybrid synthesis method by combing PLD, aerosol-jet deposition and sol-gel spinning. Growth-microstructure-property relationships of synthesized complex composites were systematically investigated to understand the magnetoelectric response in complex geometries. The films exhibited excellent ferroelectric response showing the promise of

this process. It is expected that by using this hybrid deposition process, highly anisotropic structure could be synthesized with tailored ferroelectric properties and enhanced magnetoelectric coupling.

5. Magnetoelectric Tunable Transformer

ME transformers as voltage gain devices have been investigated in literature and it has been shown that a giant voltage gain can be obtained at the resonance frequency.[63,132] In the design proposed by Dong et al., an input ac voltage was applied to the coil that generated an oscillating AC magnetic field (H_{ac}). The generated field interacted with the ME laminate and amplified the voltage output.[132] In this design, the use of winding coil around the laminated ME transformer poses challenge in its implementation. Alternatively, Islam *et al.* demonstrated a ME transformer consisting of a particulate $Pb(Zr_{0.52}Ti_{0.48})O_3$-$Ni_{0.8}Zn_{0.2}Fe_2O_4$ (PZT-NZF) composite and utilizing the electrode pattern of conventional unipoled transformer.[133] However, the small ME coupling of the particulate composites hinders its tunable feature under applied DC magnetic field. Thus, even though these structures are intriguing, their implementation for realization of miniature transformer and magnetic tunable devices will be limited. In this chapter, I will discuss different types of ME tunable transformers in addressing these challenges from three perspectives:

(1) Considering the high ME coupling of ME laminate and the easy fabricated unipoled piezoelectric transformer, two epoxy-bonded ME transformers with different operation mode will be discussed and their magnetic tunable feature will be analyzed.

(2) In addressing the concern of the bonding operation and utilization of epoxy layer with low mechanical strength, a co-fired ME transformer will be discussed.

(3) Motivated by the on-chip integration, a design and development strategy of thin film ME transformer will be proposed.

5.1 L-T epoxy bonded Metglas/PZT multilayer transformer

This study describes a magnetoelectric (ME) multi-layer piezoelectric transformer that has one direction poling, operates in a wide-frequency range and illustrate voltage gain and resonance frequency tunability on application of magnetic field. In this design, the input and output electrodes are on the same side of the square plate and are isolated from each other by a fixed gap. The electrode pattern is a square/square structure with floating connection among each layer. Metglas was attached on both side of the output electrode. Investigations were performed on the square plate with total dimension of $20\times20\times1mm^3$. The ME transformer was characterized for the changes in the voltage gain and resonance frequency shift under constant voltage condition. A dramatic change in the magnitude of the voltage gain and frequency shift was observed with applied external magnetic field. The ME transformer design presented in this study clearly shows the possibility of fabricating magnetic-field-tunable piezoelectric transformer, offering potential for tunable filter application.

5.1.1 Fabrication, characterization and Operating principle

A 2-2 laminated ME transformer was designed and fabricated by directly bonding magnetostrictive layers onto the output port of a co-fired multilayer piezoelectric transformer. Multilayered piezoelectric transformer was synthesized via low temperature co-firing process.[81] Piezoelectric composition $0.2Pb(Zn_{1/3}Nb_{2/3})$-$0.8Pb(Zr_{0.5}Ti_{0.5})O_3$ [PZNT] was chosen and synthesized by conventional mixed oxide method due to its good piezoelectricity and low sintering temperature. PZNT calcined powders were further mixed with binder

system for tape casting. Laminated green bodies with Pt/Ag conductor paste (DuPont 9770) as intermediate electrode were pyrolysis and sintered at 400^{o}C and 930^{o}C respectively. The co-fired transformer have 3 layers with total dimension 20×20×1 mm^{3}. Sintered composite was electrode using silver paint (Dupont 7713) and poled at 3.5kV/mm. After poling, 2 layers of 25-μm-thick Metglas (2605SA1, Metglas Inc., USA) sheets were attached, by using epoxy (West System, USA), on top and bottom output port of the transformer.

The transformer performance was characterized under constant voltage condition using the procedure described details elsewhere.[134] Driving voltage was generated by Agilent 33120A function generator and NF high speed bipolar power amplifier (HAS 4025). Both voltage and current were monitored by using HIOKI high power tester (HIOKI 3193). Piezoelectric equivalent circuit parameters were determined using impedance analyzer (HP4194A, USA) under short circuit condition. To observe the ME transformer performance under external magnetic field, an electromagnet was used to apply DC magnetic field (H_{dc}) along the longitudinal direction of the laminate. The generated magnetic field was tested using a gaussmeter (Walker, MG-10D) with hall probe press close to the sample surface.

Figure 5.1(a) shows the schematics of the ME transformer. In this design, the input and output electrodes are on the same side of the square plate and are isolated from each other by a fixed gap of 2mm. The electrode pattern is a square/square structure with floating connection among each layer. Metglas, with dimension of 4×4mm^{2}, is attached on both side of the output section. Figure 5.1(b) shows the electrical connection of the transformer in the step-up mode. In this case, on applying the electrical excitation to the external rectangle frame (input), the contour extensional vibration is generated and transferred to the center

square (output) through the gap. At the output, the mechanical strain is converted to electrical voltage through a direct piezoelectric effect. The multilayer section is equivalent to connecting n units in parallel, where the input motional capacitance ($C_{a,input}$) increases n times. Simplistically, the gain of the transformer is given by: Gain=$\sqrt{\frac{C_{a,input}}{C_{a,output}}}$. Thus, the multilayered structure can provide higher voltage gain. Figure 5.1(c) illustrate a synthesized ME transformer consists of a co-fired multilayer piezoelectric transformer and a ME laminate structure.

When an external magnetic field is applied to the composite, the Metglas induces strain in terms of shape change on the center square section through magnetostriction. This strain is transferred to the output section of the transformer through elastic coupling. Next, a mechanical stress is generated in the center square resulting in an electric polarization by direct piezoelectric effect. Meanwhile, the electric-field-induced strain from the input piezoelectric phase is interfered with this magnetic-field-induced strain from the magnetostrictive phase. The resulting differential strain is converted into voltage through direct piezoelectric effect and induces change in the magnitude of output voltage and working resonance frequency. In this case, external magnetic field affects the transformer performance through direct magnetoelectric effect. Thus, it is expected that the magnitude of the voltage gain and working resonance frequency of the transformer could be tuned and shifted under external magnetic field through magnetoelectric effect.

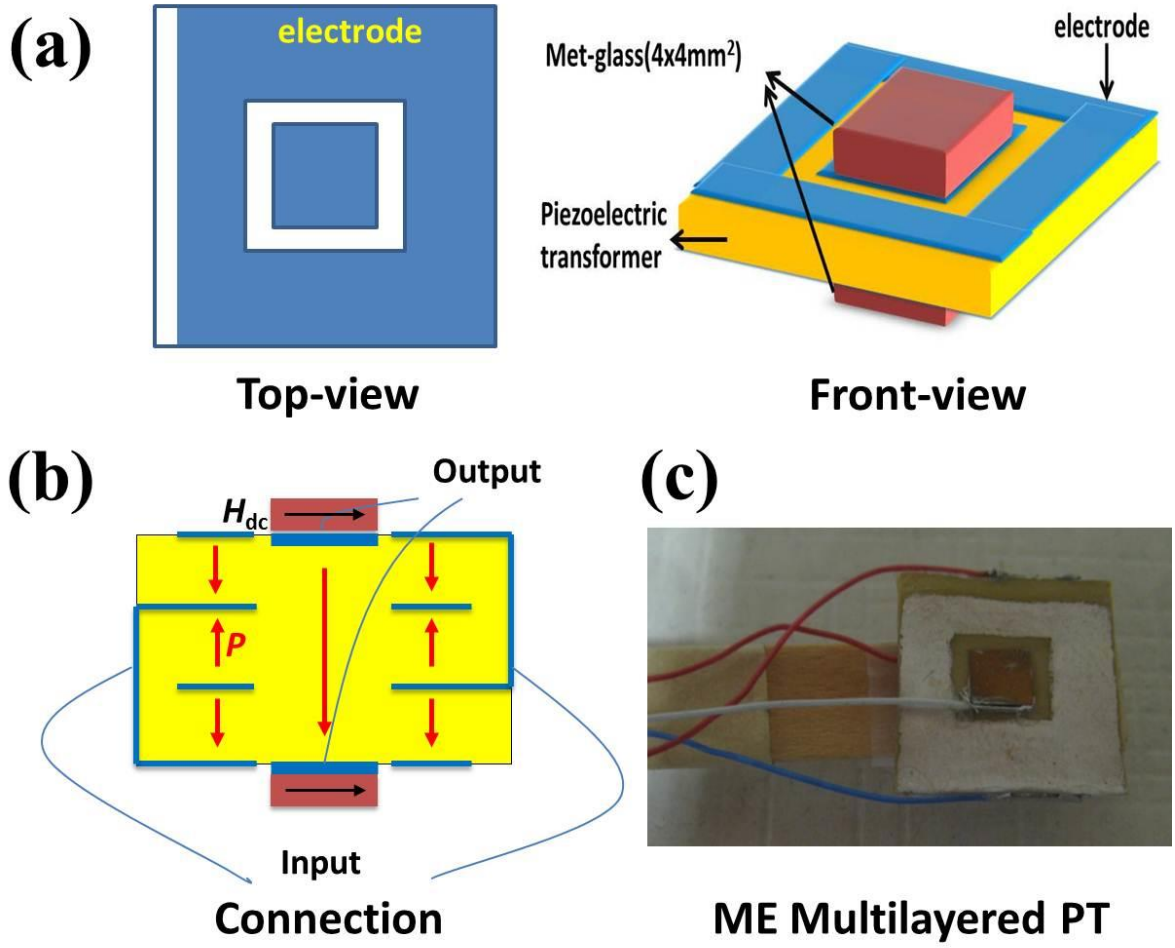

Figure 5.1 (a) Schematic diagram of the ME transformer illustrating the structure and layout of various elements, (b) Schematic of polarization direction and electrical connection and (c) Picture of fabricated ME transformer.

5.1.2 Analysis of the ME transformer

Using these considerations, the ME transformer performance was characterized by locating the longitudinally poled structure under transverse DC magnetic field (H_{dc}). Constant input voltage of $1V_{p\text{-}p}$ was applied on the rectangle frame section. Output voltage was measured from the center square section with varying H_{dc}. Figure 5.2(a) shows the measured voltage gain (G, ratio of output voltage to input voltage) of the ME transformer in the frequency range from 110 kHz to 113 kHz under varying external DC magnetic field. Without applying external magnetic field, the voltage gain was maximized at resonance frequency of 111.6 kHz with the order of 11.3. Under applied external magnetic field range from 200 Oe to 3000 Oe, the peak value of the voltage gain was found to shift with respect to different resonant frequency. Inset plot of Figure 5.2(a) shows the magnitude of resonance frequency (f_r) as a function of the external magnetic field. It can be founded that the working resonance frequency increases first with increasing H_{dc} showing the maximum at 111.6 kHz in the range of 200 Oe~400 Oe, and then drops with higher H_{dc}. The shift of fr is tightly related to the variation in piezomagnetic coefficient ($q=\partial\lambda/\partial H$, λ:magnetostriction) of Metglas, where the highest q value is expected to occur at around H_{dc}=200 Oe.[77,135,136] These data confirm the hypothesis that the magnitude of external magnetic field has direct correlation with the strain and hence working resonance of the transformer.

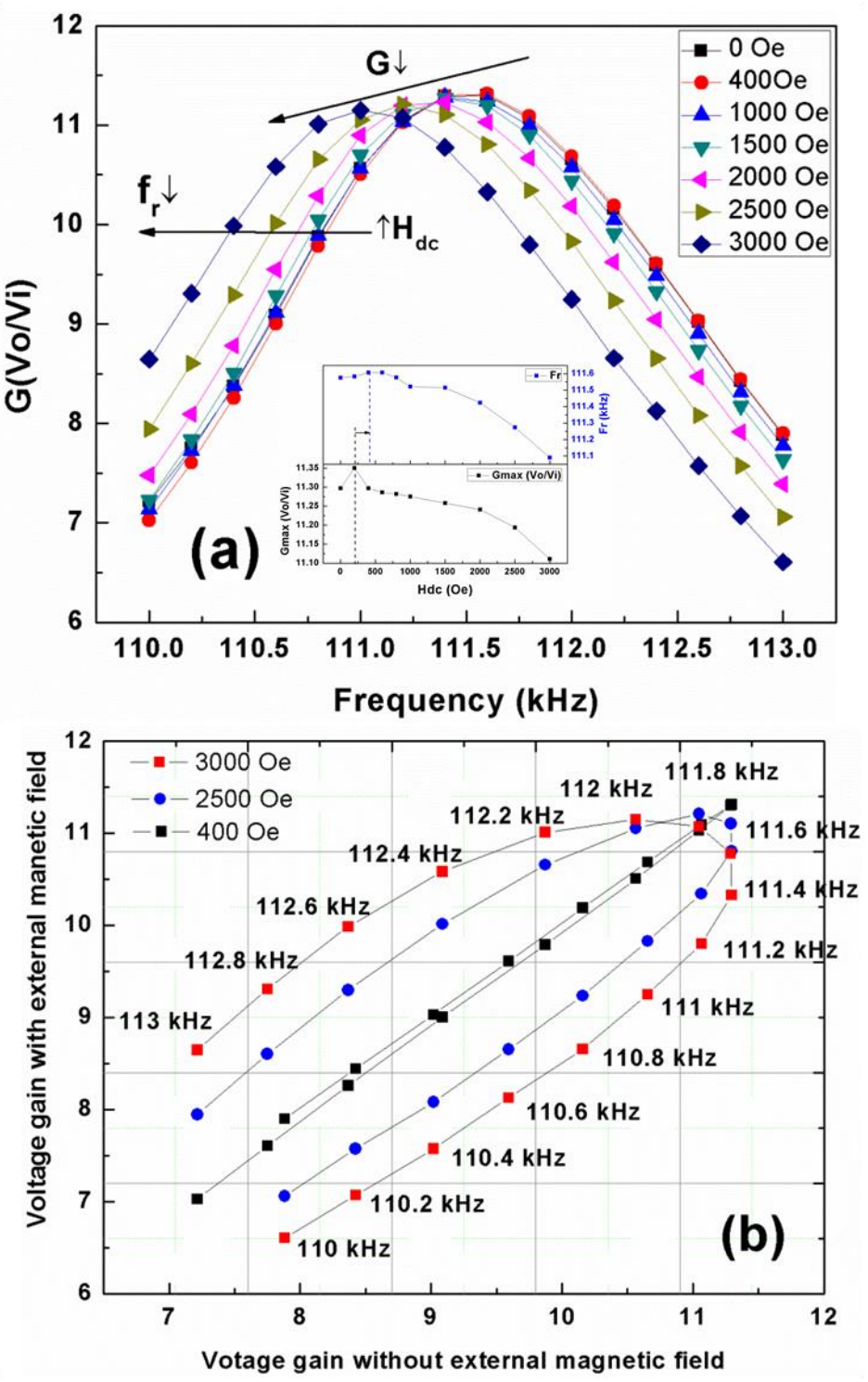

Figure 5.2 (a) ME transformer voltage gain as a function of frequency at varying external DC magnetic field from 0Oe to 3000Oe. Inset shows both voltage gain and resonance frequency variation as a function of DC bias. (b) ME transformer characterization of voltage gain change in the frequency range of 110 kHz~113 kHz with and without applied DC magnetic

field.

In order to compare the effectivity of voltage gain tunability under induced magnetic field, the voltage gain was plot with and without external magnetic field as shown in Figure 5.2(b). There is a significant change in the magnitude of the voltage gain with applied external magnetic field which increases as the frequency approaches the resonance point. Under low magnetic field (400 Oe), due to the small magnetic-field-induced strain, the voltage gain variation plot possess a slim loop, illustrating weak voltage gain tunability. However, under high external H_{dc}, a much broader G variation loop is observed, indicating an effective magnetic-field-induced tunability. Further, for the same magnitude of voltage gain, a large frequency shift comes up with the application of external magnetic field. These results prove that both voltage gain and working resonance frequency are dependent on external magnetic field.

The generation of voltage gain tunability and frequency shift under induced H_{dc} allows us to tailor the ME transformer with desired performance, offering the potential for design a mangetic-field-tunable “transfilter”. Here, “transfilter” is a combined term of transformer and filter, the device realizing an input-to-output voltage step up ratio and bandpass frequency response. Voltage step up ratio is obtained from the piezoelectric transformer part as discussed. Frequency selectivity is achieved from the mechanical vibration resulting from piezoelectric effect utilizing piezoelectric transformer as an electrical-mechanical transducer. When an external magnetic field is applied in the specimen, forced magnetostrictive strain would induce tunable features such as changes in the voltage output and working frequency due to the magnetoelectric effect. Figure 5.3(a) shows the voltage gain tunability $((G_H-G_o)/G_o$,

where G_o and G_H represent the voltage gain at zero and a non zero magnetic field, respectively) as a function of working frequency measured at varied H_{dc}. From this figure, it can be clearly identified that the magnitude of voltage gain is tunable at selected working frequency under changed magnetic field. On the other hand, Figure 5.3(b) depicted the frequency shift ($(f_{r.o}-f_{r.H})/B$) as a function of external magnetic field at resonance condition. It can be seen that there is a large resoance frequency shift, with relative constant maximum voltage gain, in proportional to the applied magnetic field. Thus, the transfilter can act as either a voltage gain tunable transformer at selected frequency or a resonance tuning bandpath filter with constant voltage gain. These data demonstrate its potential as a functional magnetic-field-tunable transfilter.

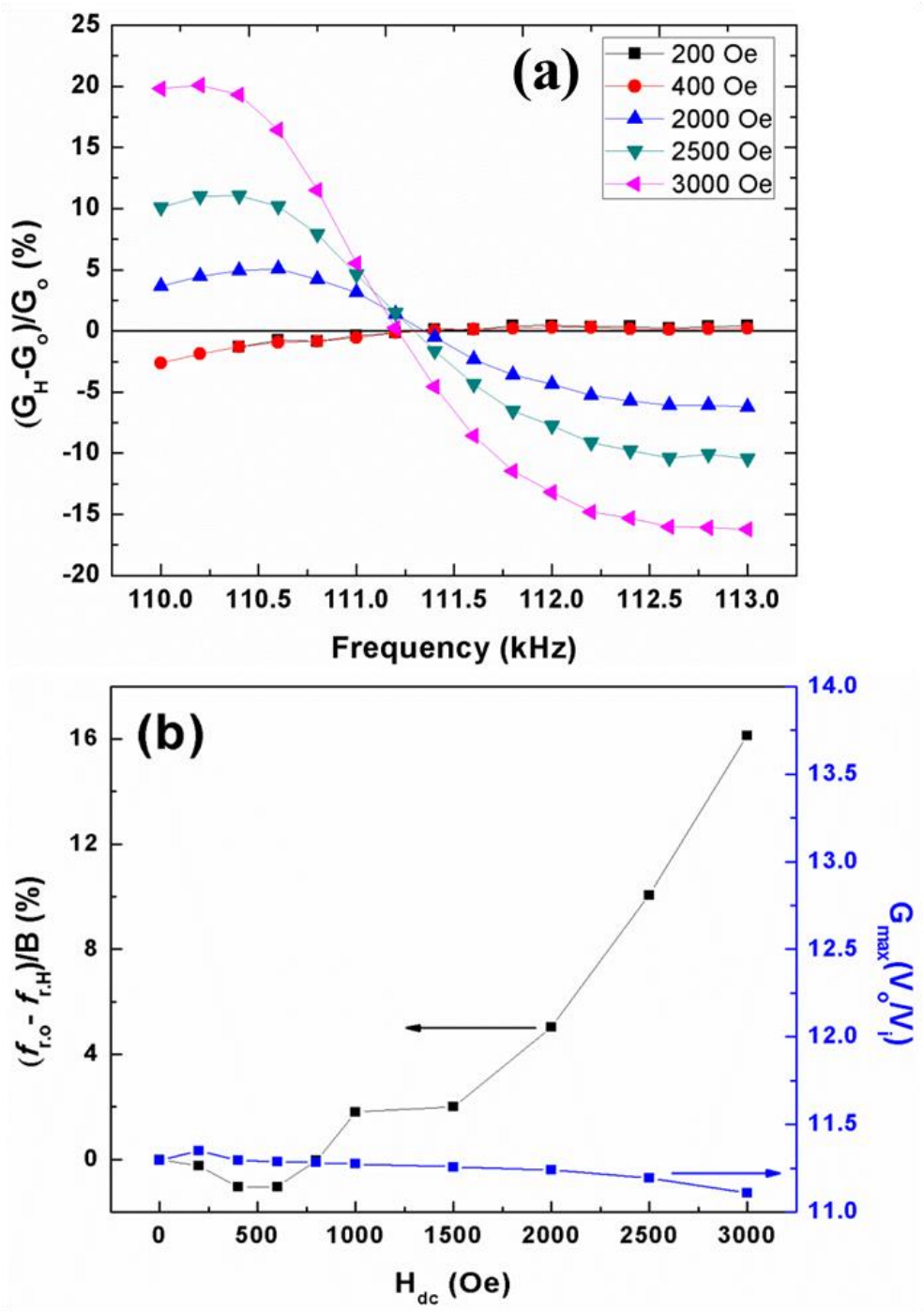

Figure 5.3 (a) Change in voltage gain as a function of frequency with respect to different external DC magnetic field. (b) Variation of maximum voltage gain and resonance frequency shift as a function of external DC magnetic, where $f_{r.o}$ and $f_{r.H}$ represent the resonance frequency at zero and a non zero magnetic field, B represent the 3-dB relative bandwidth of the transmission attenuation, respectivly.

Based on these analyses, one can notice that the effect of the magnetic field strength on the tunability of voltage gain and working resonance. In the current design, both of the voltage gain tunability and frequency shift are small at low magnetic field. The reason may be related to the fact that the generated strain through magnetostriction is limited due to small thickness ratio of the Metglas and the multilayer piezoelectric transformer. This can be enhanced by using thicker magnetostrictive layer or select magnetostrictive material with higher magnetostriction like Tefenol-D. Further, the magnitude of voltage gain can be modulated by optimizing the transformer parameters such as input voltage, input/output area ratio, material characteristics, and piezoelectric vibration modes.

In conclusion, this study reports the performance of a ME transformer utilizing the magnetostrictive material and a multilayer piezoelectric transformer. The working mechanism is based on the magnetic-field-induced strain of Metglas on the output section of the multilayer piezoelectric transformer through magnetostriction. The magnitude of voltage gain and resonance frequency in this design was found to be tailored effectively on application of external magnetic field, offering the potential for magnetic-field-tuned filter.

5.2 L-L epoxy bonded Metglas/PZT ME transformer

To achieve the best ME tunable performance, large ME coupling and more efficient stress transfer are desired. Therefore, I designed and investigated a new L-L mode (longitudinally magnetized and longitudinal poled) ME transformer.

5.2.1 L-L ME transformer design

Figure 5.4 shows the schematics of the L-L mode ME transformer. A rectangular shape piezoelectric plate (80x10x0.3mm^3) was used and poled in transversely direction on half of the plate, with the other half poled in longitudinal direction by interdigital electrode. Piezoelectric composition $0.2Pb(Zn_{1/3}Nb_{2/3})$-$0.8Pb(Zr_{0.5}Ti_{0.5})O_3$+2 mol%$MnO_2$ [PZT] was chosen and synthesized by conventional mixed oxide method.[137] Metglas with dimension (40x10x0.1mm^3) were attached on both side of the longitudinal poled area by epoxy resin, forming a push-pull-mode ME laminate.

Figure 5.4 (a) shows the electrical connection of the transformer in the step-up mode. In this design, the transversely poled part was selected as the input section with large capacitance, whereas the longitudinal poled part acts as the output port with small capacitance. When an AC voltage is applied to the transversely poled half of the PZT plate (input), a continual longitudinal vibration is generated and mechanically coupled to the longitudinally poled half of the PZT plate (output). A potential difference is therefore induced through a direct piezoelectric effect. When driven at resonance, the amplitude of the vibrations and the associated strain are maximal, leading to a voltage gain setup variation.

Similarly to that of L-T mode ME transformer discussed in section 5.1, when an external

magnetic field is applied to the composite, the strain induced from magnetoelectric effect will be coupled into the output port of the transformer, leading to a magnetic field tunable transformer.

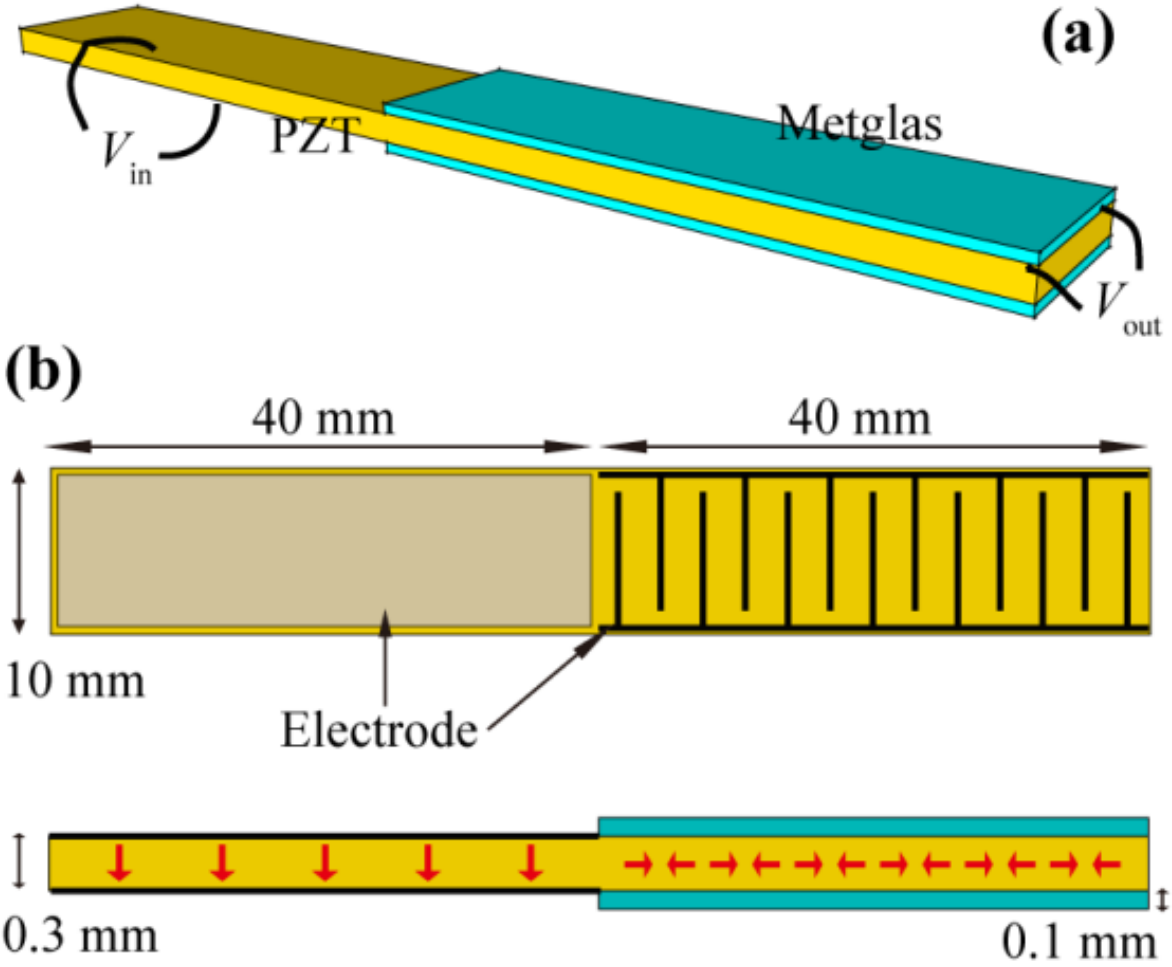

Figure 5.4 (a) Schematic diagram depicting the longitudinal-longitudinal PZT/Metglas magnetoelectric transformer, (b) Top view and front view of the ME transformer. Red arrow indicate the poling direction of the piezoelectric layer.

5.2.2 Analysis of the ME transformer

The ME coupling of the Metglas/PZT laminate was measured in L-L mode configuration. Figure 5.5 shows the ME voltage coefficent as a function of DC magnetic field and AC magnetic frequency. A giant ME coefficient of 8 V/cm.Oe was achieved in this L-L mode ME transformer under H_{dc}=21 Oe, H_{ac}=1Oe at 1 kHz. [Figure5.5 (a)] This ME voltage coefficient was further increased to 14.8 V/cm.Oe under resonance frequency of 27.32 kHz. [Figure 5.5(b)] In compared to that of the L-T mode multilayered ME transformer discussed in section 5.1, that is 133 times in ME voltage coefficient and 1/10th in optimum DC bias. High ME effect occurs due to (1) Metglas/PZT push-pull structure was developed by utilizing L-L mode. In the piezoelectric phase with longitudinal operational mode, the stress transfer more efficiently ($d_{33} > 2d_{31}$ since Poisson's ratio is smaller than 0.5), (2) the large q_{11} value and high permeability of the Metglas layer, (3) optimized magnetic phase volume ratio in the laminate. Thus, the ME voltage coefficient of this L-L mode structure is nearly two orders of magnitude higher than that of L-T type ME laminate discussed in section 5.1.

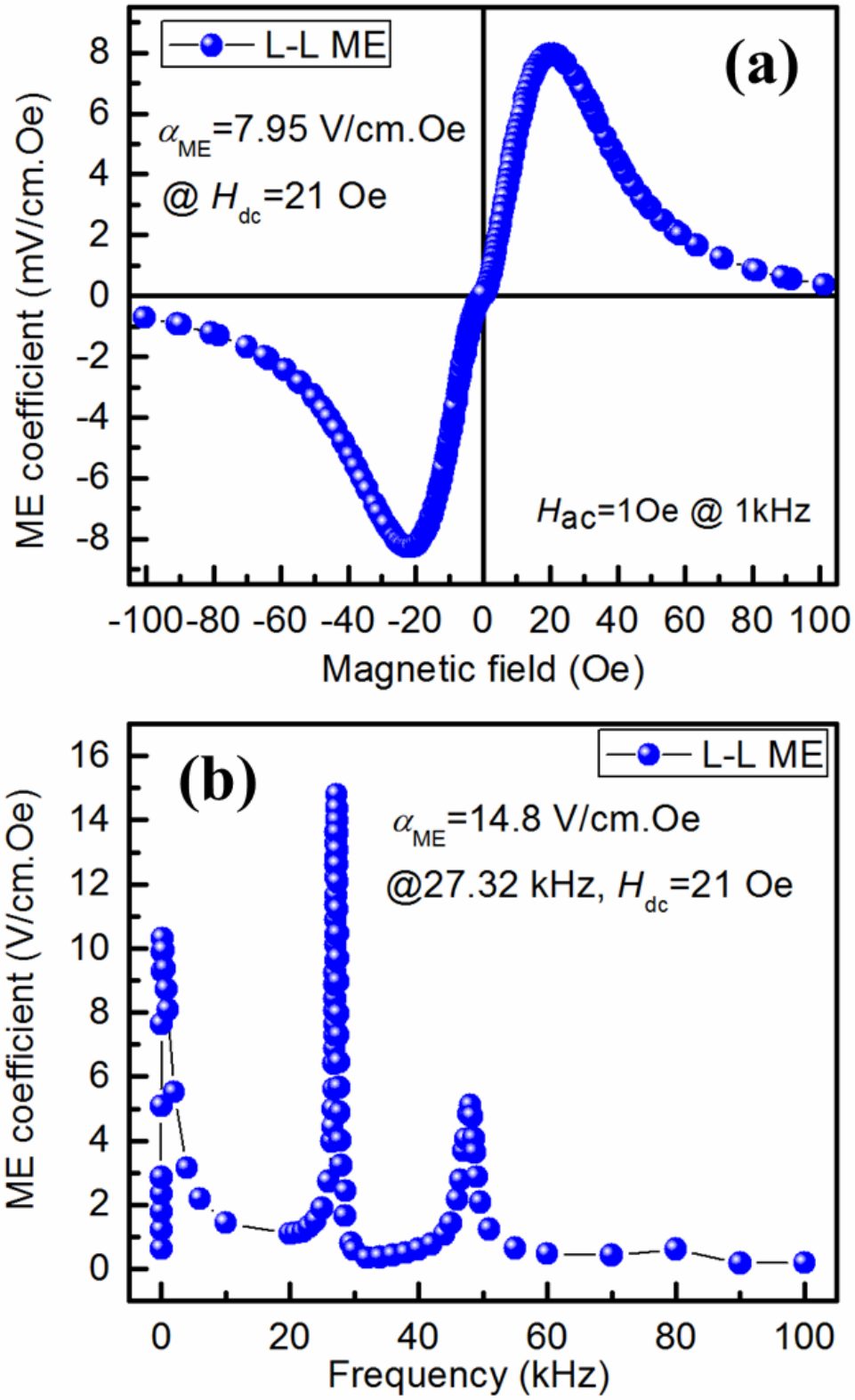

Figure 5.5 (a) ME voltage coefficient of the L-L mode PZT/Metglas laminate as a function of DC magnetic field; (b) ME voltage coefficient of the ME laminate under frequency variation.

Next, the ME transformer tunability was characterized by locating the laminate under longitudinal DC magnetic field. Figure 5.6(a) shows the transformer performance as a functional of frequency under varied DC magnetic field in the range of 0~100 Oe. There is a significant increase of the resonance frequency and voltage gain of the L-L mode ME transformer under increased DC magnetic field. To quantify this magnetic-field-induced tunability, both resonance frequency and maximum voltage gain of the transformer were compared under DC magnetic field variaiton, as shown in Figure 5.6(b). Large working resonance frequency shift of 380 Hz was obtained with only appling 100 Oe external magnetic field. The improvement of the frequency tunability may be devoted to (1) more efficientily elastic coupling in L-L mode operation and (2) high DC magnetic field sensitivity with respect to the large ME coupling and reduced optimum DC bias.

Figure 5.7 further illustrates the voltage gain variation with and without external magnetic field. Under low magnetic field range (3~30 Oe), the voltage gain variation plot transformed from slim loop to large opened hysteresis loop as H_{dc} increased, indicating an enhanced voltage gain tunability under magnetic field. While with further increase the magnetic field (30~100 Oe), there is not much change in the hysteresis loop, reflecting a reduced ME coupling. These results matches well with the ME coupling response of the laminate under DC magnetic field [Figure 5.5], where an optimized a_{ME} was realized in the range of 20~30 Oe.

In conclusion, in this section, I designed and fabricated a Metglas/PZT ME transformer by utilizing the longitudinal magnetized, longitudinal polarized (L-L mode) configuration. In this design, both voltage gain and working resonance tunability are enhanced in compared to

that of L-T mode ME transformer. A significant frequency tunability of 3.8 Hz/Oe was realized. The enhancement is based on the improved elastic coupling in L-L operation mode and the resultant giant magnetoelectric response.

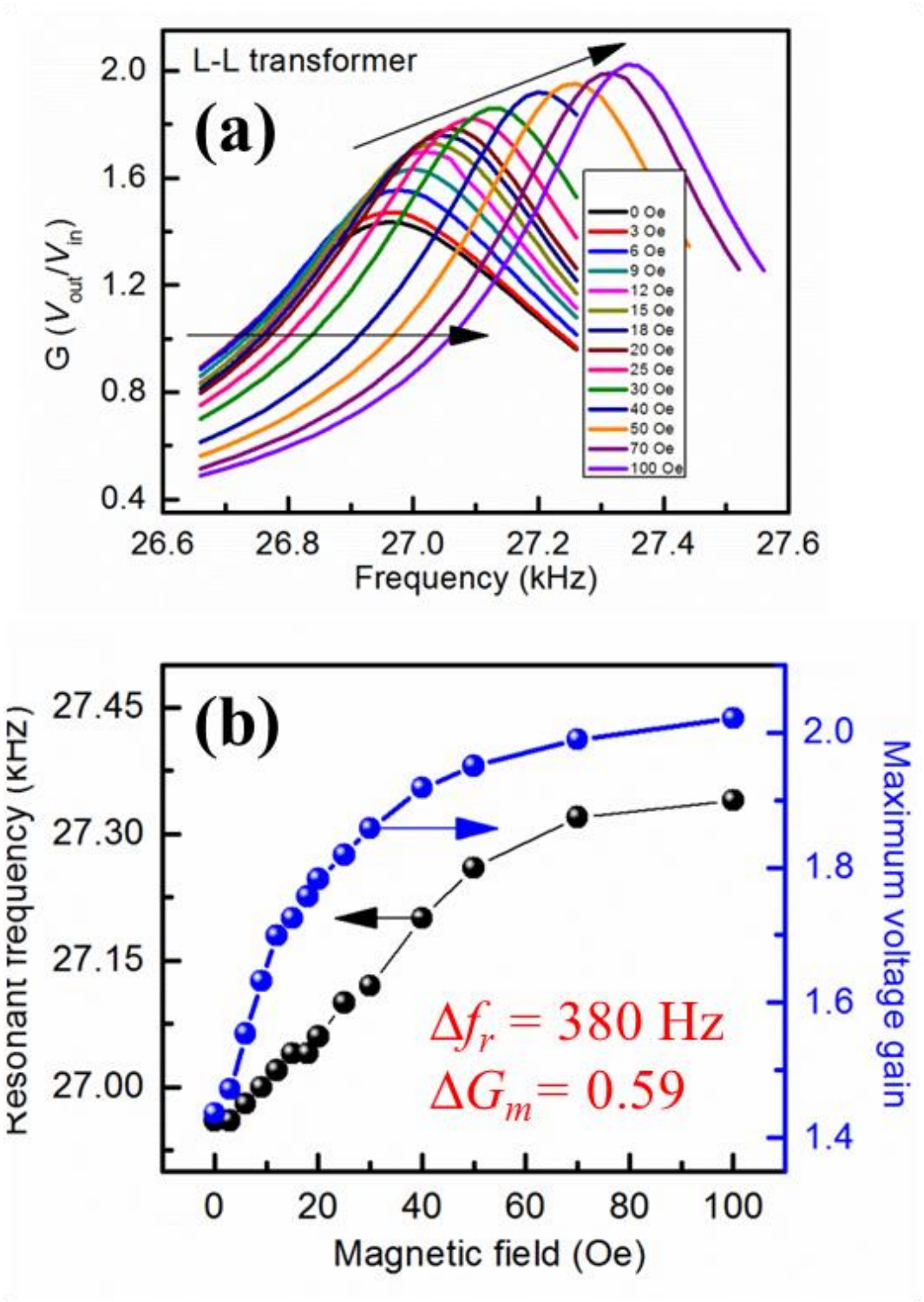

Figure 5.6 (a) ME transformer voltage gain as a function of frequency at varying external DC magnetic field from 0 Oe to 100 Oe; (c) Variation of maximum voltage gain and resonance frequency shift as a function of external DC magnetic field from 0 Oe to 100 Oe.

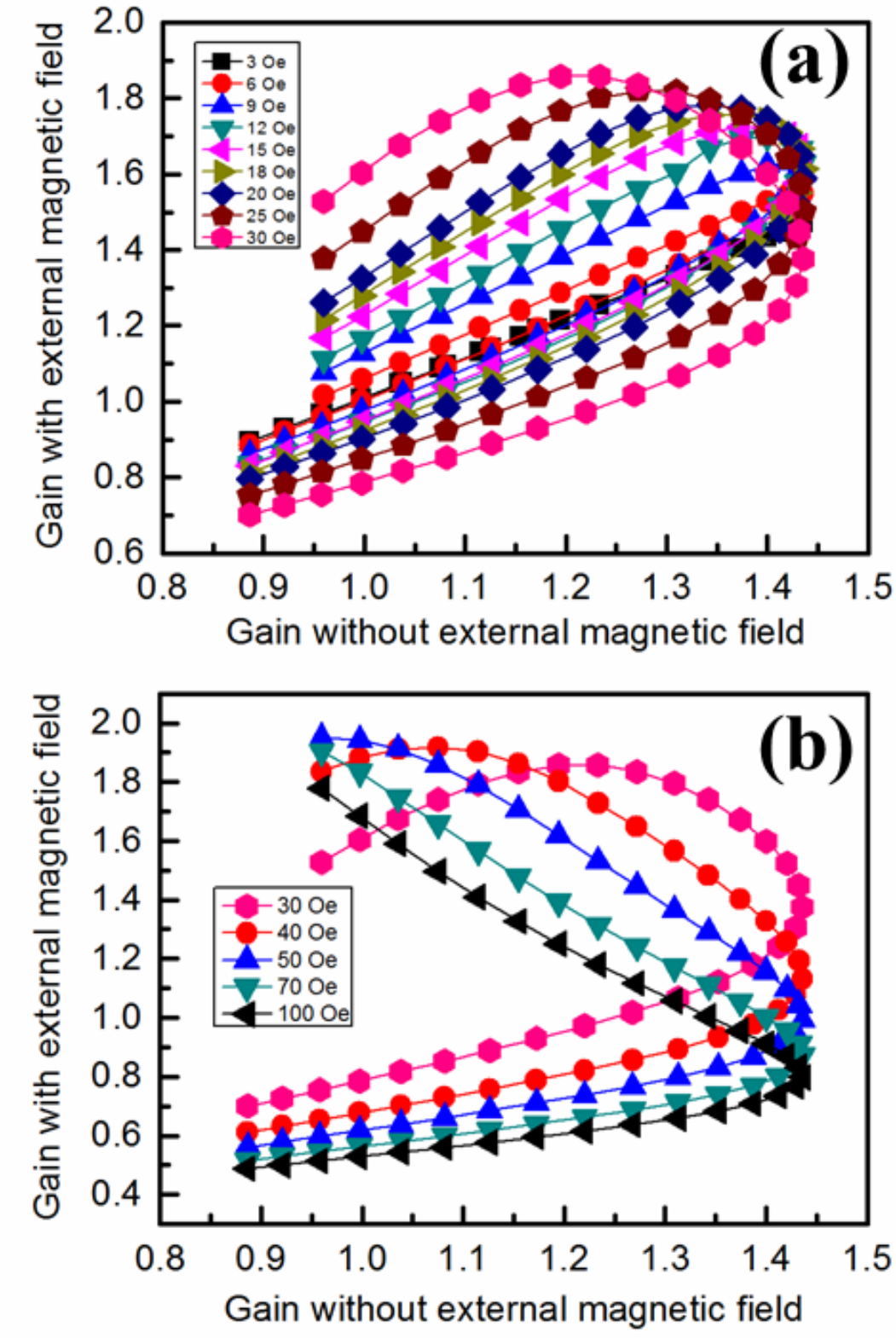

Figure 5.7 ME transformer voltage gain change in the frequency range of 26.6kHz~27.6 kHz with [(a) 3~30 Oe, (b) 30~100 Oe] and without applied DC magnetic field.

5.3 L-T co-fired NCZF/PZNT/NCZF ME transformer*

In this study, I demonstrate a co-fired magnetoelectric (ME) laminate consisting of piezoelectric/magnetostrictive/piezoelectric layers with unipoled piezoelectric transformer structure. The ME transformer was characterized by quantifying the voltage gain variation and resonance frequency shift as a function of applied DC magnetic field. I delineate the magnetic tunability feature by considering the magnetoelectric coupling and delta-*E* effect, where *E* represents the modulus of magnetic material. The ME response of the composite structure was found to be 473 mV/cm.Oe exhibiting DC field sensitivity of 100 nT under AC field of 1 Oe at 1 kHz. At a magnetic bias of 60 Oe, the transformer exhibited large frequency tunability of the order of 1.4 Hz/Oe. These results present significant advancement towards developing on-chip magnetic-field-tunable devices.

5.3.1 Dual-unipoled ME transformer design

The ME transformer was designed by combining magnetostrictive material and piezoelectric transformer in a piezoelectric/magnetostrictive/piezoelectric (PMP) laminate structure with Ag inner electrode [Figure 5.8(a)]. Composition corresponding to $0.2Pb(Zn_{1/3}Nb_{2/3})$-$0.8Pb(Zr_{0.5}Ti_{0.5})O_3$ [PZNT] and $Ni_{0.6}Cu_{0.2}Zn_{0.2}Fe_2O_4$ [NCZF] were selected as piezoelectric and magnetostricitve materials, respectively. Green tapes of above composition were prepared by tape-casting method. Laminated green bodies (20×20×0.6 mm^3) with Ag conductor paste (DuPont 9770) as intermediate electrode were pyrolyzed and sintered at 400^{o}C (2 hours) and 930^{o}C (4 hours) respectively. Sintered composite was then

*Reprinted with permission from [138], Copyright 2014, AIP Publishing LLC.

electroded using silver paint (DuPont 7713) in a square/square pattern [Figure 5.8(b)] and poled at 3.5kV/mm [Figure 5.8(c)]. In this unipoled transformer design, the input electrode "square ring" and the center output electrode "square" are on the same side of the piezoelectric plate and are isolated from each other by a fixed gap of 1mm.[139,140] Two unipoled transformers were electrically connected in series, as shown in Figure 5.8(d). When applying the electrical excitation to the external square ring (input), the contour extensional vibration is generated and transferred to the center square (output) through the gap. At the output, the mechanical strain is converted to the electrical voltage through direct piezoelectric effect. Under an applied external DC magnetic field, the magnetostrictive layer undergoes shape change, thereby, straining the piezoelectric layer resulting in an output voltage variation and resonance frequency shift.

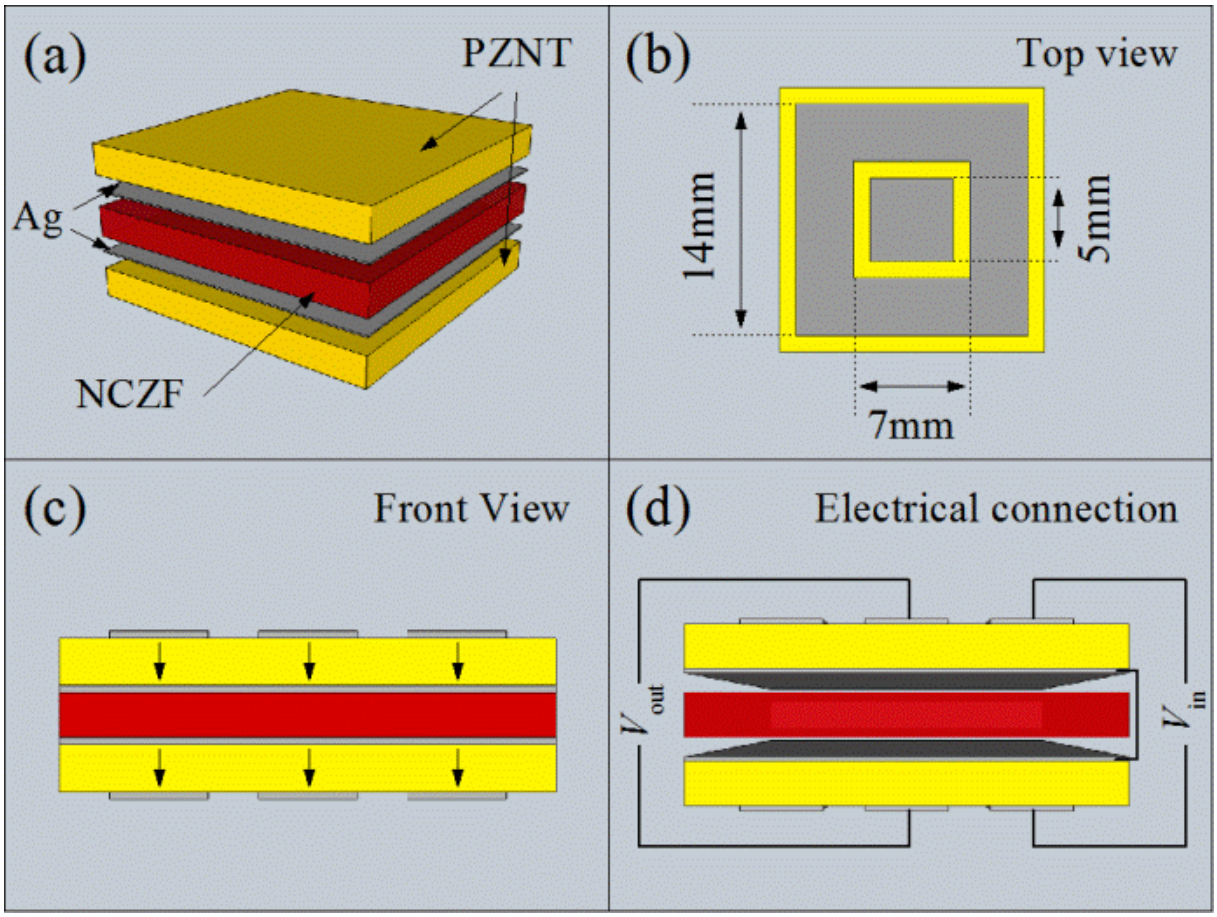

Figure 5.8 Schematic diagrams of (a) Co-fired PZNT/Ag/NCZF/Ag/PZNT laminate structure; (b) Top view of the transformer electrode pattern; (c) Front view of the polarization direction of the co-fired laminate; (d) Electrical connection of the ME transformer.

5.3.2 Performance of Co-fired ME laminate

The microstructure of the co-fired sample was examined by scanning electron microscopy (SEM, FEI Quanta 600 FEG) equipped with energy dispersive spectroscopy (EDS). The ME response was measured using a lock-in amplifier in L-T mode (Longitudinally magnetized and transversely poled) with sample placed in an AC magnetic field (Helmholtz coil) under tunable DC magnetic field (Electromagnet). Piezoelectric transformer equivalent circuit parameters were determined using impedance analyzer (HP4194A, USA) under short circuit condition. The transformer performance was characterized using HIOKI high power tester (HIOKI 3193) under constant voltage condition.[140] To study the magnetic field tunability, the ME transformer was characterized under applied longitudinal DC magnetic field.

Figure 5.9(a) shows the optical and microstructure images of co-fired PZNT/NCZF/PZNT ME transformer with dimensions 16×16×0.47 mm^3. It can be seen from Figure 5.9(a) that the thickness of NCZF and PZNT layer was ~190 μm and ~130 μm, respectively. The x-ray diffraction (XRD) pattern of corresponding layer, as shown in Figure 5.9(b), confirmed good crystallization of both spinel [NCZF] and perovskite [PZNT] phase in the co-fired ME laminate. The Ag inner electrode layer, with thickness of ~10 μm [Figure 5.9(c)], plays two important roles in this configuration: (i) a common ground bottom electrode to both input and output sections of the unipoled piezoelectric transformer, and (ii) an effective barrier layer for diffusion and chemical reaction. Prior study has demonstrated that atomic inter-diffusion and/or chemical reaction between different phases during high temperature co-firing process will dramatically decrease the ME coupling of co-fired

laminates.[141] In this case, there was no trace of interfacial elemental diffusion along the PZNT/Ag/NCZF interface, as shown in Figure 5.9(c). The corresponding EDS line scanning analysis results are shown in Figure 5.9(d), sharp elemental distribution across PZNT/Ag and Ag/NCZF interface was observed, indicating high chemical stability of each phase and effectiveness of Ag toward limiting the inter-diffusion. The co-firing techniques not only resulted in the enhancement of the elastic coupling between two phases, but also dramatically decreased the cost due to its compatibility with industrial multilayer capacitor production process.

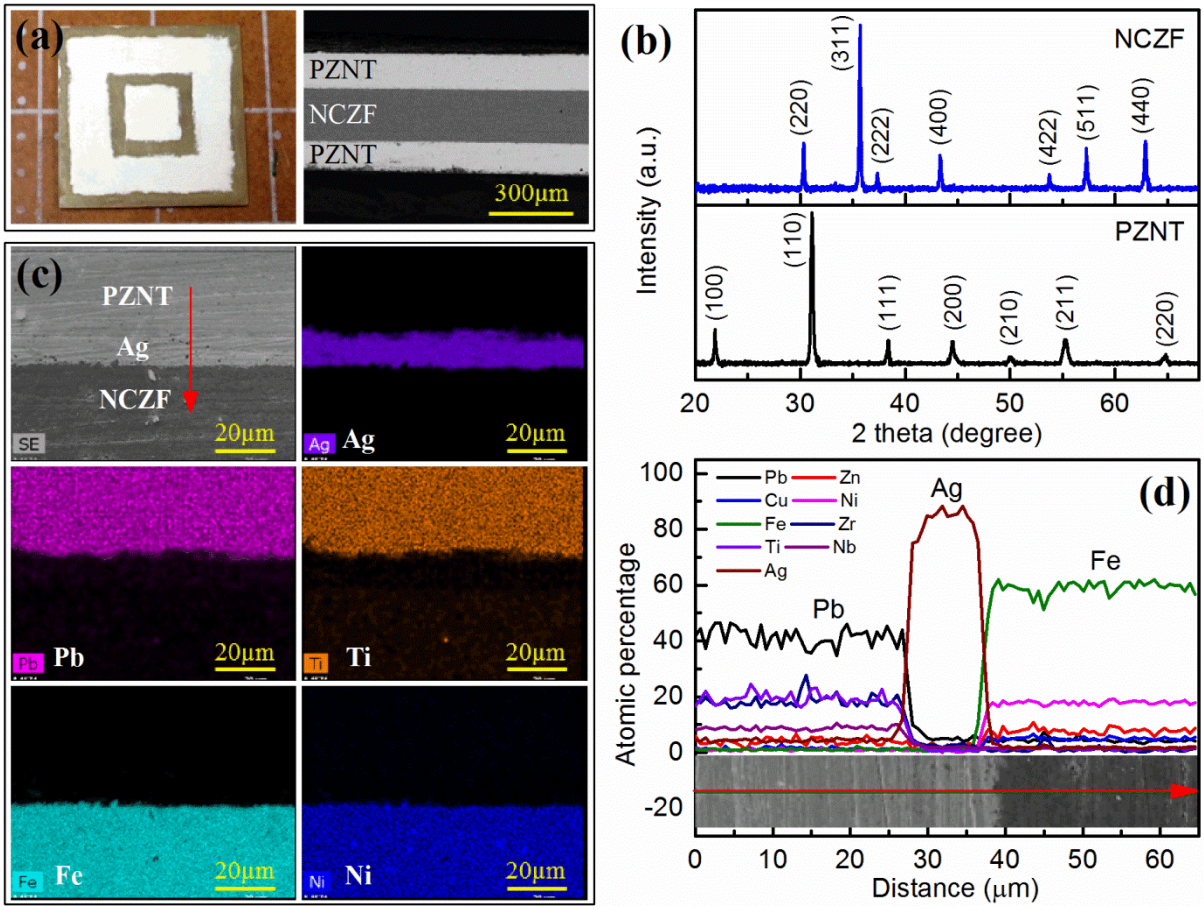

Figure 5.9 (a) Optical and cross-sectional SEM images of co-fired PZNT/NCZF/PZNT laminate; (b) XRD patterns of PZNT and NCZF layers; (c) Cross-sectional SEM images and EDS element mapping of the PZNT/Ag/NCZF interface; (d) EDS/SEM element line scanning analysis across the PZNT/Ag/NCZF interface.

Figure 5.10 shows the magnetoelectric performance of the co-fired ME laminate as a function of DC magnetic field. For ME composites, it is well-known that the ME voltage coefficient (a_{ME}) under applied DC magnetic field (H_{dc}) is tightly related with the piezomagnetic coefficient (q) of the magnetostrictive phase as:

$$\alpha_{ME} \propto \frac{\partial S}{\partial H} = \frac{d\lambda}{dH} = q, \quad (5\text{-}1)$$

Therefore, I first measured the in-plane magnetostriction (λ_{11}) of the NCZF layer as a function of applied H_{dc} along longitudinal direction by strain gauge method. It can be clearly seen from Figure 5.10(a) that the NCZF layer contracted with increasing H_{dc} and saturated at a magnitude of 15 ppm under 300 Oe. The corresponding in-plane piezomagnetic coefficient (q_{11}) reaches the maximum value of -0.33 ppm/Oe at optimum bias of H_{dc}=48 Oe. The behaviors of λ and q are identical to that of prior studies.[142,141] The ME coefficient α_{ME} of the co-fired laminate [Figure 5.10(b)] showed behavior similar to that of the pizemagnetic coefficient under AC magnetic field (H_{ac}= 1 Oe at 1 kHz), with a maximum α_{ME} (473 mV/cm.Oe) occurring at 48 Oe. The DC magnetic field sensitivity was characterized by placing the sample in a Helmholtz coil with small AC magnetic field (H_{ac}=1Oe @ 1kHz) provided by a lock-in amplifier to activate the ME laminate. Small changes in H_{dc} resulted in a step-like induced voltage change in the piezoelectric layer which was monitored by the lock-in amplifier using the time domain capture mode. DC magnetic field variation as small as H_{dc}=100 nT could be detected, as shown in Figure 5.10(c). Figure 5.10(d) shows the induced output voltages from the co-fired ME laminates in response to small changes in H_{dc}=100nT. For comparison, Park et al. have reported the ME value of 107 mV/cm.Oe at H_{dc}=80 Oe with DC sensitivity of 1 μT by using similar PMP laminates.[141] In our case, the

increase in maximum α_{ME} and DC field sensitivity was found to be 440% and 1000%, while the optimum peak ME position is 1.7 times lower. The giant improvement of ME performance can be attributed to the enhanced elastic coupling between two phases through co-fired techniques. Thus, the co-fired ME laminates exhibited high ME coupling coefficient and high sensitivity under DC magnetic field.

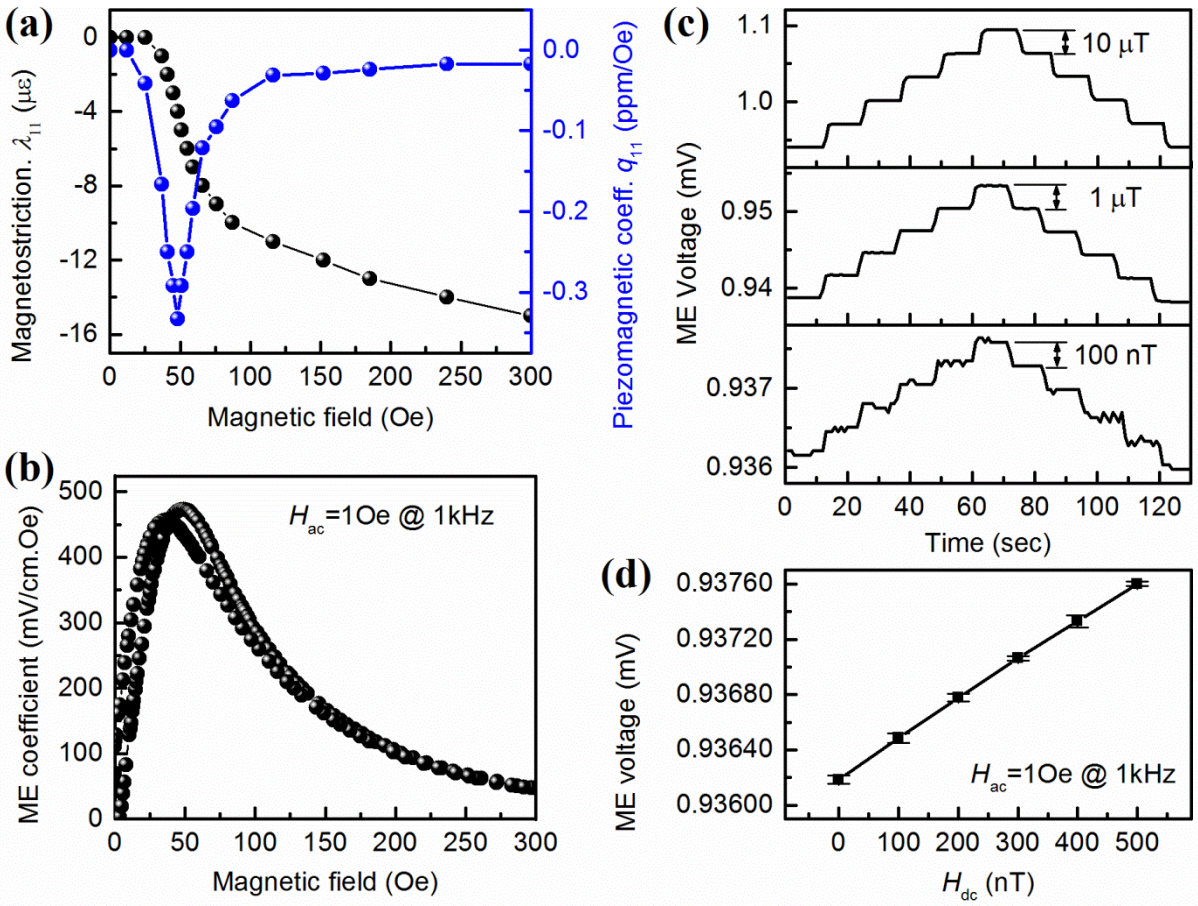

Figure 5.10 (a) Magnetostriction and piezomagnetic coefficient of NCZF; (b) ME voltage coefficient of co-fired PZNT/NCZF/PZNT laminate; (c) Comparison of the sensitivity of co-fired PMP laminate to small DC magnetic field changes (10 μT, 1 μT and 100 nT) under H_{ac}=1 Oe at f=1 kHz; (d) ME voltage output as function of DC magnetic field with sensitivity limit of 100 nT for the laminate under H_{ac}=1 Oe at f=1 kHz.

5.3.3 Performance of Piezoelectric transformer

In case of the unipoled transformer structure shown in Figure 5.8, when electrical excitation is applied to the external square ring (input), the radial extensional vibration is generated and transferred to the center square (output) through the gap (unelectroded area). At the output, the mechanical strain is converted to electrical voltage through a direct piezoelectric effect. Due to the capacitance (C) variation between the input and output section, the voltage gain of the transformer can be simply given as: Gain=$\sqrt{\frac{C_{input}}{C_{output}}}$.[140] Thus, by selecting the input/output port, the unipoled structure can provide as either a step-up or step-down voltage gain transformer. Since the two unipoled transformers are located on the opposite side of the NCZF layer, the connectivity between them is important to improve the performance. Figure 5.11(a) shows the impedance spectrum of the transformer under different electrical connections. Both radial mode (peak above 100 kHz) and bending mode (peak below 100 kHz) resonances were found to exist. Under different electrical connections, the ME transformer consisting of two unipoled structures exhibited either bending [parrallel connected] or radial [series connected] vibration mode respectively. Since the unipoled design mainly depends on the radial extensional vibration, the series connection is favourable. It should be noted that if the two transformers had perfect structural and polarization symmetry under parrallel connection, the ME voltage generated from the laminate would be completely zero under in-plane H_{dc} due to the 180^{o} voltage phase difference (opposite polarization) between the top and bottom PZNT plates.

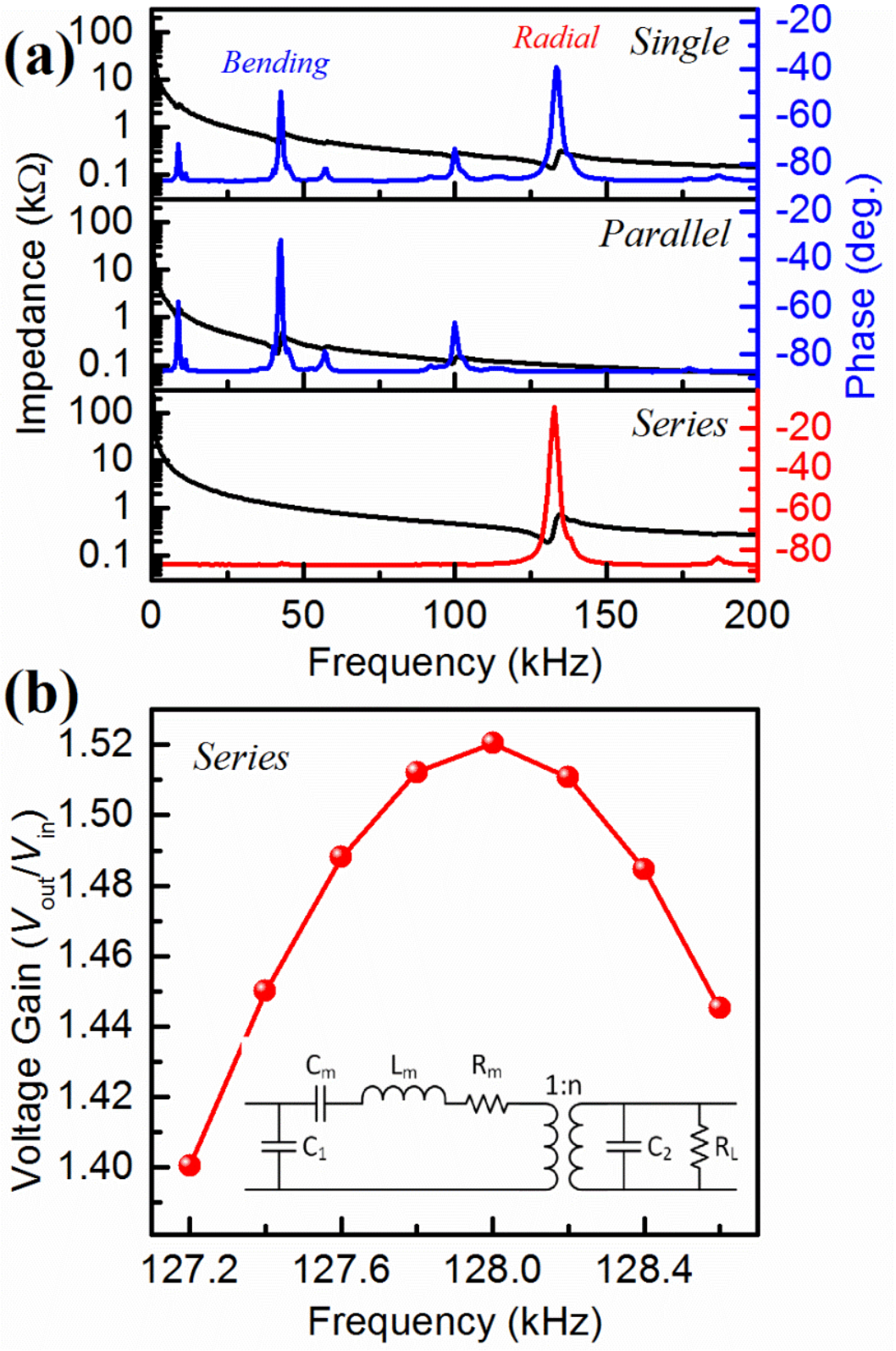

Figure 5.11 (a) Impedance and phase spectra for the co-fired transformer in single mode, parallel connection mode and series connection mode; (b) Piezoelectric transformer voltage gain as a function of frequency under series connection mode.

Next, I characterized the voltage gain performance of the ME transformer. Constant input voltage of 200 mV was applied on the square ring (input) and the output voltage was measured from the center square section. Figure 5.11(b) shows the measured voltage gain (G, ratio of output voltage to input voltage) of the ME transformer in the frequency range from 127 kHz to 129 kHz. The maximum G was obtained at resonance frequency (f_r) of 128 kHz with the magnitude of 1.52. This resonance enhanced operating mode can be explained by the equivalent circuit as shown in the inset of Figure 5.11(b). In this circuit, R_m, L_m and C_m are the motional resistance, inductance, and capacitance, n is the transformation ratio, C_1 and C_2 are the input and output damped capacitances, and R_L is the resistive load. The lumped equivalent circuit components can be determined from the impedance curve near resonance frequency by short circuiting one of the terminals.[140] The theoretical voltage gain of transformer can be calculated using the expression:[143,144]

$$G = \frac{V_2}{V_1} = \frac{1}{n\sqrt{\left(\frac{1}{n^2}+\frac{C_2}{C_m}-(2\pi f_r)^2 L_m C_2+\frac{R_m}{R_l}\right)^2+\left\{(2\pi f_r)\left(R_m C_2+\frac{L_m}{R_l}\right)-\frac{1}{2\pi f_r C_m R_l}\right\}^2}}, \quad (5\text{-}2)$$

Table 5.1 summarizes the equivalent circuit parameter of the input and output sections in the resonance-antiresonance frequency range. The optimized resistive load (2.2 kΩ) was determined by $R_L = 1/(2\pi f_r C_2)$. Using Equation (5-2), theoretical voltage gain of 1.4 was calculated, which is comparable with the experimental data shown in Figure 5.11(b).

Table 5-1 Equivalent circuit parameter of the ME transformer

Input (output short circuited)			Output (input short circuited)		
R (Ω) [R_m]		238.4	R (Ω)		2855.9
L (mH) [L_m, L_1]		10.3	L (mH) [L_2]		107.3
C_a (nF) [C_m]		0.14	C_a (nF)		0.014
C_b (nF) [C_1]		3.3	C_b (nF) [C_2]		0.56
R_m (Ω)	L_m (mH)	C_m (nF)	C_1 (nF)	C_2 (nF)	$n=\sqrt{L_2/L_1}$
238.4	10.3	0.14	3.3	0.56	3.2

5.3.4 Magnetic Field Tunability

Next, I investigated the magnetic field tunability effect of the ME transformer by exciting the specimen under varying DC bias. The ME voltage coefficient of the input and output port of the ME transformer was measured separately under a longitudinally applied $H_{dc,}$ as shown in Figure 5.12(a). Both ME responses (α_{ME}=412 mV/cm.Oe @ 65 Oe) were in the same range as that of the ME laminate [Figure 5.10(b)]. The small discrepancy of the α_{ME} between the input/output section may arise from the structural asymmetry of the ME transformer during fabrication. Next, ME transformer performance as a function of frequency was compared under varying H_{dc}. Figure 5.12(b) shows the measured voltage gain G as a function of frequency with H_{dc} varying from 0 Oe to 2500 Oe. It is clearly noticed that the magnitude of maximum voltage gain decreased and the peak position (resonance frequency) shifted as a function of H_{dc}. The magnitude of maximum voltage gain and corresponding resonance frequency shift are summarized as a function of H_{dc} in Figure 5.12(c). It is obvious that the resonance frequency decreases first with increasing H_{dc} showing a minimum magnitude of 127.9 kHz in the range of 60~80 Oe, and then increases with increasing H_{dc}. The shift of f_r is tightly related to the magnetoelectric coupling of the ME laminate, where the highest α_{ME} value was found to occur around H_{dc}=65 Oe [Figure 5.12(a)]. In order to compare the magnetic field induced voltage tunability, I plotted the voltage gain with and without external magnetic field as shown in Figure 5.12(d). There is a significant hysteresis in the magnitude of voltage gain as the frequency increases across the resonance, implying a large change in the magnitude of voltage gain under H_{dc} as compared to that of zero-field condition. It can be also noticed a large frequency shift under varying H_{dc} at the same

magnitude of the voltage gain.

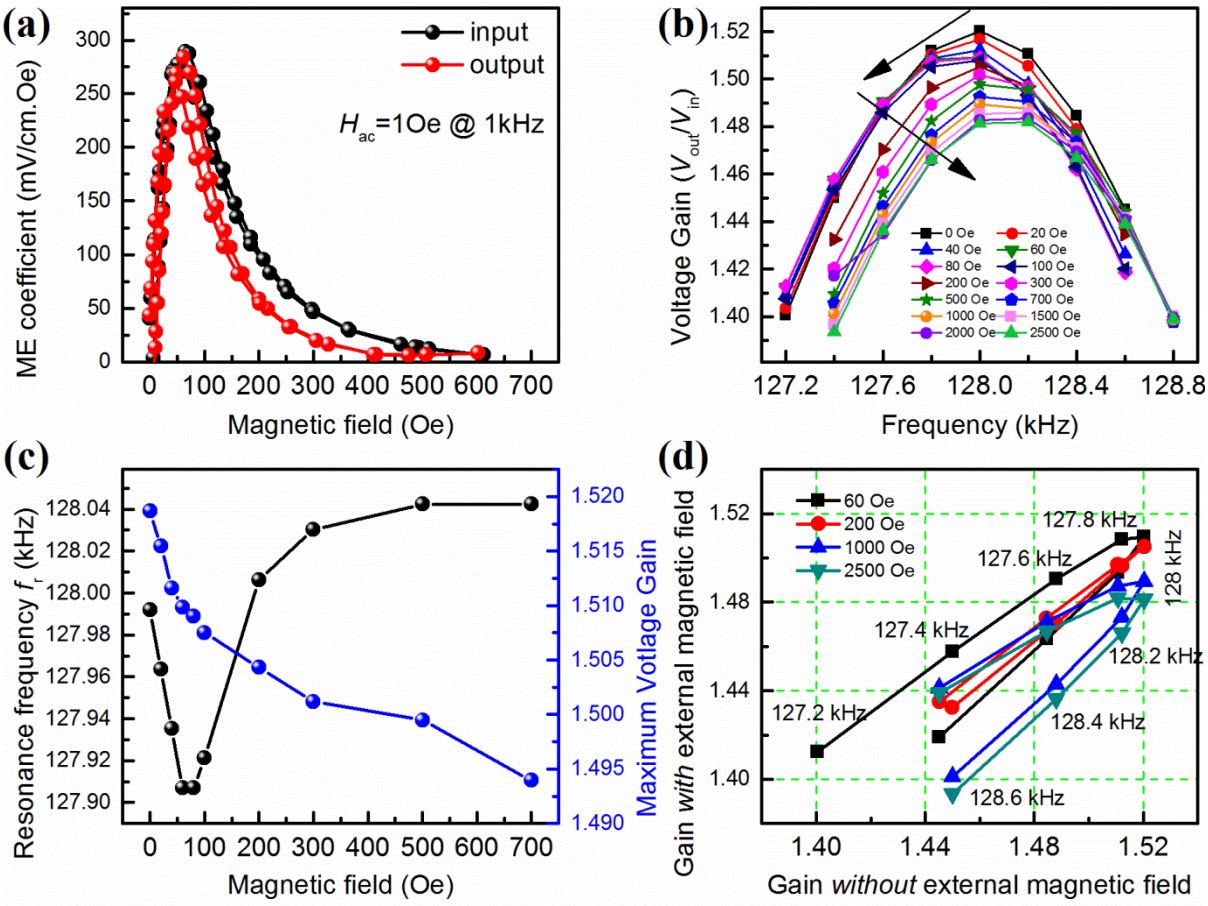

Figure 5.12 (a) ME coefficient of the input/output port of the co-fired ME transformer; (b) ME transformer voltage gain as a function of frequency under application of various external DC magnetic field range from 0 Oe to 2500 Oe; (c) Variation of resonance frequency and maximum voltage gain as a function of external DC magnetic field; (d) Characterization of ME transformer voltage gain change with and without applied external DC magnetic field in the frequency range of 127.2 kHz~128.6kHz.

From these results, two observations can be immediately made: (1) resonance frequency shift [Figure 5.12(c)] matches well with the corresponding magnetoelectric response [Figure 5.12(a)] under DC magnetic field; (2) large resonance frequency tunability [($f_{r.o}$-$f_{r.H}$)/H=1.4 Hz/Oe, where $f_{r.o}$ and $f_{r.H}$ are the resonance frequencies under zero and non-zero magnetic field condition] was realized under small DC magnetic field in the range of 60~80 Oe. Taking into account Equation (5-1) and the results of piezomagnetic coefficient in Figure 5.10(a), the corresponding magnetoelectric response can be easily explained. The shift of resonance frequency can be further understood by tracing the changes in Young's modulus (E_y) of magnetic material under DC magnetic field. The longitudinal resonance frequency is given as $f_n \approx (n/2l)\sqrt{E_y/\rho}$, where l and ρ are the average length and density of the composite and n is the harmonic mode order.[145] The percent change in E_y is widely known as the delta-E (ΔE_y) effect given as:[146,147]

$$\frac{\Delta E_y}{E_y} = \frac{E_y - E_y^0}{E_y}, \tag{5-3}$$

where E_y^0 is the Young's modulus at H=0. The variation of E_y in ferromagnetic materials is tightly related to the magnetic domains since the magnetostriciton is a result of domain rotation and domain wall motion. Thus, under external magnetic field, the forced E_y variation plays an important role in providing the shift of resonance frequency through the expression:[146]

$$\delta f_r = \frac{\Delta E_y f_r}{2E_y(1+v)z} \frac{(3+v)z^2 J_0^2(z) - 8z J_0(z) J_1(z) + [(1+v)z^2 + 4(1-v)] J_1^2(z)}{z[J_0^2(z) + J_1^2(z)] - 2J_0(z) J_1(z)}, \tag{5-4}$$

where z=kR, v=-s_{12}/s_{11} is Poisson's ratio, k=$\sqrt{\rho s_{11}(1-v^2)\omega}$, ρ is the density, ω is the angular frequency, and $J_0(k)$ and $J_1(k)$ are Bessel functions of the first kind. Further, both theoretical calculation using Equation (5-4) and experimental studies have demonstrated a

non-monotonic variation of *f*r for magnetoelectric laminate composites[145,146,148], which matches well with our results as shown in Figure 5.12(c).

For comparison, I have summarized the development of ME transformer in Figure 5.13, including PZT-NZF 0-3 type particulate ME transformer,[133] PZT/Terfenol-D 2-2 type laminate ME transformer,[149,150] PZT/Terfenol-D laminate Rosen-type ME transformer,[151] and PZNT/NCZF/PZNT 2-2 type co-fired ME transformer. The effective magnetoelectric mediated frequency tunability were calculated and are compared in this figure. Following conclusion can be drawn from this figure: (1) Compared to prior ME transformers, a larger ME frequency tunability with the magnitude of 1.4 Hz/Oe was achieved in co-fired ME transformer, which is ~4%-228% higher, (2) the direct bonding of PZNT/NCZF/PZNT laminate by co-firing process exhibited an enhanced magnetoelectric coupling than that of epoxy bonded PZT/Terfenol-D, even though the piezomagnetic coefficient of Terfenol-D (q≈1.2 ppm/Oe) is dramatically larger than that of NCZF (q≈-0.33 ppm/Oe), (3) all the 2-2 typed ME laminates presented a superior performance compared to the 0-3 type particulate composite, indicating a larger ME coupling. Based on the above observations, it can be concluded that an effective magnetic field tunable transformer was realized by co-firing two piezoelectric transformers and a magnetostrictive layer into a PMP laminate composite structure. The performance of the structure presented in this study can be further improved by optimizing the input/output area ratio through multilayering, material composition and electrical connectivity.[140,143] The ME transformer was also found promising towards the detection of the external DC magnetic field.[133,152]

In conclusion, I successfully co-fired a PZNT/NCZF/PZNT magnetoelectric laminate

composite with built-in unipoled transformer structure. The co-fired ME laminate exhibited a large magnitude of a_{ME} (473 mV/cm.Oe) with high sensitivity (H_{dc}=100 nT). These cost-effective composites with excellent magnetic tunability feature open the possibility of developing on-chip multifunctional devices and high sensitivity magnetic field sensor.

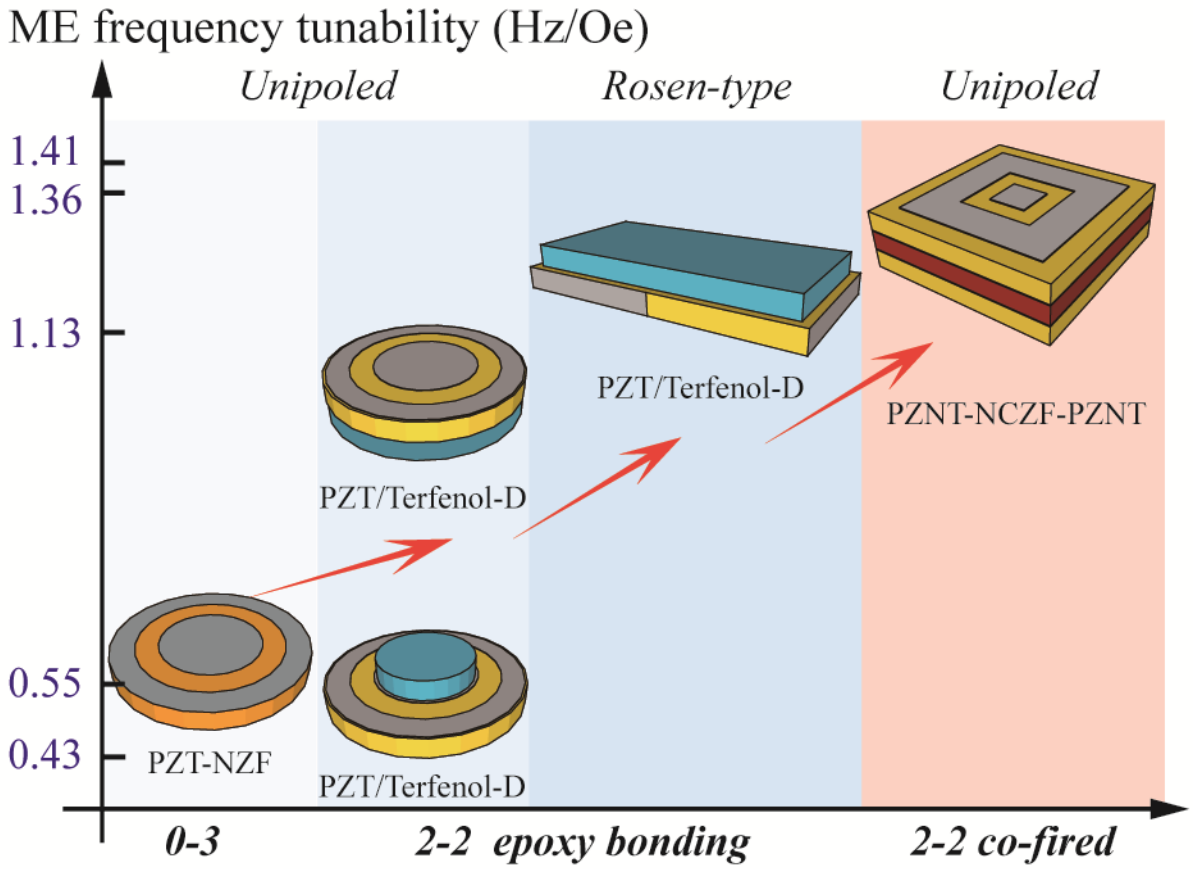

Figure 5.13 Magnetic field induced frequency tunability for different types of ME transformers.

5.4 Thin film ME transformer

Motivated by the trend of device miniaturization, many applications in electronics industry now favor small, low profile on-chip components. Magnetoelectric transformer, which consists of multiple layers of magnetostrictive materials bonded with a piezoelectric transformer, is bulky in size and incompatible with microelectronic applications. With reducing the composite dimension into micro scale and incorporate it onto silicon, studies on thin film tunable high frequency ME transformer can be obtained. In this section, I will discuss the potential of reducing the dimension of ME transformers and the process of transferring them onto silicon. A new magnetostrictive substrate based thin film ME transformer will be also proposed.

5.4.1 Design & Development strategy

Three ME transformer designs have been discussed in section 5.1~5.3 basing on the combination of piezoelectric transformers and magnetostrictive materials. Therefore, thin film magnetoelectic transformer can be split into two parts: magnetoelectric nanocomposite and thin film piezoelectric transformer. Detailed information regarding of magnetoelectric nanostructure has been discussed in Chapter 4. Thus, work on this section can be split into 3 steps: (1) Piezoelectric thin film deposition and characterization; (2) Synthesis of thin film transformer; (3) Measurement bench set up and transformer characterization.

For the ease of fabrication, a thin film ME transformer design is proposed in Figure 5.14. In this design, the ME transformer consists of a ring-dot type unipoled piezoelectric transformer and a layer of magnetostrictive material. The unipoled transformer works based

on the mechanical coupling between the input (out ring) and output (inner dot) port through radial external vibration mode. The tunability of the transformer is evoked through the induced strain from the magnetostrictive layer located on the top of transformer output port.

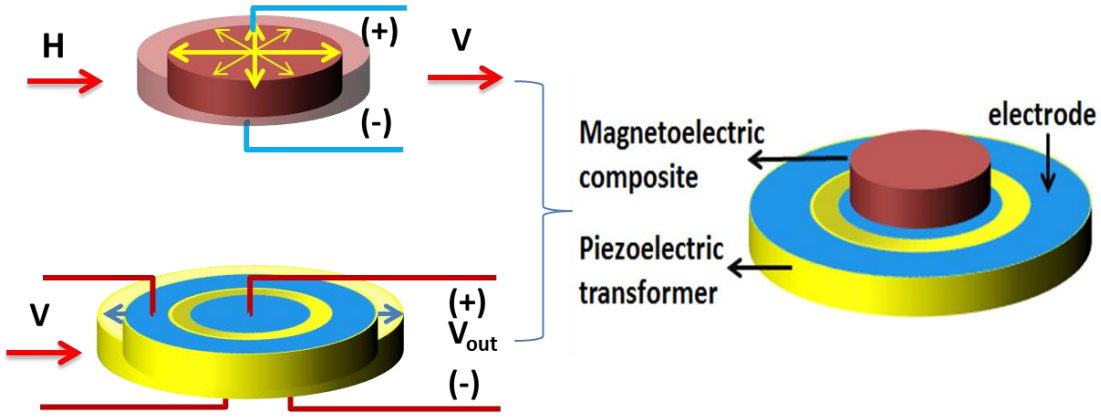

Figure 5.14 Mangetoelectric transformer consist of an unipoled piezoelectric transformer and a layer of magntostrictive material on the top of output section

5.4.2 Technical approach & Experiment results

5.4.2.1 Piezoelectric thin film deposition and characterization

The most important stage for thin film transformer fabrication is to synthesis piezoelectric thin films with high quality. Sol-gel and Pulsed laser deposition were used in the film fabrication. Sol-gel, as a low cost chemical solution deposition method, provides advantage of highly textured feasibility via optimized thermal treating.[153] However, the low deposition rate of sol-gel method is a limitation to synthesis thick piezoelectric film for device fabrication. Based on this concerning, I developed a hybrid deposition process by combining Pulsed laser deposition (PLD) and sol-gel, as shown in Figure 5.15(a). High rate of deposition and enhanced fraction of texturing on PZT thick film growth can be achieved on a pre-deposited highly textured sol-gel seed layer. Figure 5.15(b) shows highly (100)

oriented PZT film with dense, smooth and crack free surface morphology. Good piezoelectric property of the as deposited film is shown in Figure 5.15(c). Meanwhile, as discussed in chapter 4, morphology evolution and piezoelectric properties of $BaTiO_3$ films with different thickness have been studied. With a comprehensive understanding of the microstructure-properties-relation of environmental friendly lead free BTO, it can be also used as a reference for developing of thick film piezoelectric transformer based on environmental friendly materials.

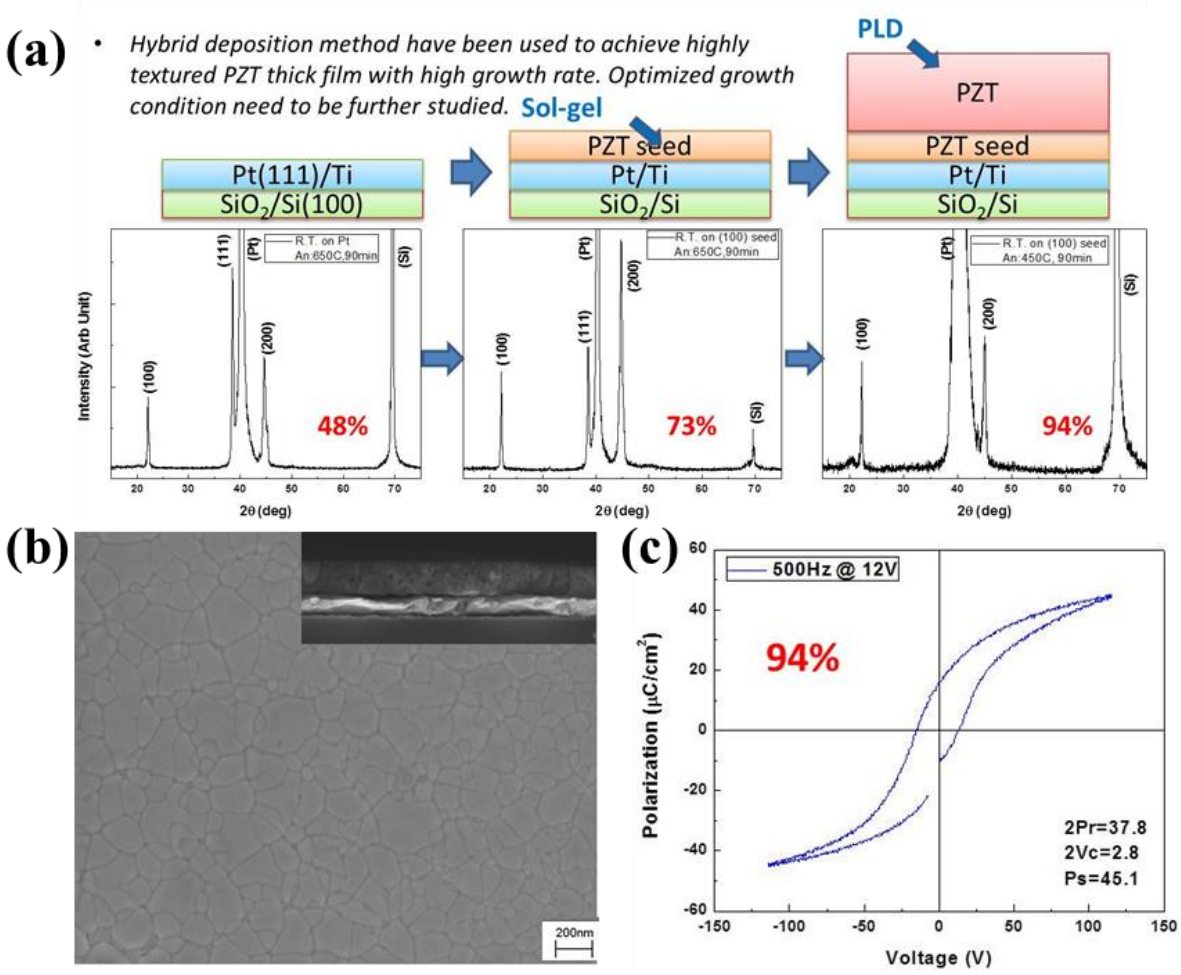

Figure 5.15 Schematic of hybrid deposition process, XRD evolution of hybrid deposited PZT films under varied annealing temperature, (b) and (c) Microstructure and piezoelectric properties of (100) highly textured $Pb(Zr_{0.6}Ti_{0.4})O_3$ thick film

5.3.2.2 Synthesis of thin film transformer

For thin film transformer fabrication, as we already successfully obtained high quality textured PZT films, the most important thing is to transfer ring-dot electrode pattern on as-deposited films. The 1st prototype unipoled PZT thin film transformer pattern was printed by Aerosol jet deposition with silver ink. Optic and scanned electron microscope images of the transformer topology and cross-section view are shown in Figure 5.16. The advantage of this work is the simple processing with eliminating the need of mask in traditional lithography process. However, the disadvantage of this prototype transformer is the thick top electrode with rough edges.

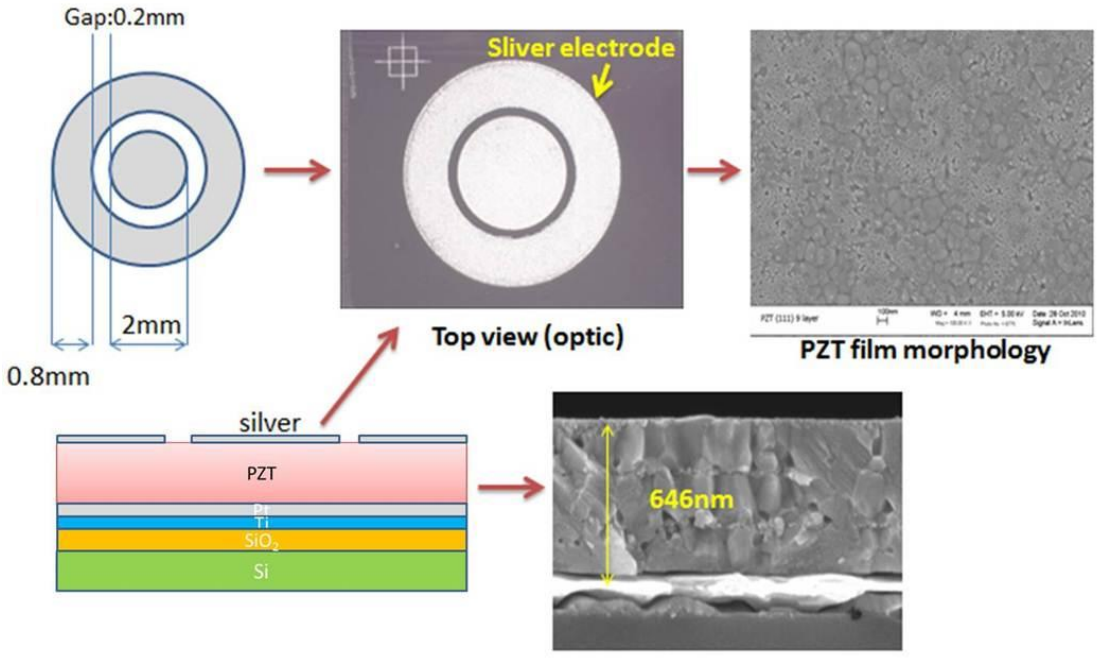

Figure 5.16 Unipoled PZT thin film transformer fabricated by Aerosol jet deposition.

Thus, I have designed and developed masks with ring-dot pattern in various dimension for our sputtering system, which provide better, thinner Pt/Au electrode for devices fabrication [Figure 5.17(a) and (b)]. In addition, the process flow has been developed as shown in Figure 5.17(c). By using this mask aided method, with the help of gold sputtering, a thin film transformer was successfully fabricated with Au ring-dot top electrode as shown in Figure 5.18. Then both input and output section of the sample were polarized @200kV/cm for 5 min at room temperature using probe station as shown in Figure 5.19.

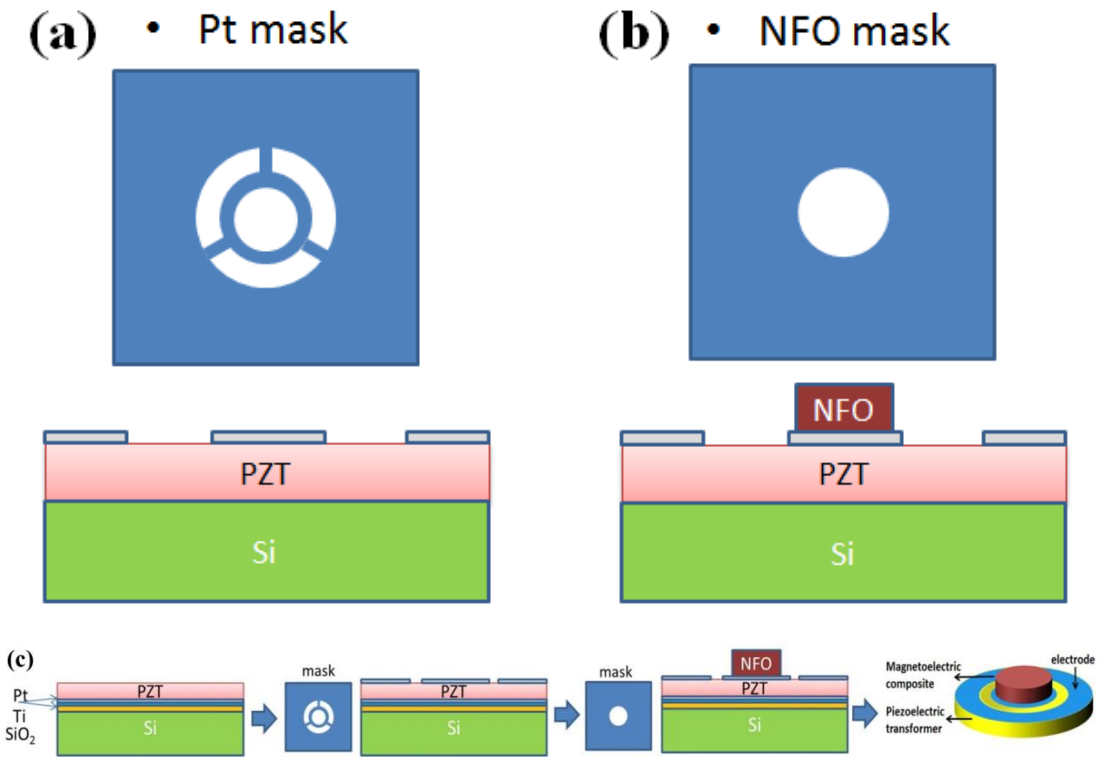

Figure 5.17 (a) and (b) Mask design for ME transformer; (c) Schematic of ME thin film transformer synthesis process flow.

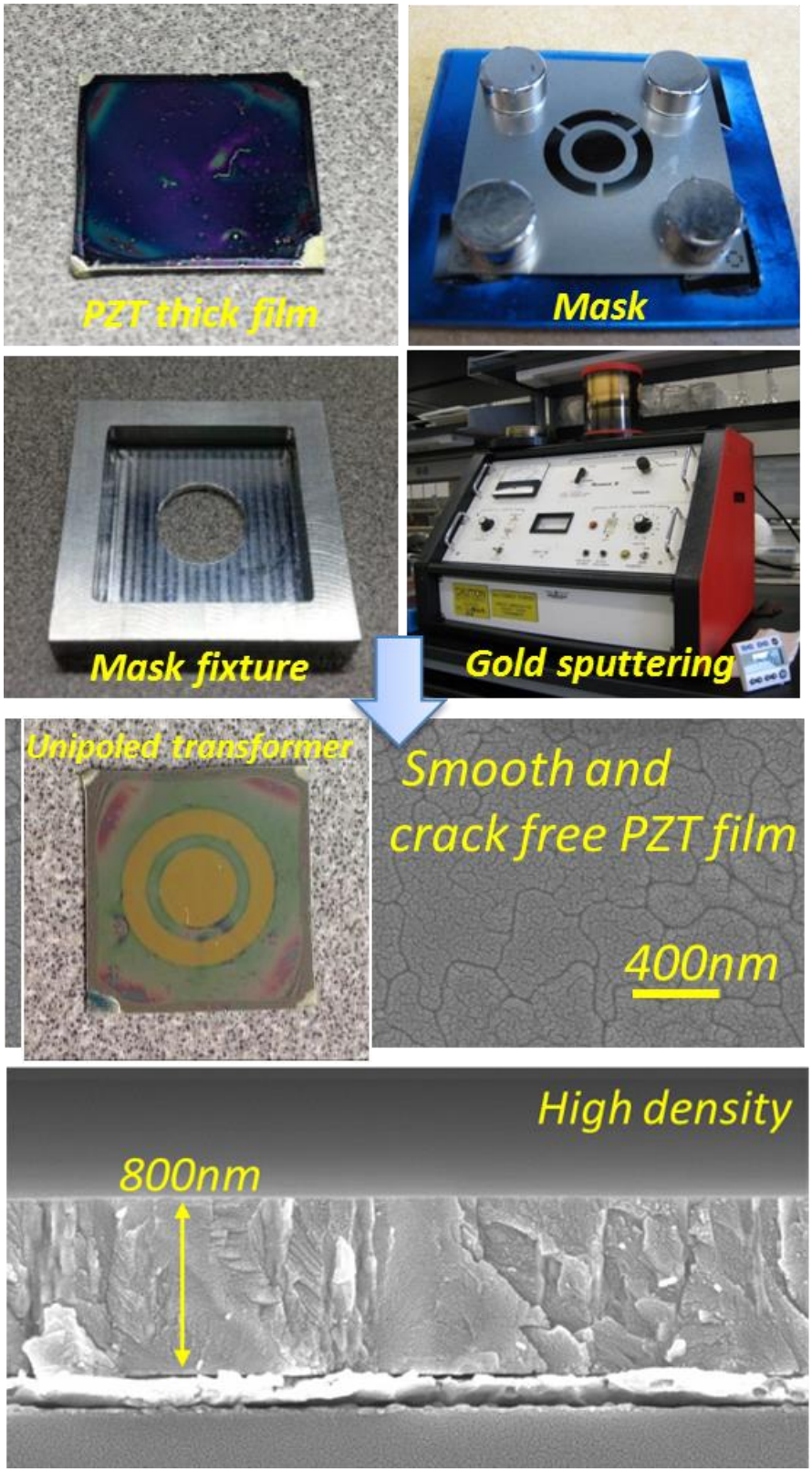

Figure 5.18 Unipoled thin film PZT transformer synthesized by Au sputtering.

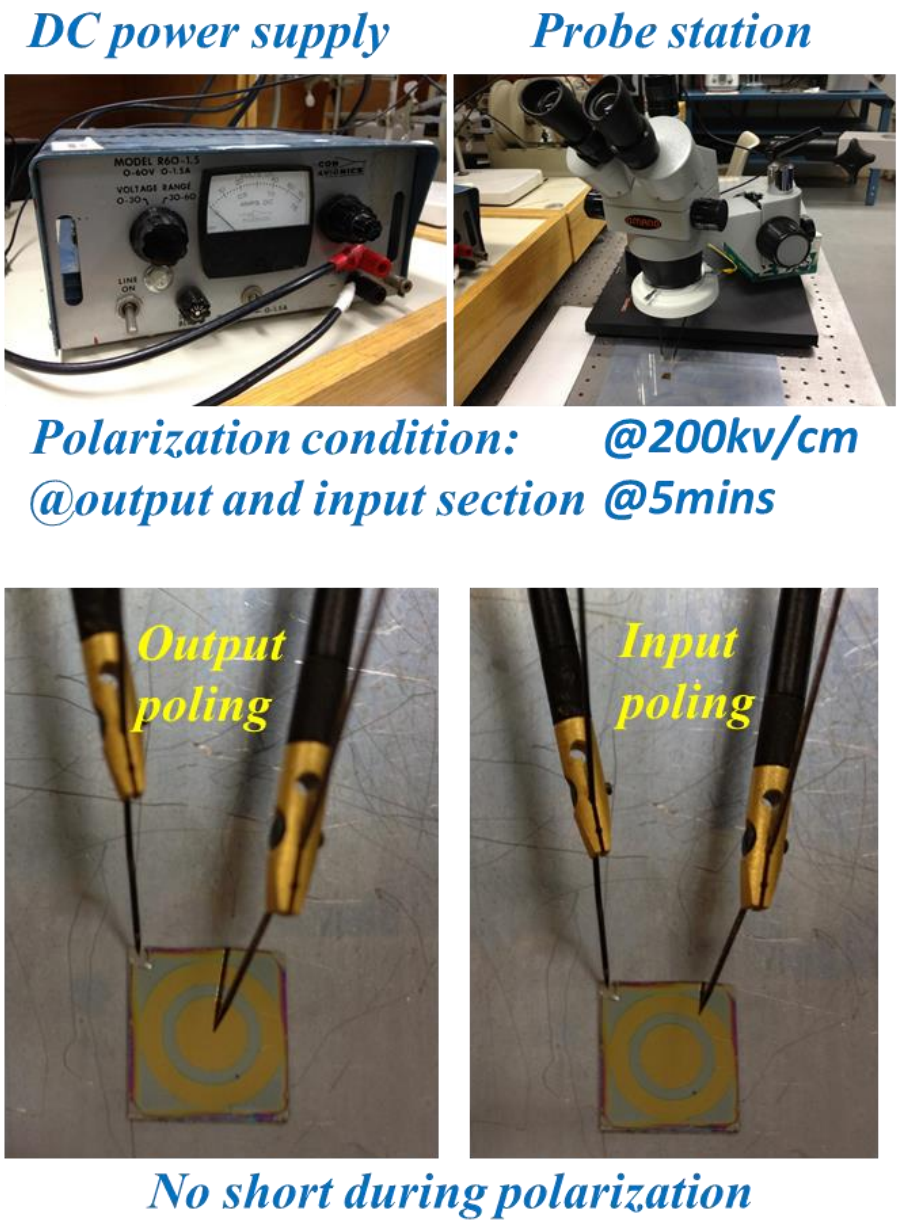

Figure 5.19 Unipoled thin film PZT transformer polarization set-up.

5.3.2.3 Measurement bench setup and transformer characterization

To further characterize the transformer performance under external magnetic field, measurement bench set-up can be sharing with bulk ME transformer characterization connection as shown in Figure 5.20.

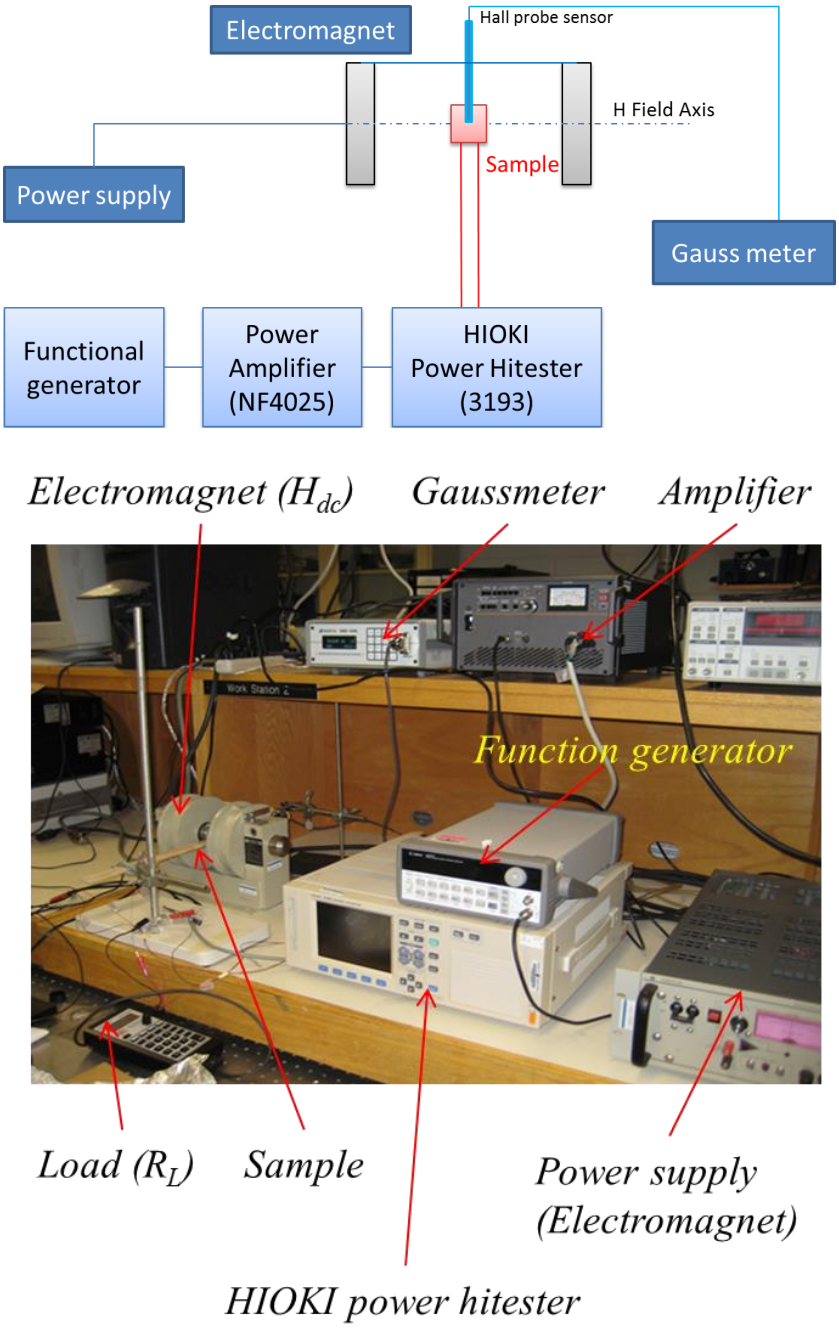

Figure 5.20 Experiment set-ups for ME transformer characterization.

5.4.3 Magnetostrictive substrate based ME thin film transformer design

Meanwhile, considering the film on substrate configuration of the current design, it may result in a relative low ME response due to the clamping effect originate from the substrate. Moreover, the tunable features of the transformers mainly depend on elastic coupling between consecutive phases. Thus, a different design in addressing this problem is needed. In this section, I proposed a new type of perovskite(film)-spinel(substrate) ME transformer, which replaces the silicon with a magnetostrictive plate as substrate. In this design, the magnetic-field-active layer can not only provide promising magnetostriction, but also rule out the clamping effect since the substrate itself is part of the ME composite.

During high quality piezoelectric film growth, high temperature with oxygen atomosphere is required. This is not an issue for common single crystal substrates like MgO, $SrTiO_3$ and so on, while for magnetostrictive substrate, this will become an difficult point for investigation. As for magnetostrictive alloy, high temperature may result in oxidization and large thermal expansion mismatch between the two phase might bring in cracks. Therefore, magnetostrictive polycrystal ceramics which can endure high temperature during thin film deposition are selected. A layer of Pt will be pre-deposited on the substrate, acting as both a bottom electrode for electrical contacting and a buffer layer for reduceing lattice mismatch.

To further illustrate the feasibility of this design, I demonstrated a prior study of depositing piezoelectric film on a polycrystalline magnetostrictive substrate.[154] Figure 5.21(a) shows the microstructure of PZT film deposited on the Pt coated $Ni_{0.8}Zn_{0.2}Fe_2O_4$ (NZF) plates at 650^{o}C by sol-gel method. The PZT film shows highly dense and homogeneous microstructure without any cracks and delimitations and maintained good adhesion with

underlying layers. Figure 5.21(b) shows the polarization-electric field (P-E) curves of the PZT films on the Pt/NZF substrate at 1kHz. As expected, remanent polarization (Pr) and coercive field (Ec) increased with increasing electrical drive. At an applied electric field of 200 kV/cm, the magnitude of Pr and Ec was measured to be 20.0 μC/cm^2 and 32.6 kV/cm, respectively. These results indicates that the high quality PZT film was successfully synthesized on the polycrystalline NZF substrate. For the ME coupling, large ME coefficient of 140 mV/cm.Oe was achieved at low DC bias field of 50 Oe under the constant condition of H_{ac}=1Oe @ 1kHz, as shown in Figure 5.21(c). This giant ME coupling is attributed to effective elastic coupling between the piezoelectric film and magnetostrictive substrate. These results indicate that the piezoelectric film on magnetostrictive substrate structure is promising for thin film ME transformer application.

Accordingly, a novel design of thin film ME transformer that possess a unipoled piezoelectric transformer on magnetostrictive substrate can be obtained, as schematics shown in Figure 5.21(d). Piezoelectric film was first deposited on a magnetostrictive substrate. Subsequently, ring/dot unipoled transformer pattern was deposited on the piezoelectric film. When the thin film ME transformer is operated under external magnetic field, the magnetostrictive substrate transfers a magnetic-field-induced strain into the thick piezoelectric film via magnetostriction, which results in an anisotropy field in the piezoelectric layer and leading to a frequency shift and voltage gain tuning. To better understand this magnetic-field-induced tunability, magnetostrictive material selection, volume/thickness ratio of two phases, buffer layer selection and electrode pattern design are important variables for investigation.

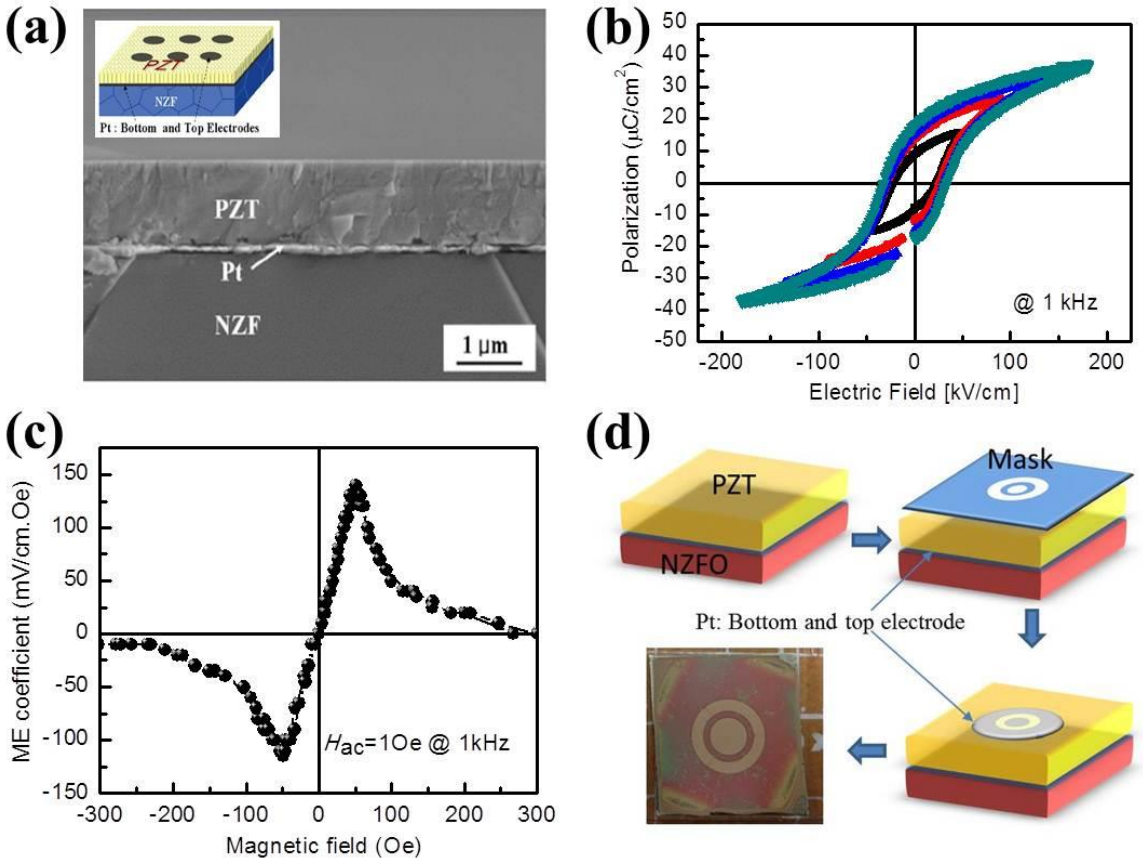

Figure 5.21 (a) SEM image of the PZT film deposited on Pt/NZF substrate, inset image is the schematic diagram of the PZT/Pt/NZF structure; (b) Polarization-electric field properties of the PZT film on Pt/NZF substrate; (c) ME coefficient of the PZT/Pt/NZF structure as a function of DC magnetic field; (d) Schematic process flow of fabricating magnetic-field-tunable thin film ME transformer.

5.5 Chapter summary

In summary of this chapter, three types of magnetoelectric transformers were developed and analyzed and their implementation into on-chip components was discussed. The magnetic-field-induced transformer tunability is characterized as working frequency and/or voltage gain variation with respect to applied DC magnetic bias, which is tightly related to the giant ME coupling of the magnetostrictive-piezoelectric laminate composites. The results of this chapter can be summarized as follows:

(1) Mulitlayer unipoled PZNT piezoelectric transformer with a high voltage gain (~9) was successfully fabricated using a tape casting and low temperature co-firing technique. With a direct bonding of Metglas foils onto the output port of the transformer using epoxy, an L-T mode ME transformer is demonstrated. This design offers the capability of broaden the working frequency bandwidth of the transformer under applied DC bias.

(2) Considering a much more efficient strain transfer and resultant giant ME coupling in L-L mode ME composites, an L-L mode Metglas/PZT ME transformer was developed using epoxy bonding technique. A giant ME coefficient of ~8 V/cm.Oe was obtained, leading to a large frequency tunability of 380 Hz under 100 Oe DC magnetic field. This design dramatically enhanced the frequency tunability feature of the ME transformer. However, the large device size and unreliable epoxy bonding hinder their application.

(3) In addressing the limitations of epoxy bonded ME transformers, a co-fired ME transformer consisting of two unipoled piezoelectric(PZNT) transformers and a magnetostrictive(NCZF) layer in a laminate configuration was demonstrated. Direct bonding of consecutive constituents through co-sintering process provides a coherent and

well-bonded interface, which is favored for effective elastic coupling. The co-fired ME transformer demonstrated a large magnetic-field-induced tunability of 1.4Hz/Oe and a high DC field sensitivity of 100 nT.

(4) Finally, the potential of implementing these ME transformers into on-chip components was discussed. A simple unipoled piezoelectric thin film transformer has been developed. A new magnetostrictive substrate based ME thin film transformer is proposed and discussed. These designs have significant promise for MEMS scalable devices.

6. Magnetoelectric Energy Harvester

The performance, capabilities, and deployment of wireless sensor networks (WSNs) and remote monitoring devices have been on the rise. This rapid proliferation of WSNs is related to the significant progress being made in CMOS electronics that has brought down the power requirements considerably. Energy harvesters are being developed to meet the power requirements of the WSNs and remote monitoring devices in order to enhance the lifetime and limitations of conventional batteries.[155,156,157,158] There are many different sources available for energy harvesting that includes solar radiations, thermal gradients, vibrations, magnetic fields, ocean waves, and wind. Among them, magnetic energy sources produce magnetic fields and vibration that can be converted into electricity through a magnetoelectric material/device.

ME composites with various connectivity and structures have been developed in order to scavenge the ambient magnetic and mechanical energies.[66,159,160] These experimental investigations have been complimented by the theoretical modeling which has led to the understanding of the role of various materials and structure parameters. To make the magnetoelectric EH practical in use, the size and weight of the harvester should be compatible with the mm-scale electronics and sensors and the ME coupling characteristics of the harvester must be tailored to match the low natural frequencies and magnitude inherent in most magnetic sources. In this section, I will briefly overview the working principle, development and design concept of the magnetoelectric energy harvester (EH). Then focus on describing magnetoelectric harvesters that can be operated in dual mode, converting vibrations and magnetic field into electricity.

6.1 Development of ME Energy Harvester

Conventional methods for vibration energy harvesting (EH) are based on the electromagnetic, electrostatic, piezoelectric and magnetostrictive mechanisms.[157,161] Among them, the piezoelectric mechanism shows relative higher power density[162], however, piezoelectric harvesters are accompanied by a narrow bandwidth or a limited operating frequency range around the center operating frequency. Piezoelectric unimorph and bimorph cantilever based structures are widely used in vibration energy harvesters as they can provide low operating frequency that can be tuned by adding the tip mass[162,163]. However, the power density available from the cantilever based structures is comparatively small at the cm-scale.[164] Electromagnetic harvesters operating on the principle of Faraday's law are able to provide higher power densities at larger dimensions.[164,165,166,167] Therefore, to enhance the power density, researchers have made an attempt at combining the cantilever structure with moving magnetic tip mass that oscillated within an inductive core.[164] Multimode energy harvesting devices with various configurations that combine electromagnetic and piezoelectric mechanism have been proposed.[167,168,169] However, under small magnetic fields, the power generated from the electromagnetic energy harvester is limited.[170] An alternative method to harvest magnetic energy is by utilizing magnetoelectric composite.[171] By selecting high performance piezoelectric and magnetostrictive materials and by optimizing the composite structure, it is expected that a high efficiency ME transducer with large voltage output under low magnetic field can be obtained.[172]

6.1.1 Working principle

For energy harvesting applications, by utilizing the product property of the ME composite, one is able to generate the electricity from stray AC magnetic field presented in the surrounding and additionally from converting the mechanical vibrations into electricity with higher efficiency. The scavenging mechanism can be described as follows: when the ME composite is placed in an AC magnetic field, the magnetostrictive layer responds by elongating or contracting, thereby, straining the piezoelectric layer that results in output voltage across the electrical load through a direct piezoelectric effect. Due to the existence of piezoelectric phase in the composite, mechanical oscillation applied on to the composite can directly create electrical voltage. Thus, a ME energy harvester can harness energy from both vibrations and AC magnetic field at the same time. The combination is expected to enhance the power output and conversion efficiency.

6.1.2 Classification

Magnetoelectric composites working as generators can produce high output voltages as the strain in the piezoelectric material is maximized with the aid of magnetostrictive material. In the following section, I will review the current status of ME energy harvesting system as a function of source as schematically depicted in Figure 6.1:

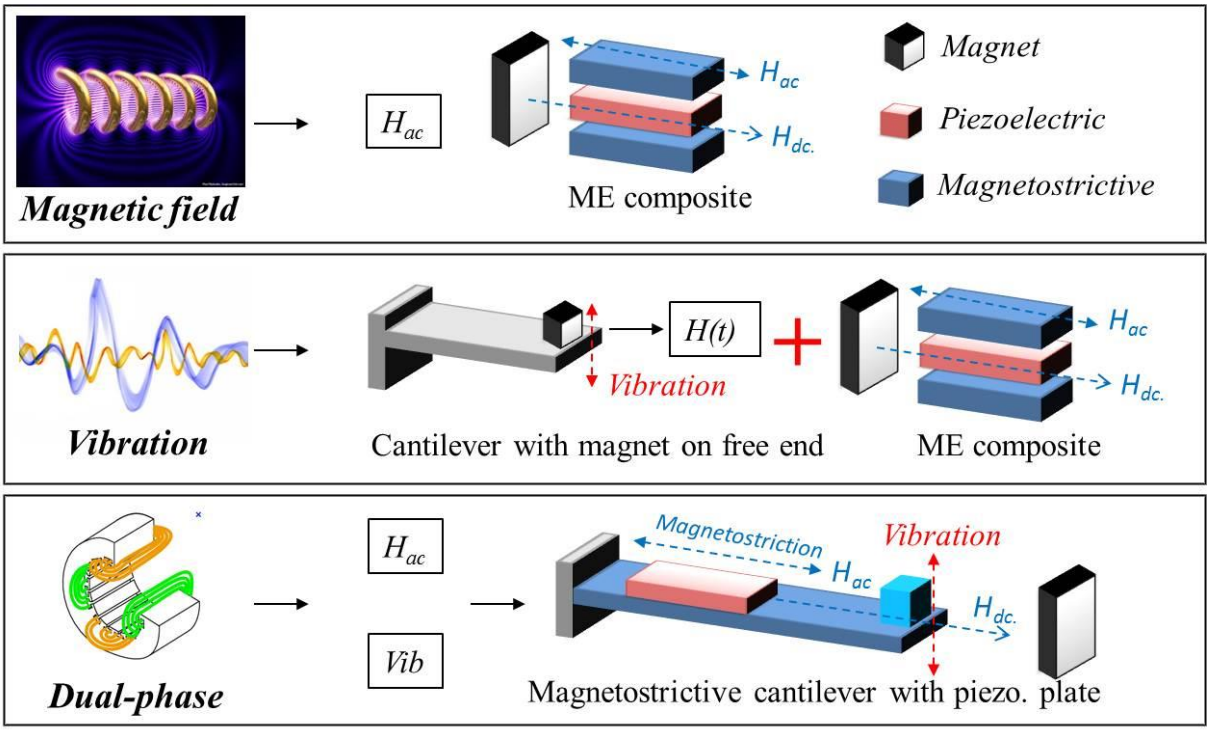

Figure 6.1 Schematic diagram depicting (a) Magnetic field ME energy harvester; (b) Vibration ME energy harvester; (c) Dual-phase ME energy harvester.

6.1.2.1 Stray magnetic field EH

Stray magnetic fields are widely present around power cables, vehicles, and industrial machines. For example, large electric motors commonly used in industrial manufacturing plants have presence of periodic stray magnetic field from the inductive windings. The oscillating magnetic field can induce an AC stress on the piezoelectric layer through magnetostriction and thereby creating electric charge through direct piezoelectric effect. The electric charge can be further processed and stored by the circuit. Recently, Li et al. developed a ME composite consisting of a magnetostrictive Terfenol-D plate, multiple piezoelectric plates and a copper ultrasonic horn, which can produce a maximum power of 6.5 μW at an AC magnetic field of 1 Oe.[159] Alternatively, Gao et al. designed an unsymmetrical bilayered Metglas/Pb(Zr,Ti)O_3 laminate in push-pull configuration with tunable resonance frequency for a 60 Hz magnetic field energy harvester and experimentally observed a power output of 16 μW/Oe with the power density of ≥200 μW/cm^3.[173] Dong et al. have demonstrated an magnetoelectric cantilever based on the push-pull type Metglas/Pb(Zr,Ti)O_3 laminate, and demonstrated a power output of 420 μW/Oe across a 50 kΩ load under an AC magnetic field of 1Oe at ~21kHz.[66]

6.1.2.2 Mechanical vibration EH

Vibration energy harvesting devices widely employ the piezoelectric or electromagnetic transduction mechanisms.[157,161,174] However, either the narrow bandwidth or the relatively low power density of these EHs hinders their potential for the practical applications. If mechanical vibration or rotation is present, AC magnetic field can be created by oscillating or

rotating a mechanical assembly that consists of magnets as schematic shown in Figure 6.1(b). Dai et al. have recently demonstrated a series of devices based on this approach where the harvester uses magnets arranged on the free end of a cantilever beam with a single or multiple ME transducers placed in the air gap between the magnets.[175,176,177,178,179,165] The ME transducers move through a concentrated magnetic flux variation and are able to provide a maximum power of ~7.13 mW (1.1 mW/cm^3) under acceleration of 2.5 g at 35 Hz.[176] Moss et al. have reported a bi-axial oscillator using a permanent-magnet/ball bearing arrangement, which produces a peak power of 121 μW from an vibration of 61 mg at 9.8 Hz.[180] Ju et al. have designed a vibration EH using a freely movable spherical permanent magnet to create time varying magnetic field for ME conversion.[181] All these approaches reported in literatures take advantage of the fact that if vibration and magnetic field are available, then magnetoelectric transducer can be used to harvest the energy simultaneously with higher power density. A vibration source can be used to create the AC magnetic field with the same frequency.

Alternatively approaches have been proposed in literatures to transform the mechanical rotation into magnetic field variation and thereby generating power through ME transducer. When a permanent magnet rotates above a ME composites, the induced magnetostriction depends on the angular position, alternates between λ_{11} and λ_{12}, and thus the piezoelectric layer is stressed and therefore generated electrical charges.[160] In their experiment, Li et al. attached a cantilever beam with magnet at the free end on a rotating host thereby creating a sinusoidal magnetic wave. The rotation induced magnetic field variation was able to generate a power of 157 μW across a 3.3 MΩ load at the rotation rate of 599 rpm.[177]

6.1.2.3 Dual-phase EH

To further enhance the efficiency and power output of the ME energy harvester, researchers have made an attempt towards generating power from mechanical vibration and alternating magnetic field simultaneously, termed as dual-phase mode. Since the ME effect in composites is a product property of magnetostrictive and piezoelectric mechanism, the induced strain from different phases is expected to be combined together. Based on this hypothesis, several ME energy harvesters have been developed.[66,182,183] As schematically depicted in Figure 6.1, by utilizing magnetostrictive layer as both magnetic field-strain conversion layer under magnetic field and flexible substrate under mechanical vibration, the composite structure can provide an additive effect. In dual mode operation, magnetoelectric energy harvesters have demonstrated the potential to scavenge magnetic field energy and vibration energy with high conversion efficiency. Dong et al. first demonstrated a multimodal system for harvesting magnetic and mechanical energy. In this design, the system consists of a cantilever beam with tip mass and a magnetoelectric laminate attached in the center of the beam, which generates an open circuit voltage of $8V_{p\text{-}p}$ under vibration of 50 mg and AC magnetic field of 2 Oe.[66] Further, by utilizing a PMN-PZT single crystal/Ni cantilever laminate, Rahul C. Kambale et al. was able to obtain a maximum a_{ME} and power output of 7.28 V/cm.Oe and 1.31mW at resonance mode under 0.7g acceleration.[182] However, in these combinations, solenoid and/or permanent magnet is required as the DC magnetic field source, which dramatically increases the size and therefore limits the power density. In the following section, I will address these issues with a newly designed self-biased dual-phase ME EH.

6.2 Dual-phase self-biased ME Energy Harvester*

The ME composites, combining piezoelectric and magnetostrictive phases, have been found useful in both magnetic and vibration harvesting applications, because of the coexistence of piezoelectric and magnetoelectric effects. That is, the electric charges can be generated from mechanical vibration at the piezoelectric layer through a direct piezoelectric effect, and the magnetic field induced magnetostriction can be converted into charges through a direct magnetoelectric effect. The combination is expected to enhance energy collection and conversion efficiency. Thus, multimode magnetoelectric energy harvesters have been developed. Dong et al. first demonstrate a multimodal system for harvesting magnetic and mechanical energy. In this design, the system consists of a cantilever beam with tip mass and a magnetoelectric laminate attached in the center of the beam, which can generate an open circuit voltage of 8 $V_{p\text{-}p}$ under vibration of 50 mg and AC magnetic field of 2 Oe.[66] Further, by utilizing a PMN-PZT single crystal/Ni cantilever laminate, Rahul C. Kambale et al. was able to obtain a maximum a_{ME} and power output of 7.28 V/cm.Oe and 1.31mW at resonance mode under 0.7g acceleration.[182] However, in these combinations, solenoid and/or permanent magnet is required as the DC magnetic field source, which dramatically increases the size and therefore limits the power density. In addressing these issues, this section I will discuss a novel ME energy harvesting system utilizing self-biased magnetoelectric response, which can generate a giant output performance in the absence of DC magnetic.[183]

---

*Reprinted with permission from [184], Copyright 2013, AIP Publishing LLC.

6.2.1 Design & Working principle

The dual-phase energy harvester was designed by combining magnetoelectric laminate [Figure 6.2(a)] and piezoelectric unimorph [Figure 6.2(b)] structure in a cantilever configuration. The schematic design of the EH is illustrated in Figure 6.2(c). The prototype consisted of a magnetostrictive/ piezoelectric (M/P) laminate structure fabricated by using a MFC (dimension 40×10 mm^2, Modal: M-4010-P1, Smart Material Corp., USA) and a layer of 0.25-mm-thick Ni beam (dimension 80×10 mm^2). The composite was laminated by using epoxy resin (West System, USA). A series of Ni disks were added as tip mass (1.1 gram) at the free end of cantilever for dynamic force excitation at the mechanical resonance. The Ni beam plays several important roles in this configuration: (i) a magnetostrictive phase in the ME laminate, (ii) a magnetic-field-active cantilever for the piezoelectric bender, (iii) a ferromagnetic phase with low field magnetic hysteresis and non-zero piezomagnetic coefficient that is essential for self-biased magnetoelectric response[46]. When placed in an AC magnetic field, the magnetostrictive layer responds by elongating or contracting, thereby, straining the piezoelectric layer that results in output voltage across electrical load. Under the external vibration, oscillation of the cantilever can directly create strain in the piezoelectric layer and therefore produce electrical voltage. In the absence of the applied DC magnetic field, large magnetoelectric (ME) voltage can still be obtained via the self-biased ME effect. Thus, by incorporating a self-biased magnetostriction layer as a substrate for the piezoelectric layer, a ME harvester can be created for harnessing energy from both vibrations and AC magnetic field at the same time without the need for DC bias. The question is: “Are these effects additive?”

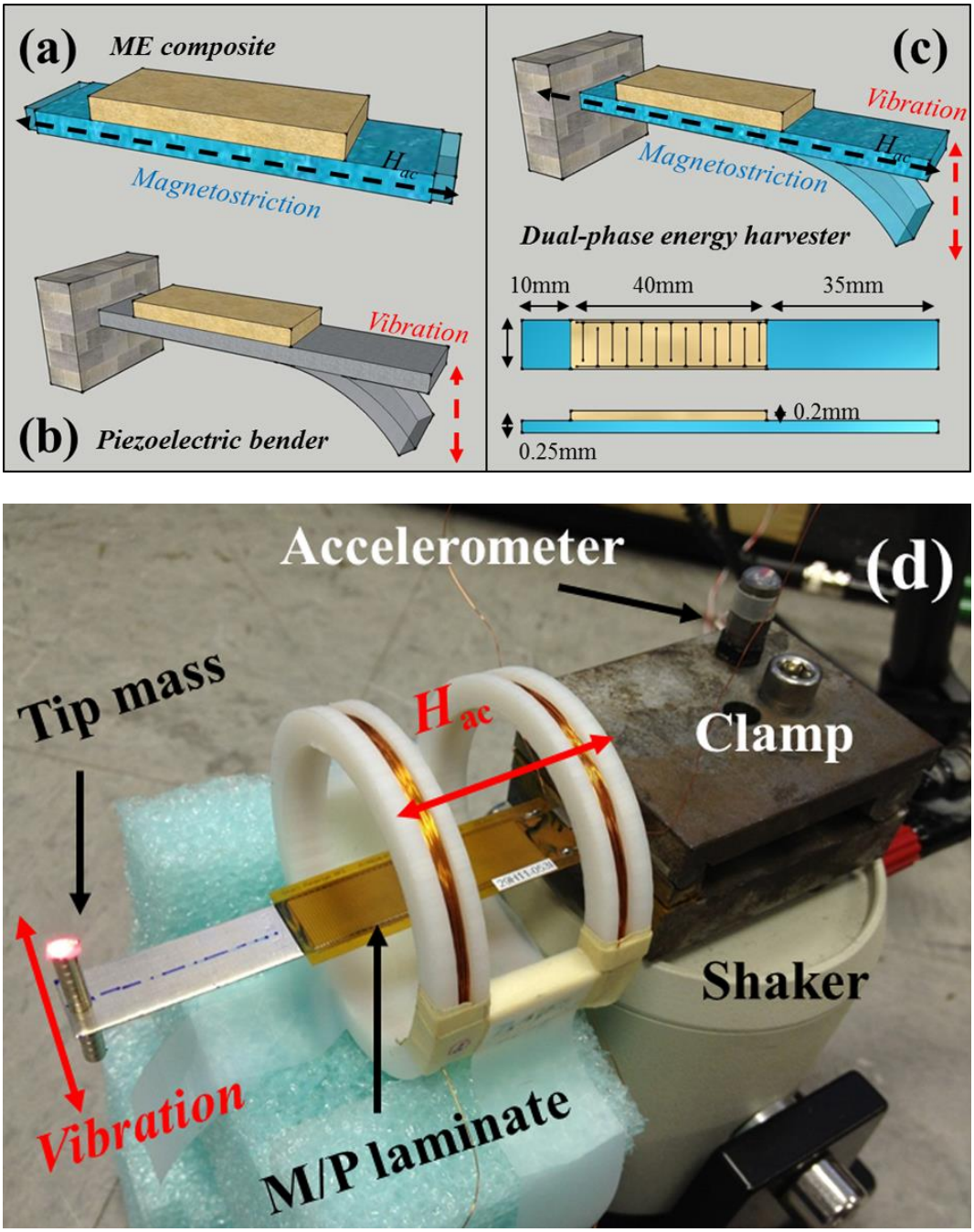

Figure 6.2 Schematic diagram depicting the (a) Magnetoelectric composite consist of piezoelectric layer and magnetostrictive layer, (b) Piezoelectric bender consist of piezoelectric layer and elastic cantilever, (c) Self-biased dual-phase energy harvester consist of magnetostrictive bender and ME composite; (d) Picture of the Ni-MFC dual-phase energy harvester and the experimental setup for characterization.

Figure 6.2(d) illustrates the working principle of the fabricated prototype and also shows the experimental setup used for characterization. To characterize the harvester under dual-phase mode, the transducer was simultaneously excited by an AC magnetic field (H_{ac}) generated by the Helmholtz coil and a mechanical oscillation generated by the shaker. The ME response was measured in the L-L mode (longitudinally magnetized and longitudinally poled) configuration with sample located in the center of the Helmholtz coil. The induced ME voltage was monitored using a lock-in amplifier. For the vibration test, the magnetostrictive cantilever was mounted on a LDS shaker (Bruel & Kjaer North America, Inc.) using a custom clamp. The mechanical excitation (acceleration, *a*, as well as frequency, *f*) was generated by the shaker using a function generator and high power amplifier (Hewlett-Packard 6862A). The shaker base acceleration and displacement at the free end of the harvester were monitored by a low mass accelerometer (PCB U352C22) and a laser vibrometer (PDV 100, Polytech, Inc.). All the signals, including output from laser vibrometer, power spectrum of acceleration, the transfer function from base acceleration to tip mass acceleration and output voltage of the harvester, were collected by spectral analyzer (SigLab, Model 20-42).

6.2.2 Harvest Magnetic Energy

I first characterized the magnetoelectric properties of the bilayer laminate as function of DC magnetic field H_{dc} with H_{ac}=1Oe at 1kHz as shown in Figure 6.3(a). For comparison, conventional Metglas-MFC bilayer composite with similar dimension and configuration was also fabricated and analyzed. The ME relationship for composites is given as: [185,78]

$$\alpha_{\mathrm{ME}} = \left|\frac{\partial T}{\partial S} \times \frac{\partial D}{\partial T} \times \frac{\partial E}{\partial D}\right| \times \frac{\partial S}{\partial H}\ , \tag{6-1}$$

where S is the mechanical strain, T is the mechanical stress, D is the electric displacement, E is the electric field, and H is the magnetic field. Since the first part of the above expressions is a non-magnetic factor, one can re-write Equation (6-1) as:

$$\alpha_{\mathrm{ME}} \propto \frac{\partial S}{\partial H} = \frac{\mathrm{d}\lambda}{\mathrm{d}H} = q, \tag{6-2}$$

which indicates that the ME coefficient is directly related to the nature of ferromagnetic phase (λ: magnetostriction, q: piezomagnetic coefficient). As most of the ferromagnetic materials exhibit zero piezomagnetic coefficient near zero bias[172], the α_{ME} of Metglas-MFC structure increased from zero to a peak value (α_{ME}=3.2 V/cm.Oe, H_{dc}=12.5 Oe) at the optimum bias and then decreased. The need of optimum DC magnetic bias to achieve maximum α_{ME} requires permanent magnet or electromagnet as external magnetic field source which increases device size and electromagnet interference. However, the α_{ME} of Ni-MFC bilayer shows a hysteretic behavior during H_{dc} sweep (anticlockwise direction) with a large response of ~±1.25 V cm^{-1} Oe^{-1} at zero DC magnetic bias, ~98% of the maximum α_{ME} value (1.38 V cm^{-1} Oe^{-1}). This results from the combination of the hysteretic behavior of magnetostriction and demagnetization effect[46]. It should be noted that alternative approaches have been suggested for the case of self-biased ME response that rely on the built-in magnetic bias through ferromagnetic graded structure[51,186] and angular dependence of exchange bias field[57]. However, in comparison with the bilayer Ni-MFC structure, these other self-biased configuration are rather complex in fabrication and implementation.

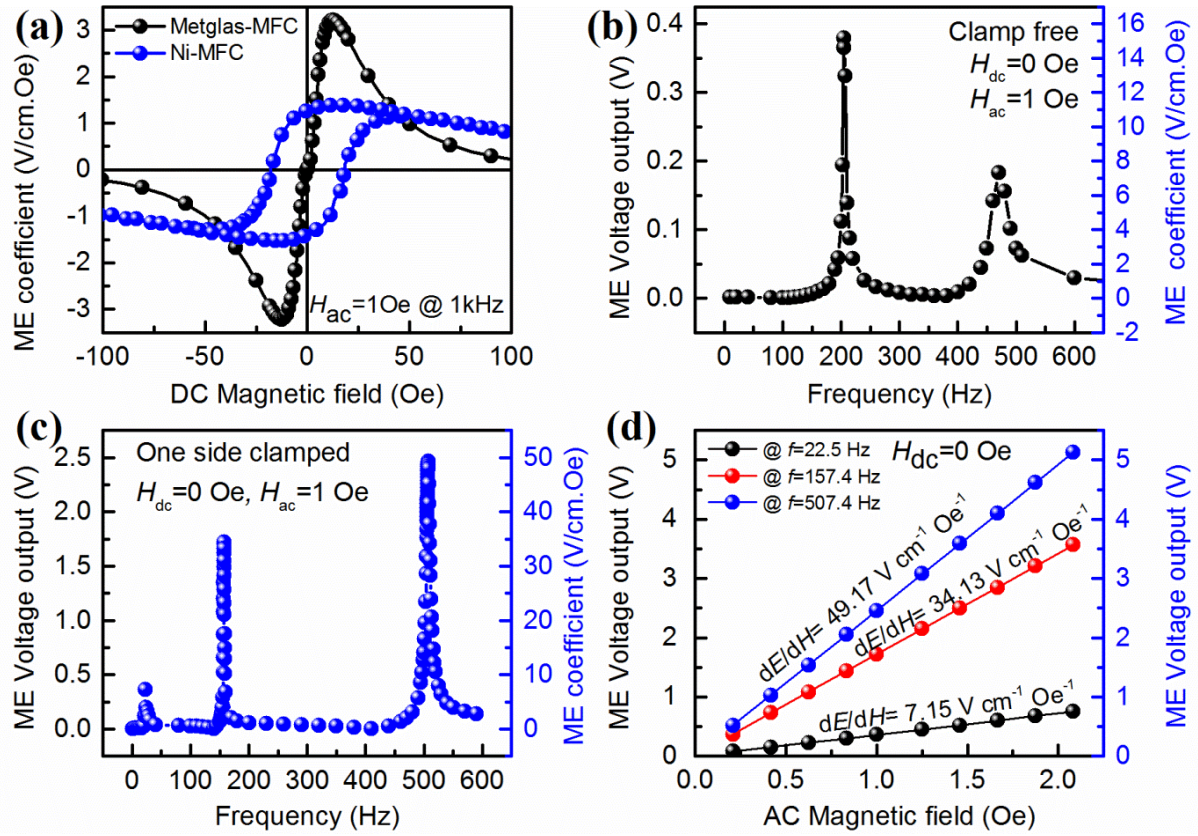

Figure 6.3 Magnetoelectric response from the as-fabricated Ni-MFC self-biased magnetoelectric composite: (a) ME coefficient of Metglas-MFC and Ni-MFC bilayer laminates as function of DC magnetic field; (b) ME voltage output as a function of applied AC magnetic field frequency for the self-biased ME composite under clamp free condition. Magnetoelectric response of the dual-phase energy harvester consist of magnetostritive Ni cantilever and Ni-MFC composite: (c) ME voltage output as a function of applied AC magnetic field frequency under zero-biased condition (H_{dc}=0 Oe); (d) Source free (H_{dc}=0 Oe) ME voltage output of the dual-phase EH measured at different frequency under various applied AC magnetic field.

Next in order to study the resonance enhanced ME coupling, I investigated the frequency dependence of self-biased ME performance in Ni-MFC laminate. Under zero-biased condition (H_{dc}=0 Oe), resonance peaks with improved ME voltage output corresponding to bending modes were observed, as shown in Figure 6.3(b). It should be noted that even though there is no applied H_{dc}, self-biased ME response follows the same trend and exhibits enhanced magnitude of voltage coefficient at resonance frequency[46]. To quantify the dual-phase operation, the ME laminate was clamped at one end and a Ni tip mass was attached at the free end for enhanced bending and reducing the resonance frequency. As shown in Figure 6.3(c), under longitudinally excited alternative magnetic field (H_{ac}=1 Oe), the first bending resonance was found to occur at 22.5Hz. The next two resonance modes occurred at 157.4 Hz and 507.4 Hz, respectively. It can be also noticed that the ME voltage output increased with increasing frequency where the maximum ME coefficient with the magnitude of ~50 V cm^{-1} Oe^{-1} was obtained at the resonance frequency of 507.4 Hz. In direct ME coupling, the measured coupling coefficient is the field conversion ratio between applied AC magnetic field (H_{ac}) and induced AC electric field (E_{ac}),

$$\alpha_{\mathrm{ME}} = \delta E_{ac}/\delta H_{ac} \tag{6-3}$$

Thus, to further enhance the ME voltage output, the effect of magnetic field strength (H_{ac}) was investigated under zero bias condition at different frequency. Figure 6.3(d) shows that the ME voltage output linearly increased with increasing AC magnetic field at three longitudinal resonance frequencies. The α_{ME} calculated from the slope was found to be 7.15 V cm^{-1} Oe^{-1} at 22.5 Hz, 34.13 V cm^{-1} Oe^{-1} at 157.4 Hz and 49.17 V cm^{-1} Oe^{-1} at 507.4 Hz. These calculated values match quite well with the measured value in Figure 6.3(c). Large ME

voltage with the magnitude of > 5V was achieved at 507.4Hz, H_{ac}= 2 Oe which can be further increased with increasing H_{ac}. These results demonstrate that by operating the ME energy harvester under AC magnetic field, large ME voltage output can be sustained under zero DC bias condition. The performance can be further improved by increasing the magnetic field strength at resonance mode.

6.2.3 Harvest Vibration Energy

Next, I measured the output power from the ME harvester under only vibration excitation as a function of frequency and acceleration. For measuring the frequency dependence, the device was subjected to vibration by applying constant voltage to the shaker and varying the frequency. Figure 6.4(a) shows the transfer function between base acceleration and seismic mass acceleration measured by input of random excitation. The resonance frequencies under mechanical oscillations were found to be 23.1Hz, 156.8Hz and 500.0Hz respectively, which are close to that measured by applying AC magnetic field [Figure 6.3(c)]. Figure 6.4(b) depicts the frequency dependence of the open circuit voltage under the acceleration of 0.17g. The first natural bending mode was found at 20.5Hz which matches well with the data from ME response. At this operating frequency and acceleration, the optimum electric load for the ME bender was determined by measuring the voltage output and the corresponding power as function of external load,

$$P = V_{\mathrm{RMS}}^2/\mathrm{R} \tag{4}$$

As shown in Figure 6.4(c), the vibration induced maximum electrical power output was 168 μW at a matching load of 4MΩ; correspondingly, the power density was calculated to be

2.9 mW g^{-1} cm^{-3} by accounting for the total volume (~0.34 cm^3, include the volume of Ni cantilever, MFC and tip mass) of the energy harvester. This power density is quite high compared to other magnetoelectric bender with similar dimension, whose power generation was ~0.4 mW g^{-1} cm^{-3} under mechanical vibration[66]. Figure 6.4(d) depicts the increased power output as a function of acceleration magnitudes. Higher acceleration can further improve the power output. These results clearly demonstrate that a high power density can be achieved by using magnetostrictive material Ni as the cantilever for the piezoelectric bender system. Thus, the self-biased ME energy harvester exhibited high performance in harnessing magnetic field or vibration energy.

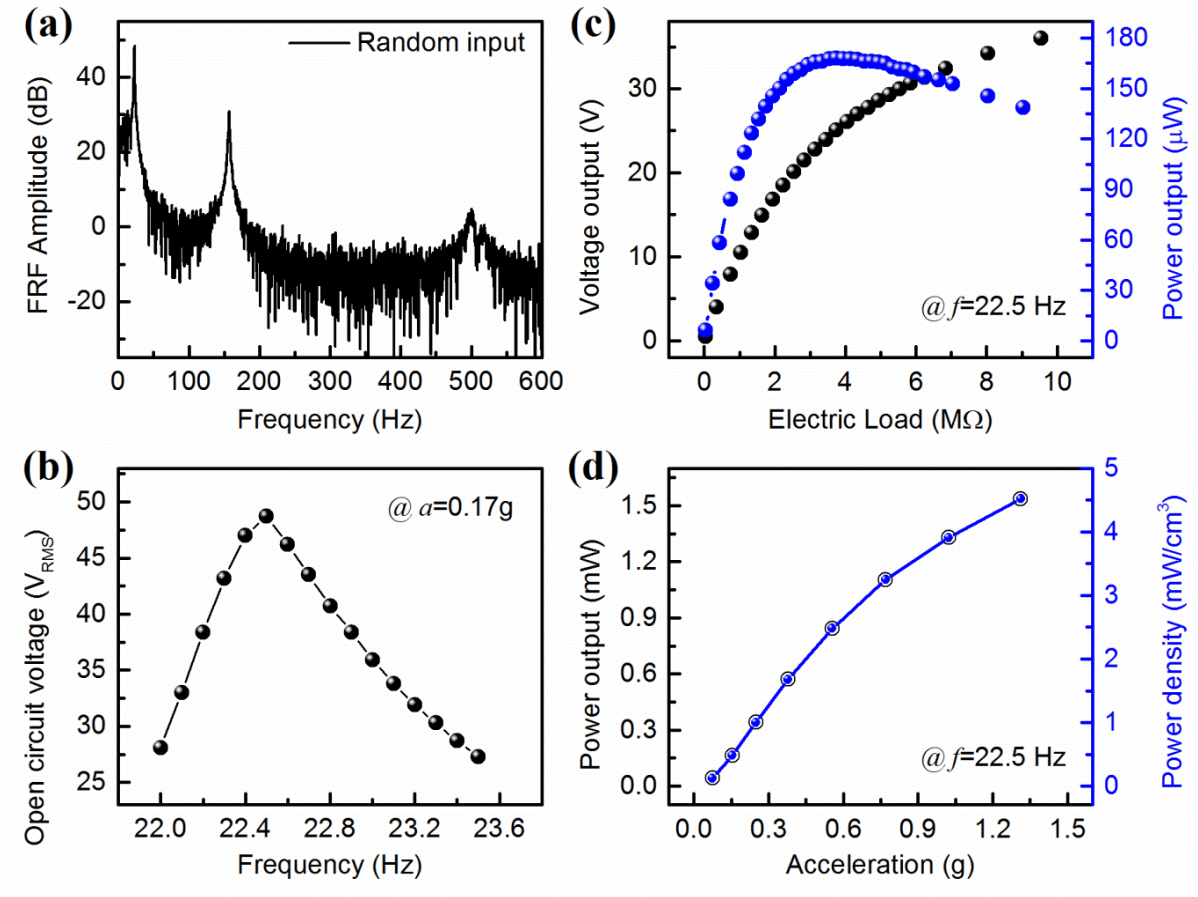

Figure 6.4 Vibration mode test of the dual-phase energy harvester: (a) Base to tip-mass transfer function used to identify the nature frequency of Ni-MFC magnetoelectric bender; (b) Open circuit voltage (RMS) output of the EH as a function of frequency under vibration condition of a=0.17g; (c) Voltage and power output of the EH as function of resistive load under vibration condition of a=0.17g, f=22.5Hz; (d) Power output of the EH for various acceleration under mechanical resonance condition.

6.2.4 Additive Effect under Dual-phase Mode

Since both magnetoelectric and piezoelectric effect occur through elastic coupling, I further investigated the additive effect of the harvester by exciting the bender with stray magnetic field and mechanical vibration simultaneously, namely in dual-phase mode. For comparison, open circuit voltage of the EH at first three resonance frequency was measured separately under: (1) stray magnetic field only (H_{ac}=1Oe), (2) mechanical vibration only (a=0.05g) and (3) dual-phase (H_{ac}=1Oe plus a=0.05g) mode, as shown in Figure 6.5(a)~(c). It can be clearly noticed that the output voltage under dual-phase mode was improved over wide range of frequency, which implies that both power density and efficiency were enhanced through additive effect. To further quantify this combined response, the peak voltage at each single mode were added and compared with the dual-phase mode as a function of operating frequency, as shown in Figure 6.5(d). In this bar chart, it is obvious that the peak voltage under dual-phase mode is close to the summation of peak voltage under each single mode, implying an additive effect was found in the dual-phase EH. The increase in voltage output at the first three resonance frequencies under dual-phase mode was found to be 2.4%, 35.5% and 360.7%.

From these results, two important observations can be made: (1) At constant acceleration and stray magnetic field, the output voltage from the vibration is much higher at lower frequency (first bending mode) while the output voltage is higher at higher frequency under magnetic field (longitudinal resonance mode). This behavior results from the strain variation along the magnetoelectric cantilever structure due to transversal (vibration) and longitudinal (magnetostriction) excitation. (2) All the voltage response measured here are under

zero-biased condition. It should be further noted here that all the previous investigations on the multimode magnetoelectric harvesters have revealed that the requirement of DC magnetic field is indispensable to enhance the power output.[66,76]

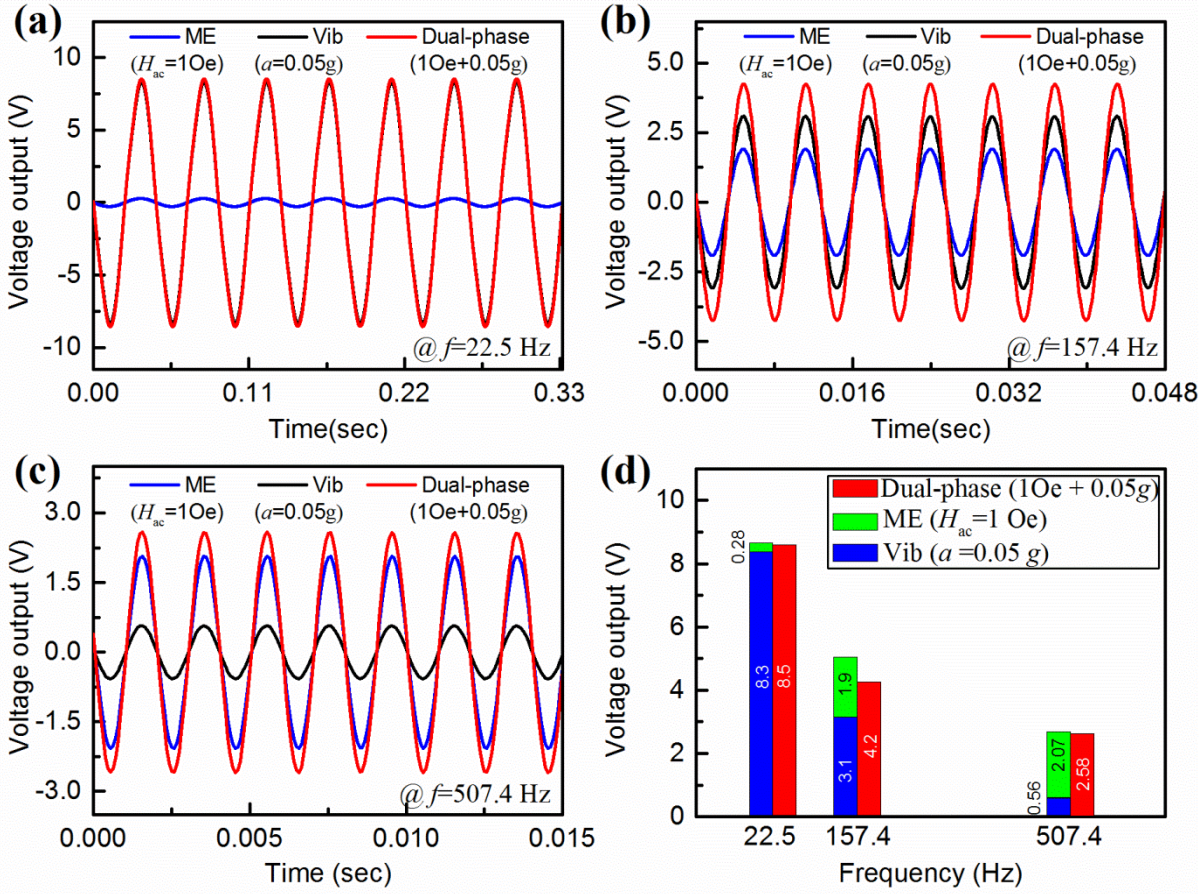

Figure 6.5 Performance of the dual-phase energy harvester working under both mechanical and magnetic condition: Open circuit voltage as function of time for the EH under only magnetic field active condition (H_{ac}=1Oe), only vibration active condition (a=0.05g) and the dual-phase mode (1Oe+0.05g) at various resonance frequency (a) 22.5 Hz, (b) 157.4 Hz, (c) 507.4 Hz. (d) Comparison of the EH voltage output at single mode and dual-phase mode under different driving frequency.

To further elucidate the performance of the EH under different (vibration/magnetic) excitations, strain distribution was simulated using the finite element model (FEM) at the first three resonance frequencies, as shown in Figure 6.6. Each simulation was conducted with a maximum element mesh size of 50μm and material contact tolerance of 1μm. The number of finite element nodes in the harvester was approximately 1 million. The simulated resonance frequencies for the harvester were 23.2Hz, 143.6Hz, and 432.7Hz. Therefore the FEM model accurately predicts the first mode but underestimates the second and third modes. The underestimation is likely due to the inhomogeneous bending behavior of the MFC, since the model does not account for imperfect bonding of the layers using epoxy. When a transverse sinusoidal force with amplitude of 1N is applied to the clamped end of the beam (similar to the case of induced mechanical vibration), the MFC at higher transversal resonance mode exhibits weaker y-strain distribution (along the thickness) [Figure 6.6(a)], which will result in decrease in voltage output. When a total longitudinal compressive force of 1N is applied to the ends of the beam (similar to the case of induced magnetostriction), the MFC at higher longitudinal resonance mode produced a much stronger x-strain distribution (along the length) as shown in Figure 6.6(b), and a resultant increase in voltage output. These trends in strain distribution agree well with the experimental results obtained from Figure 6.5(d) and imply that the higher resonance mode will generate larger strain in response to a longitudinal force. This finding is a positive step in amplifying the longitudinal or transverse strain (and thus voltage) response at a particular resonance mode.

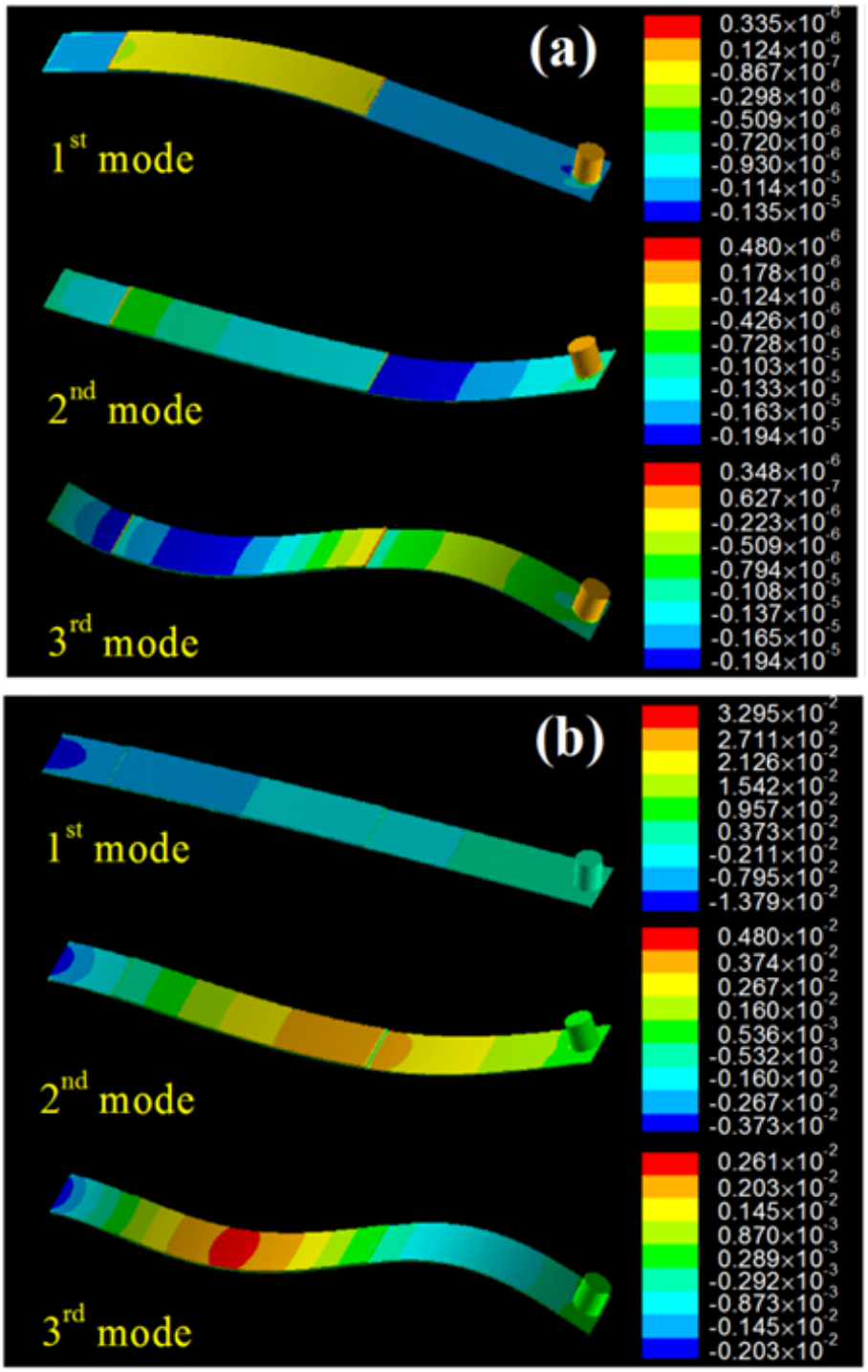

Figure 6.6 FEM simulation data of strain distribution along the magnetoelectric cantilever for the first three resonance frequency (1^{st} mode: 23.2Hz, 2^{nd} mode: 143.6Hz, 3^{rd} mode: 432.7Hz): (a) under transverse force (strain along the thickness like induced mechanical vibration), (b) under longitudinal force (strain along the length like induced magnetostriction).

In summary, the self-biased ME energy harvester consisting of Ni-MFC laminate and magnetostrictive Ni cantilever was fabricated and characterized. Large power density was achieved from the magnetoelectric cantilever under mechanical excitation which was further enhanced with the co-existence of AC magnetic field. The result of this study indicate that the power output of dual-phase self-biased ME energy harvester can be further improved by synchronizing the transversal (vibration) and longitudinal (magnetostriction) resonance frequency.

6.3 MEMS scalable potential

The simple bilayer Ni-PZT self-biased ME energy harvester in a cantilever configuration provides high capability and feasibility for incorporate into MEMS scale devices and is able to help us eliminate the effect of electromagnetic interference. To achieve this goal, growth and optimization of high quality PZT film on magnetostrictive Ni substrate is important.

Here, I investigated the potential of grown PZT film on a Ni polycrystalline magnetostrictive substrate. To prevent substrate oxidation during growth, a layer of Pt with thickness around 100 nm was coated on Ni by sputtering. PZT films were deposited by sol-gel spin coating technique with different thermal treatment conditions. Figure 6.7(a) shows the XRD pattern of Pt coated Ni substrate and as grown PZT films. PZT peaks were found in either film anneal at high temperature (675^{o}C) in air or film annealed at relative low temperature (600^{o}C) in reduced atomosphere (N_2 flow). However, second phase penetration was observed in the film anneald in air. To further confirm the performance of film grown in reduced atomosphere, PFM was conducted as shown in Figure 6.7 (b) and (c). The piezoelectric response demonstrates almost 180^{o} in phase shift and maximum amplitude around 8 pm/V in hysteresis loop with tip bias -8V to +8V. These results indicate that PZT film can be successfully synthesized on magnetostrictive substrate by optimizing the growth condition and preventing substrate oxidation.

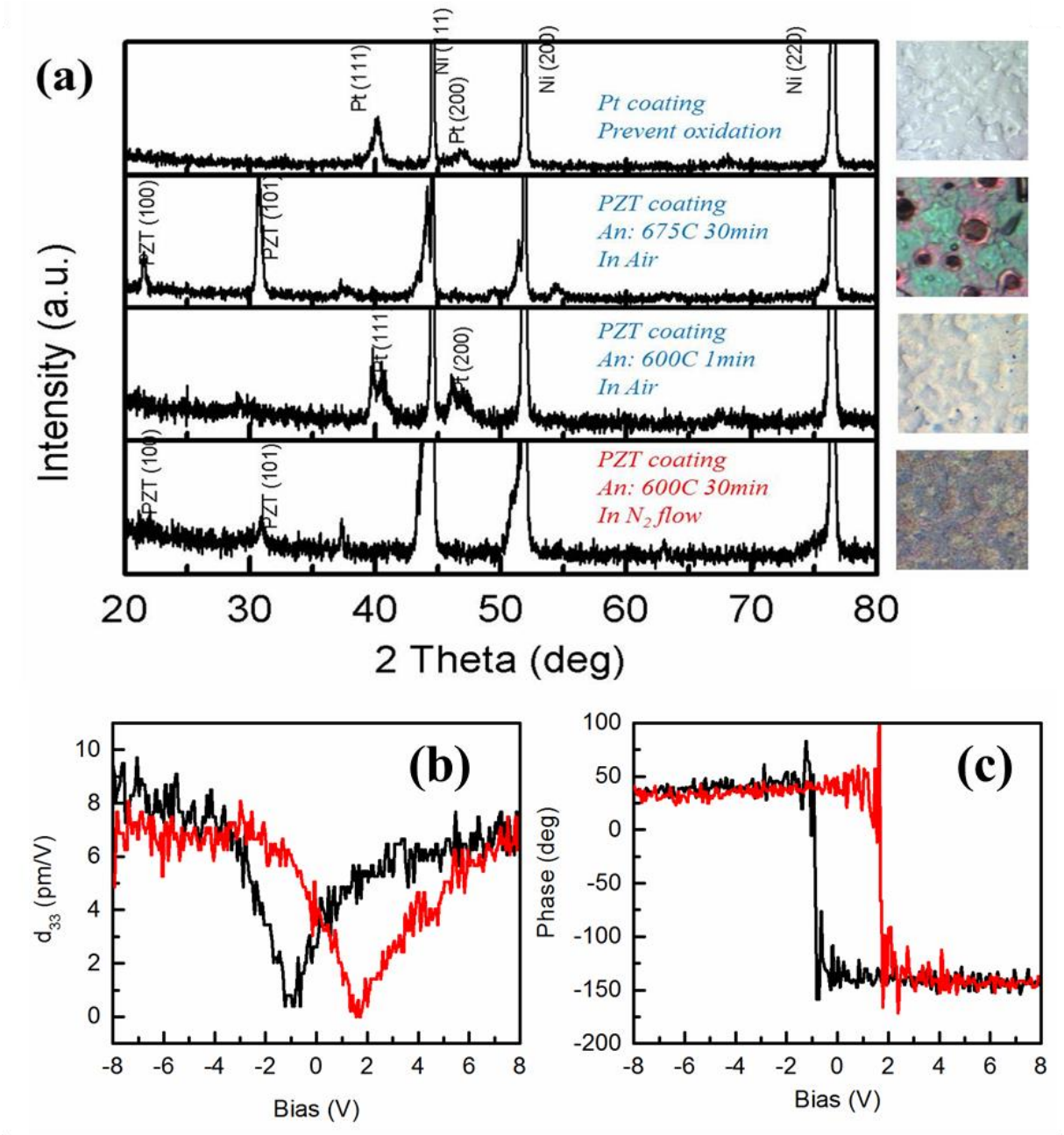

Figure 6.7 (a) XRD diffraction patterns of PZT films deposited on Pt coated Ni; (b) and (c) piezoelectric response and phase angle variation of PZT film annealed under N_2 flow.

Another challenge in the fabrication of thin film devices is the complexity of achieving heterogonous structure as required for the harvesters based upon the ME composites. The conventional top-down patterning process will require multi-step process with expensive masks. Thus, even though these harvesters are intriguing, their implementation for realization of on-chip components is limited. In order to address this issue, the mask-less hybrid synthesis method based on aerosol jet deposition (AD) was also proposed for fabrication of self-biased energy harvester composite structures.

Figure 6.8 demonstrate the capability of using aerosol jet deposition to resemble the Ni-MFC architecture at microscale, PZT film with top Ag electrode were directly printed on Ni foils. Figure 6.8(a) shows the schematic diagram of the zig-zag PZT pattern and Ag inter-digital electrode (IDE) pattern. Figure 6.8(b) shows the picture of as-printed PZT zig-zag pattern on Ni foil. The as-printed PZT film was uniform and maintained the desired morphology. In addition, good adhesion was obtained along the PZT/Ni interface with no sign of delamination. Subsequently, a layer of Ag IDE electrode was printed on top of the PZT layer [Figure 6.8(c)]. Enlarged image of the IDE pattern on PZT layer [Region marked in Figure 6.8(c)] is shown in Figure 6.8(d), where high quality Ag IDE pattern was obtained on as-printed PZT layer. The top inter-digital electrode will help in poling of the PZT film in d_{33} mode. These results demonstrate that we can successfully print and pattern continuous PZT film on Ni substrate without mask or vacuum. The mask-less aerosol jet deposition technique has great potential toward realizing the Ni-MFC architecture at microscale.

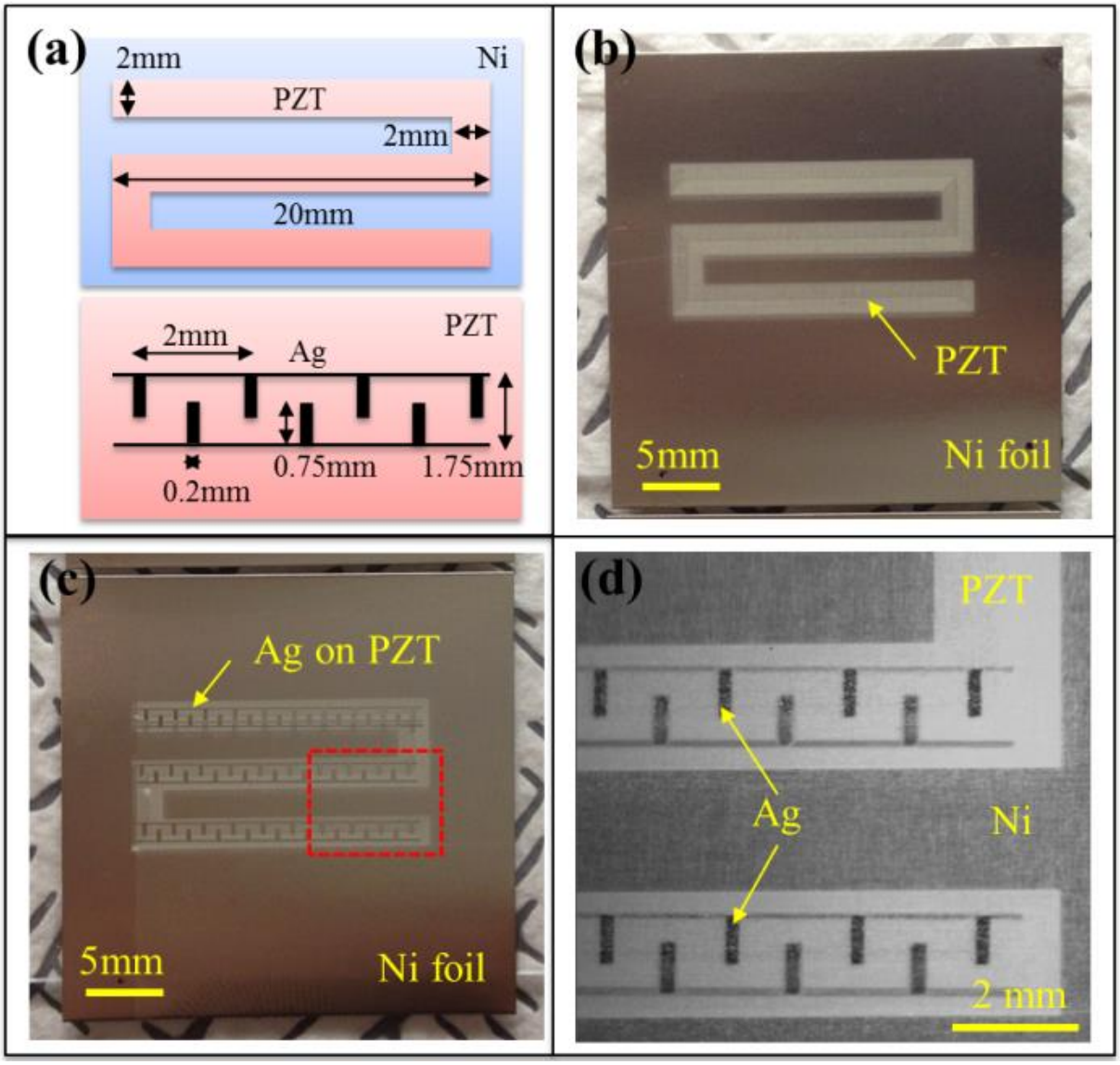

Figure 6.8 (a) Schematic diagram of the PZT pattern on Ni and Ag IDE pattern on PZT; (b) Picture of the as-printed PZT zig-zag pattern on Ni foil; (c) Picture of Ag IDE pattern printed on PZT pattern; (d) Enlarged optical image of Ag IDE pattern on PZT/Ni.

6.4 Chapter summary

In summary of this chapter, the development of magnetoelectric energy harvesters has been reviewed and a novel dual-phase self-biased magnetoelectric energy harvester was detail discussed. In this design, the self-biased composite based energy harvester can simultaneously scavenge magnetic and vibration energy without DC magnetic field. The structure consisted of a piezoelectric macro-fiber composite bonded to a Ni cantilever. Large magnetoelectric coefficient ~50 V/cm.Oe and power density ~4.5 mW/cm^3 (1g acceleration) were observed at the resonance frequency. An additive effect was realized when the harvester operated under dual-phase mode. The increase in voltage output at the first three resonance frequencies under dual-phase mode was found to be 2.4%, 35.5% and 360.7%. These results present significant advancement toward high energy density multimode energy harvesting system.

On the other hand, in this design, the simple structure could be easily incorporate into thick and thin film platform, providing great potential toward MEMS scalable components. Micro-scale piezoelectric film on Ni substrate using sol-gel process and mask-less hybrid synthesis method have all been demonstrated in this study. It is believed that, based on the self-biased ME laminate, these dual-phase energy harvesters could be easily scaled down and implemented into on-chip components.

7. Summary and Perspective

7.1 Summary

In this dissertation, the focus was on the design, synthesis and characterization of the magnetoelectric composites and their implementation in on-resonance applications. The research efforts addressed the challenges of conventional ME composites and their implementation in functional devices. The thesis covered (1) Bulk ME composites, (2) Magnetoelectric nanostructures, (3) Magnetoelectric tunable transformers, and (4) Magnetoelectric energy harvesters. Following are the important accomplishments and learning achieved in this dissertation.

1. In order to eliminate the need for DC magnetic bias to achieve maximum ME voltage coefficient, a self-biased homogenous two-phase ferromagnetic-piezoelectric laminate composite was developed. This ME composites was based on a simple Ni/PZT bilayer laminate structure and was able to exhibit a tunable ME coupling at zero bias. A detailed study was conducted to understand the working mechanism of self-biased effect and its tunable feature. This novel structure with tunable self-biased feature opens the possibility of achieving small scale functional composite for portable magnetic field sensor, energy harvester and other on-chip devices.
2. In order to expand the working bandwidth of conventional ME composites with respect to applied DC magnetic bias, a novel self-biased composite with geometry gradient structure was developed. This gradient ME structure utilized the tunable feature of self-biased laminate and was able to illustrate a near-flat ME response in a wide range of DC bias of

0~260 Oe. This broadened working bandwidth is almost 6.5~38 times higher than conventional ME composites of prior researches. This design provides a new pathway toward high stability ME applications.

3. Ceramic based ME laminate composites with giant self-biased ME voltage coupling coefficient were synthesized using low temperature co-firing technique. The coherent interface and high efficient strain transfer between consecutive phases in the co-fired sample are superior than that of conventional epoxy bonded composites. In addition, the co-firing process is cost-effective and can be easily incorporated into massive production. The build-in stress during co-sintering process and the nature of magnetostrictive hysteresis were found to be origin of the self-biased effect. This co-fired ME composite development provides a cost-effective method of achieving high-performance self-biased ME composites.
4. To better understand and control the growth of ME nanostructure, both microstructural evolution of a continuously piezoelectric BTO film and a well-ordered ME nanocomposite array were synthesized and systematically studied. First, a unique hexagram-shaped morphology evolution of thick BTO film was observed and fully discussed within the framework of structure zone model and dynamic scaling theory. Detailed information regarding of the structure-property relationships were investigated through AFM, TEM and PFM. This is the first demonstration of hexagram-shaped morphology evolution in BTO films and analysis presented here provides comprehensive fundamental understanding of columnar growth and role of twin lamellae structure in enhancing lateral growth. Second, a well-ordered ME nanocomposite array (CFO/PZT)

was developed based on a pre-deposited PZT template. The nanocomposite was synthesized using a novel hybrid deposition method, which was based on the mask less aero-sol jet printing technique. By controlling the grain orientation of the template, nanocomposite arrays with tailored performance were further investigated by conducting MFM and PFM. This hybrid deposition method provides a new way of manipulating well-ordered ME nanocomposite arrays and will help us better understanding the growth of controllable nanostructure and their intergradation into multi-functional devices.

5. To better manipulate the ME nanocomposite interface, 2-2 layered magnetoelectric thin/thick films were first synthesized and investigated, including a sol-gel deposited PZT/CFO/PZT thick film and an ion-bombardment-assisted pulsed laser deposited BTO/CFO thin film. Interfacial microstructure of these heterostructures were found to be tightly related to the corresponding ME response. Coherent interface and large contact area are favorable for enhanced ME coupling. This study helps to understand the nature of elastic coupling through consecutive phases and the interfacial effect toward ME response. Subsequently, a novel complex three-dimensional ME composites with highly anisotropy structure was developed. This complex phase connectivity was designed to solve the inherent leakage and clamping problem of conventional ME composite. Growth-microstructure-property relationships of synthesized complex composites were systematically investigated. The films exhibited excellent ferroelectric response showing the promise of this process. It is expected that by using this hybrid deposition process, highly anisotropic structure could be synthesized with tailored ferroelectric properties and enhanced magnetoelectric coupling.

6. Three types of ME tunable transformers were designed, fabricated and analyzed. The tunable feature is characterized as working resonance frequency and/or maximum voltage gain variation with respect to applied DC magnetic bias. The magnetic-field-induced tunability was found to be tightly related to the ME voltage coupling coefficient and optimum DC bias of the magnetostrictive-piezoelectric laminate composites. For simplicity, the ME transformer can be easily fabricated by direct bonding of Metglas foils onto the output port of a transversely poled piezoelectric transformer, forming an L-T mode ME transformer. This design offers the capability of broaden the working frequency of the transformer under applied DC bias. Next, in order to enhance the ME tunability, an L-L mode epoxy bonded Metlglas/PZT ME transformer was developed. The L-L mode composite exhibited a giant ME coefficient of ~8 V/cm.Oe and therefore leading to a large frequency tunability of 380 Hz under 100 Oe DC magnetic field. However, the large device size and unreliable epoxy bonding hinder their application. To overcome these problems, a unique co-fired ME transformer consisting of two unipoled piezoelectric transformers and a magnetostrictive layer in a laminate configuration was demonstrated. In this design, the ME transformer can not only demonstrate a large tunability of 1.4Hz/Oe, but also provide the potential of implementation into thin film devises.
7. A unique ME energy harvester consists of a piezoelectric micro-fiber composite bonded to a Ni plate in a cantilever configuration was developed and analyzed. This ME energy harvester can simultaneously scavenge magnetic and vibration energy in the absence of DC magnetic field, namely dual-phase self-biased ME energy harvester. Large

magnetoelectric coefficient ~50 V/cm.Oe and power density ~4.5 mW/cm^3 (1g acceleration) were observed at the resonance frequency. An additive effect was realized when the harvester operated under dual-phase mode. The increase in voltage output at the first three resonance frequencies under dual-phase mode was found to be 2.4%, 35.5% and 360.7%. This is the first demonstrate of self-biased ME effect in energy harvester devices and the design presented here provides great potential toward developing MEMS-scalable high performance multimode energy harvesting system for structure health monitoring system.

7.2 Future perspective

1. For single phase homogenous ferromagnetic based self-biased ME composites, it remains to be seen whether there exists other ferromagnetic materials in which the magnetostriction shows large hysteresis in the low field region at room temperature and it can provide a large piezomagnetic coefficient in the absence of DC bias.
2. There have been a lot of theoretical calculation devoted to the conventional ME composite with respect to understating of variables including materials properties, interfacial coupling, and composite connectivity. For self-biased ME composites, although there are some modeling efforts contributing to understand the coupling in functional graded ME composites and non-linear ME effect, but still no theoretical calculation has been conducted on defining the figure of merit for self-biased coupling coefficient.
3. Most of the self-biased effects discussed in this dissertation are direct ME effects, which reflects the polarization variation as a function of magnetic field. However, the effects of electric field E control of magnetization M on the nature of the ME coupling is rarely investigated so far, which is technologically important toward microelectronics applications.
4. A deeper understanding of the built-in stress effect arising from the synthesis conditions (co-firing or thin film deposition) would be helpful toward enhancing the magnetoelectric coupling in co-fired or thin film based ME composites. In particular, the built-in stress resulting in self-biased ME effect is of great importance toward development of thin film self-biased ME composites.

5. Design and structure of complex 3D ME composite thin films should be further modified to achieve enhanced ME coupling coefficient. A further detailed analysis of domain structure with respect to different phase connectivity should be performed.
6. Investigating the growth of piezoelectric film on magnetostrictive substrate would be interesting to obtain further insights about the interfacial coupling and enhancement of the ME response in ME nanostructures.
7. Synthesis of a L-L mode co-fired ME transformer should be performed to achieve a giant frequency tunability for tunable transformer or filter applications. Analysis of the ME tunability of the thin film transformer should be performed.
8. Synthesis of a thin film ME transformer consisting of a piezoelectric thin film transformer on magnetostrictive substrate should be performed. In this case, the substrate is magnetic and should be able to provide more effective strain transfer for frequency tunability under external magnetic field.
9. The near-flat ME response in geometry gradient self-biased ME composite should be extended for the application of energy harvester. In this case, a high stablility ME energy harvester can be achieved regardless of the external magnetic bias.
10. Synthesis of a functional MEMS scale ME energy harvester should be performed.

Publications

(a) Journal papers:

1. *Y. Zhou*, and S. Priya "Review: development of self-biased magnetoelectric composite" (Submitted)
2. *Y. Zhou*, Y. K. Yan, and S. Priya "Co-fired magnetoelectric transformer" *Applied Physic Letters*, 104, 232906, 2014
3. *Y. Zhou*, and S. Priya "Near-flat self-biased magnetoelectric response in geometry gradient composite" *Journal of Applied Physics*, 115, 104107, 2014
4. *Y. Zhou*, D. J. Apo, and S. Priya "Dual-phase self-biased magnetoelectric energy harvester" *Applied Physic Letters*, 103, 192909, 2013
5. *Y. Zhou*, C. S. Park, C. H. Wu, D. Maurya, M. Murayama, A. Kumar, R. S. Katiyar, and S. Priya "Microstructure and surface morphology evolution of pulsed laser deposited piezoelectric $BaTiO_3$ films" *Journal of Materials Chemistry C*, 1(39), 6308, 2013
6. *Y. Zhou*, S. C. Yang, D. J. Apo, D. Maurya, and S. Priya "Tunable self-biased magnetoelectric response in homogenous laminates" *Applied Physic Letters*, 101, 232905, 2012
7. D. R. Patill, *Y. Zhou*, J. Kang, N. Sharpes, D. Jeong, Y. Kim, K. H. Kim, and S. Priya "Anisotropic self-biased dual-phase low frequency magneto-mechano-electric energy harvesters with giant power densities" *APL Materials*, 2, 046102, 2014
8. Y. K. Yan, *Y. Zhou*, and S. Priya "Enhanced magnetoelectric effect in longitudinal-longitudinal mode laminate with co-fired interdigitated electrodes", *Applied Physic Letters*, 104, 032911, 2014
9. Y. K. Yan, *Y. Zhou*, and S. Priya "Enhanced electromechanical coupling in PMN-PT <001>c radially textured cylinders", *Applied Physic Letters*, 104, 012910, 2014

10. Y. K. Yan, *Y. Zhou*, and S. Priya "Giant self-biased magnetoelectric coupling in co-fired textured layered composites", *Applied Physic Letters,* 102, 052907, 2013
11. Y. K. Yan, *Y. Zhou*, S. Gupta, and S. Priya "Fatigue mechanism of textured Pb(Mg1/3Nb2/3)O3-PbTiO3 ceramics" *Applied Physic Letters*, 103, 082906, 2013
12. D. Maurya, *Y. Zhou*, Y. Yan, and S. Priya "Synthesis mechanism of grain-oriented lead-free piezoelectric Na0.5Bi0.5TiO3–BaTiO3 ceramics with giant piezoelectric response" *Journal of Materials Chemistry C*, 1, 2102, 2013
13. N. Wongdamnern, D. Maurya, *Y. Zhou*, M. Sanghadasa, R. Yimnirun, and S. Priya "Complex permittivity scaling of functional graded composites" *Materials Research Express*, 1, 016305, 2014
14. M. K. Hudait, Y. Zhu, N. Jain, D. Maurya, *Y. Zhou*, and S. Priya "Quasi-zero Lattice Mismatch and Band Alignment of BaTiO3 on Epitaxial (110)Ge" *Journal of Applied Physics*, 114, 024303, 2013
15. M. K. Hudait, Y. Zhu, N. Jain, D. Maurya, *Y. Zhou*, R. Varghese, and S. Priya "$BaTiO_3$ Integration with Nanostructured Epitaxial (100),(110) and (111) Germanium for Multifunctional Devices" *ACS applied materials & interfaces*, 5, 11446, 2013
16. R. Varghese, R. Vsiwan, K. Joshi, S. Seifikar, *Y. Zhou*, J. Schwartz, and S. Priya "Magnetostriction measurement in thin films using laser Doppler vibrometry" *Journal of Magnetism and Magnetic Materials*, 363, 179, 2014

(b) Conference proceedings:

1. *Y. Zhou*, C. S. Park, M. Murayama, and S. Priya "Interfacial effects in magnetoelectric thin/thick composite films" *Ceramic Interconnect and Ceramic Microsystems Technologies*, Orlando, FL-USA, April 2013

2. *Y. Zhou*, A. Bhalla, and S. Priya "*Self-biased dual-phase energy harvesting system*" *MRS spring meeting Proceedings*, 13-1556-w01-03, San Francisco, California-USA, 2013

(c) Book Chapters:

1. *Y. Zhou*, D. J. Apo, and S. Priya "Magnetoelectric energy harvester" (Submitted)

(d) Conference Presentations:

1. *Y. Zhou*, and S. Priya "Near-flat self-biased magnetoelectric composite for energy harvester application" *First colloquium on advances in energy harvesting and 5th anniversary celebration of CEHMS 2014*, Roanoke, VA-USA
2. *Y. Zhou*, and S. Priya "MEMS scalable self-biased dual-phase energy harvesting system" *Energy Summit 2013*, UT Dallas, TX-USA
3. *Y. Zhou*, C. S. Park, and S. Priya, "Ion-assisted Growth of BaTiO3/CoFe2O4 Heterostructures in Pulsed Laser Deposition", *EMA 2011*, Jan 19th, Orlando, Florida
4. *Y. Zhou*, C. Folgar, Y. K. Yan, and S. Priya, "Growth and microstructure of Pulsed laser deposition of BTO Thin films on Aerosol Jet printed substrates", *IWMPA 2010*, October 10th, Antalya, Turkey
5. *Y. Zhou*, and S. Priya, "Magnetoelectric composite & Multiferroic thin films", *3rd Annual CIMSS Conference*, March 2010, Roanoke

References

[1] C. W. Nan, M. I. Bichurin, S. X. Dong, D. Viehland, and G. Srinivasan, Journal of Applied Physics **103** (3) (2008).

[2] W. Eerenstein, N. D. Mathur, and J. F. Scott, Nature **442** (7104), 759 (2006).

[3] H. Schmid, Ferroelectrics **162**, 317 (1994).

[4] L. Martin, S. P. Crane, Y. H. Chu, M. B. Holcomb, M. Gajek, M. Huijben, C. H. Yang, N. Balke, and R. Ramesh, Journal of Physics-Condensed Matter **20** (43) (2008).

[5] M. Fiebig, Journal of Physics D-Applied Physics **38** (8), R123 (2005).

[6] W. Prellier, M. P. Singh, and P. Murugavel, Journal of Physics-Condensed Matter **17** (30), R803 (2005).

[7] N. A. Spaldin and M. Fiebig, Science **309** (5733), 391 (2005).

[8] Junyi Zhai, Zengping Xing, Shuxiang Dong, Jiefang Li, and Dwight Viehland, J. Am. Ceram. Soc. **91** (2), 351 (2008).

[9] Shashank Priya, Rashed Islam, Shuxiang Dong, and D. Viehland, Journal of Electroceramics **19** (1), 149 (2007).

[10] G. Srinivasan, Annu Rev Mater Res **40**, 153 (2010).

[11] R. C. Kambale, D. Y. Jeong, and J. Ryu, Adv Cond Matter Phys (2012).

[12] Pedro Martins and Senentxu Lanceros-Méndez, Advanced Functional Materials **23** (27), 3371 (2013).

[13] R. E. Newnham, D. P. Skinner, and L. E. Cross, Mater Res Bull **13** (5), 525 (1978).

[14] R. Ramesh and N. A. Spaldin, Nature Materials **6** (1), 21 (2007).

[15] Shuxiang Dong, Junyi Zhai, Jiefang Li, and D. Viehland, Applied Physics Letters **89**

(25), 252904 (2006).

[16] Junyi Zhai, Zengping Xing, Shuxiang Dong, Jiefang Li, and D. Viehland, Applied Physics Letters **88** (6), 062510 (2006).

[17] Shuxiang Dong, J. F. Li, and D. Viehland, Applied Physics Letters **84** (21), 4188 (2004).

[18] Shuxiang Dong, John G. Bai, Junyi Zhai, Jie-Fang Li, G. Q. Lu, D. Viehland, Shujun Zhang, and T. R. Shrout, Applied Physics Letters **86** (18), 182506 (2005).

[19] G. Srinivasan, E. T. Rasmussen, B. J. Levin, and R. Hayes, Physical Review B **65** (13) (2002).

[20] Deepam Maurya, Yuan Zhou, Yongke Yan, and Shashank Priya, Journal of Materials Chemistry C **1** (11), 2102 (2013).

[21] Yongke Yan, Kyung-Hoon Cho, Deepam Maurya, Amit Kumar, Sergei Kalinin, Armen Khachaturyan, and Shashank Priya, Applied Physics Letters **102** (4), 042903 (2013).

[22] J. Van Den Boomgaard, A. M. J. G. Van Run, and J. Van Suchtelen, Ferroelectrics **10** (1), 295 (1976).

[23] E. Fukada, Ieee T Ultrason Ferr **47** (6), 1277 (2000).

[24] Y. Wang, D. Gray, D. Berry, J. Gao, M. Li, J. Li, and D. Viehland, Advanced materials **23** (35), 4111 (2011).

[25] Y. J. Wang, D. Gray, D. Berry, M. H. Li, J. Q. Gao, J. F. Li, and D. Viehland, J Alloy Compd **513**, 242 (2012).

[26] Y. J. Wang, D. Gray, D. Berry, J. Q. Gao, M. H. Li, J. F. Li, and D. Viehland, Adv

Mater **23** (35), 4111 (2011).

[27] M. H. Li, D. Berry, J. Das, D. Gray, J. F. Li, and D. Viehland, Journal of the American Ceramic Society **94** (11), 3738 (2011).

[28] G. Srinivasan, E. T. Rasmussen, J. Gallegos, R. Srinivasan, Y. I. Bokhan, and V. M. Laletin, Phys Rev B **64** (21), art. no. (2001).

[29] G. Srinivasan, E. T. Rasmussen, B. J. Levin, and R. Hayes, Physical Review B **66** (2) (2002).

[30] Robert Jahns, Andre Piorra, Enno Lage, Christine Kirchhof, Dirk Meyners, Jascha Lukas Gugat, Matthias Krantz, Martina Gerken, Reinhard Knöchel, Eckhard Quandt, and D. J. Green, J. Am. Ceram. Soc. **96** (6), 1673 (2013).

[31] C. A. F. Vaz, J. Hoffman, C. H. Anh, and R. Ramesh, Advanced materials **22** (26-27), 2900 (2010).

[32] C. S. Park, J. Ryu, J. J. Choi, D. S. Park, C. W. Ahn, and S. Priya, Jpn J Appl Phys **48** (8) (2009).

[33] Nam-Kun Oh, Guifang Han, Woon-Ha Yoon, Jong-Jin Choi, Byung-Dong Hahn, Jong-Woo Kim, Cheol-Woo Ahn, Joon Hwan Choi, Dong-Soo Park, Jeong-Joo Kim, Jungho Ryu, and C. W. Nan, J. Am. Ceram. Soc., n/a (2012).

[34] Rahul C. Kambale, Deepak Patil, Jungho Ryu, Yi Sheng Chai, Kee Hoon Kim, Woon-Ha Yoon, Dae-Yong Jeong, Dong-Soo Park, Jong-Woo Kim, Jong-Jin Choi, and Cheol-Woo Ahn, Journal of Physics D: Applied Physics **46** (9), 092002 (2013).

[35] J. Ryu, A. V. Carazo, K. Uchino, and H. E. Kim, Journal of Electroceramics **7** (1), 17 (2001).

[36] A. Safari, M. Allahverdi, and E. K. Akdogan, J. Mater. Sci. **41** (1), 177 (2006).

[37] J. Ma, Z. Shi, and C. W. Nan, Adv Mater **19** (18), 2571 (2007).

[38] K. J. Choi, M. Biegalski, Y. L. Li, A. Sharan, J. Schubert, R. Uecker, P. Reiche, Y. B. Chen, X. Q. Pan, V. Gopalan, L. Q. Chen, D. G. Schlom, and C. B. Eom, Science **306** (5698), 1005 (2004).

[39] H. Zheng, J. Wang, S. E. Lofland, Z. Ma, L. Mohaddes-Ardabili, T. Zhao, L. Salamanca-Riba, S. R. Shinde, S. B. Ogale, F. Bai, D. Viehland, Y. Jia, D. G. Schlom, M. Wuttig, A. Roytburd, and R. Ramesh, Science **303** (5658), 661 (2004).

[40] Kyung-Hoon Cho and Shashank Priya, Applied Physics Letters **98** (23), 232904 (2011).

[41] S. X. Dong, J. Y. Zhai, J. F. Li, and D. Viehland, Applied Physics Letters **89** (25) (2006).

[42] M. I. Bichurin, D. A. Filippov, V. M. Petrov, V. M. Laletsin, N. Paddubnaya, and G. Srinivasan, Physical Review B **68** (13) (2003).

[43] M. Bichurin, V. Petrov, Yu Kiliba, and G. Srinivasan, Physical Review B **66** (13) (2002).

[44] M. Bichurin, V. Petrov, O. Ryabkov, S. Averkin, and G. Srinivasan, Physical Review B **72** (6) (2005).

[45] V. M. Petrov, G. Srinivasan, M. I. Bichurin, and T. A. Galkina, Journal of Applied Physics **105** (6), 063911 (2009).

[46] Y. Zhou, S. C. Yang, D. J. Apo, D. Maurya, and S. Priya, Appl Phys Lett **101** (23) (2012).

[47] J. Q. Gao, D. Gray, Y. Shen, J. F. Li, and D. Viehland, Applied Physics Letters **99** (15) (2011).

[48] Z. Fang, S. G. Lu, F. Li, S. Datta, Q. M. Zhang, and M. El Tahchi, Appl Phys Lett **95** (11) (2009).

[49] V. M. Laletin, N. Paddubnaya, G. Srinivasan, C. P. De Vreugd, M. I. Bichurin, V. M. Petrov, and D. A. Filippov, Applied Physics Letters **87** (22), 222507 (2005).

[50] S. K. Mandal, G. Sreenivasulu, V. M. Petrov, and G. Srinivasan, Applied Physics Letters **96** (19) (2010).

[51] S. C. Yang, C. S. Park, K. H. Cho, and S. Priya, J Appl Phys **108** (9) (2010).

[52] S. K. Mandal, G. Sreenivasulu, V. M. Petrov, and G. Srinivasan, Physical Review B **84** (1) (2011).

[53] G. Sreenivasulu, S. K. Mandal, S. Bandekar, V. M. Petrov, and G. Srinivasan, Physical Review B **84** (14) (2011).

[54] U. Laletin, G. Sreenivasulu, V. M. Petrov, T. Garg, A. R. Kulkarni, N. Venkataramani, and G. Srinivasan, Physical Review B **85** (10) (2012).

[55] S. C. Yang, C. W. Ahn, K. H. Cho, and S. Priya, J. Am. Ceram. Soc. **94** (11), 3889 (2011).

[56] S. C. Yang, K. H. Cho, C. S. Park, and S. Priya, Appl Phys Lett **99** (20) (2011).

[57] E. Lage, C. Kirchhof, V. Hrkac, L. Kienle, R. Jahns, R. Knochel, E. Quandt, and D. Meyners, Nature Materials **11** (6), 523 (2012).

[58] Tiberiu-Dan Onuta, Yi Wang, Christian J. Long, and Ichiro Takeuchi, Applied Physics Letters **99** (20), 203506 (2011).

[59] Y. M. Jia, S. W. Or, H. L. W. Chan, X. Y. Zhao, and H. S. Luo, Appl Phys Lett **88** (24) (2006).

[60] Y. J. Wang, F. F. Wang, S. W. Or, H. L. W. Chan, X. Y. Zhao, and H. S. Luo, Applied Physics Letters **93** (11) (2008).

[61] S. X. Dong, J. Y. Zhai, J. F. Li, and D. Viehland, Appl Phys Lett **88** (8) (2006).

[62] S. X. Dong, J. F. Li, and D. Viehland, Applied Physics Letters **84** (21), 4188 (2004).

[63] S. X. Dong, J. F. Li, D. Viehland, J. Cheng, and L. E. Cross, Applied Physics Letters **85** (16), 3534 (2004).

[64] Y. M. Jia, H. S. Luo, X. Y. Zhao, and F. F. Wang, Advanced materials **20** (24), 4776 (2008).

[65] M. I. Bichurin, V. M. Petrov, Y. V. Kiliba, and G. Srinivasan, Physical Review B **66** (13) (2002).

[66] S. X. Dong, J. Y. Zhai, J. F. Li, D. Viehland, and S. Priya, Applied Physics Letters **93** (10) (2008).

[67] S. Priya, J. Ryu, C. S. Park, J. Oliver, J. J. Choi, and D. S. Park, Sensors **9** (8), 6362 (2009).

[68] V. K. Vlasko-Vlasov, Y. K. Lin, D. J. Miller, U. Welp, G. W. Crabtree, and V. I. Nikitenko, Phys Rev Lett **84** (10), 2239 (2000).

[69] S. Ito, K. Aso, Y. Makino, and S. Uedaira, Appl Phys Lett **37** (7), 665 (1980).

[70] S. X. Dong and J. Y. Zhai, Chinese Sci Bull **53** (14), 2113 (2008).

[71] C. M. Van der Burgt, Philips. Res. Rep. **8**, 91 (1953).

[72] J. A. Osborn, Phys. Rev. **67** (1945).

[73] W. F. Brown, *Handbook of Chemistry and Physics*. (McGraw-Hill, New York, 1958).

[74] Yuan Zhou and Shashank Priya, Journal of Applied Physics **115** (10), 104107 (2014).

[75] C. M. Chang and G. P. Carman, Phys Rev B **76** (13) (2007).

[76] R. C. Kambale, W. H. Yoon, D. S. Park, J. J. Choi, C. W. Ahn, J. W. Kim, B. D. Hahn, D. Y. Jeong, B. C. Lee, G. S. Chung, and J. Ryu, J Appl Phys **113** (20) (2013).

[77] C. S. Park, C. W. Ahn, J. Ryu, W. H. Yoon, D. S. Park, H. E. Kim, and S. Priya, J Appl Phys **105** (9) (2009).

[78] Y. K. Yan, Y. Zhou, and S. Priya, Applied Physics Letters **102** (5) (2013).

[79] J. Ma, J. M. Hu, Z. Li, and C. W. Nan, Adv Mater **23** (9), 1062 (2011).

[80] C. S. Park, J. Evans, and S. Priya, Smart Mater. Struct. **20** (8) (2011).

[81] C. S. Park and S. Priya, J. Am. Ceram. Soc. **94** (4), 1087 (2011).

[82] Y. K. Yan, Y. U. Wang, and S. Priya, Appl Phys Lett **100** (19) (2012).

[83] S. E. Park and T. R. Shrout, J Appl Phys **82** (4), 1804 (1997).

[84] H. X. Fu and R. E. Cohen, Nature **403** (6767), 281 (2000).

[85] Y. J. Chen, S. M. Gillette, T. Fitchorov, L. P. Jiang, H. B. Hao, J. H. Li, X. X. Gao, A. Geiler, C. Vittoria, and V. G. Harris, Applied Physics Letters **99** (4) (2011).

[86] Inc. American Piezo Ceramics, *Piezoelectric Ceramics Materials Properties*. (Mackeyville, PA, 1998).

[87] K. H. Cho, C. S. Park, and S. Priya, Applied Physics Letters **97** (18) (2010).

[88] M. T. Buscaglia, M. Viviani, V. Buscaglia, L. Mitoseriu, A. Testino, P. Nanni, Z. Zhao, M. Nygren, C. Harnagea, D. Piazza, and C. Galassi, Phys Rev B **73** (6) (2006).

[89] R. A. Mckee, F. J. Walker, E. D. Specht, G. E. Jellison, L. A. Boatner, and J. H. Harding, Phys Rev Lett **72** (17), 2741 (1994).

[90] Y. Yano, K. Iijima, Y. Daitoh, T. Terashima, Y. Bando, Y. Watanabe, H. Kasatani, and H. Terauchi, J Appl Phys **76** (12), 7833 (1994).

[91] M. N. Kamalasanan, N. D. Kumar, and S. Chandra, J Appl Phys **74** (9), 5679 (1993).

[92] H. Tabata, H. Tanaka, and T. Kawai, Appl Phys Lett **65** (15), 1970 (1994).

[93] K. Fujimoto, Y. Kobayashi, and K. Kubota, Thin Solid Films **169** (2), 249 (1989).

[94] D. L. Polla and L. F. Francis, Annu Rev Mater Sci **28**, 563 (1998).

[95] C. W. Nan, M. I. Bichurin, S. X. Dong, D. Viehland, and G. Srinivasan, J Appl Phys **103** (3) (2008).

[96] Yuan Zhou, Chee-Sung Park, Chun-Hsien Wu, Deepam Maurya, Mitsuhiro Murayama, Ashok Kumar, R. S. Katiyar, and Shashank Priya, Journal of Materials Chemistry C **1** (39), 6308 (2013).

[97] W. L. Winterbottom, Acta Metallurgica **15** (2), 303 (1967).

[98] L. D. Marks, Rep Prog Phys **57** (6), 603 (1994).

[99] E. Ringe, R. P. Van Duyne, and L. D. Marks, Nano Lett **11** (8), 3399 (2011).

[100] A. van der Drift, Philips Res. Repts **22** (1967).

[101] M. DiDomenico, S. H. Wemple, S. P. S. Porto, and R. P. Bauman, Physical Review **174** (2), 522 (1968).

[102] N. Ortega, A. Kumar, O. A. Maslova, Y. I. Yuzyuk, J. F. Scott, and R. S. Katiyar, Phys Rev B **83** (14) (2011).

[103] R. S. Katiyar, J. F. Ryan, and J. F. Scott, Phys Rev B **4** (8), 2635 (1971).

[104] Margarita Correa, Ashok Kumar, Shashank Priya, R. S. Katiyar, and J. F. Scott, Phys Rev B **83** (1), 014302 (2011).

[105] O. A. Maslova, Yu I. Yuzyuk, N. Ortega, A. Kumar, and R. S. Katiyar, Phys Solid State+ **53** (5), 1062 (2011).

[106] H. M. Zheng, F. Straub, Q. Zhan, P. L. Yang, W. K. Hsieh, F. Zavaliche, Y. H. Chu, U. Dahmen, and R. Ramesh, Adv Mater **18** (20), 2747 (2006).

[107] H. F. Cheng, M. H. Yeh, K. S. Liu, and I. N. Lin, Jpn J Appl Phys 1 **32** (12A), 5656 (1993).

[108] I. D. Kim, Y. Avrahami, H. L. Tuller, Y. B. Park, M. J. Dicken, and H. A. Atwater, Appl Phys Lett **86** (19) (2005).

[109] Adriana E. Lita and John E. Sanchez, Phys Rev B **61** (11), 7692 (2000).

[110] J. A. Thornton, Annu Rev Mater Sci **7**, 239 (1977).

[111] R. Messier, Journal of Vacuum Science & Technology a-Vacuum Surfaces and Films **4** (3), 490 (1986).

[112] D. Y. Kim, S. G. Lee, Y. K. Park, and S. J. Park, Jpn J Appl Phys 1 **36** (12A), 7307 (1997).

[113] Rongsheng Cai, Yiqian Wang, Xuehua Liu, Weiwei Gao, Yunzhong Chen, Jirong Sun, and Yanguo Wang, J Am Ceram Soc **96** (5), 1660 (2013).

[114] Christopher Roland and Hong Guo, Phys Rev Lett **66** (16), 2104 (1991).

[115] Jian Hua Yao and Hong Guo, Phys Rev E **47** (2), 1007 (1993).

[116] E. Vasco, C. Zaldo, and L. Vazquez, J Phys-Condens Mat **13** (28), L663 (2001).

[117] Albert-László Barabási and H. Eugene Stanley, *Fractal concepts in surface growth*. (Press Syndicate of the University of Cambridge, New York, NY, USA, 1995), pp.xx.

[118] E. Vasco, C. Polop, and C. Ocal, Eur Phys J B **35** (1), 49 (2003).

[119] M. K. Kang, Y. S. Yoo, D. Y. Kim, and N. M. Hwang, J Am Ceram Soc **83** (2), 385 (2000).

[120] E. A. D. White, Acta Cryst. **8** (1955).

[121] C. L. Jia and A. Thust, Phys Rev Lett **82** (25), 5052 (1999).

[122] C. L. Jia, K. Urban, M. Mertin, S. Hoffmann, and R. Waser, Philos Mag A **77** (4), 923 (1998).

[123] J. W. Jang, W. J. Cho, J. H. Lee, S. S. Choi, and T. S. Hahn, Jpn J Appl Phys 1 **36** (11), 6942 (1997).

[124] J. W. Jang, Y. H. Kim, T. S. Hahn, S. S. Choi, and S. J. Chung, Japanese Journal of Applied Physics Part 2-Letters **35** (6A), L699 (1996).

[125] J. E. Taylor, J. W. Cahn, and C. A. Handwerker, Acta Metall Mater **40** (7), 1443 (1992).

[126] J. W. Matthews, S. Mader, and T. B. Light, J Appl Phys **41** (9), 3800 (1970).

[127] H. Zheng, Q. Zhan, F. Zavaliche, M. Sherburne, F. Straub, M. P. Cruz, L. Q. Chen, U. Dahmen, and R. Ramesh, Nano Lett **6** (7), 1401 (2006).

[128] G. Srinivasan, E. T. Rasmussen, J. Gallegos, R. Srinivasan, Y. I. Bokhan, and V. M. Laletin, Physical Review B **6421** (21), art. no. (2001).

[129] G. Srinivasan, E. T. Rasmussen, and R. Hayes, Physical Review B **67** (1) (2003).

[130] C. S. Park, J. W. Lee, G. T. Park, H. E. Kim, and J. J. Choi, J Mater Res **22** (5), 1367

(2007).

[131] L. Qiao and X. F. Bi, Journal of the European Ceramic Society **29** (10), 1995 (2009).

[132] S. X. Dong, J. Y. Zhai, S. Priya, J. F. Li, and D. Viehland, Ieee T Ultrason Ferr **56** (6), 1124 (2009).

[133] Rashed A. Islam, Hyeoungwoo Kim, Shashank Priya, and Harry Stephanou, Appl Phys Lett **89** (15), 152908 (2006).

[134] S. Priya, S. Ural, H. W. Kim, K. Uchino, and T. Ezaki, Jpn. J. Appl. Phys. Part 1 - Regul. Pap. Short Notes Rev. Pap. **43** (6A), 3503 (2004).

[135] G. Srinivasan, C. P. De Vreugd, V. M. Laletin, N. Paddubnaya, M. I. Bichurin, V. M. Petrov, and D. A. Filippov, Physical Review B **71** (18) (2005).

[136] J. Y. Y. Zhai, S. X. Dong, Z. P. P. Xing, J. Q. Gao, J. F. F. Li, and D. Viehland, J Phys D Appl Phys **42** (12) (2009).

[137] Y. Zhao, V. Bedekar, A. Aning, and S. Priya, Mater Lett **74**, 151 (2012).

[138] Yuan Zhou, Yongke Yan, and Shashank Priya, Applied Physics Letters **104** (23), 232906 (2014).

[139] P. Laoratanakul, A. V. Carazo, P. Bouchilloux, and K. Uchino, Jpn J Appl Phys 1 **41** (3A), 1446 (2002).

[140] Shashank Priya, Seyit Ural, Hyeoung Woo Kim, Kenji Uchino, and Toru Ezaki, Jpn J Appl Phys **43** (6A), 3503 (2004).

[141] Chee-Sung Park and Shashank Priya, J Am Ceram Soc **94** (4), 1087 (2011).

[142] Yongke Yan, Yuan Zhou, and Shashank Priya, Appl Phys Lett **102** (5), 052907

(2013).

[143] S. Priya, Ieee T Ultrason Ferr **53** (1), 23 (2006).

[144] H. S. Jeong, B. C. Choi, J. H. Yoo, I. H. Im, and C. Y. Park, Jpn J Appl Phys 1 **38** (9A), 5166 (1999).

[145] C. Israel, V. M. Petrov, G. Srinivasan, and N. D. Mathur, Appl Phys Lett **95** (7), 072505 (2009).

[146] G. Srinivasan, C. De Vreugd, V. Laletin, N. Paddubnaya, M. Bichurin, V. Petrov, and D. Filippov, Phys Rev B **71** (18) (2005).

[147] B. Lewis and R. Street, Proceedings of the Physical Society **72** (4), 604 (1958).

[148] Z. J. Zuo, D. A. Pan, Y. M. Jia, S. G. Zhang, and L. J. Qiao, Aip Adv **3** (12) (2013).

[149] V. Bedekar, R. A. Islam, H. Kim, M. I. Bichurin, S. N. Ivanov, Y. J. Pukinski, and S. Priya, The European Physical Journal B **71** (3), 387 (2009).

[150] M. Karmarkar, S. X. Dong, J. F. Li, D. Viehland, and S. Priya, Phys Status Solidi-R **2** (3), 108 (2008).

[151] Li Lv, Jian-Ping Zhou, Yang-Yang Guo, Peng Liu, and Huai-Wu Zhang, Journal of Physics D: Applied Physics **44** (5), 055002 (2011).

[152] Hyeoungwoo Kim, Rashed A. Islam, and Shashank Priya, Appl Phys Lett **90** (1), 012909 (2007).

[153] S. B. Majumder, Y. N. Mohapatra, and D. C. Agrawal, Ferroelectrics **215** (1-4), 1 (1998).

[154] C. S. Park, A. Khachaturyan, and S. Priya, Appl Phys Lett **100** (19) (2012).

[155] Daniel Jolomi Apo, Mohan Sanghadasa, and Shashank Priya, Energy Harvesting

and Systems **1** (1), 1 (2014).

[156] S. Priya, J. Ryu, C. S. Park, J. Oliver, J. J. Choi, and D. S. Park, Sensors **9** (8), 6362 (2009).

[157] S. P. Beeby, M. J. Tudor, and N. M. White, Measurement Science and Technology **17** (12), R175 (2006).

[158] J. A. Paradiso and T. Starner, Ieee Pervas Comput **4** (1), 18 (2005).

[159] P. Li, Y. M. Wen, and L. X. Bian, Applied Physics Letters **90** (2) (2007).

[160] Thomas Lafont, L. Gimeno, J. Delamare, G. A. Lebedev, D. I. Zakharov, B. Viala, O. Cugat, N. Galopin, L. Garbuio, and O. Geoffroy, Journal of Micromechanics and Microengineering **22** (9) (2012).

[161] Steven R. Anton and Henry A. Sodano, Smart Materials and Structures **16** (3), R1 (2007).

[162] H. A. Sodano, D. J. Inman, and G. Park, The Shock and Vibration Digest **36** (2004).

[163] S. Roundy and P. K. Wright, Smart Mater Struct **13** (5), 1131 (2004).

[164] Y. Tadesse, S. J. Zhang, and S. Priya, Journal of Intelligent Material Systems and Structures **20** (5), 625 (2009).

[165] Xiaoling Bai, Yumei Wen, Jin Yang, Ping Li, Jing Qiu, and Ying Zhu, Journal of Applied Physics **111** (7), 07A938 (2012).

[166] Y. Zhu and J. W. Zu, Ieee T Magn **48** (11), 3344 (2012).

[167] X. Xing, J. Lou, G. M. Yang, O. Obi, C. Driscoll, and N. X. Sun, Appl Phys Lett **95** (13) (2009).

[168] L. Wang and F. G. Yuan, Smart Materials and Structures **17** (4) (2008).

[169] A. Khaligh, P. Zeng, and C. Zheng, Ieee T Ind Electron **57** (3), 850 (2010).

[170] Ping Li, Yumei Wen, Jia Chaobo, and Li Xinshen, Industrial Electronics, IEEE Transactions on **58** (7), 2944 (2011).

[171] S. Priya, R. Islam, S. X. Dong, and D. Viehland, J Electroceram **19** (1), 149 (2007).

[172] Ce-Wen Nan, M. I. Bichurin, Shuxiang Dong, D. Viehland, and G. Srinivasan, J Appl Phys **103** (3), 031101 (2008).

[173] J. Q. Gao, D. Hasanyan, Y. Shen, Y. J. Wang, J. F. Li, and D. Viehland, Journal of Applied Physics **112** (10) (2012).

[174] Shashank Priya, Journal of Electroceramics **19** (1), 167 (2007).

[175] Xianzhi Dai, Yumei Wen, Ping Li, Jin Yang, and Gaoyong Zhang, Sensors and Actuators a-Physical **156** (2), 350 (2009).

[176] Xianzhi Dai, Yumei Wen, Ping Li, Jin Yang, and Ming Li, Sensors and Actuators a-Physical **166** (1), 94 (2011).

[177] Ming Li, Yumei Wen, Ping Li, Jin Yang, and Xianzhi Dai, Sensors and Actuators a-Physical **166** (1), 102 (2011).

[178] Jin Yang, Yumei Wen, and Ping Li, Journal of Intelligent Material Systems and Structures **22** (14), 1631 (2011).

[179] Jin Yang, YuMei Wen, Ping Li, and XiaoLing Bai, Science China-Technological Sciences **54** (6), 1419 (2011).

[180] S. D. Moss, J. E. McLeod, I. G. Powlesland, and S. C. Galea, Sensors and Actuators a-Physical **175**, 165 (2012).

[181] Suna Ju, Song Hee Chae, Yunhee Choi, Seungjun Lee, Hyang Woon Lee, and

Chang-Hyeon Ji, Smart Materials and Structures **22** (11), 115037 (2013).

[182] Rahul C. Kambale, Woon-Ha Yoon, Dong-Soo Park, Jong-Jin Choi, Cheol-Woo Ahn, Jong-Woo Kim, Byung-Dong Hahn, Dae-Yong Jeong, Byung Chul Lee, Gwiy-Sang Chung, and Jungho Ryu, Journal of Applied Physics **113** (20), 204108 (2013).

[183] Yuan Zhou, Daniel J. Apo, and Shashank Priya, Applied Physics Letters **103** (19), 192909 (2013).

[184] Y. Zhou, D. J. Apo, and S. Priya, Applied Physics Letters **103** (19) (2013).

[185] K. H. Cho and S. Priya, Appl Phys Lett **98** (23) (2011).

[186] S. K. Mandal, G. Sreenivasulu, V. M. Petrov, and G. Srinivasan, Appl Phys Lett **96** (19), 192502 (2010).